ORNL/Sub--88-SC863

DE92 007797

HEMP-INDUCED TRANSIENTS IN ELECTRIC POWER SUBSTATIONS

FINAL REPORT

C. M. Wiggins
D. E. Thomas
T. M. Salas

February 1992

BDM INTERNATIONAL, INC.
1801 Randolph Road S.E.
Albuquerque, New Mexico 87106

Prepared under Subcontract 17X-SC863V
for
OAK RIDGE NATIONAL LABORATORY
P.O. Box 2008
Oak Ridge, Tennessee 37831-6285
managed by
MARTIN MARIETTA ENERGY SYSTEMS, INC.
for the
U.S. DEPARTMENT OF ENERGY
under Contract No. DE-AC05-840R21400

FOREWORD

The Division of Electric Energy Systems (EES) of the United States Department of Energy (DOE) has formulated a program for the research and development of technologies and systems for the assessment, operation, and control of electric power systems when subjected to electromagnetic pulse (EMP). The DOE/EES EMP program plan is documented in a DOE report entitled Program Plan for Research and Development of Technologies and Systems for Electric Power Systems Under the Influence of Nuclear Electromagnetic Pulses, DOE/NBB-003, May 1983. The research documented in this ORNL report was conducted under program plan elements E1 and E2.

The research documented in this report considers issues associated with High-Altitude Electromagnetic Pulse (HEMP) interaction with substation high-voltage primary circuits and low-voltage control circuits. This work assesses HEMP-induced stresses, effects, and mitigation techniques on substation control and protection circuits.

ACKNOWLEDGEMENTS

We would like to thank the following :

Oak Ridge National Laboratory/ Martin Marietta Energy Systems, Inc. - P. R. Barnes for helpful discussions and suggestions.

Electric Power Research Institute - Dr. S. E. Wright and Mr. S. L. Nilsson for making results and models from EPRI project RP2674-1 available to support this effort.

Dr. F. M. Tesche, consultant, for careful reviews and helpful suggestions.

ABB Power Systems, Inc. - C. Eichler and V. J. Kruse for providing relays and surge protection packages for testing.

J. J. Bonk, ABB consultant, for identifying possible modes for relay circuit upset and failure.

R. P. Curtner, Public Service Company of New Mexico for help in configuring the relay test circuit.

D. Volska, for his helpful review of this report.

TABLE OF CONTENTS

TABLE OF CONTENTS

TABLE OF CONTENTS

TABLE OF CONTENTS

LIST OF FIGURES

LIST OF FIGURES

LIST OF FIGURES

LIST OF FIGURES

LIST OF FIGURES

LIST OF TABLES

ABSTRACT

A nuclear detonation in or above the earth's atmosphere produces an intense electromagnetic pulse (EMP). A large portion of the EMP electromagnetic energy is within the RF spectrum. The EMP produced by a nuclear detonation is often referred to as nuclear EMP (NEMP). The electromagnetic fields radiated by the blast vary greatly with weapon characteristics, yield, and detonation height. A detonation at high altitudes above 40 km produces an EMP called high-altitude EMP (HEMP). HEMP is a steep-front short duration transient with a rise time on the order of a few nanoseconds which decays to near zero in less than a microsecond. A single high-altitude burst can subject much of the continental United States to intense HEMP electric fields on the order of tens of kilovolts per meter. The intense transient HEMP will induce fast transients in high-voltage transmission lines and bus structures, instrumentation cables, and control wires in power transmission and distribution (T&D) substations. A system of traveling wave coupling models for a 500 kV substation, including models for the high voltage primary bus, components (circuit breakers, disconnect switches, power transformers, and current and voltage instrument transformers), low voltage control wiring circuits, and a number of conducted and radiated interference coupling modes, had been developed earlier by EPRI under project RP2674-1 to study substation interference effects caused by switching transients, faults, and lightning. These EPRI models served as the baseline for the present HEMP coupling investigations. The HEMP effects on protective relays were assessed for a nominal HEMP environment using several new field coupling models merged with the switching transient data. It is found that a representative solid state relay is unlikely to be damaged or to misoperate by the nominal HEMP threat with a peak field strength of 50 kV/m. However, it is possible for both DC control wires to flash over to ground simultaneously, causing fuses to blow and placing the relay in an inoperative state.

EXECUTIVE SUMMARY

Calculations of CHAP-fit HEMP coupling to relay circuits are made using models validated against switching transient measurements in transmission substations. The incident HEMP fields were compared with the electromagnetic fields generated by disconnect switching transients. The current and voltage transients induced by HEMP and switching transients in relay control wiring in air-insulated substations were also compared. The results show considerable overlap in terms of amplitudes, bandwidths, and other norms. Measured data and predictions are used to assess interference levels at relay inputs. The predictions are developed using traveling wave models for a substation with both long connected transmission lines and relay control wiring. Transfer functions for important radiated and conducted coupling mechanisms are determined and described. Coupling via parasitic (primary-to-secondary) capacitance of a current transformer (CT), field to cable shield, cable shield to wire transfer impedance, and inductive shield pigtail to wire are considered. Effects of relay load impedance versus frequency on the resulting interference current and voltage wave shapes are calculated using measured impedances for a representative relay.

Short range HEMP is the very intense HEMP located in a region a relatively short distance south of the burst point. It was found to produce the maximum HEMP stress on substation equipment. Short range HEMP is characterized as a steep front (5 ns risetime) electric field transient with a peak amplitude of 50 kV/m, decaying in about 100 ns as seen at the substation. Predicted coupling of short range HEMP to shielded control wires produced maximum transient currents of 12.7 A and voltages of 1.4 kV at the relay. These values are less than those predicted for worst-case switching transients (currents of 24.3 A and voltages of 4.9 kV at the relay). The large switching transient responses are due mainly to the conducted coupling mechanism, which is very effective at intermediate (switching transient) frequencies. For other coupling mechanisms, most notably field coupling to cables and cable shields, the HEMP-induced voltages were comparable to the

switching transient responses, and the HEMP-induced currents were found to be larger than those for switching transients. HEMP-like transients injected into a transformer differential relay caused flashovers at nominal voltages of 5 kV and higher, and an upset/failure (susceptibility) occurred at 12.3 kV on the relay battery wiring.

When predicted HEMP stresses were compared to the measured relay susceptibility, there was no vulnerability. Instead, the survivability margin for this relay ranged from 6 dB to 20 dB depending on the calculated range of HEMP stresses. However, since no other relays were tested for susceptibilities, no general statement regarding relay vulnerability to HEMP can be drawn from these studies. When the expected HEMP relay control wire stresses were compared with relay surge withstand capability (SWC) test waveforms, no margin was found. This suggests that mitigation could be required.

The susceptibility of relay battery (DC) circuit wiring is of concern since these wires are commonly unshielded. Therefore, the levels at which failures occur in other relays should be investigated more thoroughly and compared to the expected HEMP stresses. Surge protection packages, normally used on AC wires, were found to raise flashover thresholds by more than a factor of 2 on DC circuits and thus are effective in mitigating HEMP. The surge protection device is a shunt 0.5 microfarad capacitor between each wire and ground.

1.0 INTRODUCTION

1.1 OBJECTIVE

The objective of this study is to compare substation switching transients with HEMP induced transients, and to obtain an indication of the HEMP vulnerability of control and protective relay circuits. This study estimates the stresses and effects of a high-altitude electromagnetic pulse (HEMP) on a representative high voltage transmission substation and its protective relay circuits. HEMP stresses from direct field illumination at relatively high-angle incidence on the substation, as well as from currents driven into the substation from attached long transmission lines excited by HEMP at grazing incidence angles, are calculated. Conducted and radiated coupling from HEMP sources to relay control wiring are calculated as transient current and voltage stresses at representative relay loads. These stresses are compared with measured upset and failure levels for a representative relay in order to estimate potential relay circuit vulnerability to HEMP. Mitigation techniques and their effectiveness are assessed experimentally for a representative relay protection package.

HEMP sources and effects are also related to measured and predicted electromagnetic interference (EMI) caused by disconnect switching transients in substations.

1.2 BACKGROUND

A HEMP is produced as a by-product of the decay of radiation from a nuclear detonation as it interacts with the atmosphere. If a nuclear burst occurred at high altitude above Kansas or Oklahoma, HEMP would be produced across most of the continental United States. Since HEMP is a large amplitude electromagnetic field transient with broad spectral content, it would interact nearly simultaneously with the entire U.S. electric power grid. Typically, the unclassified HEMP electric fields are characterized by peak amplitudes of 50 kV/m occurring within several nanoseconds of the initial rise of the pulse and falling to 1/e of peak within a few hundred nanoseconds. In addition,

very low frequency tailing amplitudes of only a few volts/m may persist for several minutes. Therefore, significant spectral amplitudes exist from DC to more than 100 MHz. There is concern that HEMP may produce potentially disruptive EMI effects in the electric power grid. A particular focus of this concern for the present study are HEMP-induced interference effects in power transmission substations, especially in their protective relay and control circuits. In project RP2674-1, the Electric Power Research Institute (EPRI) has ongoing investigations to determine the effects caused by substation switching transients on protective circuits [1]. Under the EPRI project, a large measured database of conducted and radiated EMI sources and their coupling into control wiring circuits has been developed. Models characterizing the origin, propagation, and coupling of EMI within the substation have also been developed and validated against the measured data in EPRI RP2674-1. Using these data, comparisons between HEMP and switching transient EMI can be made at several levels within substations: transient currents induced directly on the high voltage primary bus, transient electric and magnetic fields incident to ground, and resultant voltages and currents coupled into control wiring at protective relays. Furthermore, the transfer functions determined in project RP2674-1 provide a means for increasing the reliability of estimates of HEMP coupling effects on control wire circuits.

1.3 APPROACH

The overall approach of this project was to use the methods and results developed for substation switching transient EMI under EPRI RP2674-1, extending them where necessary to include HEMP sources, coupling, and effects.

In RP2674-1, traveling-wave models were developed describing switching transients in 115 kV through 500 kV substations [1]. These models characterize switching transient EMI at three levels: as voltage and current transients on the high voltage primary bus; as transient electric and magnetic fields resulting from bus excitations; and as voltage and current transients from these conducted and radiated excitations coupled in various ways to control wiring as seen near relay equipment.

1.3.1 Model Substation

The substation is modeled as a single phase network of components (circuit breakers, disconnect switches, transformers, capacitor banks, reactors, instrument transformers) interconnected via traveling wave transmission line segments representing the primary bus (ringbus) and the transmission lines entering and leaving the substation. At switching transient and HEMP frequencies, all components are modeled as shunt capacitances of appropriate values between the transmission lines or buswork and ground.

1.3.2 Model Switching Transient Bus Currents

Switching transient voltages and currents are calculated on the substation bus model using METAP, a time domain traveling-wave code. The transient bus currents become the excitation sources of electric and magnetic fields inside the substation. These transients are calculated based on 2 PU initial conditions across a typical air-break disconnect switch and represent the highest amplitudes expected to occur in substations.

1.3.3 Determine Switching Transient Fields

The three-dimensional geometry of the substation transmission line structure is modeled to properly sum the field components from each individual radiating transmission line segment accounting for its relative location and spatial orientation. Switching transient fields are calculated at arbitrary locations in the near-field region of the source (bus excitations) using TRAFIC, a time domain code developed under RP2674-1.

1.3.4 Determine Substation Coupling

Several types of coupling modes to relay control wiring inside the substation are modeled. The most important coupling pathways to control wiring are through the instrument transformers. These current transformers (CTs) and voltage (potential) transformers (PTs) directly connect the low-voltage control wiring of the relay protection circuit to the high voltage bus. Both conducted and radiated coupling to instrument transformer wiring are important. Conducted current or voltage coupling occurs through the parasitic capacitance between CT or PT primary (the bus) and its secondary (a control wire). Radiated field coupling to CT or PT wires can also occur. Where these control wiring circuits are shielded, the fields first couple

along the cable shield as distributed voltage sources. Since the control wiring is also modeled as a traveling-wave transmission line structure, these excitations drive currents along the cable shield. Two additional coupling pathways from the cable shield to the wires inside are modeled. CT and PT shields are typically grounded in pigtails at both ends. Pigtails provide a most important mechanism for inductively coupling shield currents to internal control wires. The important parameters for pigtail coupling are: the length of the pigtail, that is, the distance over which the shield pigtail is parallel to a wire; their separation distance; and the wire diameter. These parameters can vary significantly from pigtail to pigtail within the substation. Another shield-to-wire coupling mechanism is via the cable transfer impedance, although its contribution to the total coupling will normally be smaller than that from pigtail coupling in well designed cables. Frequency domain models are developed for field-to-cable shield coupling, shield pigtail-to-control wire coupling, and cable shield transfer impedance-to-control wire coupling in shielded PT and CT control cables.

Field-to-wire coupling is also modeled for shielded and unshielded DC control wires running between the circuit breaker trip coil, the relay, and the substation batteries.

1.3.5 Substation Switching Transient Model Validation

The substation bus transient, field transient, coupling, and control wire transient models were validated against measured data. Time domain switching transient bus currents and principal component, ground-plane electric and magnetic fields were validated by directly overlaying predictions with measured waveforms in 115 kV and 500 kV substations. Transfer functions for high-frequency conducted primary-to-secondary CT coupling and field-to-shielded CT control wire coupling were measured in a 115 kV substation. These transfer functions relate the primary bus current at the input of a CT primary to the current on a relay wire inside a shielded CT cable as seen at the relay rack where the equipment is located. The transfer impedance of a typical shielded 12-wire CT cable bundle was measured in the laboratory. Models for these transfer functions were then based on simple analytical fits to the data.

1.3.6 Determine Relay Loads

The amount of coupled interference seen on control wires near the relay depends upon the wire load impedances. Control wire loads were modeled using both measured frequency dependent impedances and assumed

constant impedances. Frequency dependent impedances were measured on all inputs to a representative relay in the laboratory in differential and common mode configurations. Due to budget constraints, measurements could only be made on one relay. A solid state transformer differential relay was selected as a compromise between electromechanical and microprocessor types. How representative this relay's frequency dependent impedance characteristics are of other types of relays is not known. The importance of these measurements, however, are that they showed that load impedance can vary by several orders of magnitude with frequency and that impedance versus frequency characteristics vary significantly depending on the input selected, e.g., CT versus DC inputs. A fixed load impedance of 150 ohms was also used. The 150 ohm value was selected because it matched the load to surge withstand capability (SWC) test waveforms.

1.3.7 Global Validation of Substation Switching Transient Coupling to Relays

From the preceding discussions, it is clear that field coupling to control wires inside shielded cables involves several sequential as well as parallel coupling modes. Also, since conducted coupling modes are present (e.g., CT primary-to-secondary wire), the total coupling on a wire is the sum of contributions from all of these component coupling modes. Since control wire current and voltage transients from switching operations were measured near the relay interface, they include contributions from all effective coupling pathways under actual load impedances, whether modeled or not, and therefore globally bound the total coupling. This data can therefore be used to ensure that collectively the coupling and load models are predicting the correct total amount of coupling.

1.3.8 Describe HEMP Sources

Optimized HEMP sources are incorporated into the substation EMI and coupling models as follows. In this study, HEMP sources are described by the unclassified environments which have been developed as curve-fits to results of the CHAP computer program [2], [3]. The location of the nominal maximum value CHAP-fit electric field strength on the ground, including its polarization and angular directions from a 400 km altitude burst over Kansas, are determined. This field is then scaled to a maximum of 50 kV/m and defines short range HEMP. The coupling of short range HEMP to the substation is calculated using CASSANDRA, a frequency domain transmission line model. The CASSANDRA model of the substation is rotated in azimuth until maximum short range HEMP coupling is achieved. Three long transmission lines are connected

to a CASSANDRA model of a 500 kV substation. The ground location, polarization, and incidence angles of the CHAP-fit electric field that drives maximum currents into the substation from grazing-angle incidence on the long transmission lines is found and is termed long range HEMP. The CASSANDRA methodology is validated by comparison with calculations made by Bridges and Shafai in [4] and [5].

1.3.9 Determine HEMP Substation Bus Currents and Fields

The currents driven onto the substation primary bus by the short and long range HEMP fields couple conductively and re-radiatively to the control wiring through the same coupling modes described earlier for switching transients. However, the fields re-radiated from the long range HEMP-driven primary bus currents were found to be 5 times less than the incident HEMP fields. (Bus currents driven by short range HEMP were even smaller.) For this reason only the short and long range HEMP fields incident on the substation are used to drive the field coupling models; re-radiated field coupling is ignored.

Short and long range HEMP primary bus currents, voltages, and incident fields are compared with the corresponding quantities produced by switching transients. These comparisons are made using several different norms such as risetime, peak amplitude, peak time derivative, peak integral, and action integral.

1.3.10 Estimate HEMP Control Wiring Stresses

Using the same coupling and load models described earlier for switching transients, HEMP-induced control wire currents and voltages are predicted. These results are compared with those of switching transients. Together, the control wire EMI produced by switching transients and HEMP describe the current and voltage stresses on the relay equipment. Once the relay susceptibilities are known, these EMI stresses will be compared with them to determine if the relay equipment appears vulnerable.

1.3.11 Estimate Relay Susceptibilities

Relay susceptibilities are determined by injecting HEMP-like impulses into the relay terminals and increasing the drive level until the relay either upsets or fails. Susceptibilities are found only for a representative relay. Since only a single relay could be tested, a solid

state transformer differential relay was chosen as representative in the expectation that its susceptibilities might lie somewhere between those of electromechanical and microprocessor type relays. This relay contained no special transient circuit protection features. Since susceptibilities of other relays could be quite different from the one tested, depending on their inherent hardness or incorporated protection, the results of this study cannot be generalized. This test simply gives a single, hopefully nominal, reference point for the susceptibilities of a relay.

1.3.12 Estimate Relay Vulnerabilities

Measured relay susceptibilities are compared with switching transient and (long and short range) HEMP stresses to estimate relay vulnerabilities. Optimized drive levels for both switching transients and HEMP are used. However, switching transient stresses are optimized for a 500 kV substation; they could be higher or lower in amplitude in substations of higher or lower voltage. Estimates for other substation voltages can be made using the scales provided in [1]. Both the HEMP and switching transient control wire current and voltage stresses predicted near the relay inputs depend on the numerous coupling modes and the parameter values modeled. Variations in wire and cable sizes, use of shielded vs. unshielded cables, lengths and orientations of cable shield pigtails, relay input load impedances, etc. could be almost random when considering the large number of control wires in a substation. As mentioned earlier, relay susceptibilities in general could vary widely from those found in this study. For these reasons a single precise estimate of vulnerability cannot be given for the relay tested, much less one that is valid for all relays. A matrix of EMI stresses resulting from coupling parameter excursions to bound uncertainties in the models can be developed and compared with the test relay susceptibilities to show whether vulnerabilities are likely or not. The highest relay susceptibility that results in upset or damage to the relay is found and compared with the EMI stress parameter space to estimate vulnerability margins and their sensitivity to the parameter values used.

1.3.13 Assess Mitigation

Tests and analysis to assess HEMP and switching transient mitigation concepts and their effectiveness are performed. The effectiveness of using a surge protection package, a shunt filter commonly used to protect AC circuit wires, is investigated for protecting DC circuits.

1.4 ORGANIZATION

The research described above is presented in four parts. Section 2.0 describes the various models used and their validations in more detail. Relay susceptibility tests, frequency dependent loads measurements, and mitigation studies are described in Section 3.0.

Results are presented in Section 4.0. Here bus currents, voltages and fields incident to ground produced by short and long range HEMP and switching transients are compared. Current and voltage stresses produced in control wiring near the relay equipment are compared for a range of coupling parameter and relay load conditions. EMI stresses are compared with the measured relay susceptibilities to estimate vulnerability margins. The effectiveness of a transient EMI suppression technique is discussed. Section 5.0 emphasizes certain limitations of this study. It draws a number of conclusions concerning the relative strengths and effects of HEMP and switching transients in substations. It summarizes relay vulnerability margins based on this study. Several recommendations for extending the analysis and improving some of the estimates are discussed.

2.0 MODELS

In this section, the analytical models used to generate drives (bus currents and radiated fields) and coupled responses to these drives (shield currents and control circuit currents/voltages) are presented. The analyses of switching transient (ST) and high-altitude nuclear electromagnetic pulse (HEMP) phenomena are different in some respects, but substantially similar in others. In the case of ST, the transient currents on the ring bus produce radiated fields; in the case of HEMP, the radiated fields produce transient ring bus currents. However, once the radiated fields and bus currents are calculated, the same models for coupling these drives to control circuits can be used for both ST and HEMP. Overviews of the flow of analysis results between models are shown in Figure 2.1 (for switching transients) and Figure 2.2 (for HEMP). For switching transients, bus currents and voltages are calculated with METAP (the McGraw-Edison Transient Analysis Program); the bus currents are used in TRAFIC (the Transient Field Integration Code) to produce radiated electric and magnetic fields. In the case of HEMP, the radiated fields are created with MAKECHAP, based on Longmire's CHAP-fit HEMP model; these fields are input to CASSANDRA (an admittance-based transmission-line model) for computation of the resultant bus currents and voltages. Incident ST and HEMP electric fields are used to drive induced currents and voltages on both unshielded and shielded control cables with the UNSHLD-E (shallowly-buried unshielded cable) and ZTNPIG-E (shallowly-buried shielded cable) programs respectively. In addition, local magnetic fields produced by currents flowing to ground via current transformer (CT) ground straps (due to either ST or HEMP) are used for calculation of coupled currents/voltages on unshielded and shielded control cables with the UNSHLD-H and ZTNPIG-H programs. For shielded cables, load responses for both transfer-impedance coupling and pigtail-termination coupling are calculated simultaneously in the ZTNPIG-E and ZTNPIG-H programs. And finally, both ST and HEMP bus currents are used in the calculation of conducted coupling to control circuits via devices physically connected to the high-voltage bus, such as current transformers (CT's) and potential transformers (PT's); these calculations are performed with the DIRCOUP (direct coupling) program. These models are

described more fully in the rest of this section, and model results are compared to actual 500kV ST measurements at the end of this section.

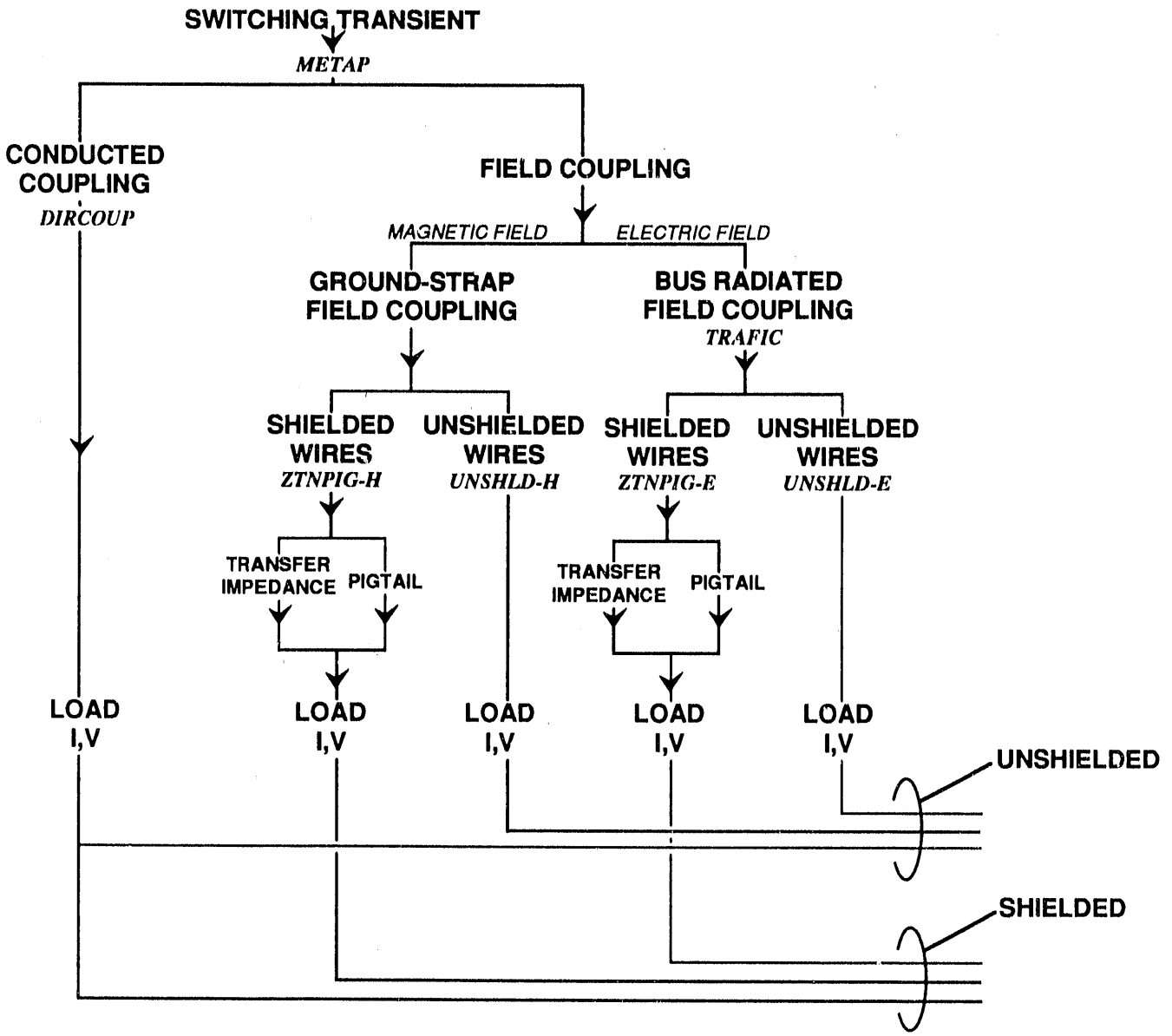

Figure 2.1. Flow Diagrams for Switching Transient Analysis Models

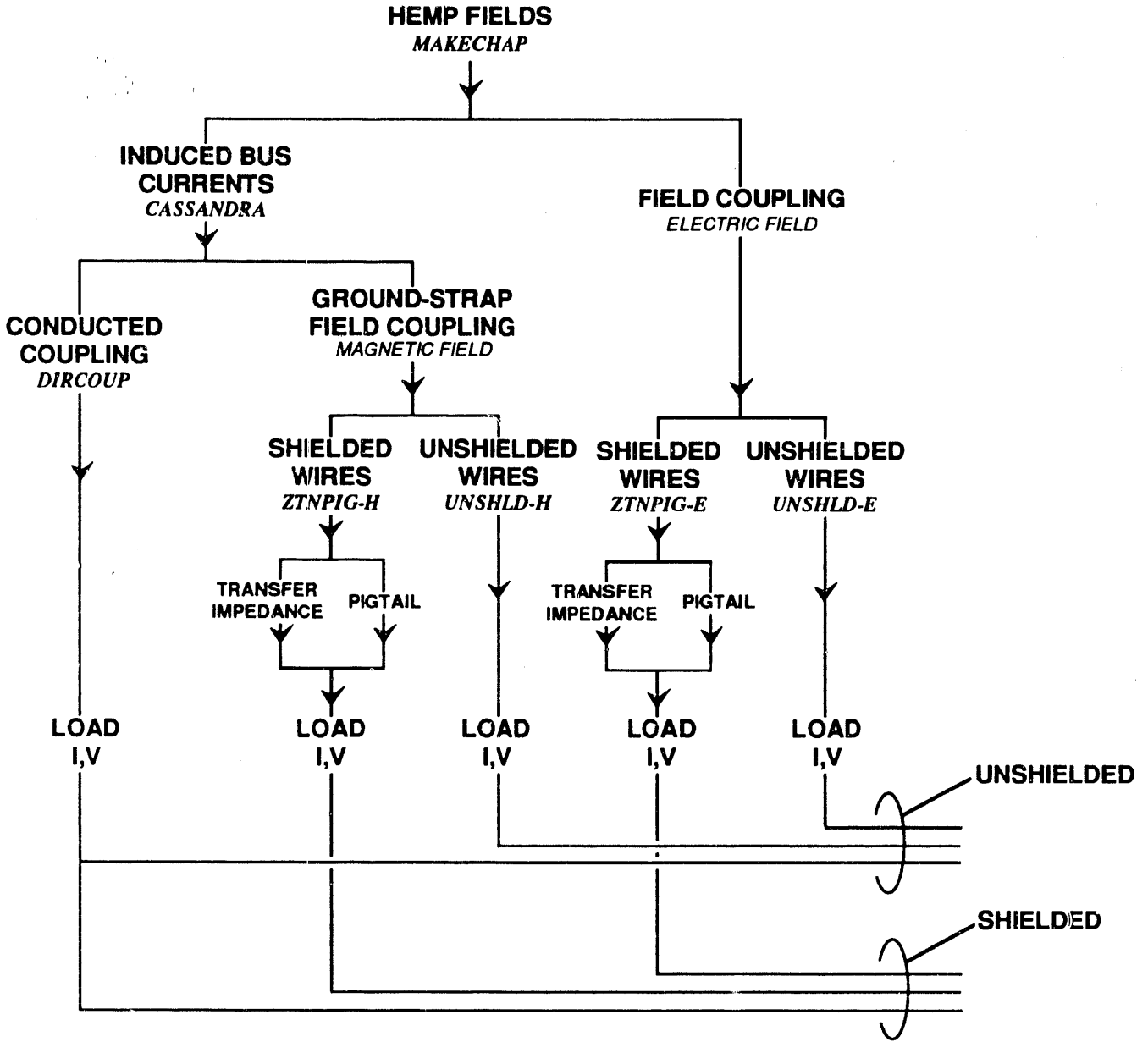

Figure 2.2. Flow Diagrams for HEMP Coupling Analysis Models

2.1 SUBSTATION SWITCHING TRANSIENT MODELS

2.1.1 METAP Program for ST Bus Currents/Voltages

The METAP program is a general-purpose network analysis model having many special capabilities for electric power applications. Typically, lossless single-phase transmission lines are used for the bus itself, while devices such as bushings or internal breaker components are modeled with capacitors, inductors, and resistors. A representative example of a METAP network model is pictured in Figure 2.3, along with a brief description of the solution methodology. Detailed diagrams of the METAP model and device submodels for the 500 kV air-insulated substation analyzed in this study appear in Figure 2.4. The use of METAP for analysis of ST phenomena is discussed more fully in references [1,6].

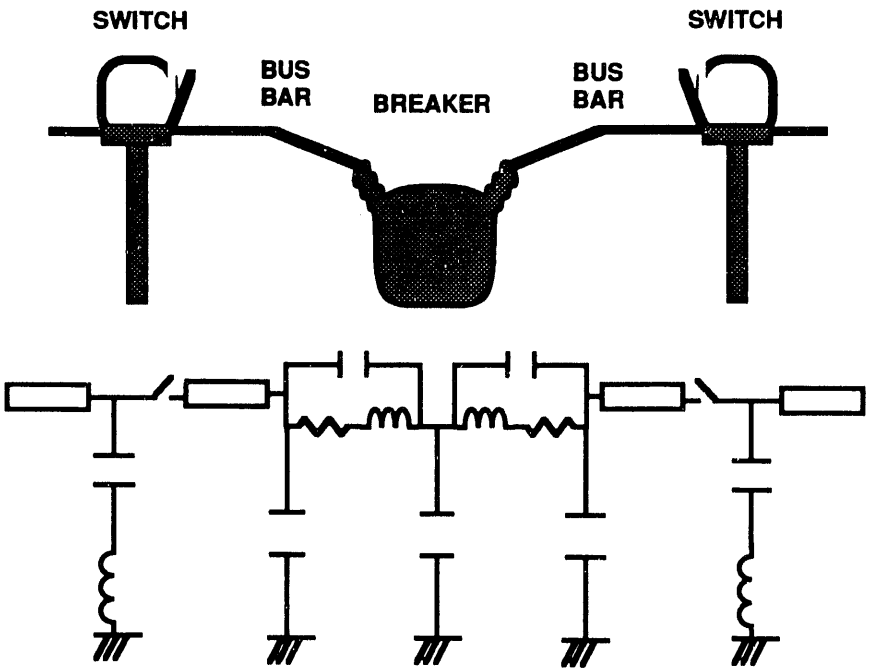

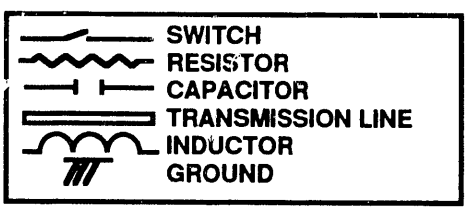

LEGEND

- DESCRIBE SWITCHYARD WITH NETWORK COMPOSED OF TRANSMISSION LINES, RESISTORS, INDUCTORS, CAPACITORS, AND/OR SPECIAL ELEMENTS (ARC MODELS, SYNCHRONOUS MOTORS, ETC.)
- USE KIRCHOFF'S LAWS, FOR GIVEN SET OF INITIAL CONDITIONS
- TIME-DOMAIN SOLUTION FOR NETWORK TRANSIENTS, USING COMBINATION POINT-JACOBI / NEWTON-RAPHSON ITERATION METHOD

Figure 2.3. The METAP Network Analysis Program

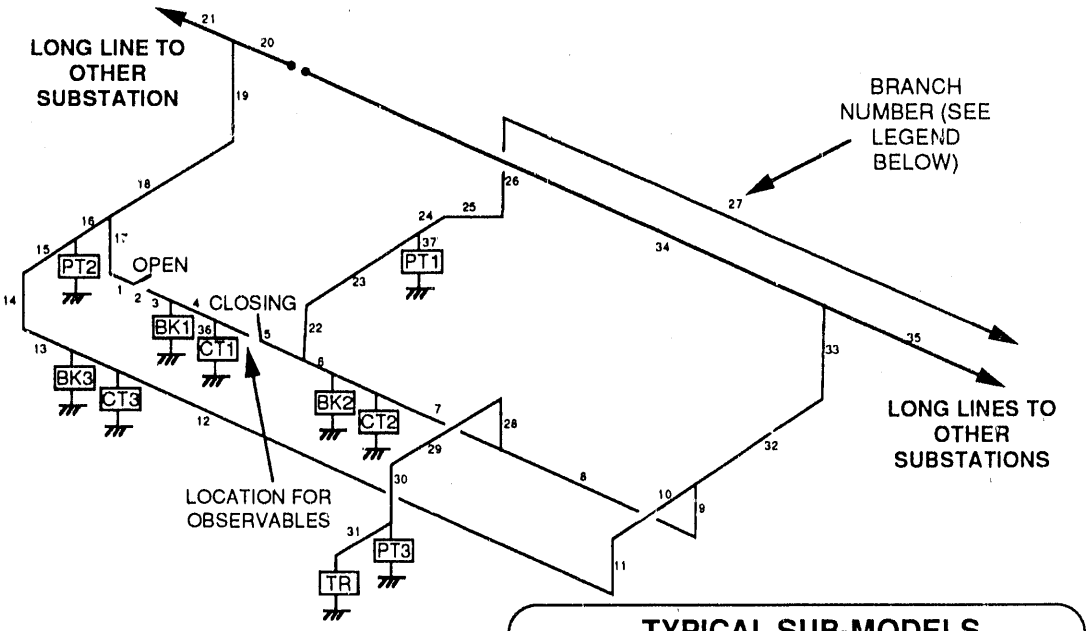

KEY

BK1 - OPEN CIRCUIT BREAKER
BK2, BK3 - CLOSED CIRCUIT BREAKERS
CT1, CT2, CT3 - CURRENT TRANSFORMERS
PT1, PT2, PT3 - POTENTIAL TRANSFORMERS
TR - 230 kV/500 kV TRANSFORMER
— — - HAND-OPERATED DISCONNECT

TYPICAL SUB-MODELS

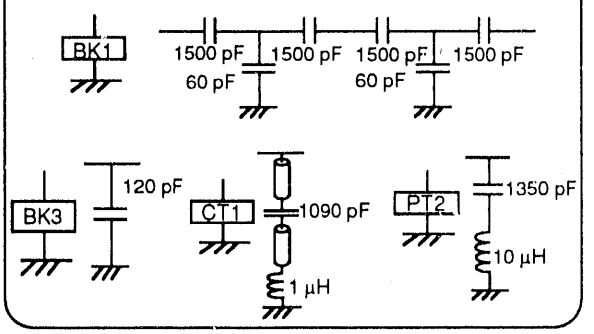

BRANCH DATA

KEY : BRANCH #
L=LINE LENGTH
a=LINE RADIUS
h=LINE HEIGHT
$Z_B = \frac{377\Omega}{2\pi} \cosh^{-1}\frac{2h}{a}$

BR. 1	BR. 2	BR. 3	BR. 4	BR. 5	BR. 6	BR. 7	BR. 8	BR. 9	BR. 10
4.89 m	12.6 m	7.40 m	5.07 m	23.1 m	18.0 m	35.7 m	53.6 m	5.22 m	27.3 m
2.57 cm	2.57 cm	2.57 cm	2.57 cm	2.57 cm	2.57 cm	2.57 cm	2.57 cm	2.57 cm	2.57 cm
7.58 m	7.58 m	7.58 m	7.58 m	7.58 m	7.58 m	7.58 m	7.58 m	10.2 m	12.8 m
BR. 11	BR. 12	BR. 13	BR. 14	BR. 15	BR. 16	BR. 17	BR. 18	BR. 19	BR. 20
5.22 m	147 m	13.4 m	5.22 m	23.6 m	3.81 m	5.22 m	40.5 m	6.10 m	15.24 m
2.57 cm	2.57 cm	2.57 cm	2.57 cm	2.57 cm	2.57 cm	2.57 cm	2.57 cm	2.57 cm	2.57 cm
10.2 m	7.58 m	7.58 m	10.2 m	12.8 m	12.8 m	10.2 m	12.8 m	15.9 m	18.9 m
BR. 21	BR. 22	BR. 23	BR. 24	BR. 25	BR. 26	BR. 27	BR. 28	BR. 29	BR. 30
1.5 km	5.22 m	40.5 m	5.18 m	12.9 m	6.10 m	1.5 km	5.22 m	35.1 m	5.22 m
2.57 cm	2.57 cm	2.57 cm	2.57 cm	2.57 cm	2.57 cm	2.57 cm	2.57 cm	2.57 cm	2.57 cm
18.9 m	10.2 m	12.8 m	12.8 m	12.8 m	15.9 m	18.9 m	10.2 m	12.8 m	10.2 m
BR. 31	BR. 32	BR. 33	BR. 34	BR. 35	BR. 36	BR. 37			
18.0 m	40.5 m	6.10 m	144 m	1.5 km	6.00 m	12.6 m			
2.57 cm	2.57 cm	2.57 cm	2.57 cm	2.57 cm	2.57 cm	2.57 cm			
7.58 m	12.8 m	15.9 m	18.9 m	18.9 m	4.58 m	6.50 m			

Figure 2.4. METAP Model for Switching Transients in a 500 kV Substation

2.1.2 TRAFIC Program for Radiated Fields

The Transient Field Integration Code, called TRAFIC, was developed under EPRI RP2674-1 for the calculation of radiated field environments in substations. The basis of the TRAFIC model appears in Figure 2.5; a current waveform I(t) is injected into one end of a transmission line, which usually represents a section of high-voltage bus. The transient bus current waveform is expressed as a sum of ramp-shaped basis functions; it turns out that the radiated fields due to a single ramp can be calculated in closed form in the time domain, for any length of transmission line, and for field points both in the near zone and the far zone of the transmission line itself. A simple superposition of the fields radiated by individual ramps yields the total fields radiated by the given transient bus current waveform. Ramp descriptions for arbitrary current waveforms can be developed by simply calculating the differences in slopes of adjoining segments of the current waveform; in general, radiation from currents along both directions of the segment of bus must be calculated. TRAFIC permits calculation of field radiation from dozens of sections of bus simultaneously; the bus sections can have arbitrary lengths and orientations, thus permitting detailed substation representations. Reflected electric and magnetic fields are calculated rapidly by a procedure known as recursive convolution, thus providing estimates of both incident fields and total (incident + reflected) fields. The use of TRAFIC for analysis of ST radiated fields is discussed more fully in references [1,6].

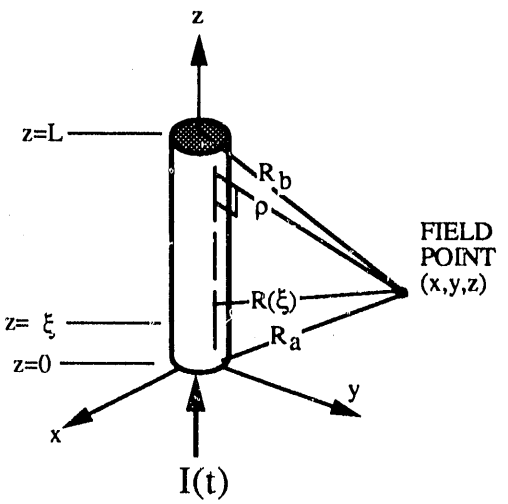

$$\rho = \sqrt{x^2 + y^2}$$

$$R(\xi) = \sqrt{\rho^2 + (z-\xi)^2}$$

$$R_a = R(0)\ ,\ R_b = R(L)$$

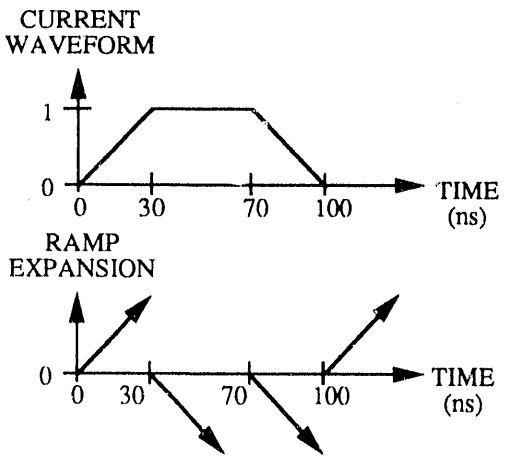

GET NODE CURRENTS FROM METAP (Z=0)

$$I(t),\ t = t_i,\ i = 1,2,3,\ldots N$$

FIND RAMP EXPANSION OF CURRENT WAVEFORM :

$$I(t) = \sum_{i=1}^{N} \alpha_i\,(t - t_i)\,U(t - t_i)$$

α_i = ramp coefficient (slope), U = Unit Step Function

FIND VECTOR POTENTIAL IN CLOSED FORM :

$$A_z^i(t) = \int_{\xi_1}^{\xi_2} \frac{I(\xi,t')}{R(\xi)}\,d\xi$$

$$= \begin{cases} 0,\ 0 \le t \le T_a \\ \dfrac{a_i}{4\pi c}\left[\Theta \ln\left(\dfrac{\Theta}{R_a - z}\right) - \Theta + R_a - z\right],\ T_a \le t \le T_b \\ \dfrac{a_i}{4\pi c}\left[\Theta \ln\left(\dfrac{R_b + L - z}{R_a - z}\right) - R_b + R_a - z\right],\ T_b \le t \le \infty \end{cases}$$

$$T_a = t_i + \frac{R_a}{c}\ ,\ T_b = t_i + \frac{R_b}{c}\ ,\ \Theta = c(t - t_i) - z$$

FIND TRANSIENT FIELDS

$$\vec{H} = \frac{\nabla \times \vec{A}}{\mu_o}\ ,\ \vec{E} = \int \frac{\nabla \times \vec{H}}{\varepsilon_o}\,dt$$

Figure 2.5. The Transient Field Integration Code (TRAFIC)

2.2 HEMP MODELS

A commonly used, unclassified description of the HEMP environment is the well-known "Bell Laboratory EMP Waveform"; however, studies have shown that the use of this waveform can lead to over-estimates of HEMP line and equipment responses by more than an order of magnitude. This report makes use of another unclassified HEMP environment which has been developed, and which is based on curve-fits to results of the CHAP computer program [2,3]; the program developed for this work is called MAKECHAP. A contour map of the peak CHAP-fit electric field strengths over the CONUS for a 400-km altitude burst is shown in Figure 2.6. The CHAP-fit fields have a nominal maximum value of 39 kV/m; in this study, these HEMP fields have been scaled up to a maximum of 50 kV/m. A three-dimensional representation of the peak HEMP fields is given in Figure 2.7.

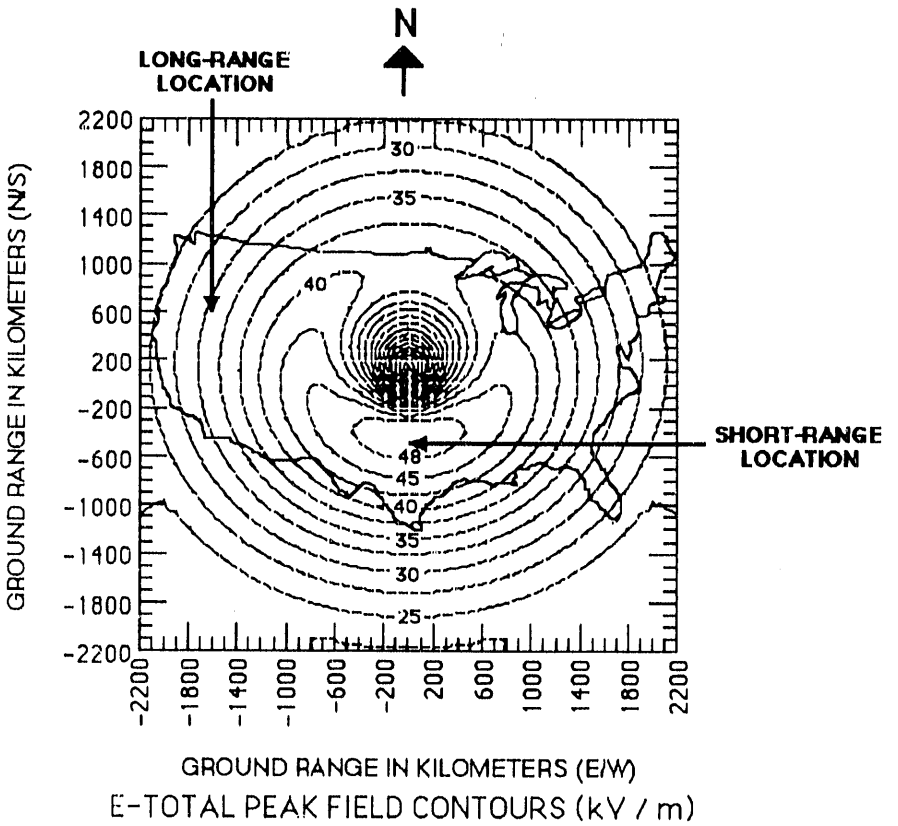

Figure 2.6. Peak-Field Contour Map for CHAP-fit Model of HEMP Radiated Fields

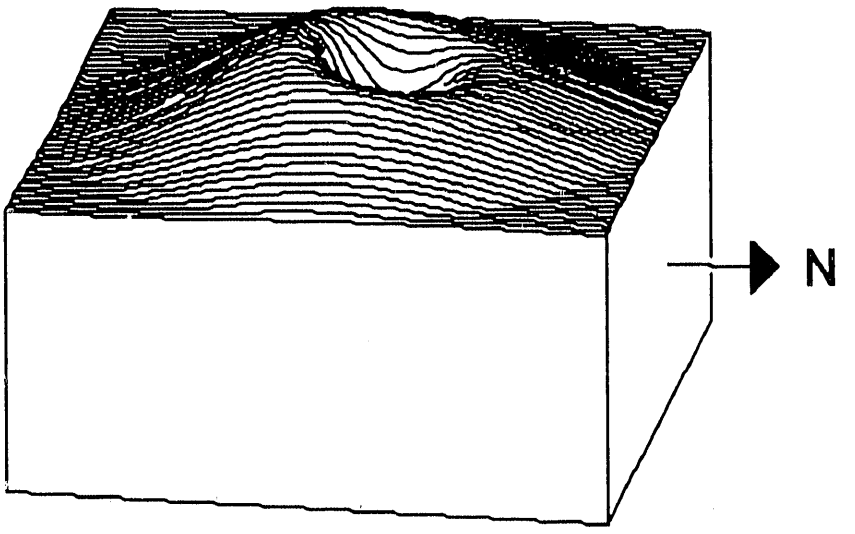

Figure 2.7. Peak-Field 3-D Represention for CHAP-fit Model of HEMP Radiated Fields

Time-domain plots of the horizontally-polarized components of MAKECHAP HEMP waveforms for two locations are presented in Figure 2.8; the thin curve is the field at the 50 kV/m maximum-field location, which lies at a ground range of about 500 km south of ground zero (hereinafter "short range"). The bold curve of Figure 2.8 is the field at a ground range of 1660 km, to the west-northwest of ground zero (hereinafter "long range"). The long-range field waveform has a lower peak, a longer rise-time, and a longer fall-time than the short-range waveform. These short-range and long-range locations are also indicated in Figure 2.6 for reference; the elevation angles (measured from the horizon) for the short-range and long-range HEMP fields are 35.4° and 5.6° respectively. The θ-component of the radiated electric field, which lies at right angles to both the horizontal component and to the direction of propagation, is primarily vertical (more so for shallow elevation angles than for steep angles), and is thus referred to as the "vertical" component. The corresponding vertical-field waveforms for short-range and long-range HEMP electric fields are displayed in Figure 2.9. The vertical component for the long-range field waveform (bold curve) has a much larger peak than does the short-range field waveform (thin curve). The short-range location was chosen because it represents the region containing peak field strengths; the long-

range location was chosen because it is the region where the vertical component of HEMP, at very shallow incidence angles, can produce very large transients in long horizontal lines lying more or less along the direction of propagation.

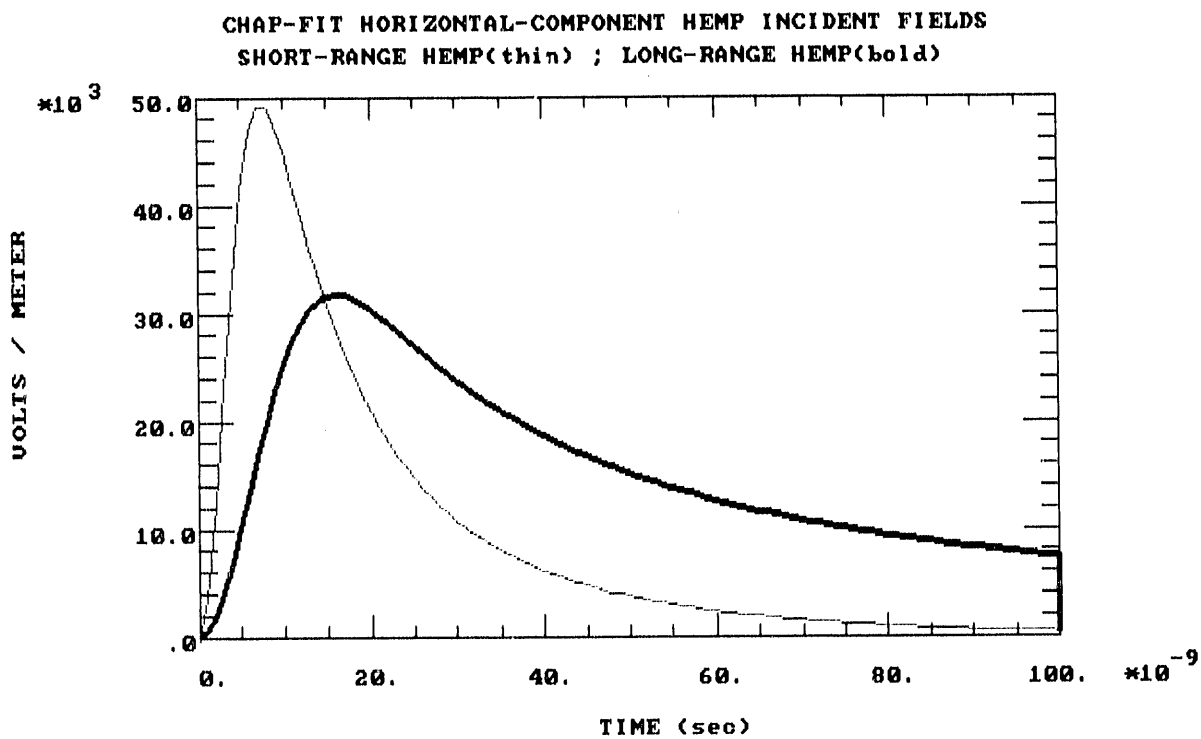

Figure 2.8. Time Domain Waveforms for Horizontal Component of Short Range (thin) and Long-Range (bold) HEMP Fields

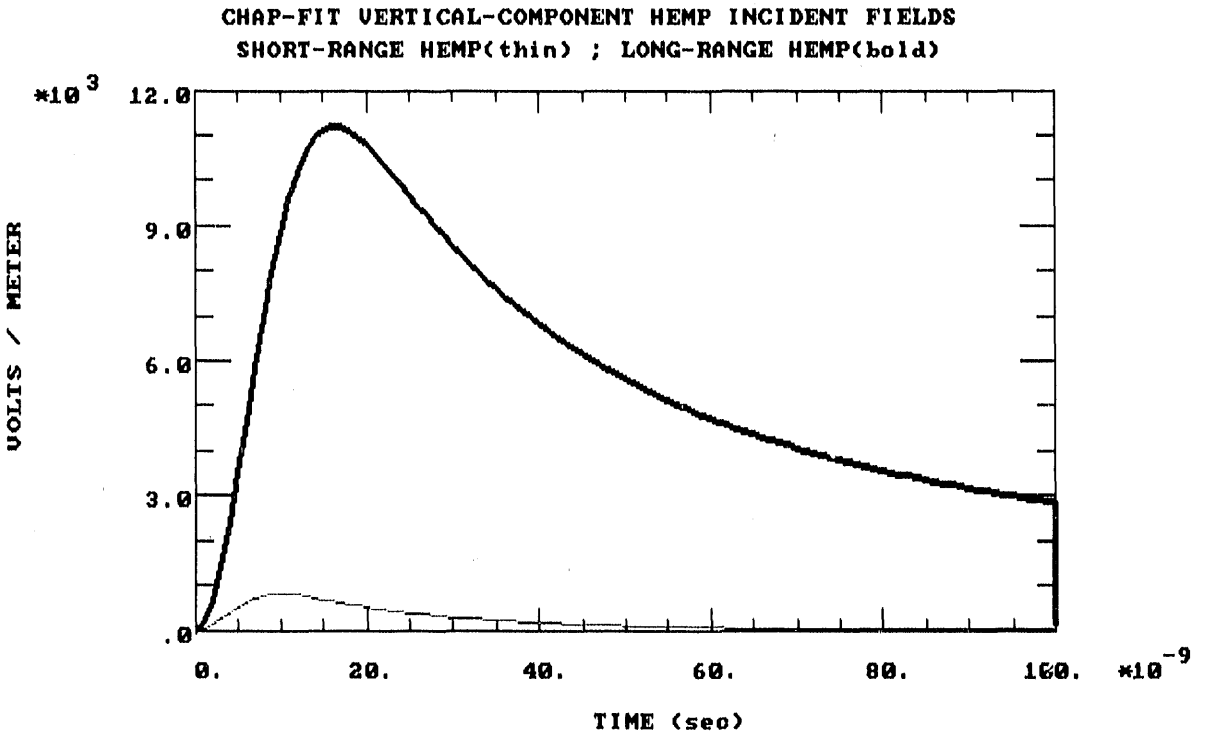

Figure 2.9. Time Domain Waveforms for Vertical Component of Short Range (thin) and Long-Range (bold) HEMP Fields

2.3 COUPLING MODELS

2.3.1 HEMP Coupling to a High-Voltage Ring Bus

HEMP field-induced current transients on electric power lines or high-voltage substations are computed with the CASSANDRA program; this program is an admittance-based transmission line model, and most of the calculations are performed in the frequency domain. CASSANDRA permits multiple-branch models of ring buses or other structures; the electric fields parallel to each branch are integrated over the length of the branch, to yield source currents at the nodes of the model. The admittance matrix for the multi-branch model, which depends on geometrical and ground parameters only,

is inverted at each frequency of interest to develop node voltages for all frequencies. These voltages can then be used to calculate transient shield currents and or voltages anywhere along any branch. Branches can be above ground, buried, or on the ground.

The detailed CASSANDRA transmission-line model for a 500 kV ring bus appears in Figure 2.10. This ring bus is the CASSANDRA analog of the METAP ring bus model of Figure 2.4, and was used for the HEMP coupling analyses presented in this report. The HEMP orientation angle ϕ shown in this figure was varied, and peak responses were calculated for the prediction location indicated; the largest peaks were found for $\phi = 0^{o}$ (long-range HEMP, elevation = 5.6^{o}) and for $\phi = 45^{o}$ (short-range HEMP, elevation = 35.4^{o}).

A comparison of CASSANDRA results to more exact coupling calculations, for the case of a Bell-lab HEMP waveform incident on a long line 5 meters above ground at an elevation angle of 10 degrees, is presented in Figure 2.11 (see reference [4], Bridges/Shafai); CASSANDRA provides good agreement with the more rigorous calculations for a wide variety of line geometries and incidence angles (see reference [5] for examples).

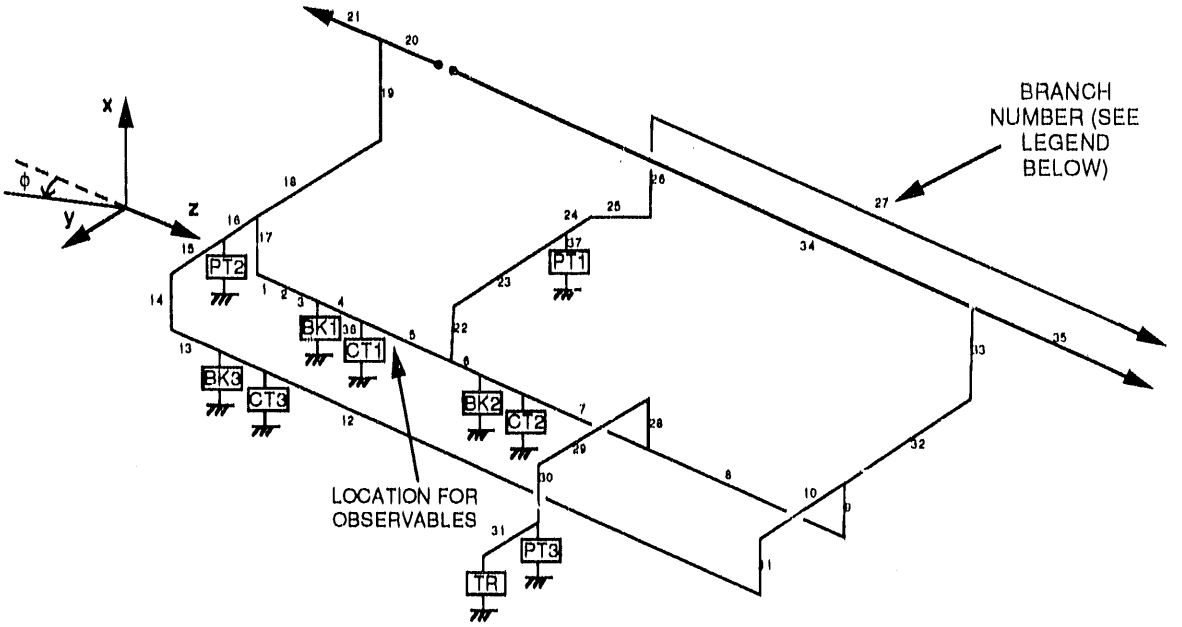

KEY

BK1, BK2, BK3 - CLOSED CIRCUIT BREAKERS
CT1, CT2, CT3 - CURRENT TRANSFORMERS
PT1, PT2, PT3 - POTENTIAL TRANSFORMERS
TR - 230 kV/500 kV TRANSFORMER
ALL HAND-OPERATED DISCONNECTS CLOSED

BRANCH DATA

KEY : BRANCH #
L=LINE LENGTH
a=LINE RADIUS
h=LINE HEIGHT

$$Z_B = \frac{377\Omega}{2\pi} \cosh^{-1}\frac{2h}{a}$$

BR. 1	BR. 2	BR. 3	BR. 4	BR. 5	BR. 6	BR. 7	BR. 8	BR. 9	BR. 10
4.89 m	12.6 m	7.40 m	5.07 m	23.1 m	18.0 m	35.7 m	53.6 m	5.22 m	27.3 m
2.57 cm	2.57 cm	2.57 cm	2.57 cm	2.57 cm	2.57 cm	2.57 cm	2.57 cm	2.57 cm	2.57 cm
7.58 m	7.58 m	7.58 m	7.58 m	7.58 m	7.58 m	7.58 m	7.58 m	10.2 m	12.8 m
BR. 11	BR. 12	BR. 13	BR. 14	BR. 15	BR. 16	BR. 17	BR. 18	BR. 19	BR. 20
5.22 m	147 m	13.4 m	5.22 m	23.6 m	3.81 m	5.22 m	40.5 m	6.10 m	15.24 m
2.57 cm	2.57 cm	2.57 cm	2.57 cm	2.57 cm	2.57 cm	2.57 cm	2.57 cm	2.57 cm	2.57 cm
10.2 m	7.58 m	7.58 m	10.2 m	12.8 m	12.8 m	10.2 m	12.8 m	15.9 m	18.9 m
BR. 21	BR. 22	BR. 23	BR. 24	BR. 25	BR. 26	BR. 27	BR. 28	BR. 29	BR. 30
1.5 km	5.22 m	40.5 m	5.18 m	12.9 m	6.10 m	1.5 km	5.22 m	35.1 m	5.22 m
2.57 cm	2.57 cm	2.57 cm	2.57 cm	2.57 cm	2.57 cm	2.57 cm	2.57 cm	2.57 cm	2.57 cm
18.9 m	10.2 m	12.8 m	12.8 m	12.8 m	15.9 m	18.9 m	10.2 m	12.8 m	10.2 m
BR. 31	BR. 32	BR. 33	BR. 34	BR. 35	BR. 36	BR. 37			
18.0 m	40.5 m	6.10 m	144 m	1.5 km	6.00 m	12.6 m			
2.57 cm	2.57 cm	2.57 cm	2.57 cm	2.57 cm	2.57 cm	2.57 cm			
7.58 m	12.8 m	15.9 m	18.9 m	18.9 m	4.58 m	6.50 m			

Figure 2.10. The CASSANDRA Model for HEMP Coupling to a 500 kV Ring Bus

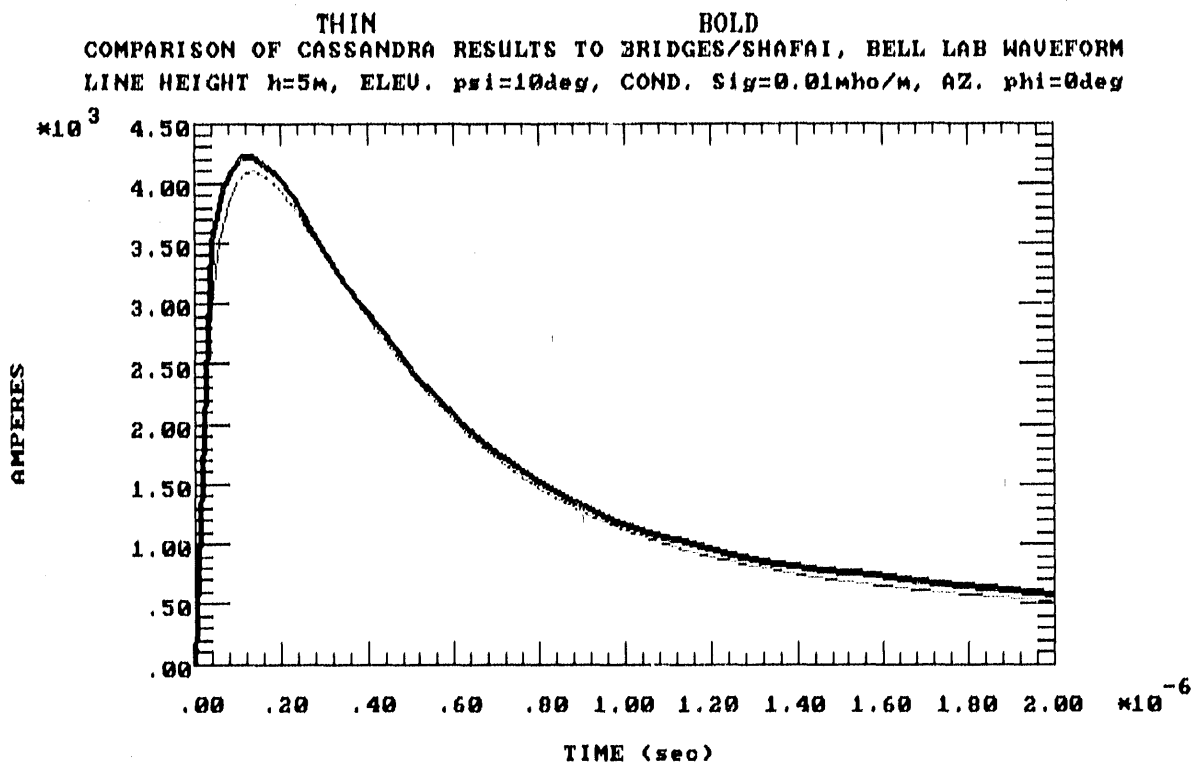

Figure 2.11. Comparison of CASSANDRA Results to Bridges/Shafai for HEMP Coupling to a Long Line with Height = 5 m, Elevation = 10°, Ground Conductivity = 0.01 mho/m, and Orientation = 0°

2.3.2 Conducted Coupling from a High-Voltage Ring Bus

The DIRCOUP model is used for predictions of conducted coupling between high-voltage bus current transients and low-voltage circuit loads (relays, for example) via the parasitic capacitance of bus-monitoring devices such as current transformers or potential transformers. Current transformers (CT's) are often connected to the ring bus next to circuit breaker attachments. The circuit used for the DIRCOUP CT model is presented in Figure 2.12.

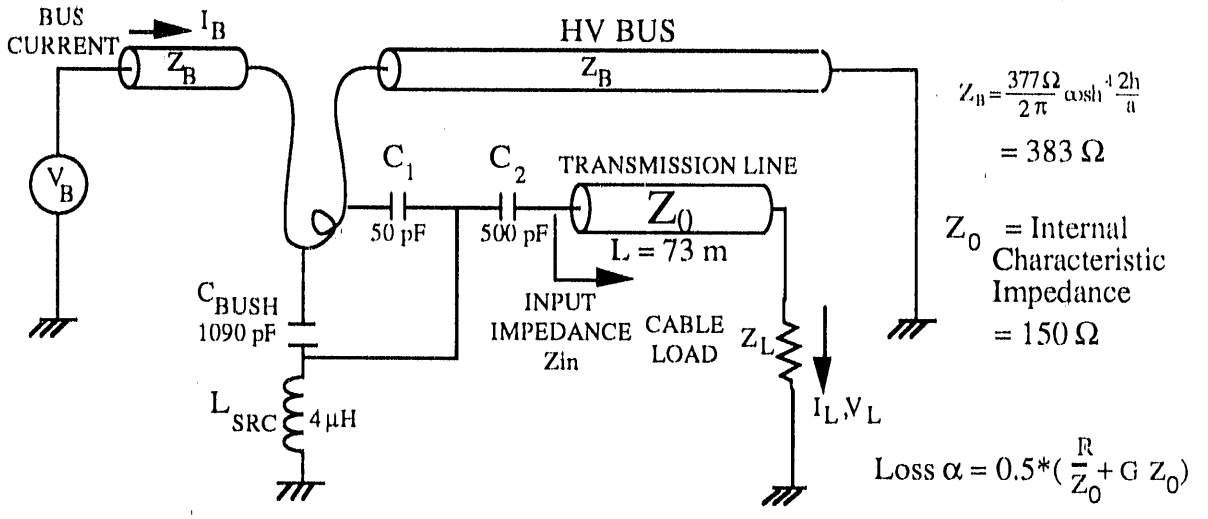

Figure 2.12. Diagram for Calculation of Bus Current Coupling to Relay Loads Via Parasitic CT Capacitance

In the figure, C_1 is the capacitance between the CT primary and the CT Faraday shield ground casing, and C_2 is the capacitance between the CT secondary and the Faraday shield.

The bushing current I_{BUSH} produces a voltage ΔV across the bushing capacitance C_{BUSH} given by :

$$\Delta V \ \text{across}\ C_{BUSH} = \frac{I_{BUSH}}{s\, C_{BUSH}} \ ,$$

where $s = j\omega = j\,2\pi f$, with f = the frequency in Hertz. The voltage ΔV_S across the ground-strap inductance L_{SRC} is given by:

$$\Delta V_S \ \text{across}\ L_{SRC} = \frac{s\, L_{SRC}\, \Delta V}{\frac{s\, L_{SRC} C_2 / C_1}{1 + sC_2 Z_{IN}} + \frac{1}{s\, C_1} + s\, L_{SRC}} \ .$$

Here, Z_{IN} is the input impedance of the circuit looking into the transmission line (of length L) to the load :

$$Z_{IN} = Z_0 \left(\frac{1 + \rho_2 e^{\ 2\gamma L}}{1 - \rho_2 e^{-2\gamma L}} \right), \qquad \text{where } \rho_1 = \frac{Z_{SRC} - Z_0}{Z_{SRC} + Z_0}, \ \rho_2 = \frac{Z_L - Z_0}{Z_L + Z_0},$$

and Z_0 = Line Impedance , Z_L = Load Impedance, and $Z_{SRC} = sL_{SRC} + \frac{1}{sC_{SRC}}$.

The transmission line propagation constant γ is given by :

$$\gamma = \alpha + s\frac{\omega}{v}, \text{ where } \alpha = \frac{1}{2}\left(\frac{R}{Z_0} + GZ_0\right) = \text{cable loss term, and}$$

$$v = \frac{c}{\sqrt{\varepsilon_r}} = \frac{3x10^8 \frac{m}{s}}{\sqrt{1.1}} = \text{cable propagation velocity.}$$

The current and voltage at the load are given by :

$$I_L = \frac{\Delta V_s}{Z_0}\left[\frac{e^{-\gamma L}(1-\rho_2)}{\Delta}\right], \quad V_L = \Delta V_s\left[\frac{e^{-\gamma L}(1+\rho_2)}{\Delta}\right],$$

$$\text{where } \Delta = 1 - \rho_1 \rho_2 e^{-2\gamma L} .$$

The values of primary and secondary capacitance that gave the best comparisons to the extensive set of RP2674-1 measurements are indicated in the figure. These values are based on the work of Greenwood [12], and provide very reasonable predictions of load responses produced by conducted coupling of switching transients. Conducted coupling predictions were produced for several types of load impedance Z_L, including both constant impedance and measured frequency-dependent impedances. This coupling pathway will be seen to quite significant, especially for intermediate-frequency switching transient drives.

2.3.3 Electric Field Coupling to Cables

Models based on Vance's work in Coupling to Shielded Cables [7] are used to calculate electric field-driven coupling to control cables. In these models, the cables are considered to be shallowly buried, as is common for control circuits running in troughs through high-voltage substations. The geometry for electric field coupling to shielded cables appears in Figure 2.13, and that for electric field coupling to unshielded cables appears in Figure 2.14.

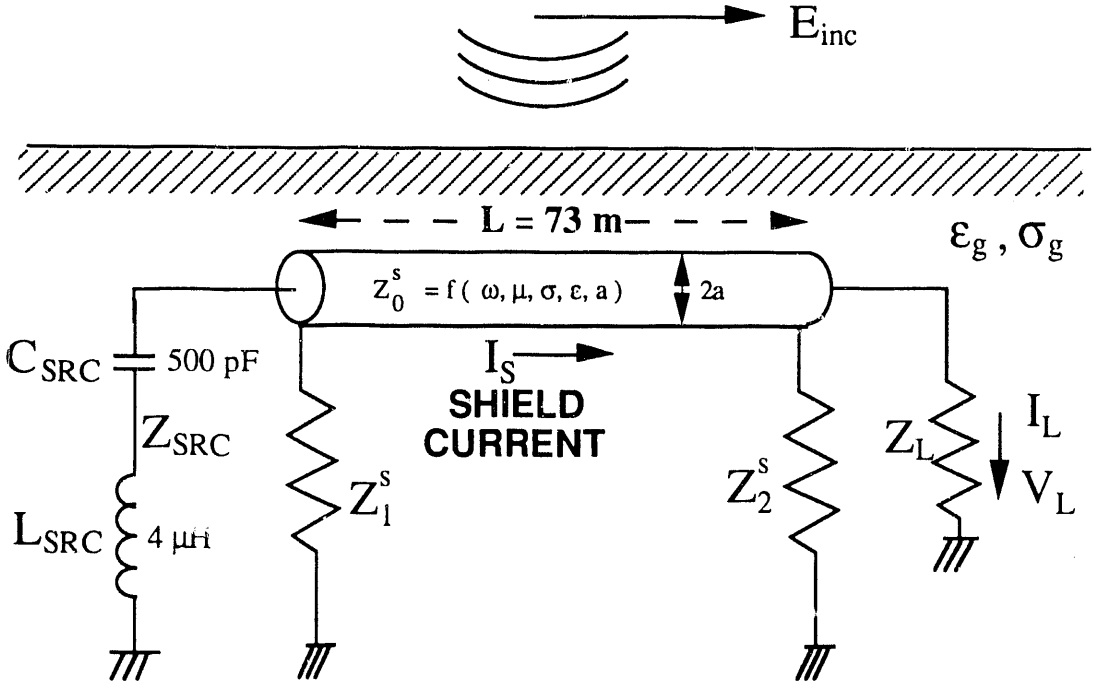

Figure 2.13. Model for Calculation of Electric Field Coupling to Shielded Cables

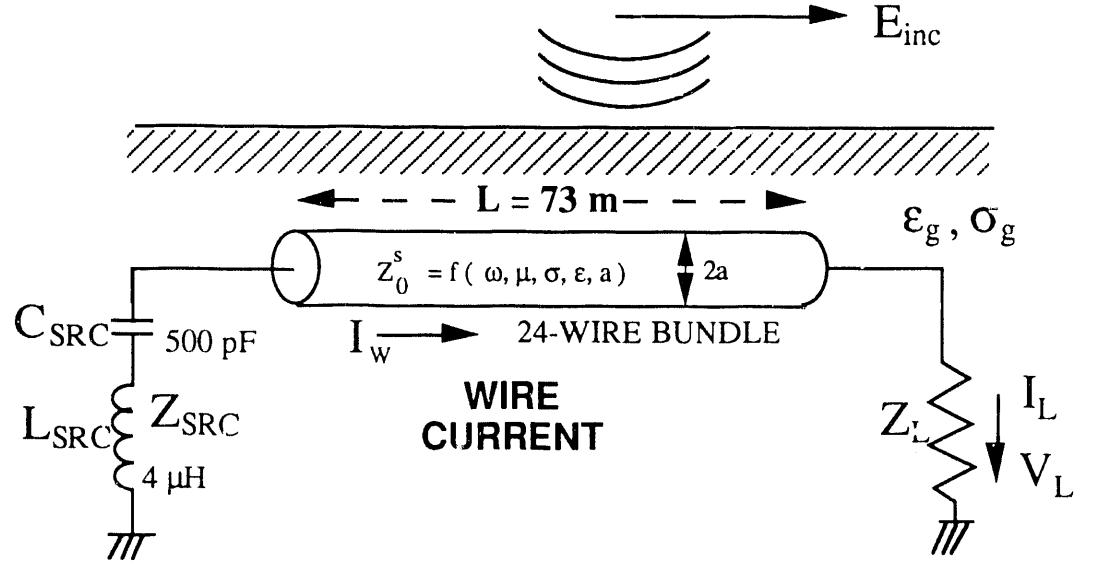

Figure 2.14. Model for Calculation of Electric Field Coupling to Unshielded Cables

For a given incident electric field $E_{inc}(\omega)$ (produced by either HEMP or a switching transient), the net field parallel to the cable just below the surface is given as

$$E_z = E^v_{inc}(1 - R_v)\sin\psi \cos\phi = E^v_{inc}\sqrt{\frac{j\omega\varepsilon}{\sigma}}\ 2\cos\phi$$

or

$$E_z = E^h_{inc}(1 + R_h)\sin\phi = E^h_{inc}\sqrt{\frac{j\omega\varepsilon}{\sigma}}\ 2\sin\psi \sin\phi$$

where E^v_{inc} is the vertical component of incident field, E^h_{inc} is the horizontal component of incident field, R_v and R_h are the vertical and horizontal reflection coefficients, ψ is the elevation angle, ϕ is the azimuth angle, ω is the radian frequency, ε is the earth permittivity, σ is ground conductivity, and z is the direction of the cable axis. For the case of HEMP, the incident electric fields are assumed to be uniform with respect to position. For switching transient-induced fields, however, the incident fields from a single segment of the high-voltage bus vary with position along the ground; in addition, the fields from several nearby bus segments must be superposed at a given position for an adequate representation of the total electric field there.

In the case of shielded cables, the shield current at a point z on the shallowly-buried cable is found from

$$I_S(z,\omega) = [K^s_1 + P^s(z)]\, e^{-\gamma z} + [K^s_2 + Q^s(z)]\, e^{\gamma z}$$

where

$$P^s(z) = \frac{1}{2 Z^s_o}\int_0^z e^{\gamma\zeta} E_z(\zeta)\, d\zeta$$

$$Q^s(z) = \frac{1}{2 Z^s_o}\int_z^L e^{-\gamma\zeta} E_z(\zeta)\, d\zeta$$

$$K^s_1 = \rho^s_1 [\rho^s_2 P^s(L)\, e^{-\gamma L} - Q^s(0)\, e^{\gamma L}] / \Delta^S$$

$$K_2^s = \rho_2^s e^{-\gamma L}[\rho_1^s Q^s(0) - P^s(L)] / \Delta^S$$

$$\rho_1^s = \frac{Z_1^s - Z_0^s}{Z_1^s + Z_0^s}, \rho_2^s = \frac{Z_2^s - Z_0^s}{Z_2^s + Z_0^s}, \Delta^S = e^{\gamma L} - \rho_1^s \rho_2^s e^{-\gamma L}$$

and where the cable shield runs from z=0 to z=L, has a characteristic impedance Z_o^s, is terminated into Z_1^s at z=0 and Z_2^s at z=L. Using the propagation constant $\gamma = \sqrt{j\omega\mu(\sigma + j\omega\varepsilon)}$,

$$Z_0^s = \frac{Z_G}{\gamma} = \frac{\frac{\omega\mu}{8} + j\frac{\omega\mu}{2\pi}\log_e(\frac{\sqrt{2}\,\delta}{\gamma_0 a})}{\gamma}$$

where γ_0 = 1.781, δ = skin depth = $1/\sqrt{\pi f \mu \sigma}$, μ = magnetic permeability = $4\pi x 10^{-7}$ H/m, and (a) is the cable radius. These calculations are performed in the frequency domain for many frequencies (typically 400-500 on a logarithmic scale from 1 kHz to 1 GHz), and a slope-difference Fourier integral transform algorithm is used to generate time-domain results. The shield currents produced by electric-field coupling are used to drive coupling to the cable loads via the mechanisms of transfer-impedance and pigtail coupling; these mechanisms are discussed later in this section.

In the case of unshielded cables, the induced current and voltage along wires in a bundle of length L are taken as:

$$I_{WIRE}(z,\omega) = \left[[K_1^s + P^s(z)]\, e^{-\gamma_s z} + [K_2^s + Q^s(z)]\, e^{\gamma_s z} \right] \frac{1}{\sqrt[3]{N_{WIRE}}}$$

$$V_{WIRE}(z,\omega) = \left[\frac{[K_1^s + P^s(z)]\, e^{-\gamma_s z}}{Z_0} - \frac{[K_2^s + Q^s(z)]\, e^{\gamma_s z}}{Z_0} \right] \frac{1}{\sqrt[3]{N_{WIRE}}}$$

where K_1^s , K_2^s, P^s, and Q^s are defined as before, with

$$\rho_1 = \frac{Z_{SRC} - Z_0}{Z_{SRC} + Z_0}, \rho_2 = \frac{Z_L - Z_0}{Z_L + Z_0}, \text{ and } Z_{SRC} = s L_{SRC} + \frac{1}{s C_{SRC}} .$$

The term involving the cube root of the number of wires has often been used to estimate, fairly conservatively, the current division in a bundle of N_{WIRE} cables [13]. However, the cube root rule is only one of

several simple scaling laws often used to estimate the division of bulk current inside a cable bundle, depending on how conservative an estimate is required. However, the precise amount of current division among wires in a cable bundle is, in fact, a highly complex problem for which no simple solution may be expected to apply in all cases. Other scales sometimes used are N^{-1}, $N^{-1/2}$, and a worst case estimate that assumes that the current on any single wire equals the bulk cable current.

2.3.4 Local Magnetic Field Coupling to Cables

This model is an extension of the approach used by Greenwood and Kotheimer [12] for calculation of ST coupling to secondary (low-voltage) cables. The transient current flowing down from the high-voltage bus to ground via a current transformer's bushing capacitance and ground strap couples magnetically to secondary cables, whether shielded or unshielded. The geometry for coupling of these local magnetic fields to shielded cables appears in Figure 2.15, and that for unshielded cables in Figure 2.16.

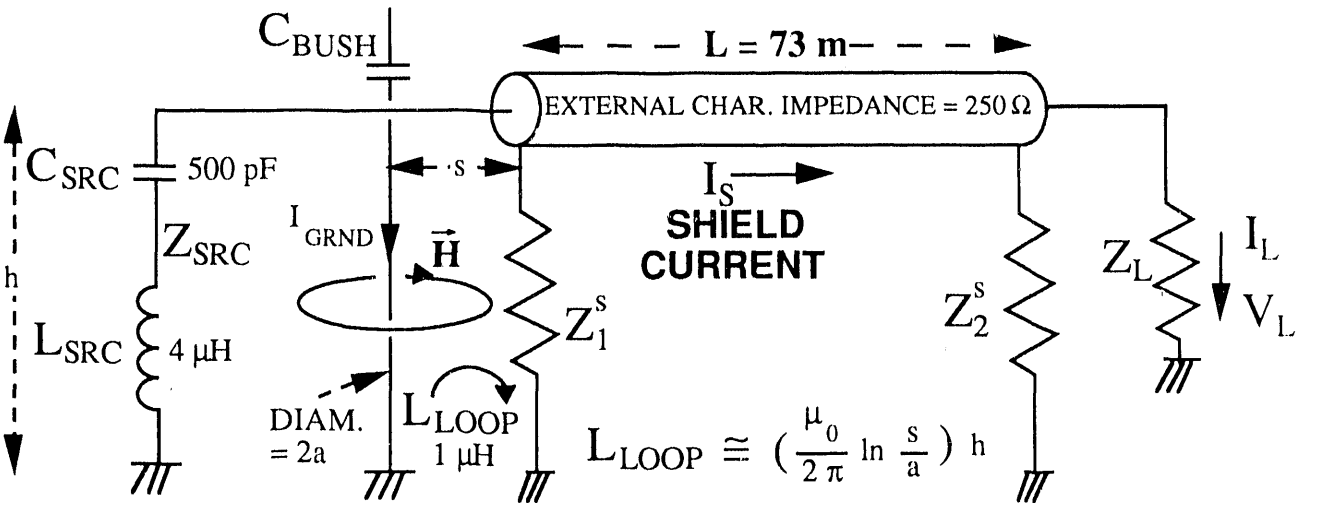

Figure 2.15. Model for Calculation of Magnetic Field Coupling to Shielded Cables

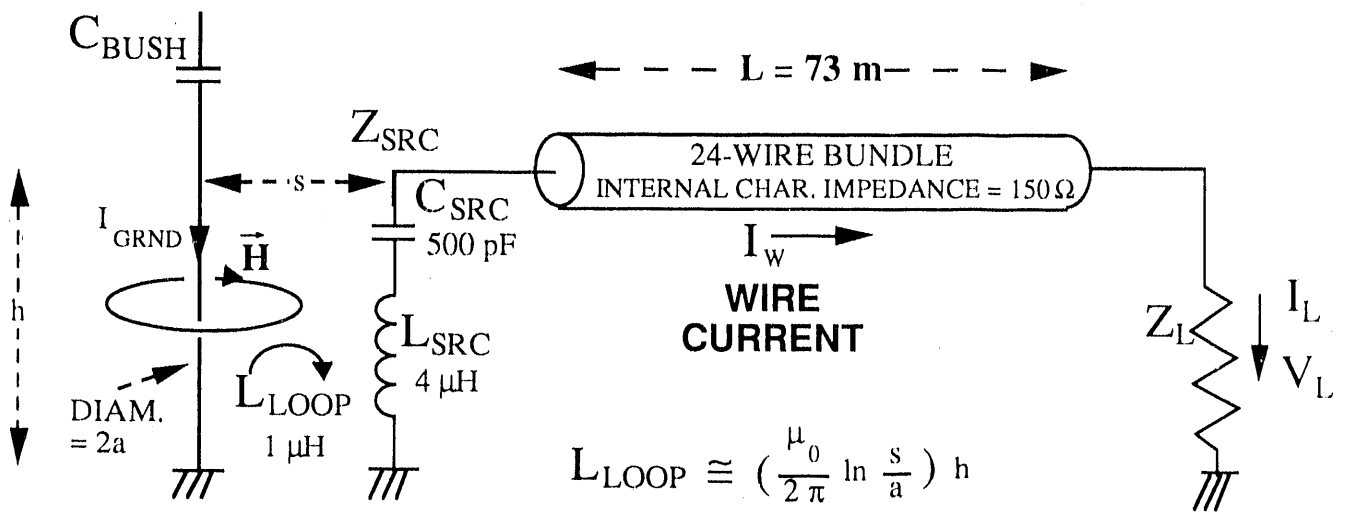

Figure 2.16. Model for Calculation of Magnetic Field Coupling to Unshielded Cables

For shielded cables, the magnetic-field induced voltage across the ground strap / secondary cable shield loop is given by :

$$V_0 = s\, L_{LOOP}\, I_{GRND}$$

The loop inductance is typically on the order of 1 - 2 μH. The shield current produced by V_0 is given by :

$$I_{SHIELD}(z) = \frac{V_0}{Z_0^S}\left[\frac{e^{-\gamma_S z} - \rho_2^S e^{-\gamma_S (z - 2L)}}{1 - \rho_1^S \rho_2^S e^{-2\gamma_S z}}\right] \quad \text{, where}$$

$$\rho_1^s = \frac{Z_1^s - Z_0^s}{Z_1^s + Z_0^s}\,,\ \rho_2^s = \frac{Z_2^s - Z_0^s}{Z_2^s + Z_0^s}\,.$$

The shield currents produced by magnetic-field coupling are used to drive coupling to the cable loads via the mechanisms of transfer-impedance and pigtail coupling; these mechanisms are discussed in subsections 2.3.5 and 2.3.6.

For a bundle of N_{WIRE} unshielded cables, the inductively-coupled loop voltage produces wire currents and voltages are given by [Reference 13]:

$$I_{WIRE}(z,\omega) = \frac{V_0}{Z_0^S}\left[\frac{e^{-\gamma_S z} - \rho_2^S e^{-\gamma_S (z-2L)}}{1 - \rho_1^S \rho_2^S e^{-2\gamma_S z}}\right]\frac{1}{\sqrt[3]{N_{WIRE}}}$$

$$V_{WIRE}(z,\omega) = V_0\left[\frac{e^{-\gamma_S z} + \rho_2^S e^{-\gamma_S (z-2L)}}{1 - \rho_1^S \rho_2^S e^{-2\gamma_S z}}\right]\frac{1}{\sqrt[3]{N_{WIRE}}}$$, where

$$\rho_1^S = \frac{Z_{SRC} - Z_0}{Z_{SRC} + Z_0},\ \rho_2^S = \frac{Z_L - Z_0}{Z_L + Z_0},\ Z_{SRC} = s L_{SRC} + \frac{1}{s C_{SRC}},\ \text{and } V_0 = s L_{LOOP} I_{GRND}.$$

2.3.5 Transfer Impedance Coupling to Shielded Cable Loads

Currents induced on the shields of shielded cables can couple to the inner conductors of the cables, and thus to the cable loads. The transfer-impedance model used for coupling of these shield currents to shielded cable loads is based on Vance [7]. The general features of this model are shown in Figure 2.17.

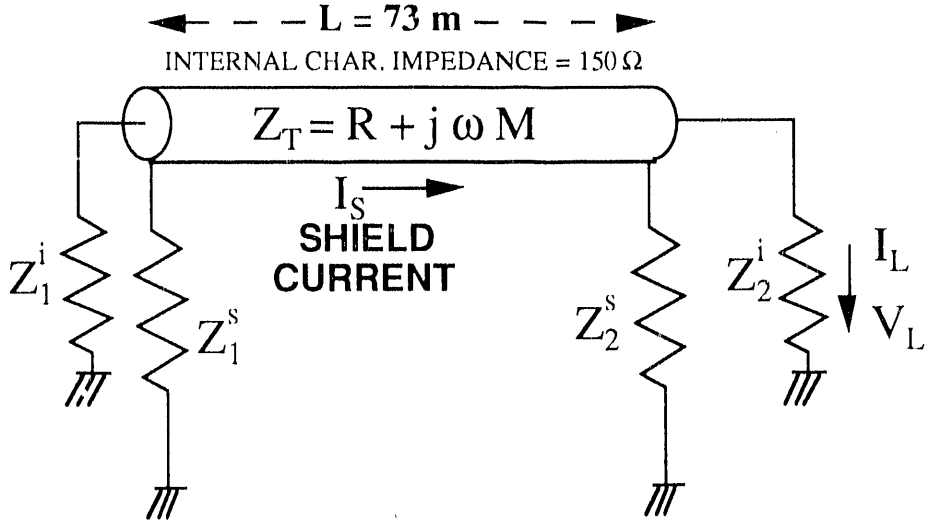

Figure 2.17. Model for Calculation of Cable Shield Current Coupling to Cable Loads Via Transfer Impedance

The current at an arbitrary point z along the center conductor of the shallowly-buried shielded cable is found from

$$I_i(z,\omega) = [K_1^i + P^i(z)]\, e^{-\gamma_i z} + [K_2^i + Q^i(z)]\, e^{\gamma_i z}$$

where

$$P^i(z) = \frac{1}{2Z_o^i}\int_0^z e^{\gamma_i \zeta}[I_s(\zeta,\omega)e^{-jk\zeta}Z_T(\omega)]\,d\zeta$$

$$Q^i(z) = \frac{1}{2Z_o^i}\int_z^L e^{-\gamma_i \zeta}[I_s(\zeta,\omega)e^{-jk\zeta}Z_T(\omega)]\,d\zeta$$

$$K_1^i = \rho_1^i[\rho_2^i P^i(L)\, e^{-\gamma_i L} - Q^i(0)\, e^{\gamma_i L}]/\Delta^i$$

$$K_2^i = \rho_2^i e^{-\gamma_i L}[\rho_1^i Q^i(0) - P^i(L)]/\Delta^i$$

$$\rho_1^i = \frac{Z_1^i - Z_0^i}{Z_1^i + Z_0^i},\ \rho_2^i = \frac{Z_2^i - Z_0^i}{Z_2^i + Z_0^i},\ \Delta^i = e^{\gamma_i L} - \rho_1^i \rho_2^i e^{-\gamma_i L}$$

and where the conductor runs from z=0 to z=L, has a characteristic impedance Z_o^i, and is terminated into Z_1^i at z=0 and Z_2^i at z=L. The propagation constant is $\gamma_i = j\omega\frac{\sqrt{\varepsilon_r}}{c}$, where ε_r is the permittivity of the cable insulation and c is the speed of light. The wave number k is given by $\frac{\omega}{c}$. The cable transfer impedance Z_T, typically obtained by measurement, is expressed with simple resistive and inductive terms : $Z_T = R + j\omega M$. For this study, the measured transfer impedance of a typical relay cable is approximated as

$$Z_T = 3.5\times10^{-3}\,\frac{\Omega}{m} + j\omega 4.8\times10^{-9}\,\frac{H}{m}$$ (reference [1]).

A special-case solution of the conductor current, for z = L, is given by:

$$I_L = (1 - \rho_2^i)[P^i(L) - \rho_1^i Q^i(0)]/\Delta^i$$

For arbitrary position z, the voltage is

$$V_i(z,\omega) = \left\{ [K_1^i + P^i(z)]\, e^{-\gamma_i z} - [K_2^i + Q^i(z)]\, e^{\gamma_i z} \right\} Z_0^i \quad .$$

At the position $z = L$, the voltage across the load impedance is given by

$$V_L = Z_2^i I_L \quad .$$

Well-shielded cables have a very low transfer impedance. For the most part, transfer-impedance coupling was not found to be the primary driver for relay interference coupling via well-shielded control cables. Results were generated for several types of load impedance Z_2^i, including constant impedance, and measured frequency-dependent impedances of real relays.

2.3.6 Pigtail-Termination Inductive Coupling of Shield Currents to Shielded Cable Loads

Even though transfer-impedance coupling might not adversely affect a well-shielded control cable's load, coupling effects at the shield terminations often do produce interference. The calculation of shield termination coupling to cable loads via the mutual inductance of the shield termination ("pigtail") and the load wires is based on an article by C. R. Paul [8]; relevant model parameters are summarized in Figure 2.18.

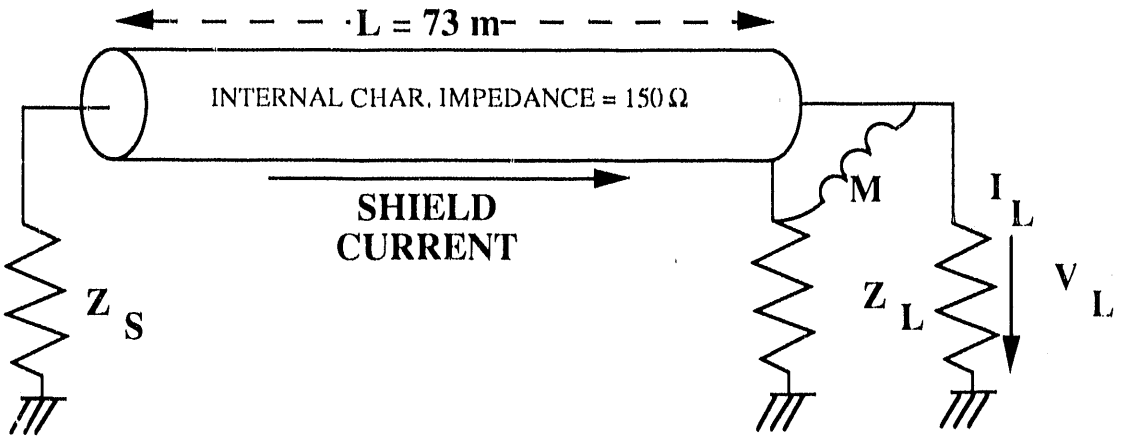

Figure 2.18 Model for Calculation of Cable Shield Current Coupling to Relay Loads Via Pigtail Inductance

The induced current at the load, I_L, is given by

$$I_L = \frac{1}{Z_S + Z_L} j\omega M I_{SHIELD} ,$$

where Z_S and Z_L are the source and load (relay) impedances respectively, ω is the radian frequency, I_{SHIELD} is the shield current at the pigtail, and M is the pigtail/relay wire mutual inductance. M is calculated with the formula $M = \frac{\mu_o}{\pi} \cosh^{-1}\frac{s}{2a} L_{pig}$, where s is the pigtail/wire separation, a is the wires' common radius, and L_{pig} is the length of the pigtail. This coupling mode turns out to be significant for assessment of field-driven responses of typical shielded control cables. Pigtail coupling predictions were generated for several types of load impedance Z_L, including both constant impedance and measured frequency-dependent impedances.

2.4 MODEL VALIDATIONS

Comparisons of measured and predicted waveforms help to validate model approaches and assumptions; these comparisons have been performed for switching transients, but are difficult and impractical at best for HEMP environments. A 500 kV air-insulated ring bus was used for an extensive series of both measurements and predictions [1,6,9] for several ST phenomena.

A METAP-produced bus current for a hand-operated disconnect-switch closing is compared to the corresponding measurement in Figure 2.19.

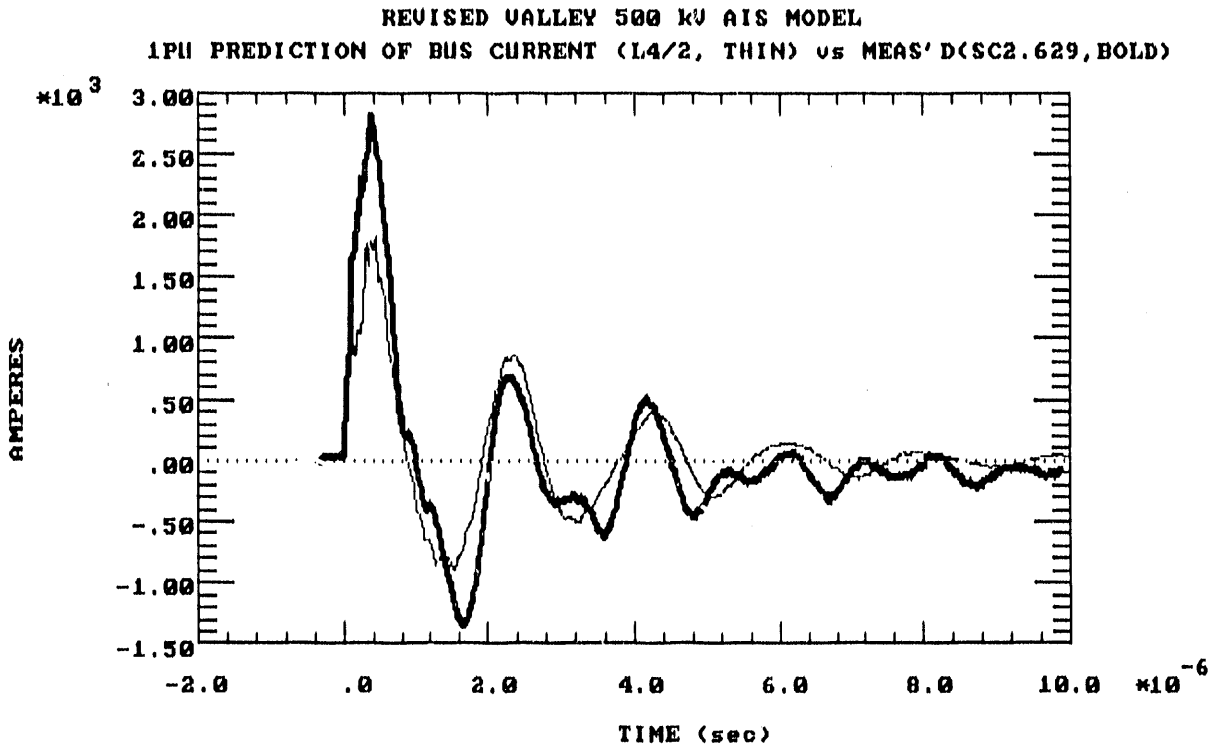

Figure 2.19. METAP Prediction (thin) and Measurement (bold) of Transient Bus Current Waveforms on a 500 kV Ring Bus

A TRAFIC calculation for an ST-generated vertical electric field is overlaid with a measured field in Figure 2.20; for the TRAFIC calculation, the METAP prediction for the bus current of the previous figure was assumed. The TRAFIC solution for an ST-generated horizontal magnetic field is compared to actual measurement in Figure 2.21.

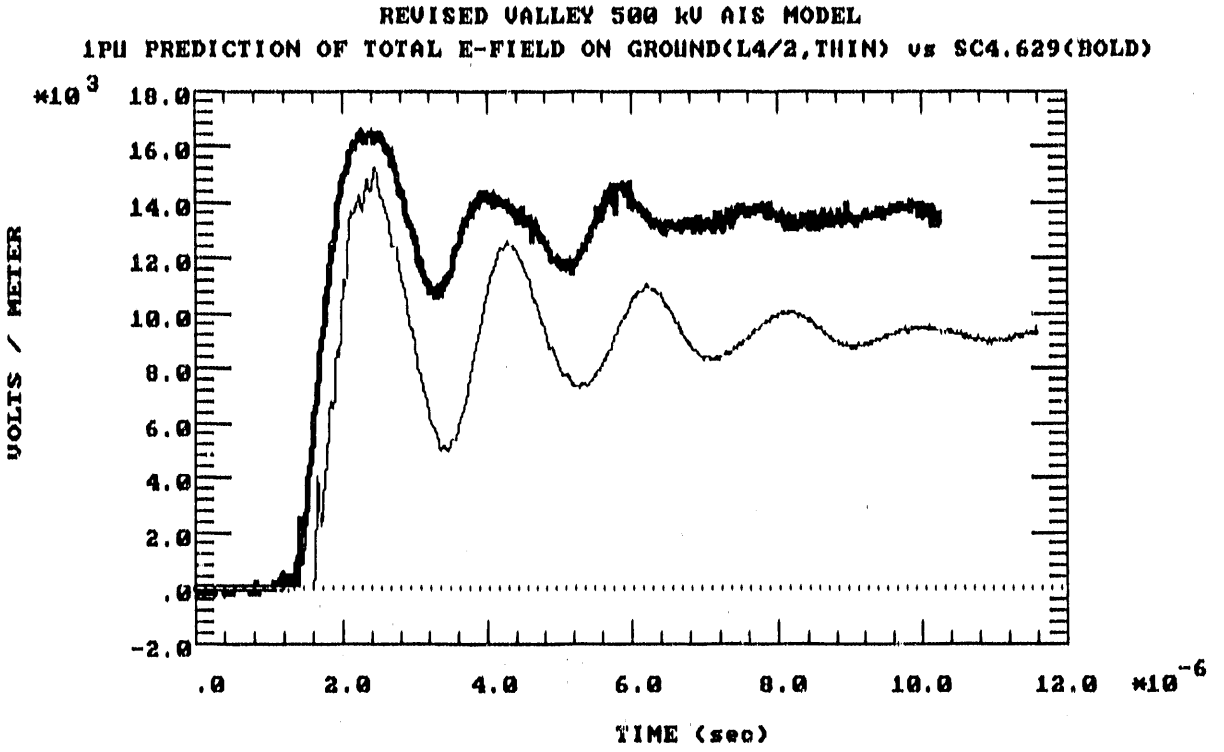

Figure 2.20. TRAFIC Prediction (thin) and Measurement (bold) of Vertical Radiated Electric Field on the Ground Beneath a 500 kV Ring Bus

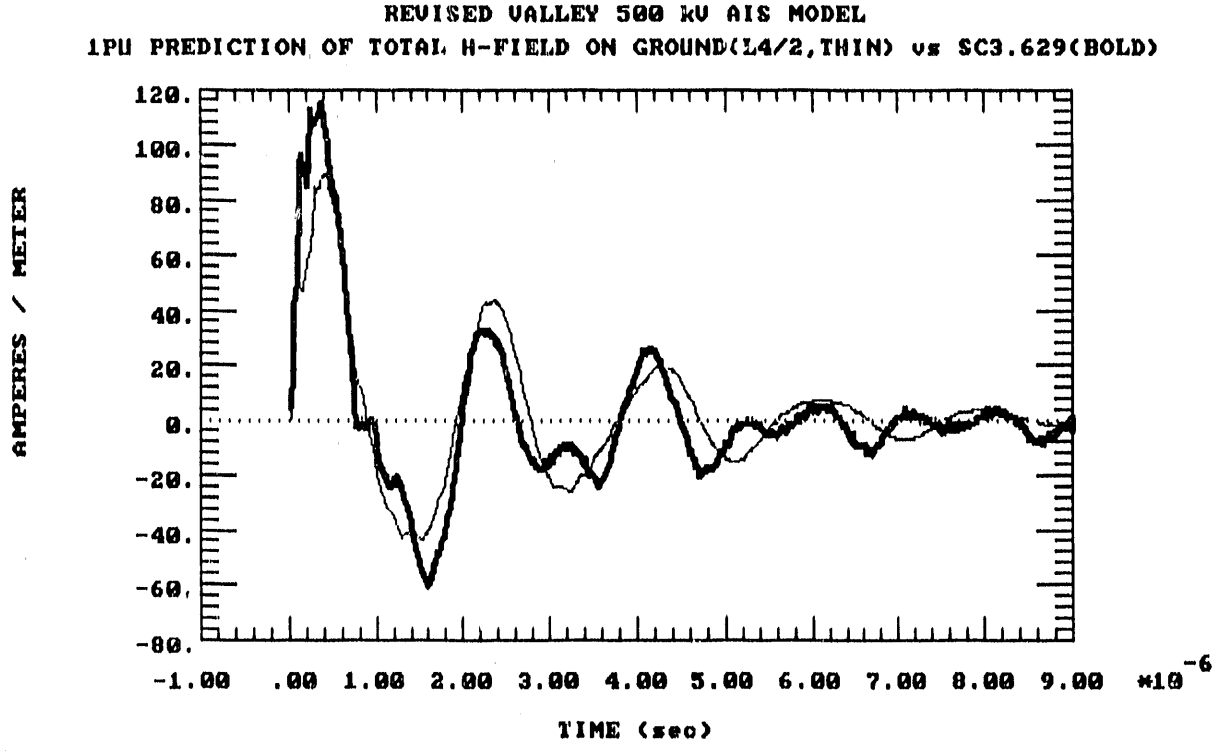

Figure 2.21. TRAFIC Prediction (thin) and Measurement (bold) of Horizontal Radiated Magnetic Field on the Ground Beneath a 500 kV Ring Bus

A prediction for an ST-generated relay load response current is compared to a measured load response in Figure 2.22. For the prediction, both METAP bus currents and TRAFIC fields were used, and all shielded-cable coupling modes (electric field, magnetic field, transfer-impedance, pigtail, and conducted) were included. Prediction and measurement of a relay's voltage response are compared in Figure 2.23. The voltage waveforms are characterized by much higher ringing frequencies than are the current responses.

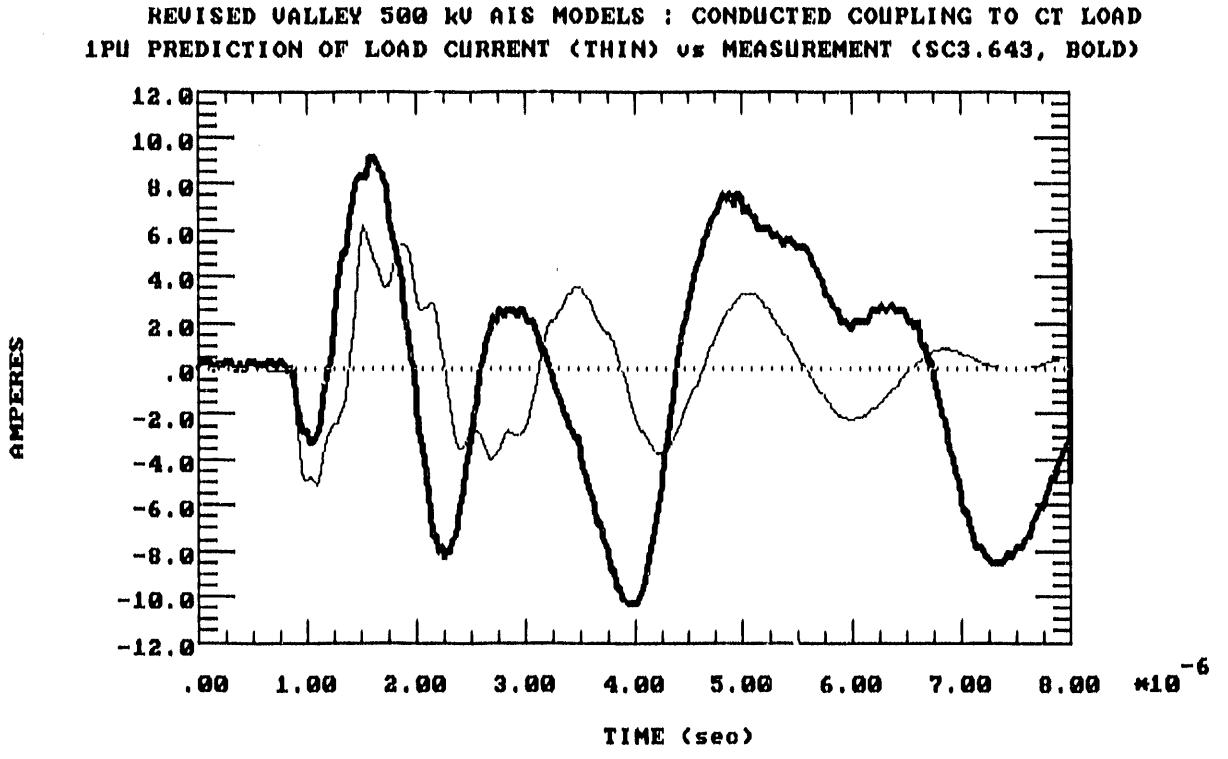

Figure 2.22. Prediction (thin) and Measurement (bold) of ST-Induced Relay Current at Terminal Rack of a 500 kV Ring Bus CT

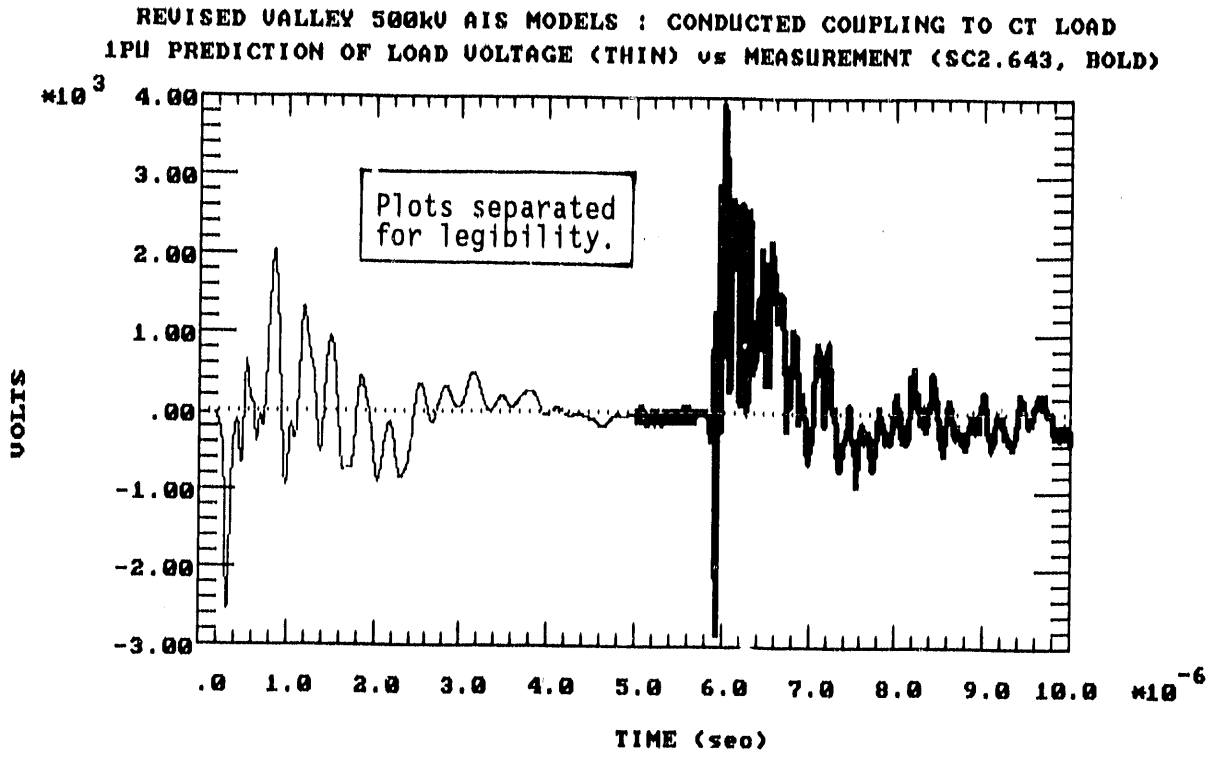

Figure 2.23. Prediction (thin) and Measurement (bold) of ST-Induced Relay Voltage at Terminal Rack of a 500 kV Ring Bus CT

In terms of peak amplitudes and resonant frequencies, the comparisons above are very encouraging. Predictions for the initial observables (bus current and radiated fields) compare quite well to measurements, while those for the final observables (relay current responses) compare less favorably. This is most likely due to the large number of assumptions (regarding cable loads, lengths, insulation, orientation, etc.) required to go from the initial models to the final models. Results produced with the models discussed above are presented in section 4.0 of this report for both ST and HEMP coupling to a 500 kV substation.

3.0 RELAY SUSCEPTIBILITY TESTS

Electromagnetic transients, particularly those produced by a nuclear induced high altitude electromagnetic pulse (HEMP), may adversely affect relay systems used for transmission substation protection, causing them to upset or fail. The transients can couple onto the relay circuits by a combination of any of the following: propagation through the relay sensing element (current transformer, potential transformer, etc.), direct free-field coupling onto the relay control cables or other auxiliary cables, or re-radiated field coupling from a nearby ring bus or transmission line. Regardless of the coupling mechanism, a voltage transient will develop at the terminals of the relay, either across terminal pairs or across the terminals and ground, depending on the shielding scheme employed. In turn, these voltage transients may interfere with control signals and may possibly lead to false relay trips or other relay system misoperations.

Limited laboratory tests were performed to investigate the response of a representative relay to a fast rise transient impulse. The objective of the investigation was to determine voltage levels and locations at which arcing occurs, and voltage thresholds where relay upset or failure occurs. In addition, measurements were performed to determine the impedance at the terminals of the relay for use in the coupling models. Upset is defined here as a false trigger of the relay. A relay system failure is any system misoperation, including a failure of the relay to respond as appropriate. Through consultations with a local utility company and relay manufacturers, a General Electric type STD15C transformer differential relay was selected from among the twelve relays in Table 3.1 which were made available to BDM for testing.

The selection of this relay was based on the fact that the type STD15C relay, containing solid-state components, represents a compromise between an electromechanical relay, expected to be relatively immune to transient damage, and a microprocessor based relay which can potentially be more susceptible to transient impulses. A schematic diagram and photographs of the type STD15C relay are shown in Figures 3.1 and 3.2. Results presented in this chapter are

applicable only to the STD15C relay and should not be considered typical of all relays. Additional testing of other relays need to be performed before any generalized statements can be made.

Table 3.1. Relays Available at BDM for Testing (From DOE/ORNL)

Item	Quantity	Manufacturer	Type	Style Number	Description
1	1	Westinghouse	CO-8H1111N	264C900A07	Overcurrent Relay
2	1	Westinghouse	SI-I	6681D78A02	Overcurrent Relay
3	1	Westinghouse	KD-10	719B195A11	Compensator Distance Relay
4	1	Westinghouse	IRD-9	289B449A10 A	Directional Overcurrent Ground Relay
5	1	Westinghouse	HU-1	290B346A10 B	Transformer Differential Relay
6	1	Westinghouse	CA-16	671B157A09	Percentage Differential Relay
7	1	Westinghouse	CV-5	1875512 A	Voltage Relay
8	1	Westinghouse	CA	290B893A09	Percentage Differential Relay
9	1	General Electric	Model 12	PJC15F1A	Instantaneous Overcurrent and Voltage Relay
10	1	General Electric	Model 12	GCX51B13A	Directional Distance (Reactance) Relay
11	1	General Electric	Model 12	STD15C3A Rev. B	Transformer Differential relay with Percentage and Harmonic Restraint
12	1	General Electric	Model 12	PVD21B1A	Differential Voltage Relay

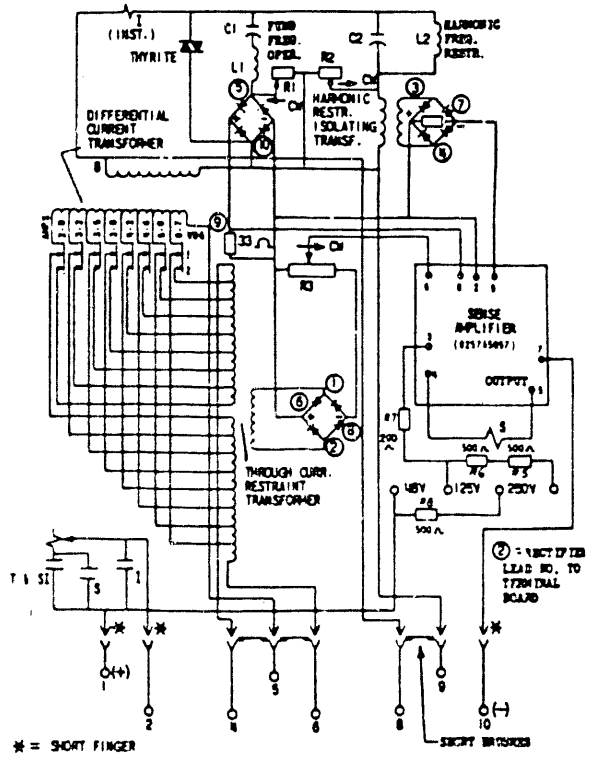

Figure 3.1. Schematic Diagram of Type STD15C Transformer Differential Relay

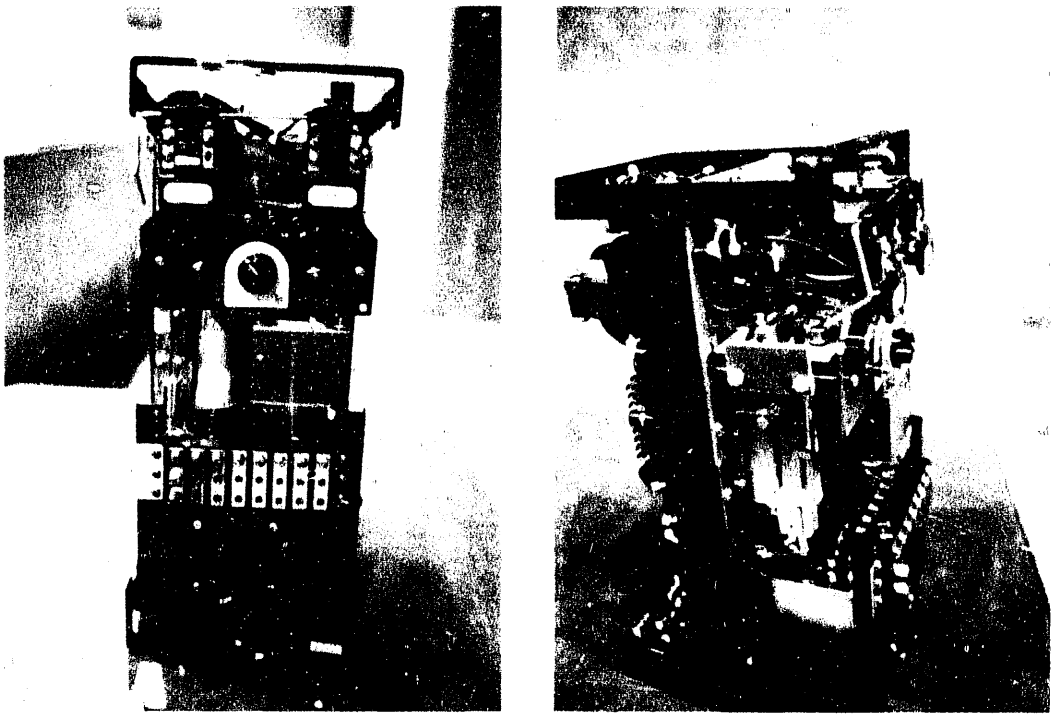

Figure 3.2. Photograph of the Type STD15C Relay

3.1 GENERAL IMPULSE TEST CIRCUIT

In order to simulate an actual relay installation, the relay was flush-mounted on an aluminum panel which was bolted to a 0.48 m by 1.42 m (19 inch by 56 inch) rack. Terminal/shorting blocks were mounted on the rack below the relay and were wired to the appropriate relay terminals using 0.91 m (3 feet), 12 AWG switchboard wire supplied by the Public Service Company of New Mexico. The relay rack itself was tied to an earth ground via the earth grounding blocks in the laboratory. A 48 volt DC battery power supply was connected to the relay to provide power to the sensing circuits and output circuits during pulse testing. A block diagram and photographs of the complete test installation are shown in Figures 3.3 and 3.4. Normally, the output line of the relay would feed a relay trip coil. However, since a relay trip coil was not available, it was substituted by a 25 ohm wirewound resistor.

In typical installations, the cabling between the relay and the current transformers (ct's) utilize multiconductor cables spanning a few hundred

meters. The cables may or may not be shielded. Even if they are shielded, shield termination methods vary among the utilities. Two specific shielding arrangements were examined in the laboratory. In one case, the shield was left unterminated, and in the other case, the shield was grounded at the relay rack. The majority of the tests were performed with the shield unterminated. For the test installation in the laboratory, 30.5 m (100 feet) of four conductor shielded cable, purchased from the Public Service Company of New Mexico, was used. This cable had a measured relative propagation velocity of 0.65 and a characteristic impedance of approximately 65 ohms from conductor-to-conductor or 41 ohms from conductor-to-shield.

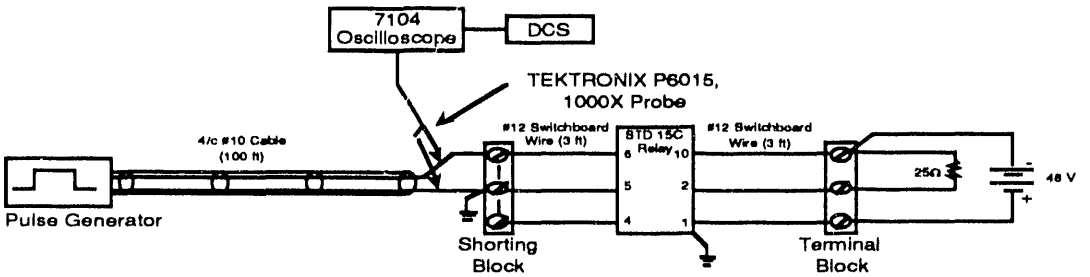

Figure 3.3. General Impulse Test Circuit

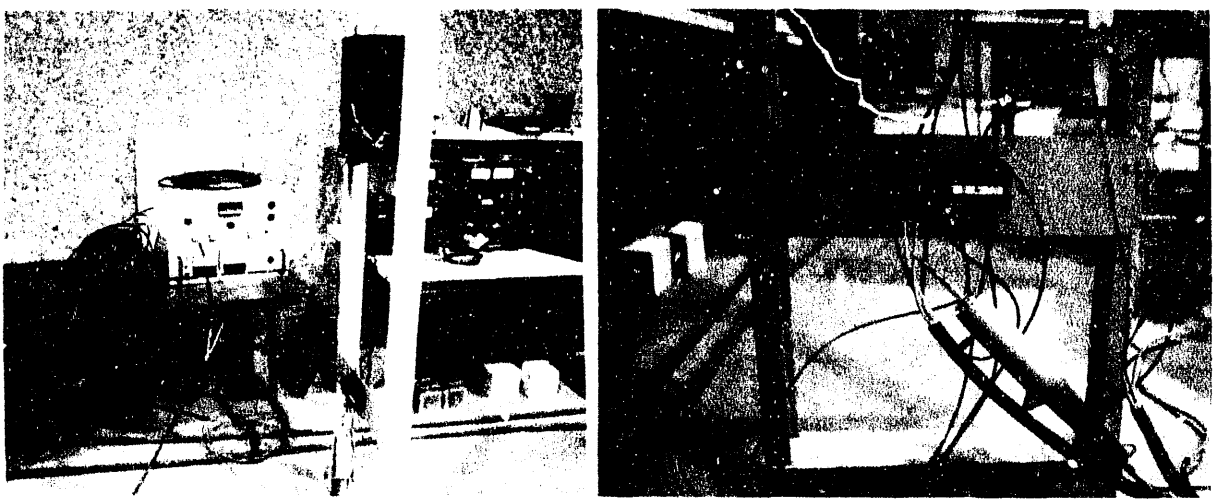

Figure 3.4. Test Set-Up for Relay Impulse Tests

3.2 TEST PROCEDURE

The relay tests were divided into three categories: input impedance tests, upset/failure tests, and surge protection package tests. The input impedance tests were performed to geather information on typical load impedances that may be present on the control cables. Upset and failure tests were performed on the relay circuits to establish threshold levels at which normal relay operation is disrupted. During these tests, voltage levels and locations at which arcing occurs was recorded. The SPP tests were performed to determine whether additional protection is provided to the DC circuits with a SPP device installed. Both the upset/failure tests and the SPP tests made use of impulse-type measurements while the impedance tests were continuous wave, swept frequency measurements.

The impedance of the relay at its terminals, as a function of frequency, was measured with an HP3577A network analyzer and an HP35677A s-parameter test set. After calibrating the network analyzer, it was attached to the relay terminals under test and the impedance was displayed directly on the CRT. The frequency was swept bewteen 100 kHz and 200 MHz. An HP9826 computer provided automated control of the network analyzer and recorded the impedance data.

For the last two tests, pulses were injected onto the relay circuits at the terminal/shorting block where the voltage was monitored with a Tektronix P6015 high voltage probe and a Tektronix 7104 oscilloscope. Voltage waveforms were processed and stored using a digital camera system attached to the oscilloscope. HEMP induced voltage transients were simulated by injecting impulses onto the relay circuits using either a charged-line square pulse generator (SPG), or a high voltage capacitive discharge pulser. The SPG delivers a square pulse whose pulse width is governed by the length of the charge line. The capacitor discharge pulser, on the other hand, delivers a pulse whose shape is influenced by the impedance of the load. Both pulse generators are variable in amplitude with rise times on the order of a few nanoseconds. Waveforms produced by the two pulsers into a 50 ohm load are shown in Figure 3.5.

The original intent of the test program was to test each terminal pair on the relay with impulses simulating different HEMP induced transient

parameters such as rise time and pulse width. The test matrix in Table 3.2 was developed to satisfy this approach. However, only a representative subset of the configurations listed in Table 3.2 were actually implemented. These are denoted in the table by asterisks. Early in the test program it was thought that relay susceptability and flashovers were synomonous; therefore, emphasis was given to identifying flashover voltage levels. It became apparent that flashovers were suficient but not necessary for the relay to be susceptable to upsets or failures. Thus, emphasis shifted toward exploring larger ranges of upset parameters, including possible failures associated with the DC trip circuits.

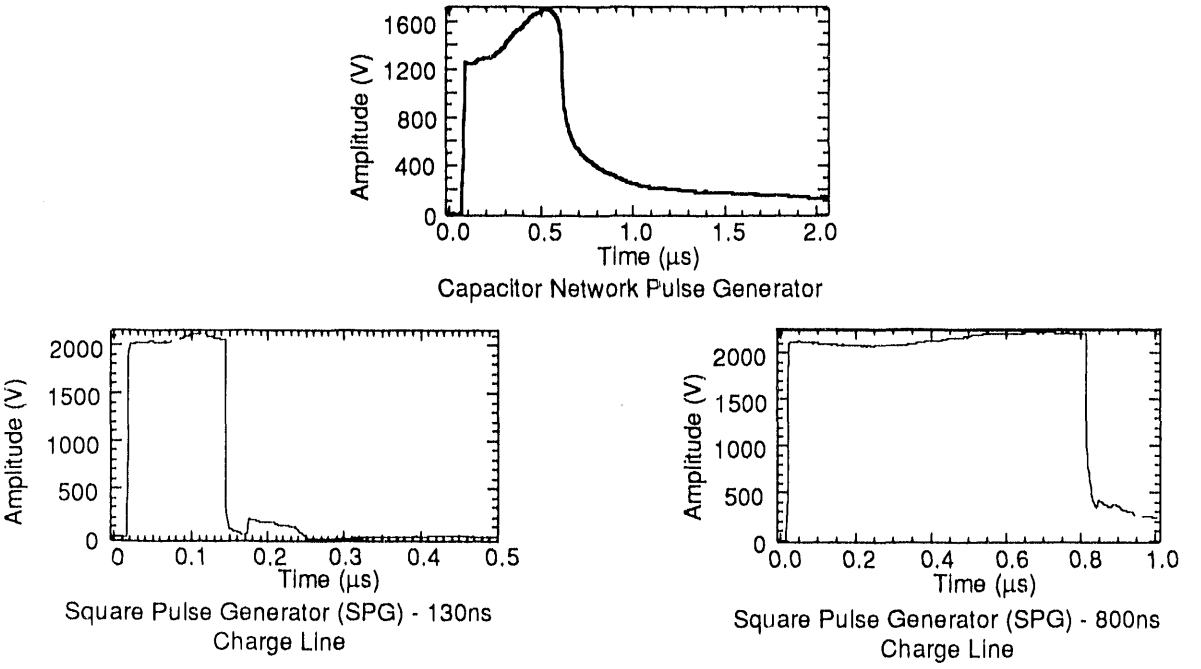

Figure 3.5. Pulse Generator Waveforms into a 50 Ohm Load

Table 3.2. Relay Test Configuration Matrix

Circuit Type	Pulsed Terminal Pair (+,-)	Pulse Generator
CT Differential Mode	6, 5 (Gnd)*	SPG, 130 ns
	6, 5 (Gnd)*	SPG, 800 ns
	6, 5 (Gnd)*	Cap
CT Differential Mode	4, 5 (Gnd)	SPG, 130 ns
	4, 5 (Gnd)	SPG, 800 ns
	4, 5 (Gnd)	Cap
OUTPUT Common Mode	2, Gnd*	SPG, 130 ns
	2, Gnd*	SPG, 800 ns
	2, Gnd*	Cap
OUTPUT Differential Mode	2, 10*	SPG, 130 ns
	2, 10*	SPG, 800 ns
	2, 10*	Cap
DC POWER	1, 10 (Gnd)	SPG, 130 ns
	1, 10 (Gnd)	SPG, 800 ns
	1, 10 (Gnd)*	Cap
DC POWER	10, 1 (Gnd)	SPG, 130 ns
	10, 1 (Gnd)	SPG, 800 ns
	10, 1 (Gnd)*	Cap

3.3 RELAY OPERATION VERIFICATION

Correct operation of the STD15C relay was verified periodically during the test using a Multi Amp model SR-76A relay test set. The test set is a versatile instrument capable of performing a number of tests to calibrate and evaluate relay performance. Six measurements were performed to evaluate the performance of the STD15C relay:

1) Minimum pick-up current of the main unit.

2) Minimum pick-up current of the target and seal-in unit.

3) A single point check on the timing characteristics.

4) A single point check on through current restraint.

5) A single point check on harmonic restraint.

6) Minimum pick-up current of the instantaneous unit.

Deviations between these results, manufacturer specifications, and previous measurements would indicate a compromised performance and possible failure of the relay after being subjected to the high voltage, fast rise pulses.

3.4 EXPERIMENTAL RESULTS

3.4.1 Control Cable

Basic propagation characteristics of the multiconductor cable were measured. The conductor-to-conductor and conductor-to-shield characteristic impedances of the cable were measured with a Tektronix 1502 TDR cable tester. The cable tester displays the value of the reflection coefficient, ρ, from which the characteristic impedance may be determined using the relation,

$$Z_0 = Z_1 \frac{(1 + \rho)}{(1 - \rho)}$$

where Z_1 is the reference load impedance (50 ohms). The results of this measurement yield an average conductor-to-conductor impedance of 65 ohms and an average conductor-to-shield impedance of 41 ohms. The time domain technique was also used to determine the propagation velocity of the cable. In this case, the test circuit of Figure 3.6 was implemented where a relatively large amplitude pulse was injected on the cable while monitoring the voltage waveform at the drive end of the cable. Propagation velocity is given by

$$V_p = \frac{2L}{t}$$

where L is the measured length of the cable and t is the round trip transit time between the drive point and open end of the cable. Figure 3.7 shows that for 30.5 m (100 feet) of the 4 conductor shielded cable, the round trip transit time is 311 ns which implies a propagation velocity of 1.960×10^8 m/sec (6.431×10^8 ft/sec), or a relative velocity of 0.654.

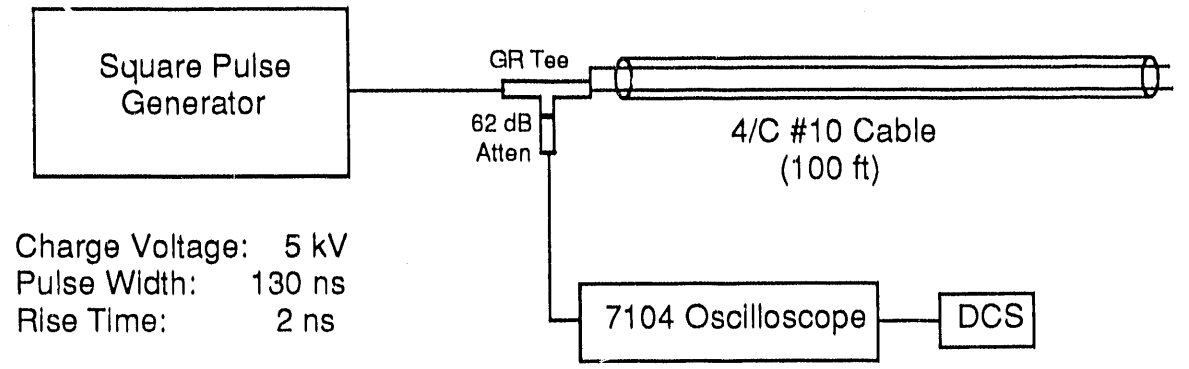

Figure 3.6. Time Domain Reflectometry Test Circuit

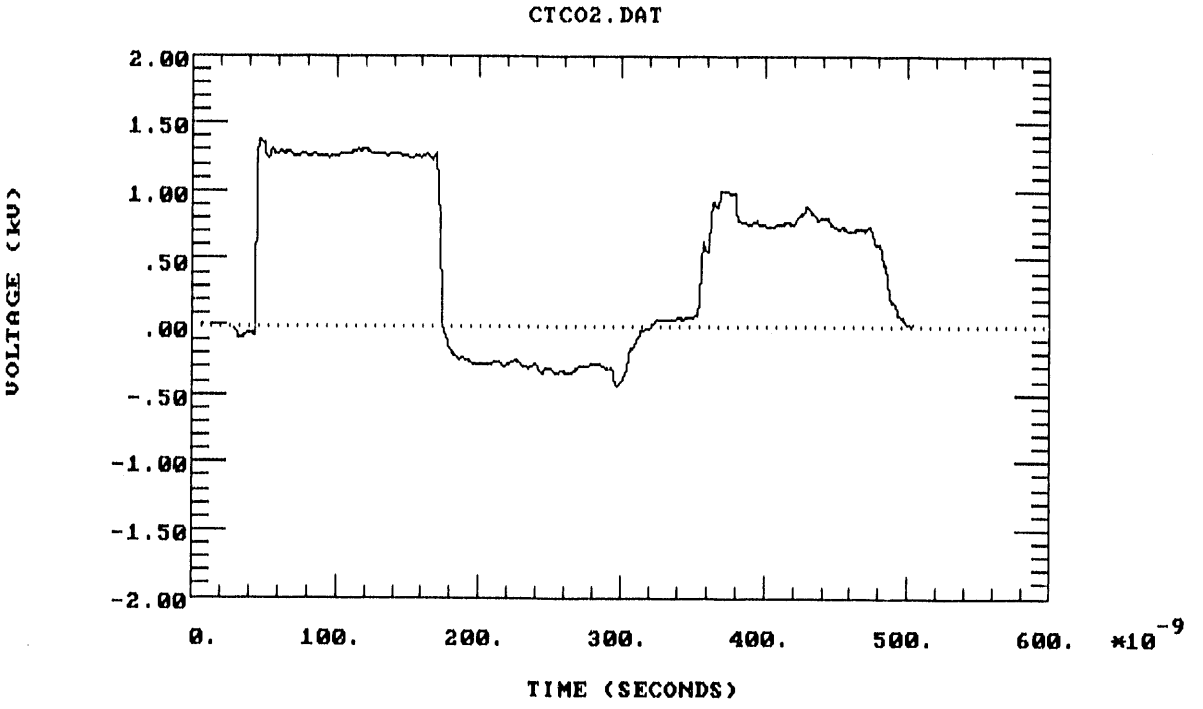

Figure 3.7. TDR Measurement of a 4-Conductor, 30.5 m Control Cable

3.4.2 Input Impedance

The input impedance of the relay between terminal pairs and between the terminals and ground were measured in the laboratory with an HP3577A network analyzer. Plots of the terminal impedance as a function of frequency are given in Figure 3.8. The terminals of the STD15C relay were

shown schematically in Figure 3.1 and are listed below in Table 3.3 for reference. Note that the impedances are very much frequency dependent, thus yielding a different response for any given stimulus. The differential transformer (CT) leads have two distinct resonances at 3 MHz and 100 MHz. Voltage waveform frequency spectra not at these frequencies are suppressed at the relay. With respect to ground, the DC circuit leads also display a unique characteristic. At DC, the input impedance is infinite, but at frequencies above 1 MHz, the impedance is quite low (less than 200 ohms). Thus low frequency voltage and high frequency current components are dominant at the DC circuit terminals.

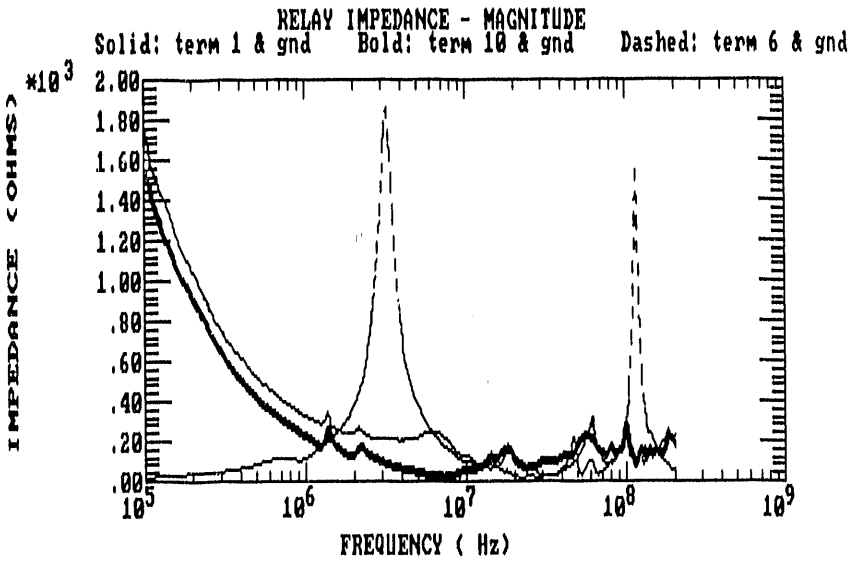

(a) Solid: Terminal 1 to Ground
Bold: Terminal 10 to Ground
Dashed: Terminal 6 to Ground

Figure 3.8. STD15C Relay Impedance - Magnitude

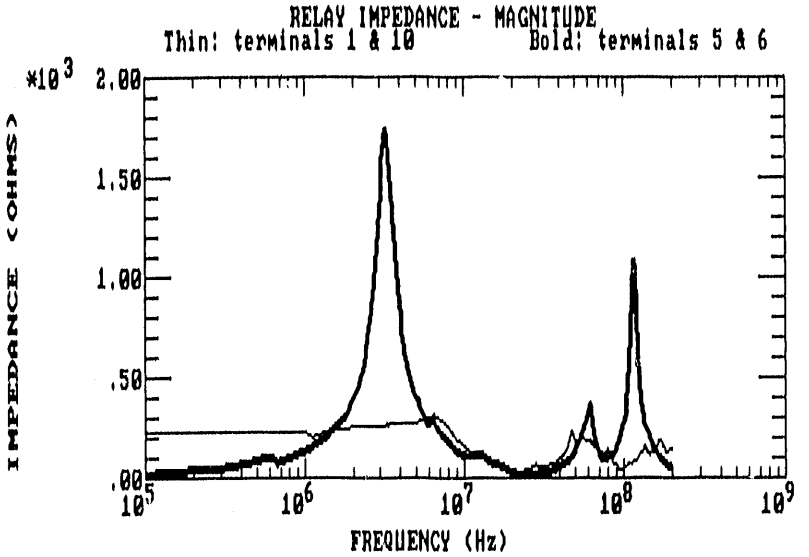

(b) Thin: Terminal 1 to Terminal 10
Bold: Terminal 5 to Terminal 6

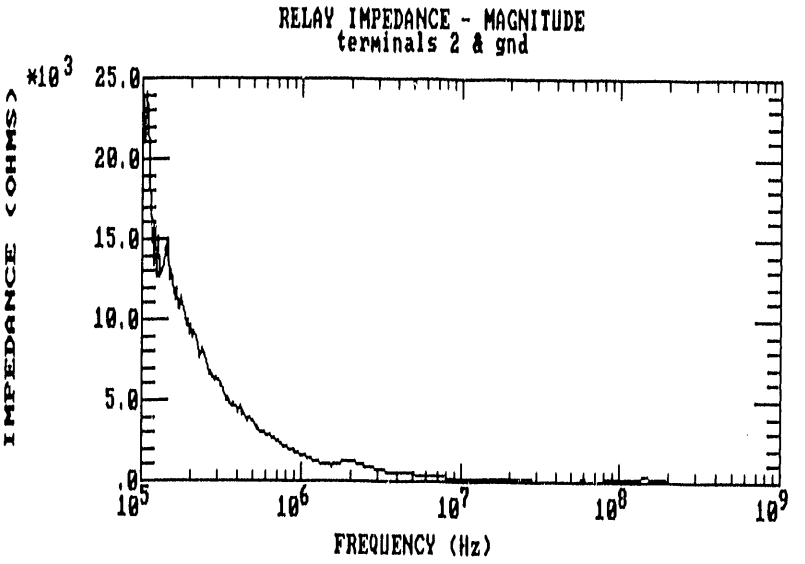

(c) Terminal 2 to Ground

Figure 3.8 (Concluded). STD15C Relay Impedance - Magnitude

Table 3.3 STD15C Relay Terminal List

TERMINAL	DESCRIPTION
1	DC BATT. (+)
2	RELAY OUTPUT
4	CT (A)
5	CT COMMON
6	CT (B)
10	DC BATT. (-)

3.4.3 Shorting Block

Two conductors of the multiconductor cable were attached to adjacent terminals on the shorting block with the shorting bar connected to one of the terminals. The 0.91 m (3 feet) switchboard wires, that would later connect to the relay, were attached to the shorting block on one end and left open on the other end. As in actual installations, the terminal attached to the shorting bar was also grounded at the relay rack. The other end of the cable was connected to the square pulse generator (SPG) which was configured to deliver a 130 ns wide pulse. A Tektronix P6015 high voltage probe was clipped onto the conductors approximately one inch from the shorting block and was connected to the oscilloscope equipped with a digital camera system. Over a series of single shot events, the charge voltage level was increased from 500 volts until flashover was detected on the shorting block. The occurrence of flashover at the shorting block was easily detected from the voltage waveform data and by observation.

Figures 3.9 through 3.12 illustrate the effects of flashover on the voltage waveform at the shorting block as the charge voltage was increased on the SPG. In Figure 3.9, where no flashover was observed, the incident 130 ns pulse traverses the length of the multiconductor cable until it reaches the shorting block. Since the shorting block appears as an open circuit, the pulse is reflected back towards the SPG and charge line. When the pulse reaches the open end of the charge line, it is again reflected and moves toward the shorting block. Cable losses attenuate the pulse during each traversal which causes damping in the waveform. Eventually, the cable is charged to some nominal voltage potential since the system is essentially an open circuit transmission line.

When the charge voltage was increased to 7.75 kV, a faint arc was observed across the shorting bar. Its effect is apparent in Figure 3.10

where the pulse reflections tend to rapidly diminish over a portion of the waveform. The peak breakdown voltage level measured at the shorting block was approximately 3.8 kV; this defined the flashover voltage threshold of the shorting block.

Finally, when the charge voltage was set to 8 kV, a distinct arc occurred which was significant enough to completely discharge the cable, as shown in Figure 3.11. Of special interest is the fact that the flashover did not occur on the initial pulse but rather on one of the reflected pulses. This statistical nature of flashover events is further exemplified by comparing Figure 3.11 with Figure 3.12 which shows a repeat of the measurement. Although none of the instrumentation was changed, flashover occurred on the third reflected pulse in Figure 3.12 whereas it occurred on the second reflected pulse in Figure 3.11. The significance of this behavior is that successive pulses on a relay circuit may induce breakdown, even though the individual pulses will not cause breakdown on their own. Moreover, it shows how the relay may be subjected to multiple pulses even though the event causing the disturbance may only be a single pulse.

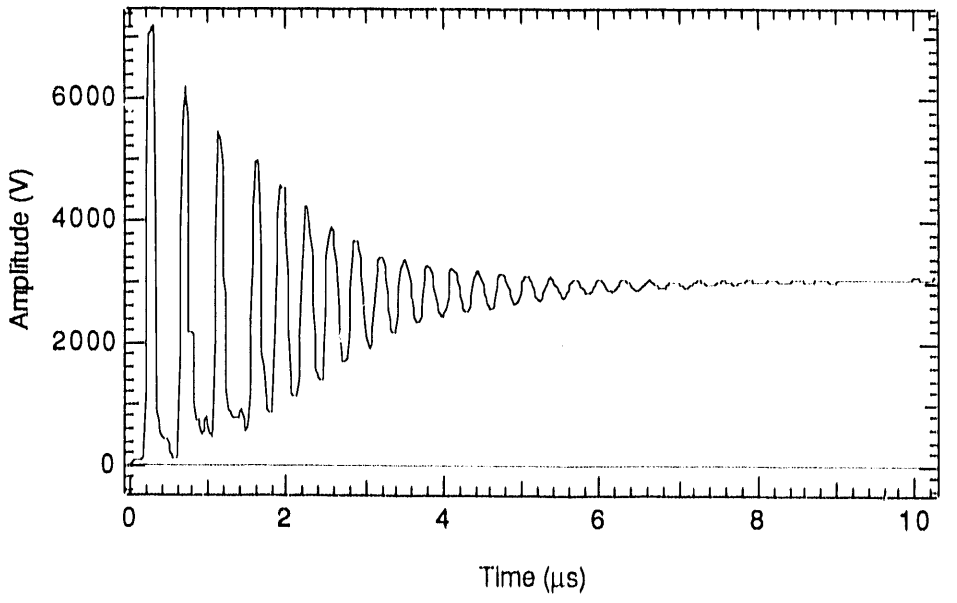

Figure 3.9. Voltage Measured at the Shorting Block with SPG Charge Voltage Set to 7.5 kV - No Breakdown

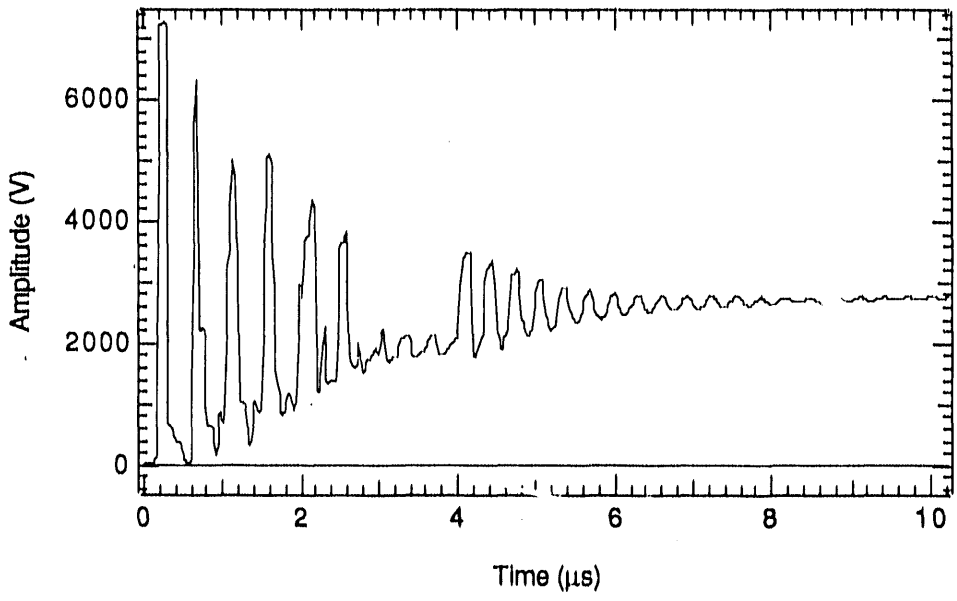

Figure 3.10. Voltage Measured at the Shorting Block with SPG Charge Voltage Set to 7.75 kV - Weak Breakdown

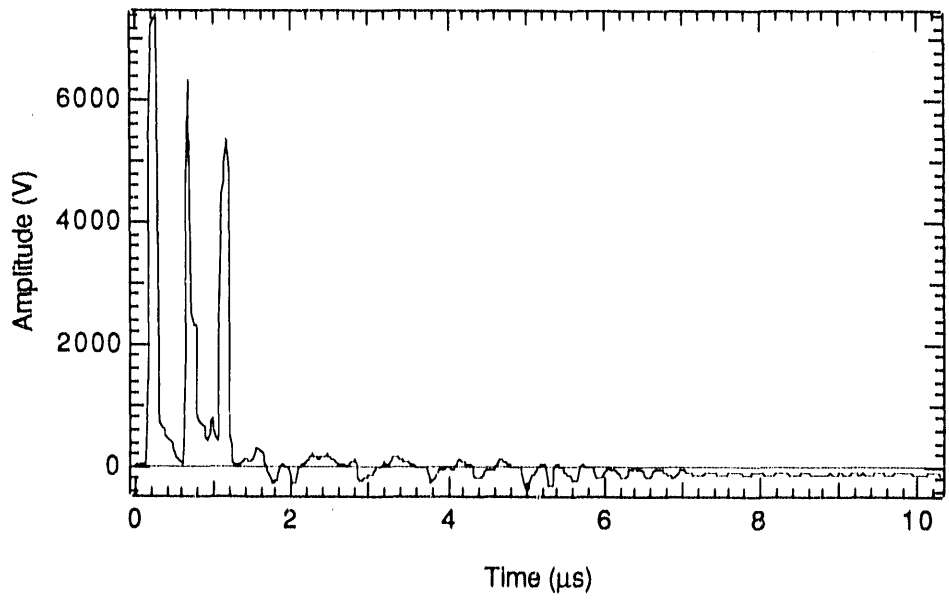

Figure 3.11. Voltage Measured at the Shorting Block with SPG Charge Voltage Set to 8 kV - Strong Breakdown

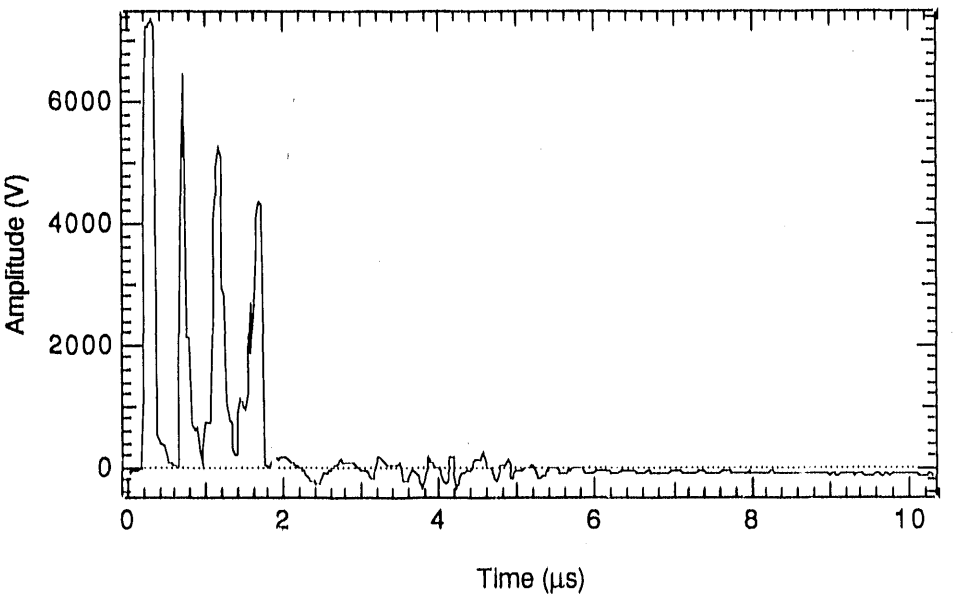

Figure 3.12. Repeated Measurement at the Shorting Block with SPG Charge Voltage Set to 8 kV - Strong Breakdown

3.4.4 Relay AC Circuits

The STD15C relay was connected as shown in Figure 3.3 with the current tap plugs in the 5 ampere position and the target & seal-in unit current pick-up tap in the 0.6 ampere position. Model predictions show that the pulse width of HEMP induced voltage transients at the relay terminals can vary from hundreds of nanoseconds to a couple of microseconds. Therefore, the effects of two different pulse widths, 130 ns and 800 ns, were examined using the SPG. With the introduction of the complex impedance of the relay, the waveform data did not indicate whether or not breakdown occurred. It was, however, essential for determining threshold levels. Therefore, voltage was monitored at the terminal block but flashover was determined solely by observation. The voltage waveform plots are included in Appendix A for completeness and are referenced in the text by file names enclosed in brackets ( ). For a pulse width of 130 ns, arcing was observed near the 2.9 ampere current tap at a voltage level of 6.5 kV (RL15.DTL). Moving the current tap plugs to the 2.9 ampere position resulted in a lower breakdown threshold. Flashover began at 4.3 kV (RL51.DTL) and this time occurred near the 8.7 ampere current tap. Keeping the tap at the 2.9 ampere position, the pulse width of the injected pulse was changed to 800 ns. For this case, arcing

occurred on the instantaneous unit coil and on the differential current transformer at a voltage level of 4 kV (RL73.DTL). When the amplitude was increased above 6 kV (RL76.DTL), arcing occurred at the 8.7 ampere tap as before.

The SPG is limited to a maximum output voltage of approximately 8 kV. Therefore, in an effort to achieve higher levels to investigate damage margins, the experiments were repeated using a capacitive discharge pulse generator capable of injecting 15 kV on the relay circuits. With the capacitive discharge pulser, flashover was observed near the 8.7 ampere current tap, beginning at 2.3 kV (ORL8.DTL). After reaching a limit of 10 kV (ORL14.DTL), the relay's performance was re-examined. None of its operating characteristics were altered and the relay performed within specifications.

3.4.5 Relay: DC Circuits

The DC circuits of the STD15C relay are composed of the relay contacts and the solid-state sensing circuit as shown in Figure 3.1. In a typical relay station installation, the DC contacts of the relay are connected to a circuit breaker trip coil, as shown in the electrical diagram in Figure 3.13, which is usually located in the switch yard. Since an actual trip coil was not available, it was substituted by a 25 ohm wirewound resistor for many of the tests. In addition, the station batteries are not normally grounded. Therefore, only in a few specialized circumstances were the batteries grounded in the laboratory.

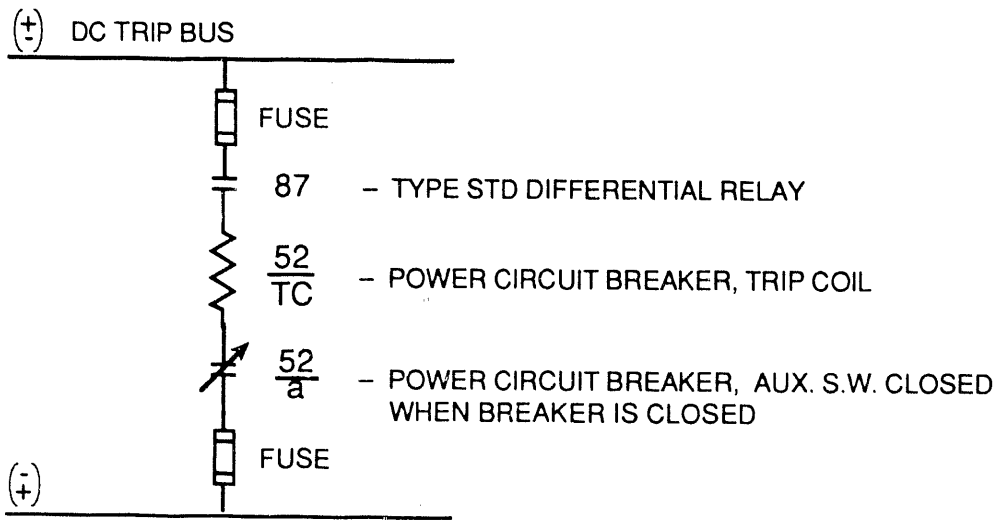

Figure 3.13. Typical Relay System Application

Using the capacitor discharge pulse generator, pulses were injected on the output port of the relay with respect to ground. Terminal 5 was also tied to ground as its normal configuration. Flashovers were observed on the relay contacts beginning at 3.8 kV (OPG2.DTL). As the amplitude was increased beyond 8 kV (OPG9.DTL), flashovers were observed on the relay contacts and on the instantaneous unit. In spite of the intense arcing, no upsets or failures were noted.

Through discussions with ABB Power Systems Inc, four possible methods for upset or failure were identified. These are depicted in Figure 3.14. In three of the four cases, upset or failure occurs when two wires simultaneously arc to ground, effectively shunting key elements in the relay circuit. The most likely scenario is shown in Figure 3.14(a). Both the output cable from the relay and a DC battery cable run out into the switch yard and are exposed to direct free field coupling. In Figures 3.14(b) and 3.14(c), the trip bus in or near the relay house would have to breakdown to ground in order for the DC trip circuit to upset or fail. In Figure 3.14(d), the breakdown is induced across the relay contacts which, for the STD15C relay, has a similar outcome to that of Figure 3.14(c).

The first case was simulated by injecting the pulse on the output line of the relay with respect to terminal 10 which was connected to the negative DC battery lead. The battery was not grounded in this case. In an authentic installation, a short across these two points is equivalent to a short across the circuit breaker trip coil, in which case relay operation will not trip the breaker. Since a trip coil was not available, the relay output was left open in order to establish a lower bound on the flashover threshold.

Using the SPG with a 130 ns charge line, breakdown across the telephone relay contacts occurred at 4.7 kV (OP18.DTL). When the pulse width was lengthened to 800 ns, arcing began at 2.1 kV (OP45.DTL). Thus, with increased pulse width, breakdown occurred at a lower voltage level. When the capacitor discharge pulse generator was used, the breakdown threshold was approximately 2.5 kV (OOP2.DTL).

The second case (Figure 3.14(b)) was simulated by grounding one of the battery leads and injecting the pulse on the other lead with respect to ground. A short across the battery circuits of an actual relay system would disable the relay trip circuits. In order to protect the batteries in the laboratory, a three ampere fuse was inserted. The fuse also served as an indicator, detecting relay system failures due to battery shorts. Results from grounding the negative battery terminal and pulsing the positive terminal show that breakdown begins at 4.7 kV (DCG12.DTL) near the base of the telephone relay contacts. The three ampere fuse did not fail, even when the

amplitude was increased to 19 kV (DCG26.DAT), suggesting that current flow from the batteries through the arc was insufficient to cause the relay to upset or fail in this configuration. When the positive battery terminal was grounded and the negative terminal was pulsed, flashover was observed on the instantaneous unit starting at 4.8 kV (DCG34.DTL) with no upsets or failures. However, when the voltage level of 12.3 kV (DCG40.DTL) was reached, a sufficiently large amount of current passed through the arc, causing the fuse to blow. This provided a failure threshold for the relay under the prescribed conditions.

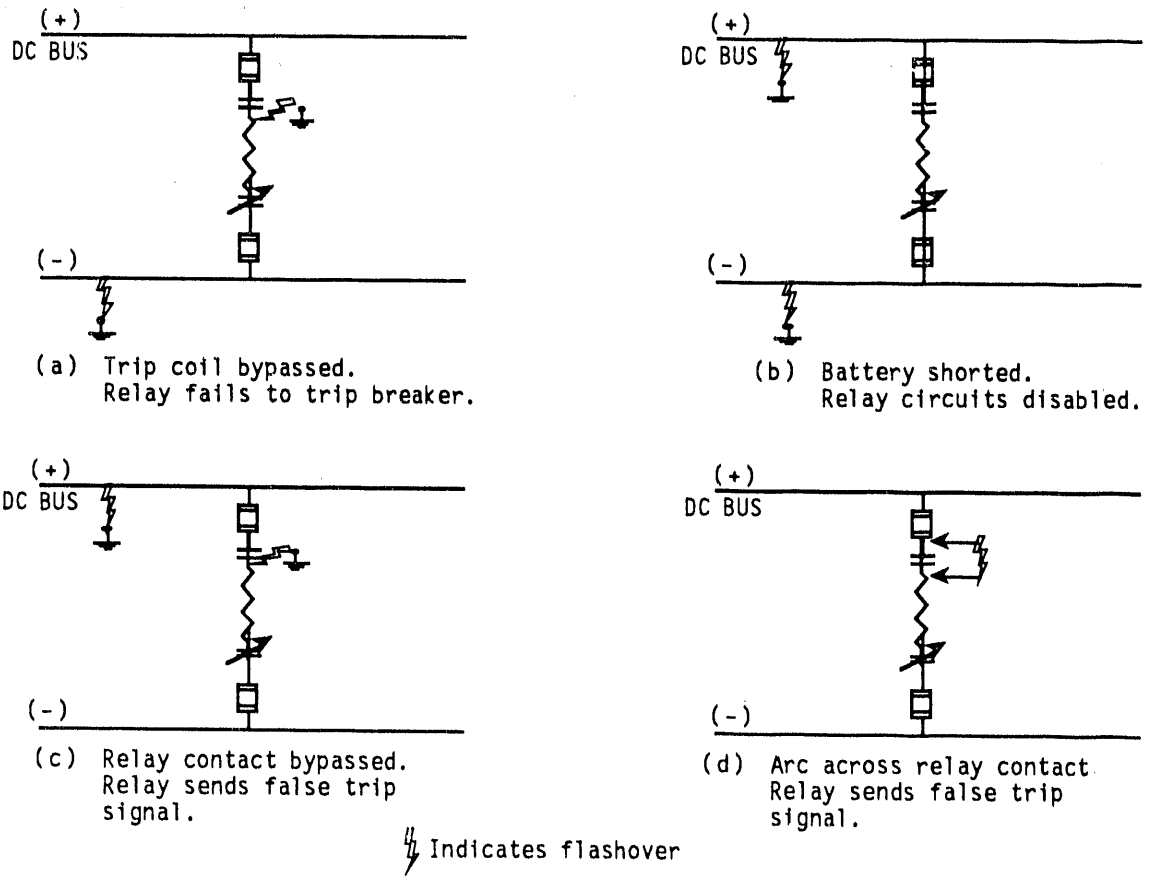

Figure 3.14. Protective Relay System Upset and Failure Conditions.

As a control experiment, the pulse generator was attached directly to the fuse and battery with an adjustable spark gap inserted as shown in Figure 3.15. The battery was pulsed using wide and narrow spark gap settings. For the wide gap, no arcing occurred and the relatively short

pulses had no noticeable effect on the fuse or battery. Conversely, with the narrow gap, arcing occurred and was sustained by the DC battery current until the fuse blew. These results were observed for both 3 ampere and 6 ampere fuses.

The third and fourth upset scenarios were not implemented, although arcing across the relay contacts did occur in previous tests with no adverse effects to the relay.

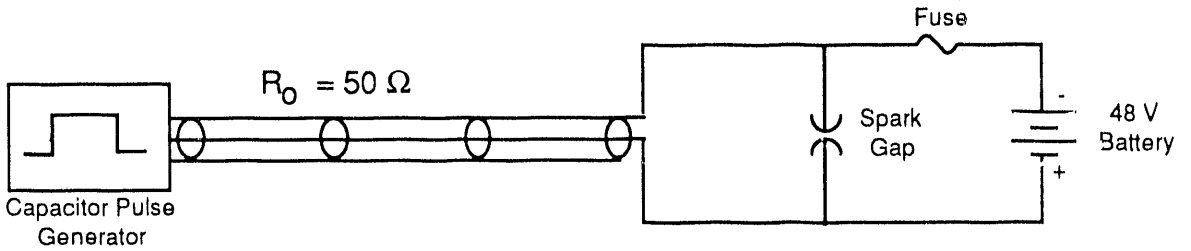

Figure 3.15. Control Test Circuit.

3.4.6 Surge Protection Package (SPP)

The effectiveness of a Westinghouse style 6299D27G02 surge protection package in extending the protection margin of a relay's DC power lines was examined. The SPP, pictured in Figure 3.16, consists of 0.5 μf capacitors tied to ground. All DC power lines from the relay were connected to the SPP which was mounted on the relay rack in place of the terminal block. After grounding the negative battery terminal, the capacitor discharge pulser was used to inject a fast rise pulse to the positive DC power terminal on the relay. The amplitude of the pulse was raised until indications of upset, failure, or arcing occurred. Voltages for the SPP tests were measured at the terminal block. Comparing these results with those from the corresponding DC circuit relay test show that the SPP extended the margin of protection to a voltage impulse by as much as a factor of two. The protection afforded by the SPP is shown in Figure 3.17. Without the SPP (Figure 3.17(a)), arcing was observed near the telephone relay contacts at a capacitor charge voltage of 5 kV. After inserting the SPP, flashovers were no longer present at the same charge voltage. Figure 3.17(b) shows that the inclusion of the SPP significantly reduced the amplitude of the pulses on the battery lead at the SPP. Arcing on the relay was not detected until a charge voltage level of 12 kV was reached. Figure 3.17(c) shows the resulting waveform. The ramping characteristic shown in the figures is caused by a charge build-up on the

control cable between the pulse generator and the relay. This behavior was seen on the shorting block tests and is indicative of pulses on a transmission line where the load impedances are greater than the characteristic impedance of the line.

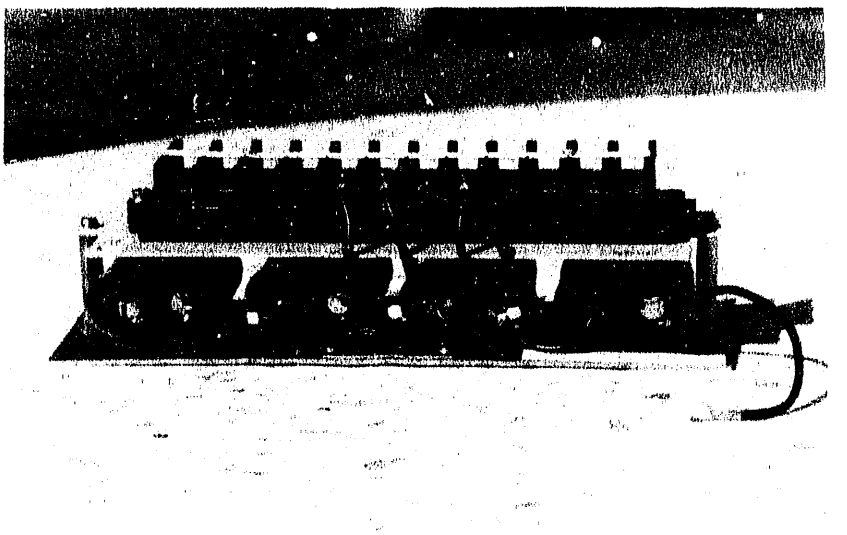

Figure 3.16. Westinghouse Style 6299D27G02 Surge Protection Package

3.5 SUMMARY

Susceptability tests were performed on a transformer differential relay by injecting HEMP-like impulses onto its circuits. Voltage levels at which flashovers occur on the relay circuit due to the fast rise impulse were determined. These levels are summarized in Table 3.4. It was observed that breakdown does not necessarily result in upsets or damage, nor does it necessarily occur on the initial voltage impulse. In fact, it was shown that reflected pulses produced by impedance mismatches in the relay circuit play a statistical role in inducing breakdown.

Under certain circumstances, arcing on the DC battery circuits can lead to relay system failures. One such failure was observed when the negative battery terminal was injected with a 12.3 kV pulse causing a short across the battery terminals (with the positive battery terminal grounded). Although many flashovers occured for input voltages ranging from 2 kV to 20 kV, the relay's performance was generally not affected. The relay itself incurred no physical or electrical damage as a result of the pulse testing.

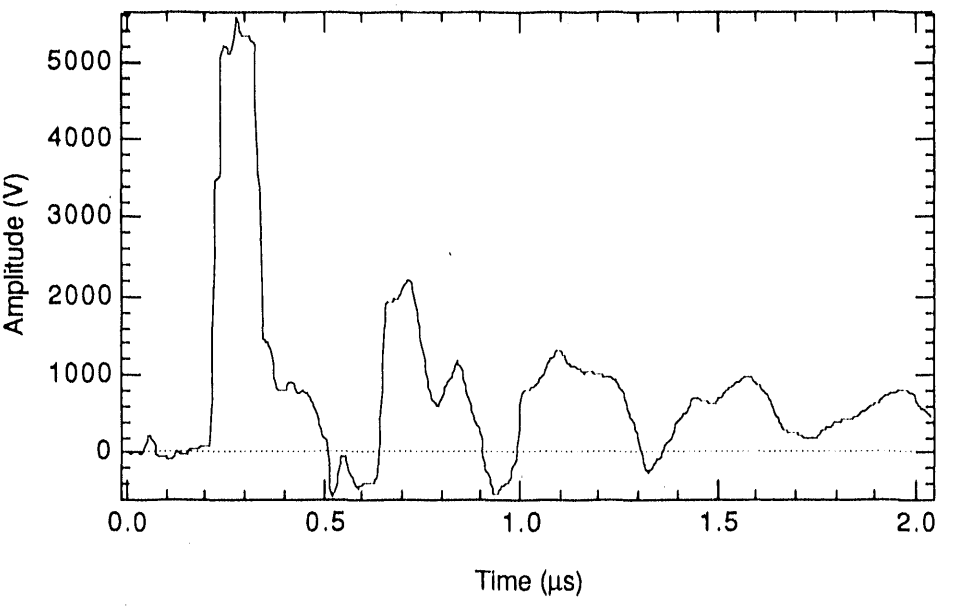

(a) Measured Voltage without SPP Installed at Charge Voltage of 5 kV. Flashover Observed near Telephone Relay Contacts.

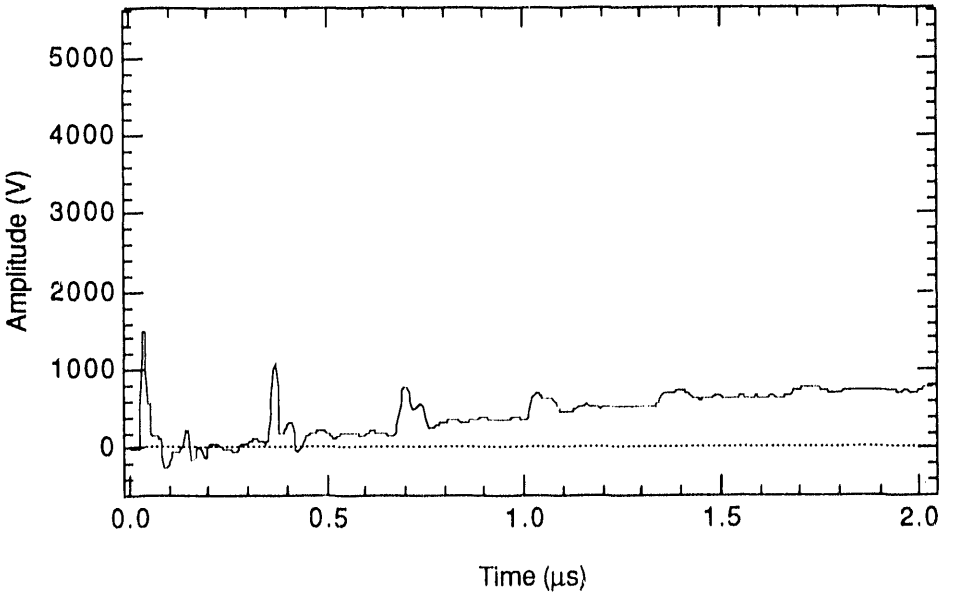

(b) Measured Voltage with SPP Installed at a Charge Voltage of 5 kV. No Flashover Observed.

Figure 3.17. Effectiveness of Surge Protection Package

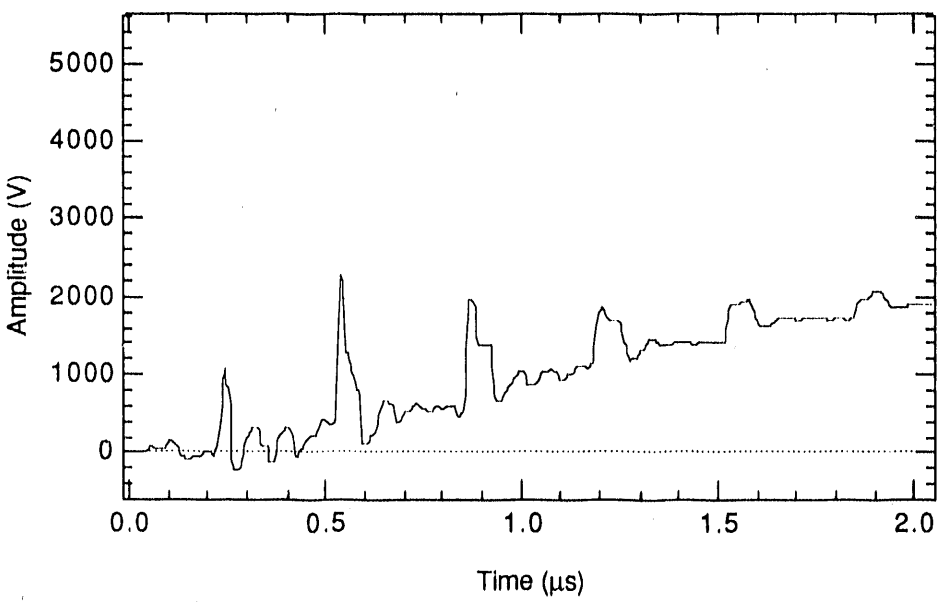

(c) Measured Voltage with SPP Installed at a Charge Voltage of 12 kV. Flashover Observed near Contacts.

Figure 3.17 (Concluded). Effectiveness of Surge Protection Package

Table 3.4. Relay Test Summary

CIRCUIT TYPE	PULSE INJECTION POINTS	PULSE GENERATOR	RELAY CONFIGURATION	FLASHOVER VOLTAGE	FLASHOVER LOCATION
AC	Term. 5 to Term 6	SPG 130ns	Current ratio matching plugs on 5A taps	6.5 kV	2.9A current tap
AC	Term. 5 to Term 6	SPG 130ns	Current ratio matching plugs on 2.9A taps	4.3 kV	8.7A current tap
AC	Term. 5 to Term 6	SPG 800ns	Current ratio matching plugs on 2.9A taps	4.0 kV	Instantaneous unit & differential current transformer
AC	Term. 5 to Term 6	SPG 800ns	Current ratio matching plugs on 2.9A taps	6.0 kV	8.7A current tap
AC	Term. 5 to Term 6	Capacitor	Current ratio matching plugs on 2.9A taps	2.3 kV	8.7A current tap
DC	Term. 2 to Term. 5 (Gnd)	Capacitor	Terminal 5 grounded	3.8 kV	Near relay contacts
DC	Term. 2 to Term. 5 (Gnd)	Capacitor	Terminal 5 grounded	8.0 kV	Near relay contacts & Instantaneous unit
DC	Term. 2 to Term. 10	SPG 130ns	Battery leads not grounded, No 25Ω resistor	4.7 kV	Telephone relay contacts
DC	Term. 2 to Term. 10	SPG 800ns	Battery leads not grounded, No 25Ω resistor	2.1 kV	Telephone relay contacts
DC	Term. 2 to Term. 10	Capacitor	Battery leads not grounded, No 25Ω resistor	2.5 kV	Telephone relay contacts
DC	Term. 1 to Term. 10 (Gnd)	Capacitor	Terminal 10 grounded	4.7 kV	Near base of relay contacts
DC	Term. 10 to Term. 1 (Gnd)	Capacitor	Terminal 1 grounded	4.8 kV	Instantaneous unit
DC	Term. 10 to Term. 1 (Gnd)	Capacitor	Terminal 1 grounded	12.3 kV*	Instantaneous unit.

* Susceptibility observed. DC circuit fuse blown due to current follow-through

The effectiveness of a surge protection package in protecting the DC relay circuits was also examined. Arcing caused by a 5 kV steep front impulse was effectively eliminated by the SPP. Moreover, the SPP provided protection against arcing induced by impulses with magnitudes as high as 12 kV.

Upset and failure mechanisms are not confined only to the relay; they encompass the entire protective relay circuit. Therefore, future tests should incorporate a circuit breaker trip coil in the test circuit to examine its contribution to the system response. Also, future tests should include microprocessor based relays since their mechanism for upset is determined not only by threshold levels but also by synchronization with the system clock.

4.0 RESULTS

In this section, analytical and experimental results will be presented and compared. Time-domain waveforms, frequency-domain spectra, and signal norms (zero-peak amplitudes, local rise times, peak derivatives, and action integrals) are discussed for several variables, including transient bus currents and voltages, radiated electric and magnetic fields, induced cable-shield currents, shielded-cable load responses, and unshielded-cable load responses. Plots of waveforms and spectra provide a visual assessment of the different types of responses; values for norms provide quantification of signal strength (zero-peak amplitude), frequency content (rise times and peak derivatives), and waveform energy (generally proportional to the action integral, which is given by the integral of the square of the observed variable over time). The predicted quantities are used in conjunction with measured data to develop assessments of relay susceptibility and vulnerability. Mitigation techniques are addressed as well.

Analytical predictions of coupling phenomena are presented for three types of environments: (a) 500 kV switching transients (ST), (b) long-range HEMP events, and (c) short-range HEMP events. For the 500 kV ST, a switch closing was simulated with the maximum potential difference between switch arms; this condition, called 2 per unit (PU), represents a worst-case ST. Switching transient generated electric fields were coupled to shallowly-buried control cables (both shielded and unshielded) lying underneath and parallel to a section of the 500 kV bus. Switching transient magnetic fields caused by transient currents flowing in a CT pedestal and ground strap were also coupled to adjacent and parallel shielded and unshielded cables. In this case, the coupling is to a length of cable above ground. For the long-range HEMP, both field components (horizontal and vertical) were used to drive currents on the 500 kV ring bus model; the elevation of the HEMP field was 5.6°, and the azimuth angle, ϕ, was 0° (see Figure 2.10 for ring bus geometry and azimuthal orientation). The vertical component of the long-range HEMP field was also used for coupling to shallowly-buried control cables lying roughly along the direction of HEMP propagation. For the short-range HEMP, both field

components (horizontal and vertical) were again used to drive currents onto the 500 kV ring bus; the elevation of the HEMP field was 35.4°, and the azimuth angle, ϕ, was 45°. In each case, these particular angles had been found earlier (see Section 2) to produce the largest HEMP coupled responses. In addition, the horizontal component of the short-range HEMP field was used for coupling to shallowly-buried control cables lying parallel to this component, which represents the peak strength (50 kV/m) HEMP field.

Most of the results presented below were developed with a single set of geometrical and physical parameters, which were used for both the ST and HEMP calculations; parameter values were based on typical substation installation practices, laboratory measurements of cables and relays, and measured switching transient phenomena. Models describing a 500 kV substation including a high voltage ringbus and typical low voltage control cable circuits were used to generate ST bus currents, their resultant radiated fields, and the coupled control wiring voltage and current responses. The same models were used to calculate long and short range HEMP coupling and responses, as explained in Section 2. ST and HEMP coupling to both shielded and unshielded cables was investigated. Three principal control cable coupling sources have been examined: magnetic field, electric field, and primary bus current. As modeled, magnetic field and primary bus current coupling occurs at the end of a control cable near instrument transformers (CTs and CCVTs) where they come in proximity to the high voltage bus and the instrument transformer bushing ground circuits, while electric field coupling occurs along the length of the control cable (typically below ground level) for both switching transient and HEMP environments.

For shielded cables, both electric and magnetic field coupling modes initially drive currents and voltages onto the cable shield, which then couple onto internal cable wires via transfer impedance and pigtail coupling mechanisms. The effect of the earth on electric field coupling calculations was accounted for with a relative permittivity (dielectric constant) of ε_r = 10, and a conductivity of σ_g = 0.1 mho/m. The diameter of shallowly-buried shielded control cables was taken as 1 inch (2.54 cm); the length of the cable assumed was 73 m. The cable internal characteristic impedance was 150 Ω. The cable shield terminations were prescribed to be 4 μH, in order to represent

the common practice of grounding both ends of a shielded cable. The shield termination length, termination/load separation, and wire radius for the pigtail-coupling calculations were set at 0.3 m, 5 cm, and 2 mm respectively. For the circuits inside the shielded cables, a transfer impedance of the form

$$Z_T = 3.5\text{x}10^{-3}\,\frac{\Omega}{m} + j\omega 4.8\text{x}10^{-9}\,\frac{H}{m}$$

was postulated based on measured data; the cable insulation's relative permittivity was taken as 1.1. For unshielded cables, the electric and magnetic fields couple directly to cable wires, thus transfer impedance and pigtail coupling modes are not present.

For assessments of conducted coupling to shielded and unshielded cables, the bushing capacitance was set at 1090 pF, and the primary-to-Faraday shield and secondary-to-Faraday shield parasitic CT capacitances were set at 50 pF and 500 pF, respectively. The inductance of the CT ground strap was taken to be 4μH.

For shielded control cables, responses for five different load impedances were investigated: 150 Ω (constant over all frequencies), measured CT-lead common-mode impedances (pin 6 to ground), measured DC battery-lead common-mode impedances (pin 1 to ground), open circuit load, and short circuit load. The first three load impedances were described in Figure 3.8. For coupling to unshielded cables all five load impedances were investigated, with emphasis given to the measured DC battery-lead, open circuit, and short circuit load impedances. Open circuit voltage and short circuit current responses for shielded and unshielded cables driven by 2 PU ST and short range HEMP were compared with current IEEE/ANSI surge withstand capability (SWC) test waveforms [10]. The source impedance used for the cables is effectively given by the CT model described in Section 2. The parameters listed above were used for almost all the calculations presented in this section; exceptions are noted as they occur.

Appendix B contains high resolution plots of each waveform calculated in this investigation.

4.1 BUS CURRENTS AND VOLTAGES

Transient current waveforms on the 500 kV ring bus are shown in Figure 4.1 for a 500 kV 2 PU ST, a long-range HEMP event, and a short-range HEMP event; the corresponding spectra for all three situations are overlaid in Figure 4.2. Transient 500 kV ring bus voltage waveforms are displayed in Figure 4.3 for 500 kV 2 PU ST, long-range and short-range HEMP; the resultant spectra are plotted together in Figure 4.4. Signal norms for both transient bus currents and voltages are listed in Table 4.1. The waveform plots reveal that the ST currents and voltages persist much longer than their HEMP-induced counterparts; this observation is reinforced by examination of the spectra, which show the largest low-frequency values for switching transients. The ST also exhibit higher amplitude levels at high frequencies than HEMP bus transients. The table of norms indicates that the 2 PU ST bus currents and voltages are larger in both amplitude and action integral (i.e. energy) than those for either HEMP environment. Both ST and HEMP results are characterized by short local rise times.

Local risetime, rather than 10 - 90 percent peak amplitude, is reported in the table of norms because it is less ambiguous to determine for complex waveforms. The local risetime is calculated by dividing the peak time derivative of amplitude found in the entire waveform into its local peak amplitude. Thus, the reciprocal of the local risetime gives an estimate of the highest frequency content present in the waveform. Local risetime may or may not represent the 10 - 90 percent risetime of the peak amplitude of a waveform: in cases where the waveform is relatively simple and the local peak amplitude is the peak amplitude of the waveform (e.g. incident HEMP fields), the local risetime correlates well with the 10 - 90 percent risetime. The 10 - 90 percent peak amplitude risetime for ST bus currents, voltages, and fields are typically much slower than those of HEMP, on the order of 250 - 500 ns. The 10 - 90 percent risetime for all responses may be estimated using the data provided in Appendix B.

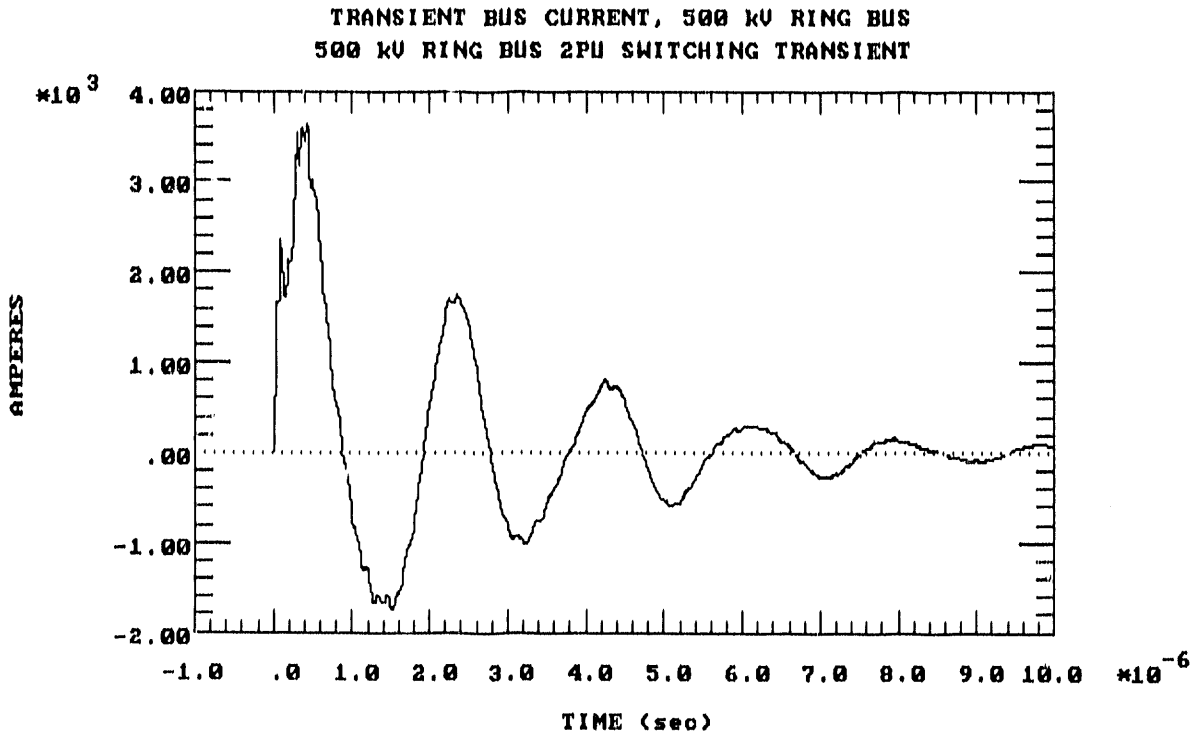

(a) 500 kV 2 PU Switching Transient

Figure 4.1. Transient Bus Current Waveforms on a 500 kV Ring Bus

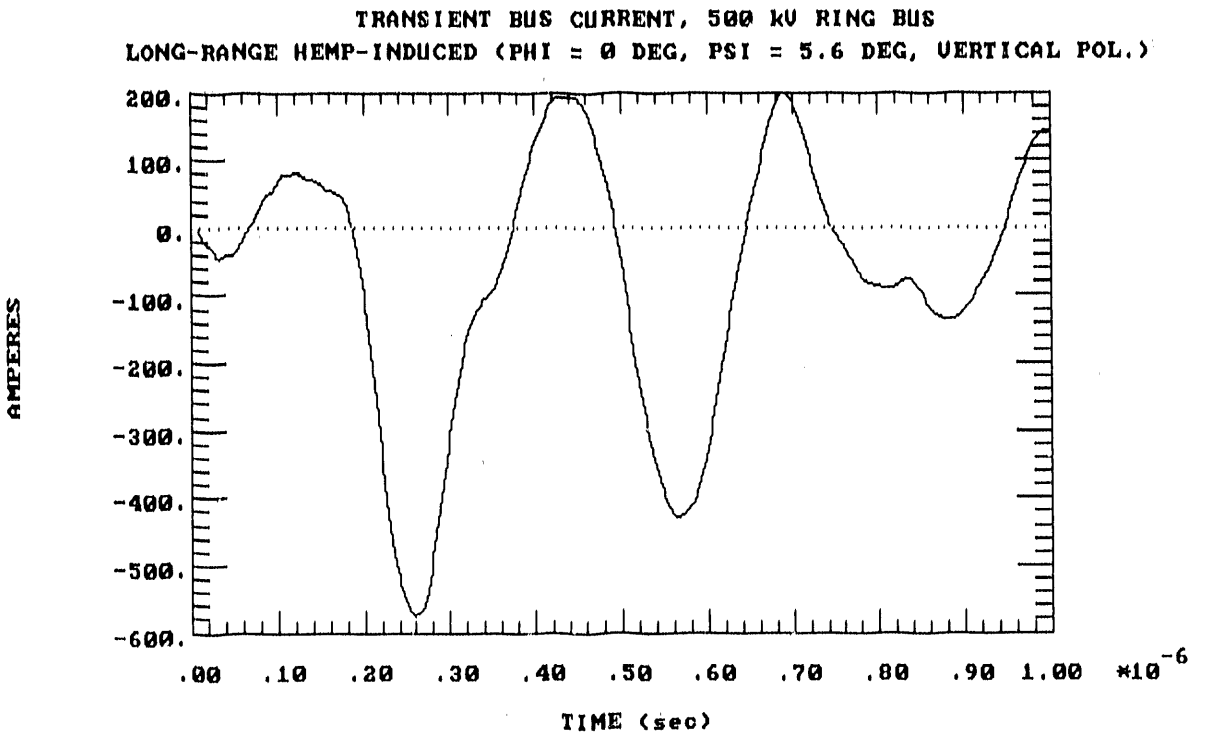

(b) Long-Range HEMP

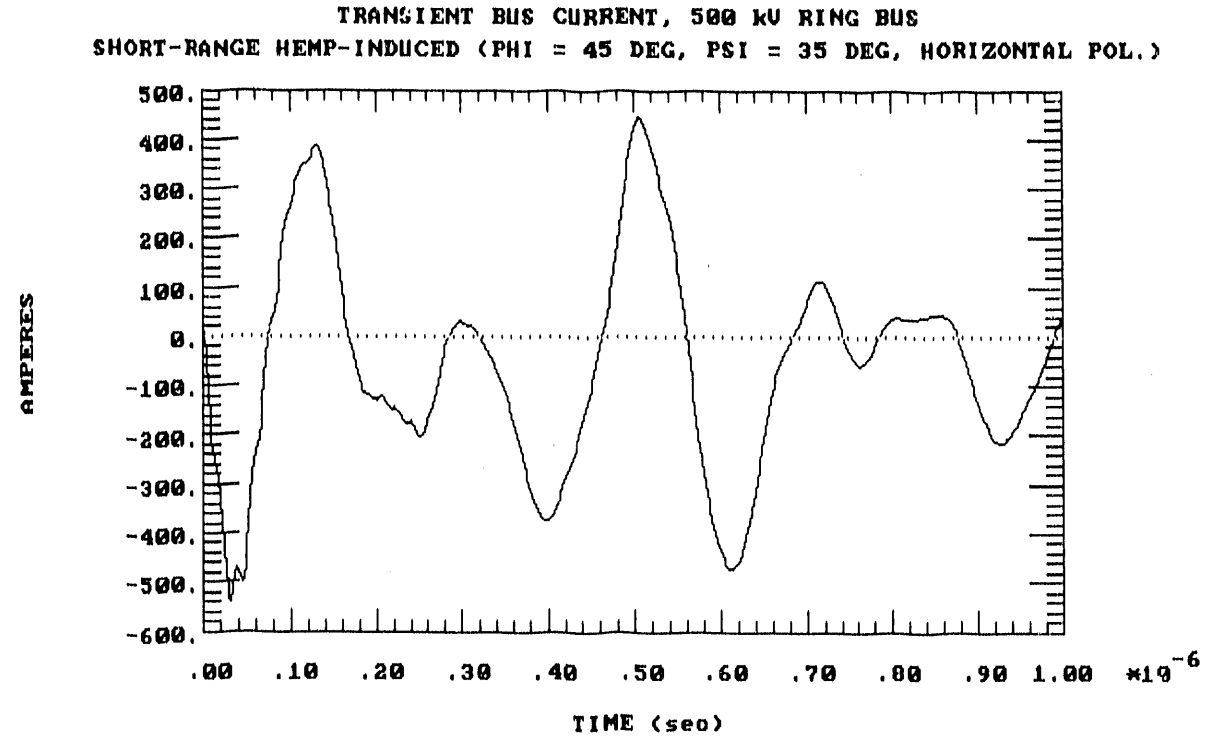

(c) Short-Range HEMP

Figure 4.1 (Concluded). Transient Bus Current Waveforms on a 500 kV Ring Bus

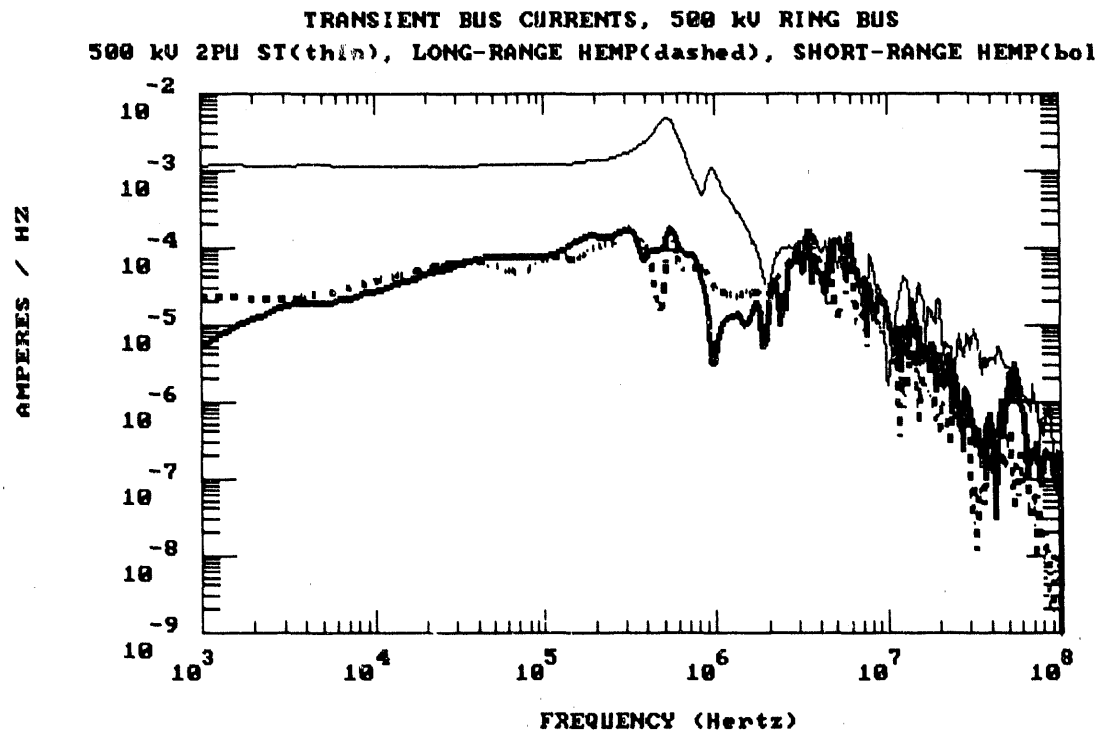

Figure 4.2. Transient Bus Current Frequency-Domain Spectra: 500 kV 2 PU ST(thin), Long-Range HEMP(dotted), Short-Range HEMP (bold)

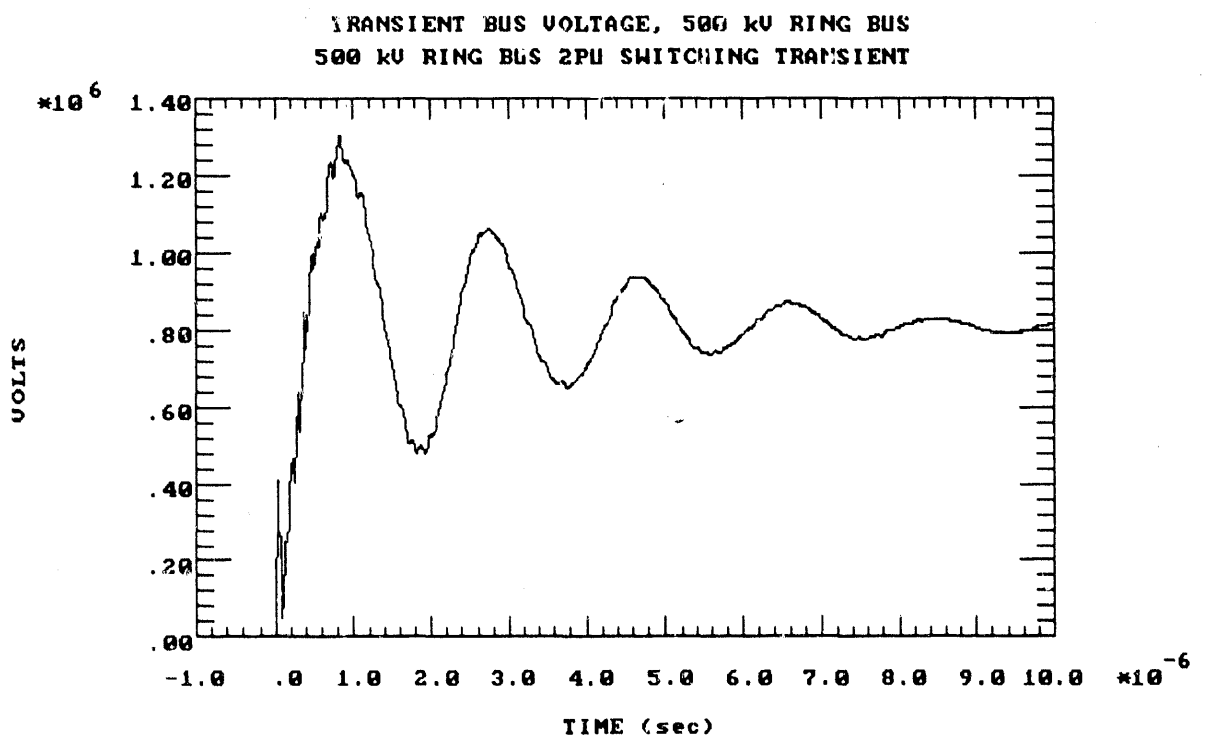

(a) 500 kV 2 PU Switching Transient

Figure 4.3 Transient Bus Voltage Waveforms on a 500 kV Ring Bus

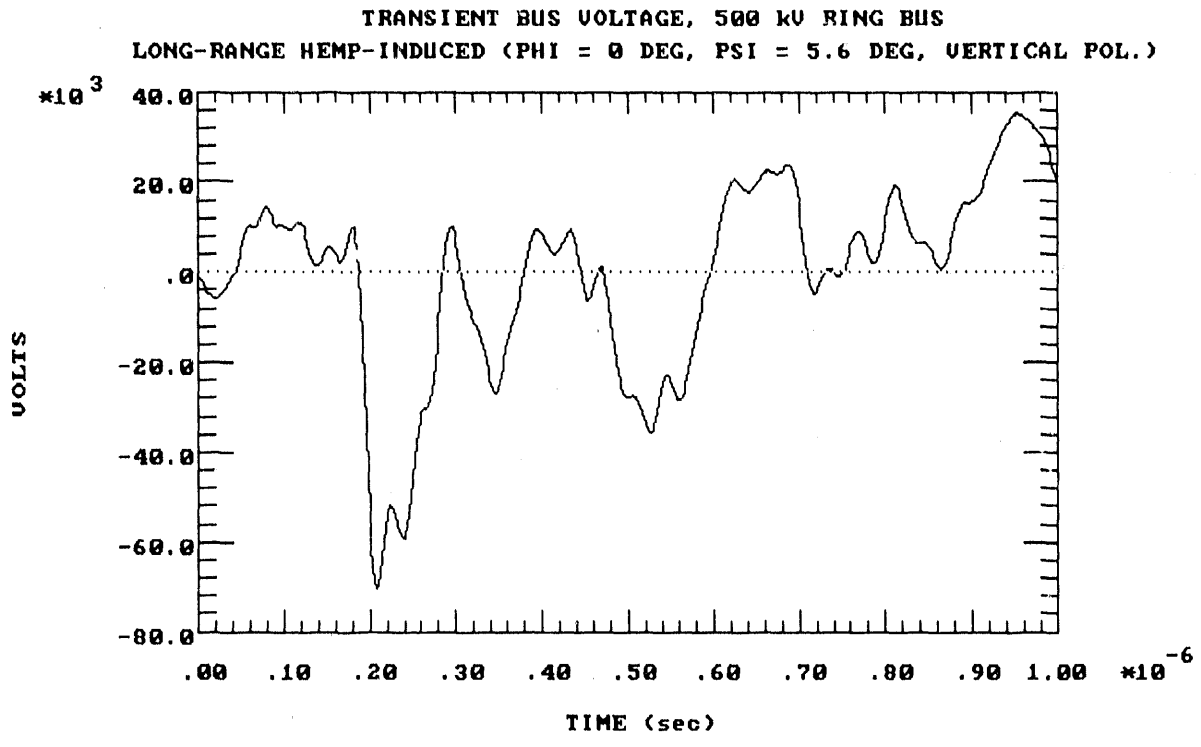

(b) Long-Range HEMP

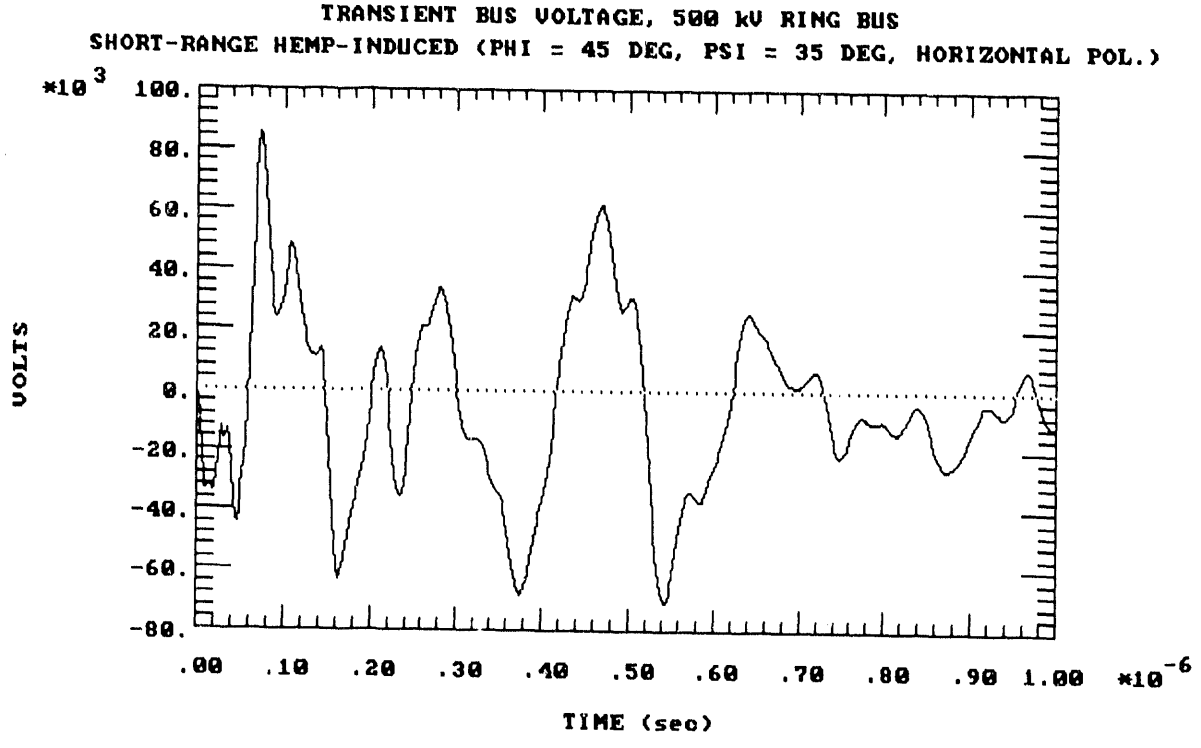

(c) Short-Range HEMP

Figure 4.3 (Concluded). Transient Bus Voltage Waveforms on a 500 kV Ring Bus

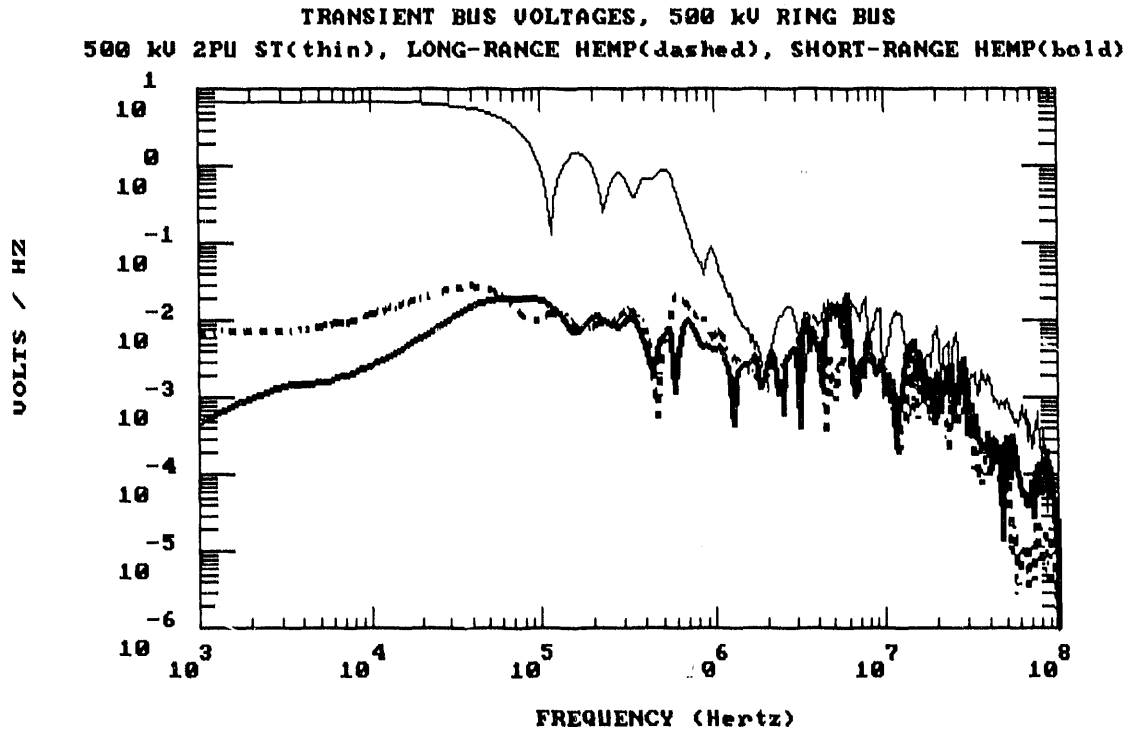

Figure 4.4. Transient Bus Voltage Frequency-Domain Spectra: 500 kV 2 PU ST (thin), Long-Range HEMP (dotted), Short-Range HEMP (bold)

Table 4.1. Norms for Transient Bus Currents and Voltages

	500 kV 2 PU ST		Long-Range HEMP		Short-Range HEMP	
	Bus Current	Bus Voltage	Bus Current	Bus Voltage	Bus Current	Bus Voltage
Zero-Peak Amplitude	3.63 kA	1.30 MV	0.575 kA	70.3 kV	0.538 kA	84.9 kV
Local Risetime	13 ns	10 ns	22 ns	9 ns	15 ns	9 ns
Peak Derivative	1.24E11 $\frac{A}{sec}$	4.08E13 $\frac{V}{sec}$	1.25E10 $\frac{A}{sec}$	5.05E12 $\frac{V}{sec}$	3.36E10 $\frac{A}{sec}$	7.94E12 $\frac{V}{sec}$
Action Integral	8.54 A^2sec	6.86E6 V^2sec	0.042 A^2sec	454 V^2sec	0.049 A^2sec	896 V^2sec

4.2 INCIDENT E AND H FIELDS AT THE GROUND

Electric field waveforms incident at the ground below a 500 kV ring bus are shown in Figure 4.5 for a 500 kV 2 PU ST, a long-range HEMP event, and a short-range HEMP event. The corresponding spectra for all three situations are overlaid in Figure 4.6. Magnetic field waveforms are displayed in Figure 4.7 for 500 kV 2 PU ST, long-range and short-range HEMP. Signal norms for both electric and magnetic fields are listed in Table 4.2. The ST electric field amplitudes are similar to those for the long-range HEMP fields, but less than the short-range HEMP electric fields. Peak ST magnetic field amplitude is greater than that of both short and long range HEMP magnetic fields. The short range HEMP fields exhibit higher amplitudes at all frequencies higher than about 1 MHz than either ST or long range HEMP fields (Figure 4.6). However, the ST fields possess the largest action integrals.

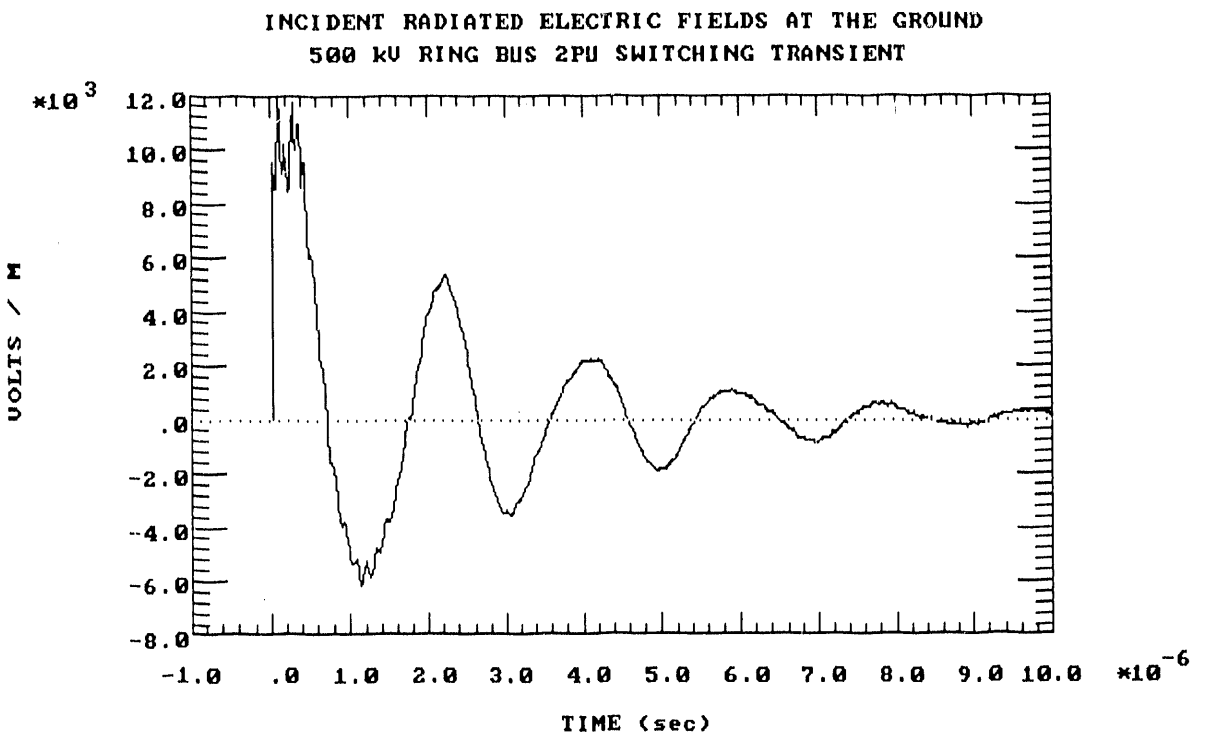

(a) 500 kV 2 PU Switching Transient

Figure 4.5. Radiated Incident Electric Field Waveforms at the Ground

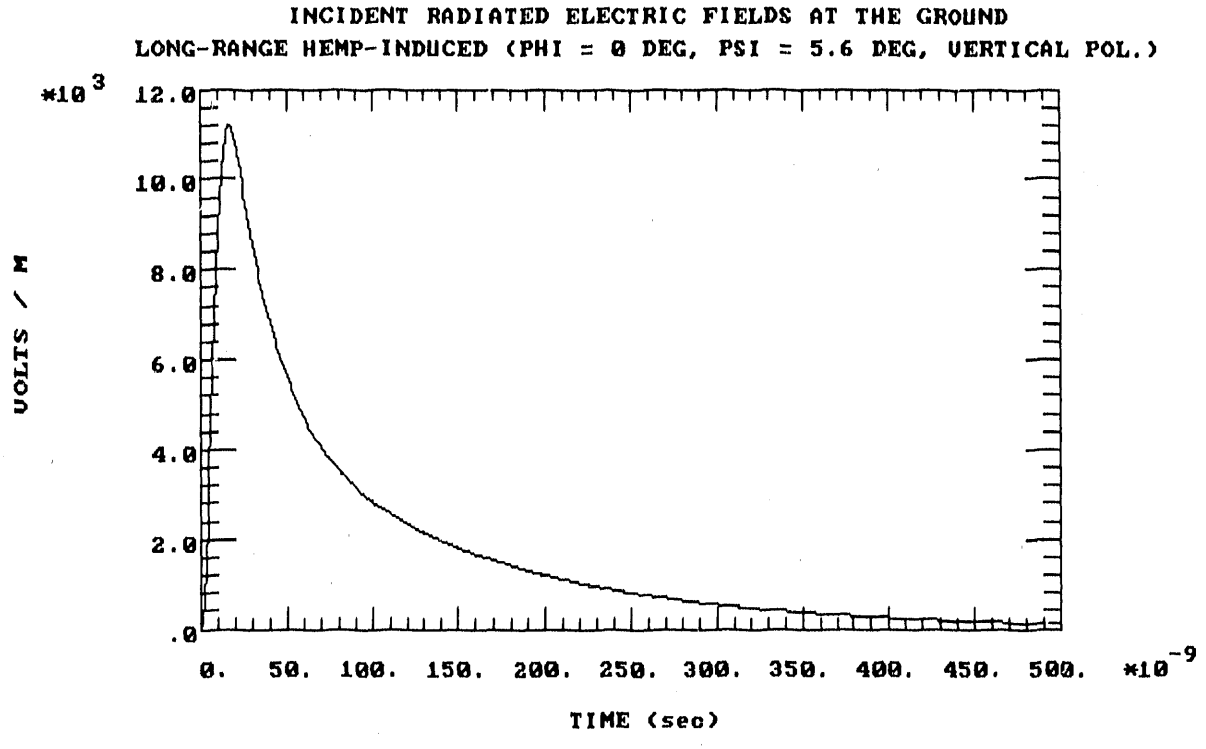

(b) Long-Range HEMP

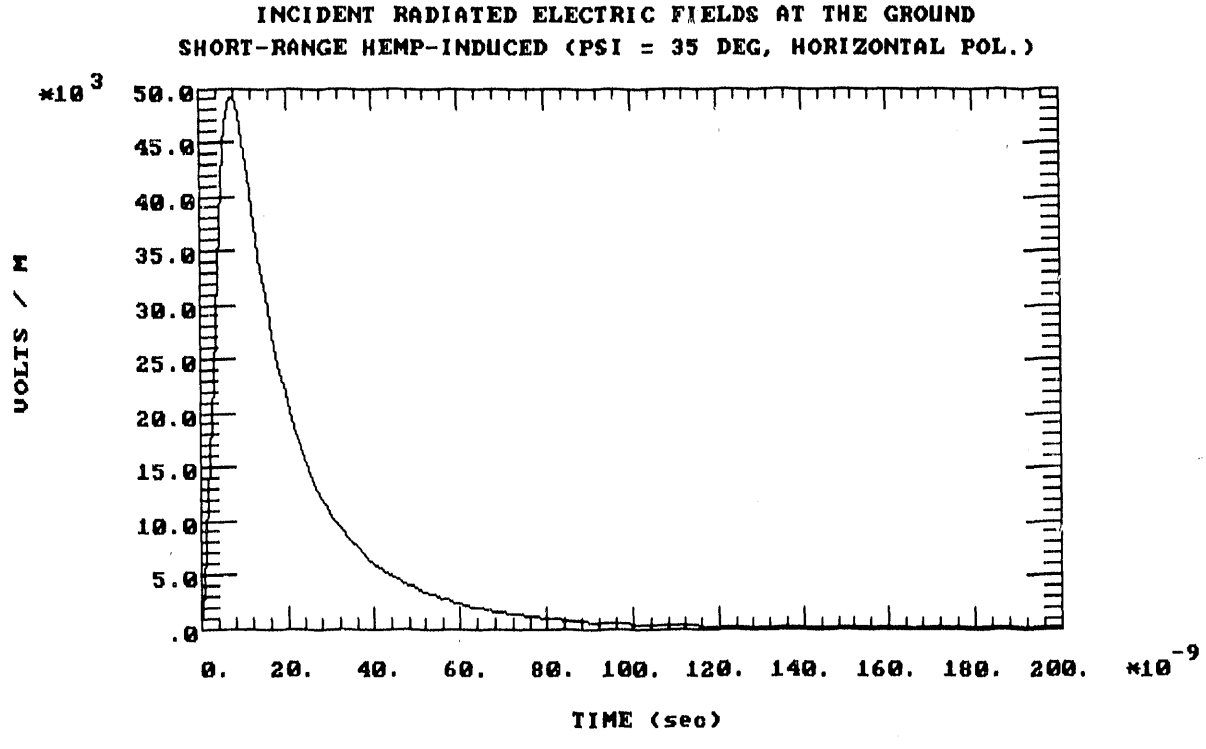

(c) Short-Range HEMP

Figure 4.5 (Concluded). Radiated Incident Electric Field Waveforms at the Ground

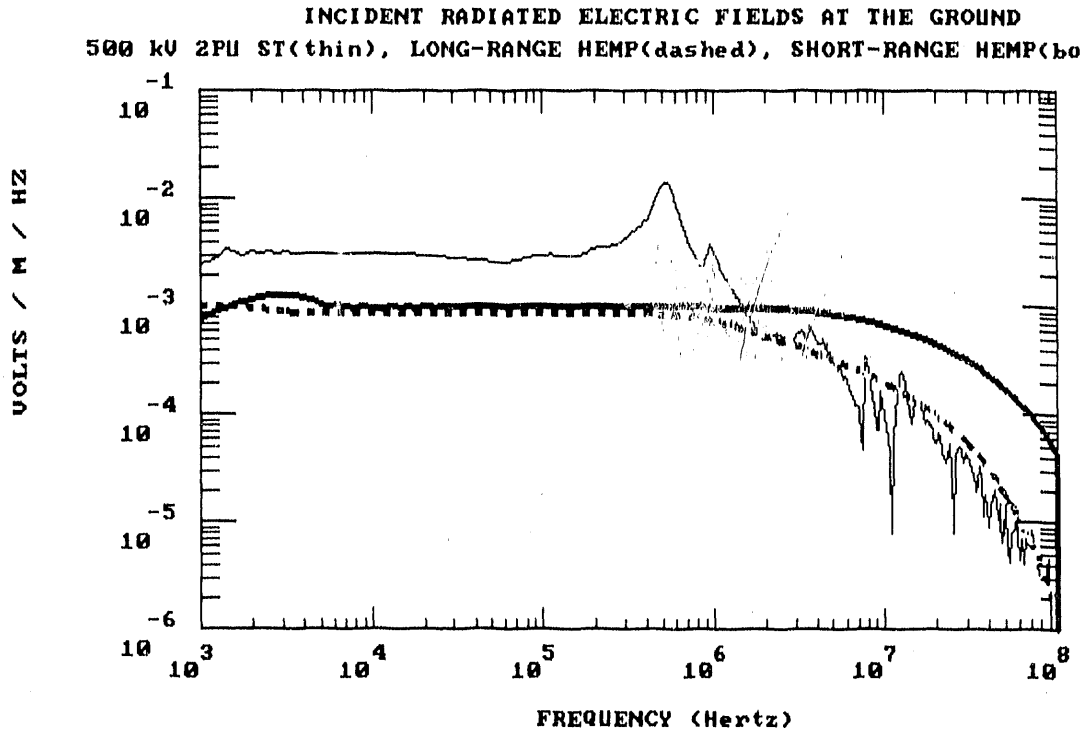

Figure 4.6. Radiated Incident Electric Field Spectra: 500 kV 2 PU ST (thin), Long-Range HEMP (dotted), Short-Range HEMP (bold)

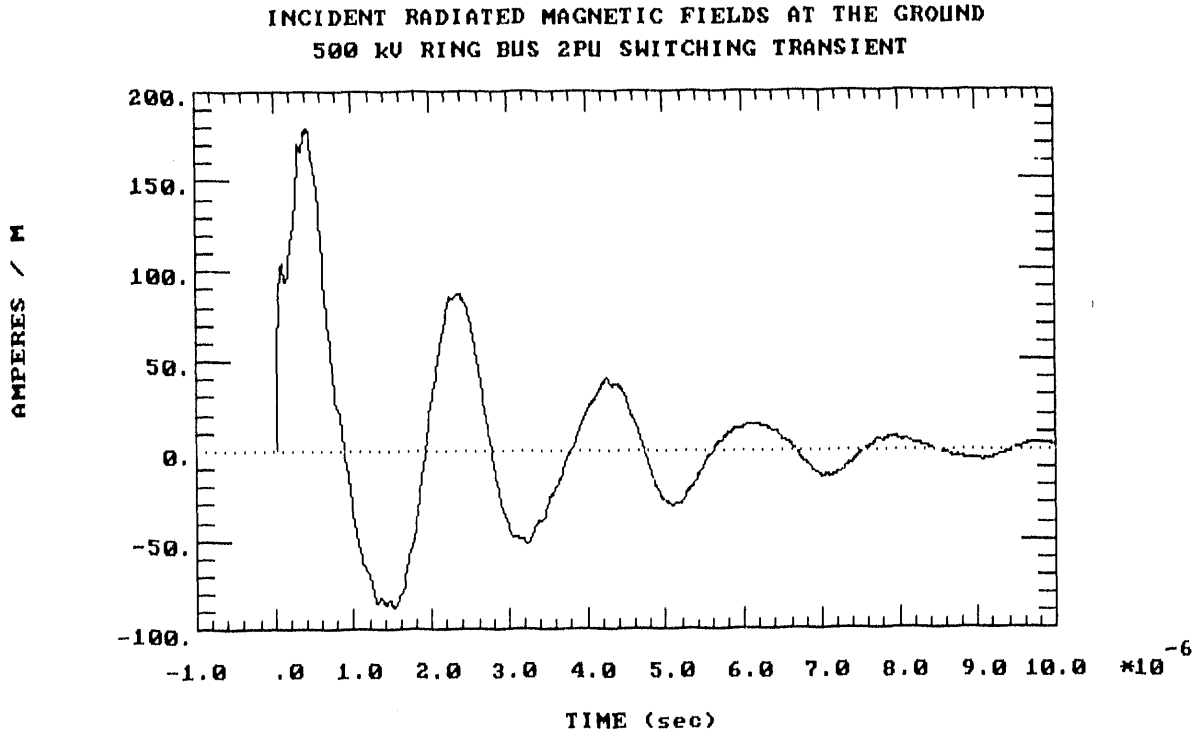

(a) 500 kV 2 PU Switching Transient

Figure 4.7. Radiated Magnetic Field Waveforms at the Ground

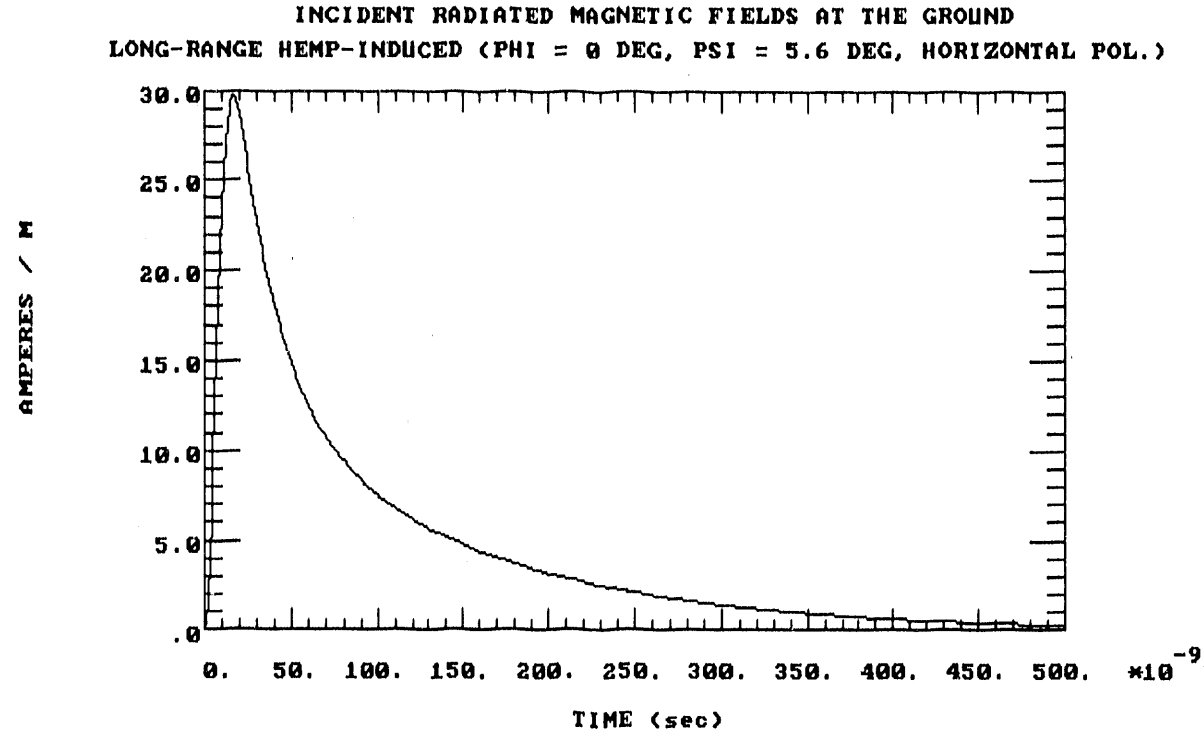

(b) Long-Range HEMP

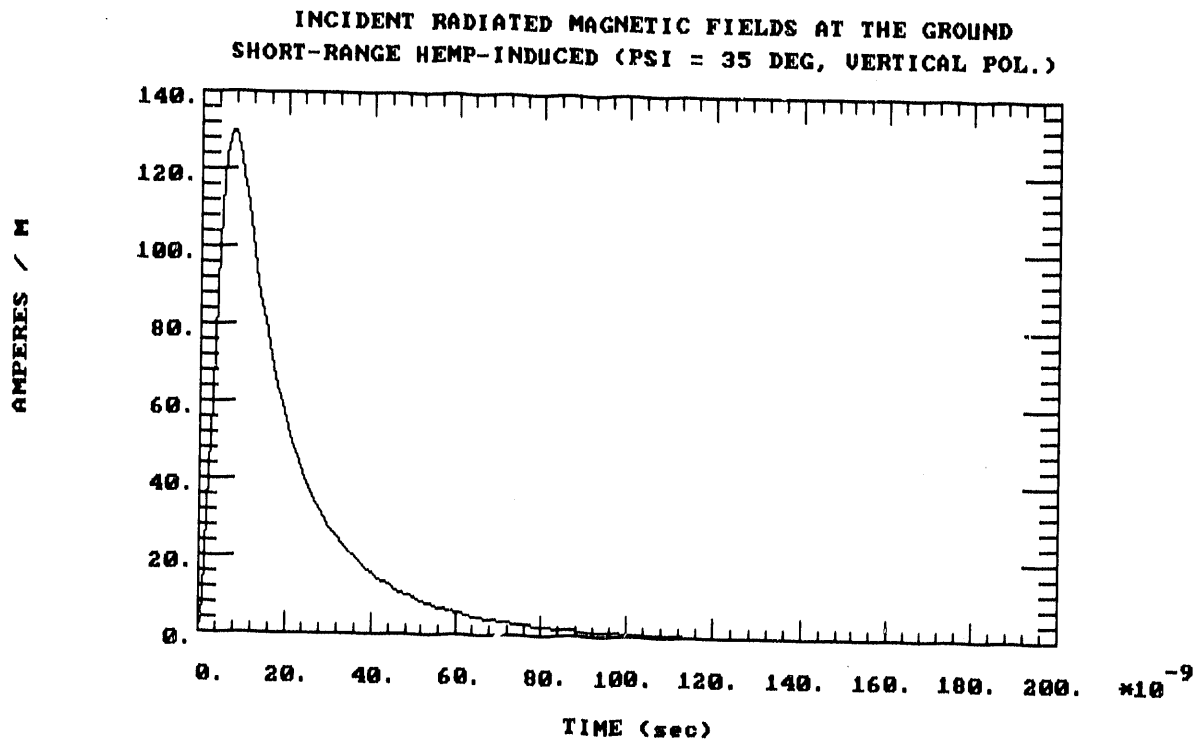

(c) Short-Range HEMP

Figure 4.7 (Concluded). Radiated Incident Magnetic Field Waveforms at the Ground

Table 4.2. Norms for Incident Electric and Magnetic Fields at Ground

	500 kV 2 PU ST		Long-Range HEMP		Short-Range HEMP	
	Electric Field	Magnetic Field	Electric Field	Magnetic Field	Electric Field	Magnetic Field
Zero-Peak Amplitude	11.9 $\frac{kV}{m}$	179 $\frac{A}{m}$	11.2 $\frac{kV}{m}$ (vert. compt.)	29.7 $\frac{A}{m}$ (horiz. compt.)	50.0 $\frac{kV}{m}$ (horiz. compt.)	130 $\frac{A}{m}$ (vert. compt.)
Local Risetime	10 ns	23 ns	6.6 ns	6.6 ns	3.4 ns	3.4 ns
Peak Derivative	6.42E11 $\frac{kV/m}{sec}$	4.26E9 $\frac{A/m}{sec}$	1.16E12 $\frac{kV/m}{sec}$	3.08E9 $\frac{A/m}{sec}$	1.08E13 $\frac{kV/m}{sec}$	2.87E10 $\frac{A/m}{sec}$
Action Integral	86.6 $\left(\frac{V}{m}\right)^2$sec	0.022 $\left(\frac{A}{m}\right)^2$sec	4.54 $\left(\frac{V}{m}\right)^2$sec	3.19E-5 $\left(\frac{A}{m}\right)^2$sec	27.7 $\left(\frac{V}{m}\right)^2$sec	1.94E-4 $\left(\frac{A}{m}\right)^2$sec

4.3 COUPLING TO CONTROL CIRCUITS

4.3.1 Field Coupling to Cable Shields

Shield current waveforms are displayed in Figure 4.8 for 500 kV 2 PU ST, long-range HEMP, and short-range HEMP environments. These have been calculated at the center of a 73 m cable, using the sum of both electric and local magnetic field coupling modes. The shield currents (and their reflections from the shield terminations) for these modes typically affect the cable's center at different times. The corresponding spectra are overlaid in Figure 4.9, and shield current norms are listed in Table 4.3. The switching transient currents show the largest peak amplitudes at frequencies below 3 MHz, while short range HEMP currents possess the highest amplitudes above 10 MHz. For short range HEMP, the azimuth angle ϕ was set at 90° in order to represent worst-case angle of incidence of the electric field (parallel to the shield).

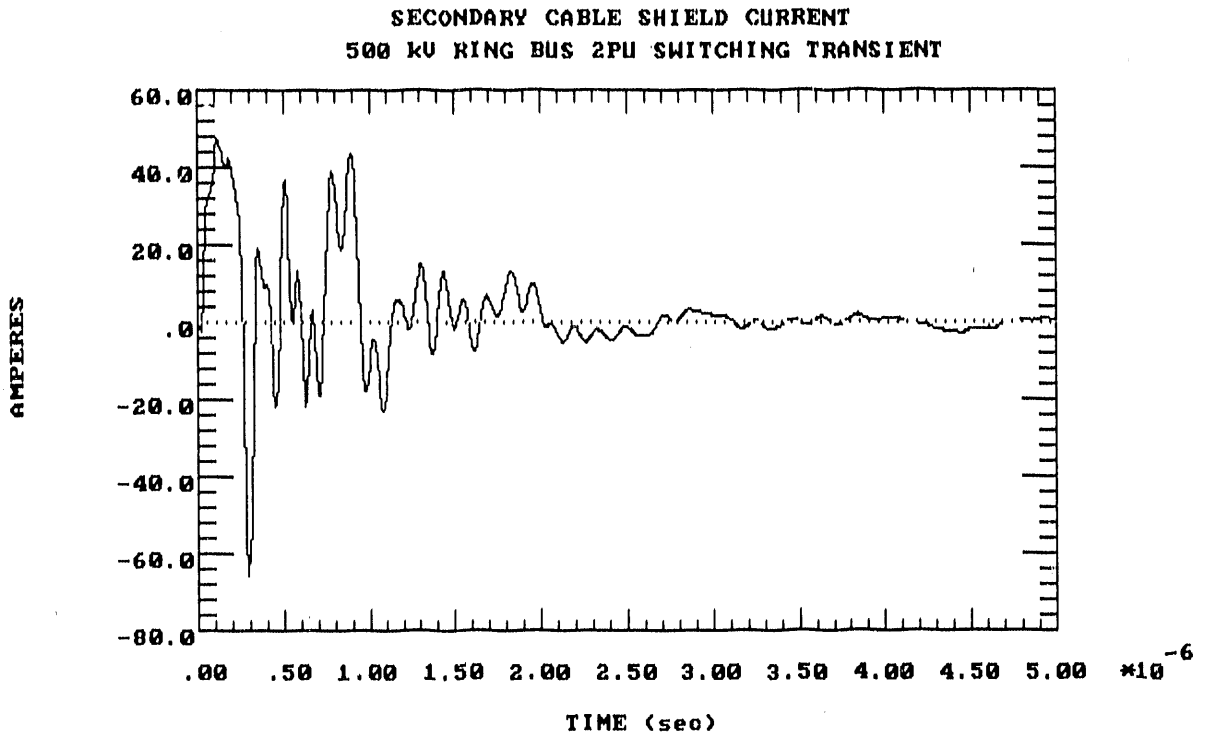

(a) 500 kV 2 PU Switching Transient

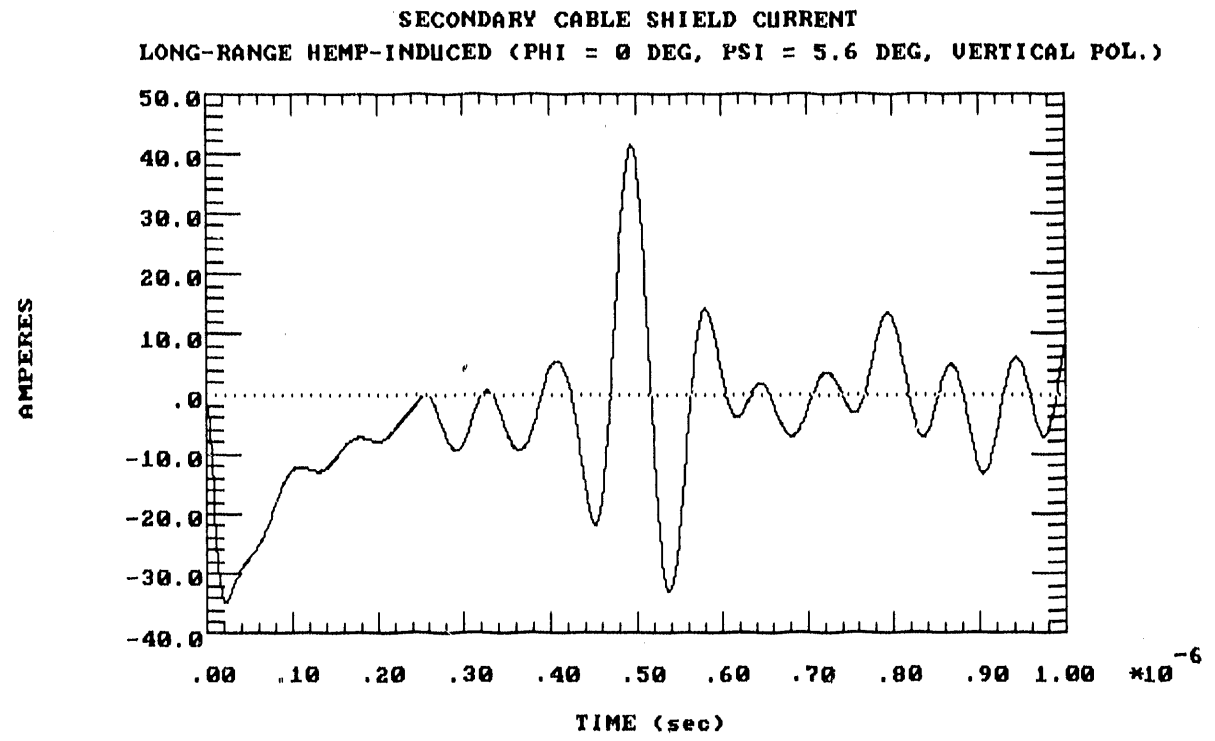

(b) Long-Range HEMP

Figure 4.8. Coupled Cable Shield Current Waveforms

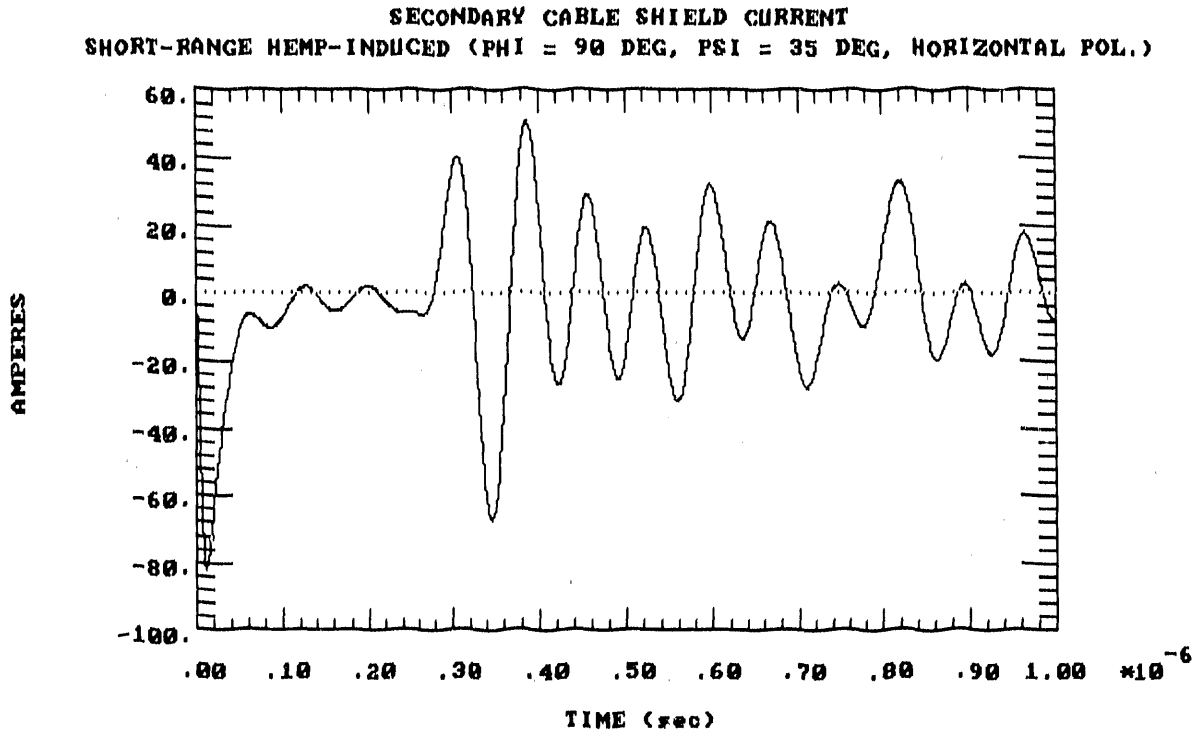

(c) Short-Range HEMP

Figure 4.8 (Concluded). Coupled Cable Shield Current Waveforms

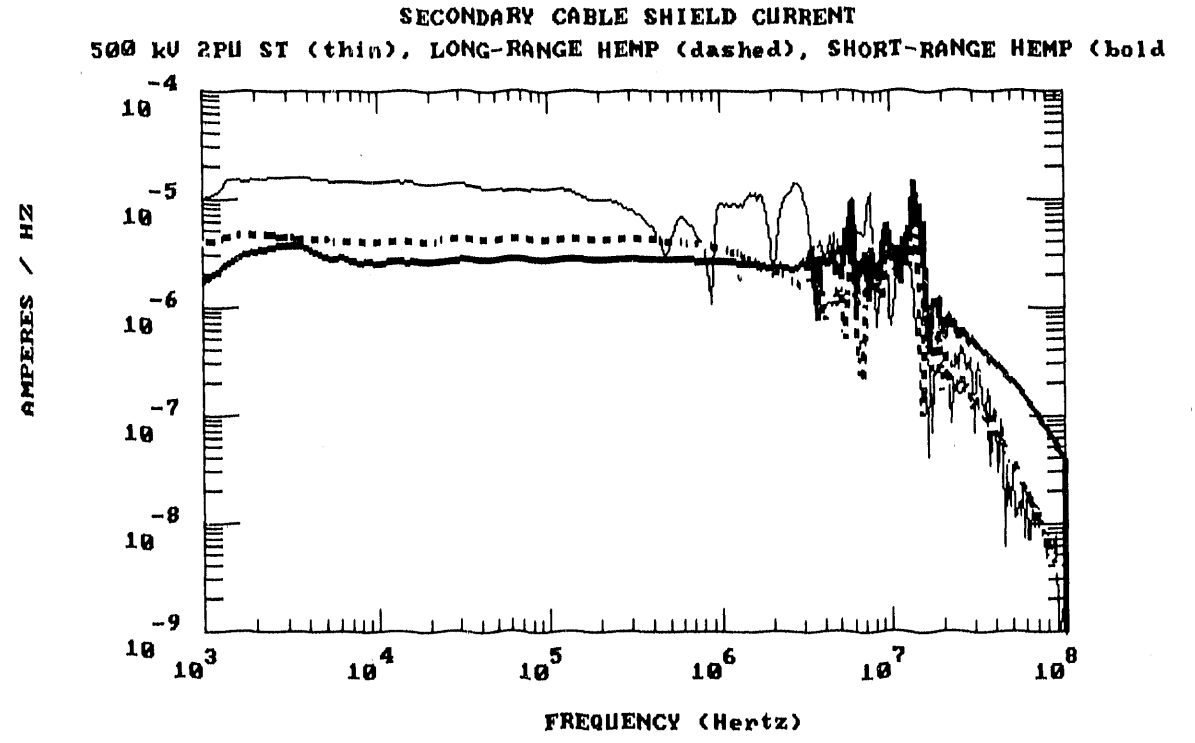

Figure 4.9. Coupled Cable Shield Current Spectra: 500 kV 2 PU ST (thin), Long-Range HEMP (dotted), Short-Range HEMP (bold)

Table 4.3. Norms for Induced Shield Currents

	500 kV 2 PU ST	Long-Range HEMP	Short-Range HEMP
Zero-Peak Amplitude	65.2 A	41.2 A	81.8 A
Local Risetime	11.5 ns	7.1 ns	4.6 ns
Peak Derivative	3.64E9 $\frac{A}{sec}$	2.77E9 $\frac{A}{sec}$	1.31E10 $\frac{A}{sec}$
Action Integral	8.44E-4 A^2sec	1.69E-4 A^2sec	4.75E-4 A^2sec

4.3.2 Shielded-Cable Load Responses

Shielded cable load responses were calculated for five coupling modes: shield-current driven transfer-impedance coupling (from both E and H fields), shield-current driven pigtail-inductance coupling (from both E and H fields), and bus-current driven conducted coupling. Induced currents and voltages for the different modes arrive at the load at different times. In addition, five different impedance conditions were used for the cable load: 150 Ω impedance (constant over all frequencies), measured relay CT-lead load impedance, measured relay DC battery-lead load impedance, open circuit load, and short circuit load. For short range HEMP, the azimuth angle ϕ was again set at 90° in order to represent worst-case angle of incidence of the electric field (parallel to the cable shield).

The induced load currents for the 500 kV 2 PU ST environment, summed over all coupling modes, and with separate curves overlaid for each of the impedance values, are displayed in Figure 4.10(a) (time-domain) and 4-10(b) (frequency-domain). For all load impedances, the current waveforms display a similar ringing frequencies at about 500 kHz and near 8 MHz. The CT-lead load impedance contributes the highest peak amplitude. The corresponding load voltages for the ST case, again summed over all coupling modes, and again with separate curves for each of the impedance values, are displayed in Figure 4.11(a) (waveforms) and 4.11(b) (spectra). Here, the CT-lead relay load impedance shows the highest peak amplitude. The voltages for all three impedance values display principal frequencies similar to the currents.

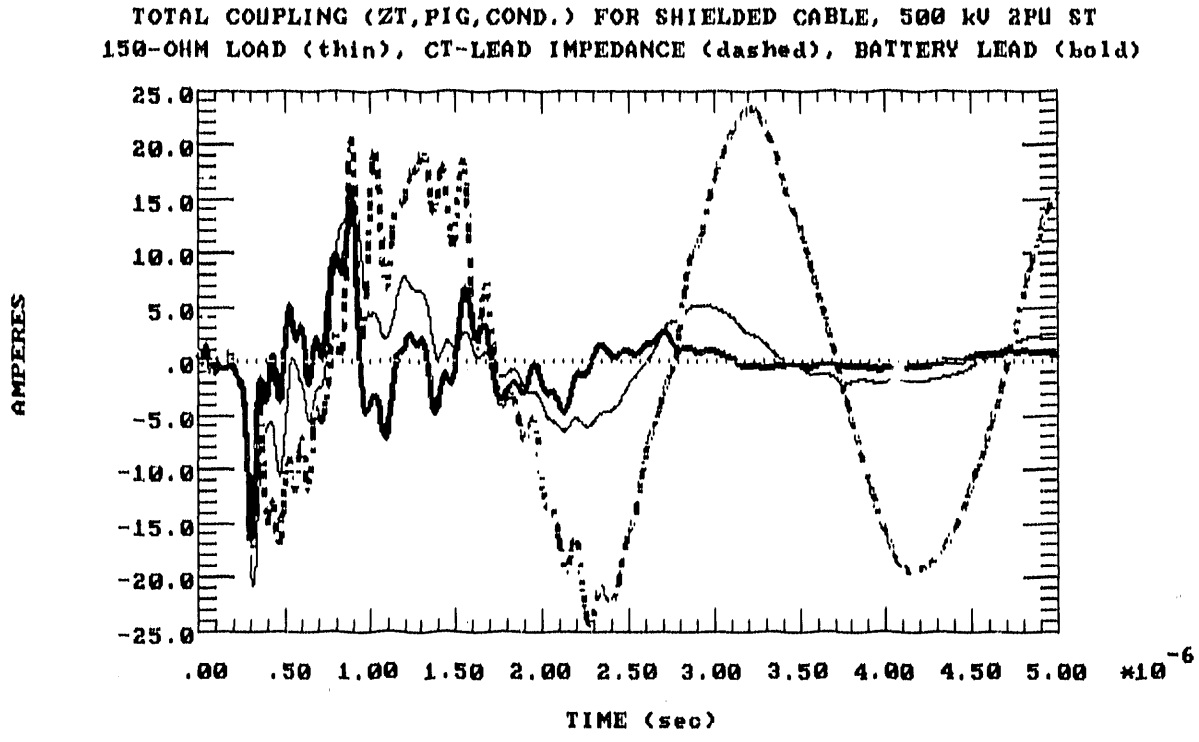

(a) Time-Domain Waveforms

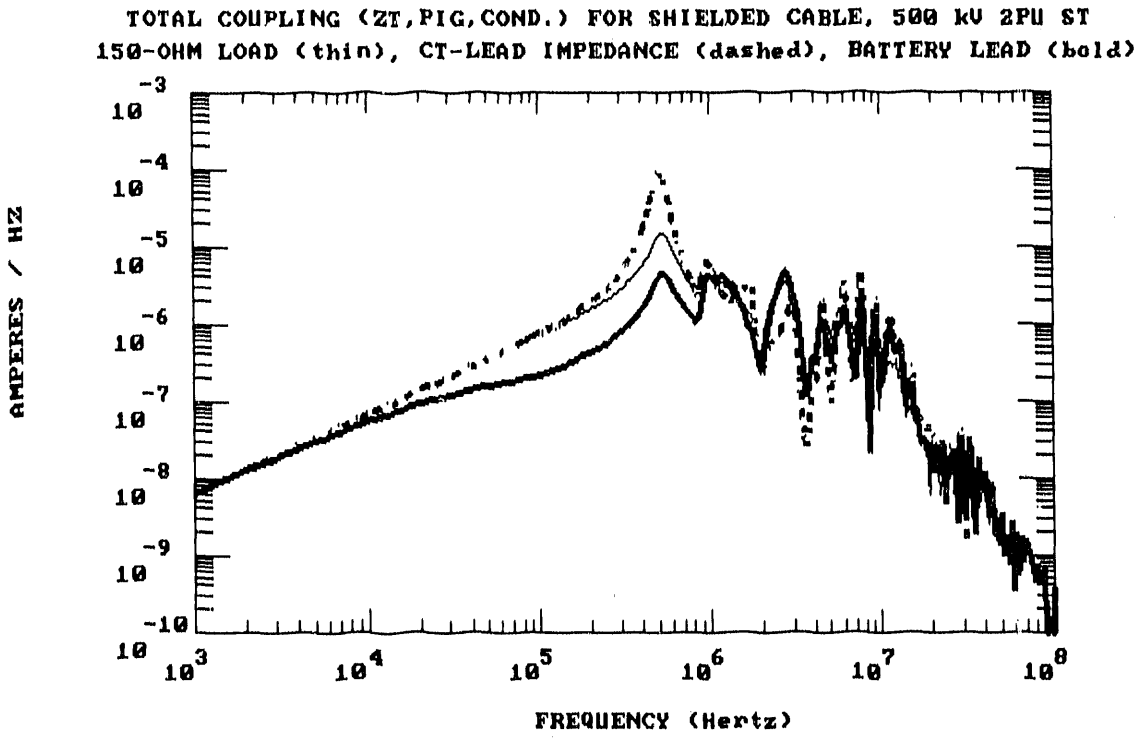

(b) Frequency-Domain Spectra

Figure 4.10 500 kV 2 PU ST-Induced Currents for Shielded-Cable Loads: 150 Ω Load (Thin), Measured CT-Lead Impedance (Dotted), Measured DC Batt.-Lead Impedance (Bold)

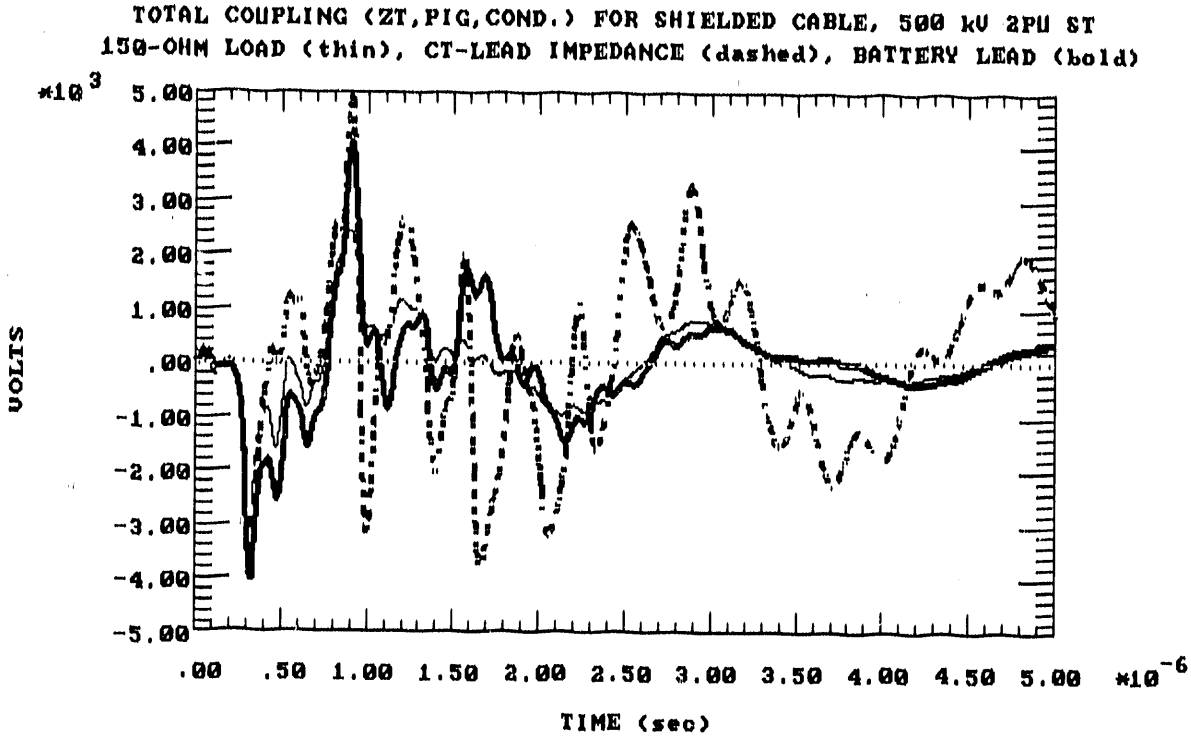

(a) Time-Domain Waveforms

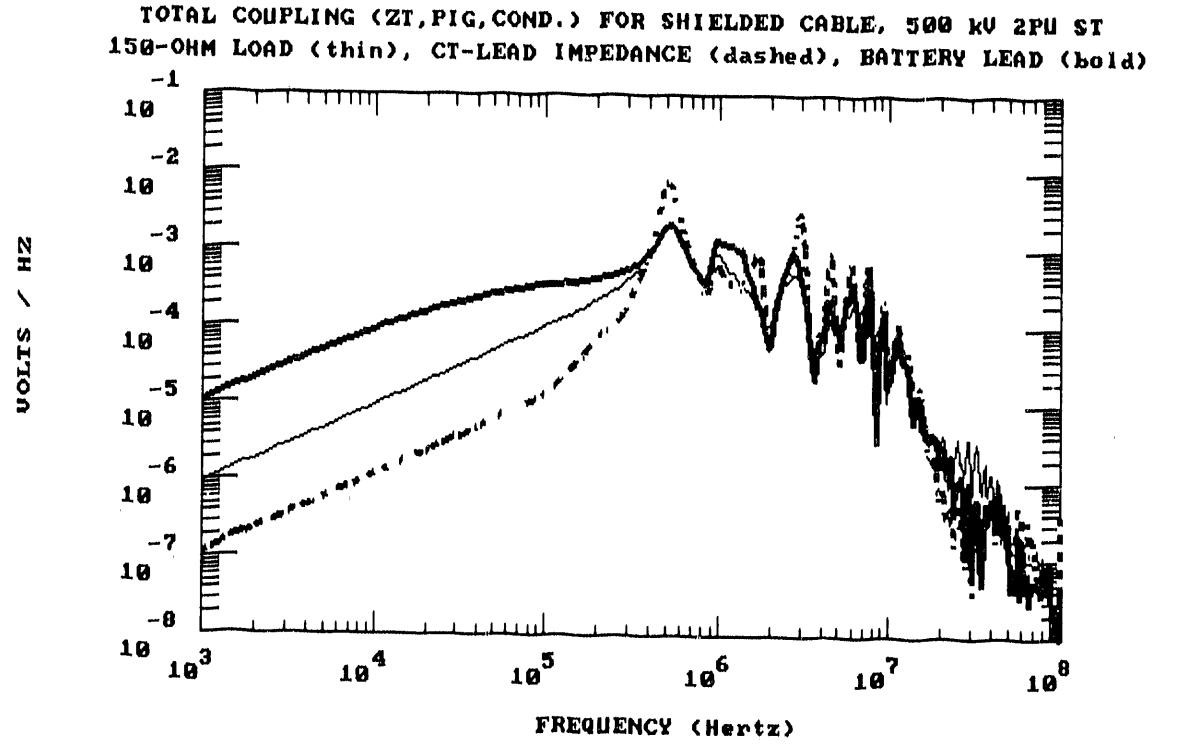

(b) Frequency-Domain Spectra

Figure 4.11 500 kV 2 PU ST-Induced Voltages for Shielded-Cable Loads: 150 Ω Load (Thin), Measured CT-Lead Impedance (Dotted), Measured DC Batt.-Lead Impedance (Bold)

The induced load currents for the long-range HEMP environment, summed over all coupling modes, and with separate curves overlaid for each of the impedance values, are displayed in Figure 4.12(a) (time-domain) and 4-12(b) (frequency-domain). All three impedance values produce large currents with decaying periods of around 100 ns (10 MHz); the CT-lead impedance current produces the largest peak amplitude. The corresponding load voltages for the long-range HEMP case appear in Figure 4.13(a) (waveforms) and 4.13(b) (spectra). Here, the CT-lead relay load impedance again shows somewhat larger amplitude than the DC-battery load impedance; peak spectral voltages occur from about 3 - 12 MHz.

The induced load currents for the short-range HEMP environment, summed over all coupling modes, and with separate curves overlaid for each of the impedance values, are displayed in Figure 4.14(a) (time-domain) and 4-14(b) (frequency-domain). All three impedance values produce large currents with decaying periods of around 70 ns (14 MHz); the CT-lead impedance current again produces the largest peak amplitude. The corresponding load voltages for the short-range HEMP case appear in Figure 4.15(a) (waveforms) and 4.15(b) (spectra). From about 3 - 15 MHz, all three voltage responses show very similar spectral amplitudes.

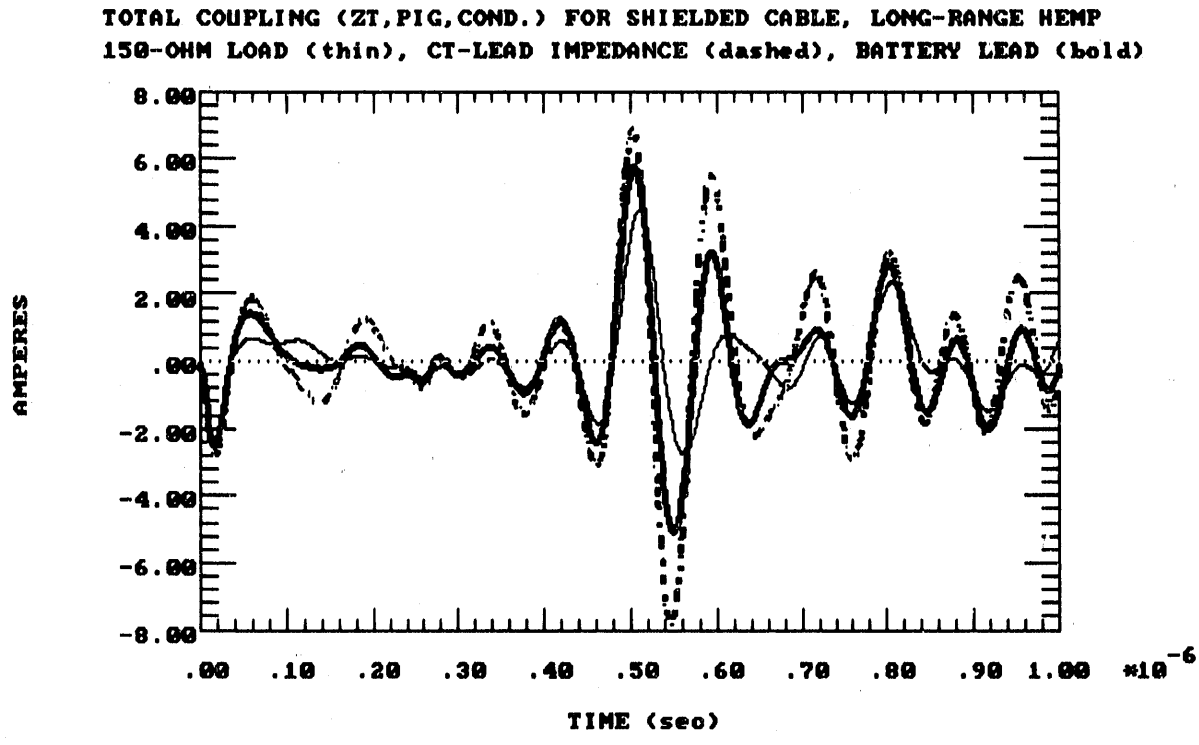

(a) Time-Domain Waveforms

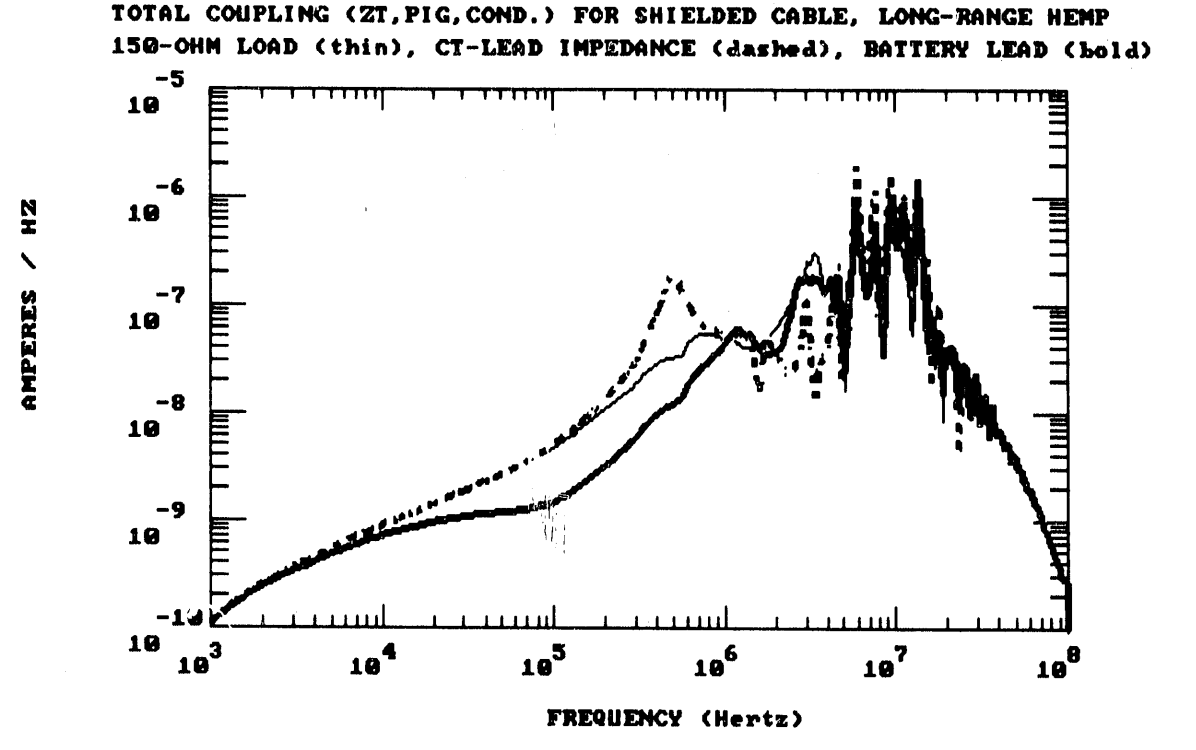

(b) Frequency-Domain Spectra

Figure 4.12. Long-Range HEMP-Induced Currents for Shielded-Cable Loads: 150 Ω Load (Thin), Measured CT-Lead Impedance (Dotted), Measured DC Batt.-Lead Impedance (Bold)

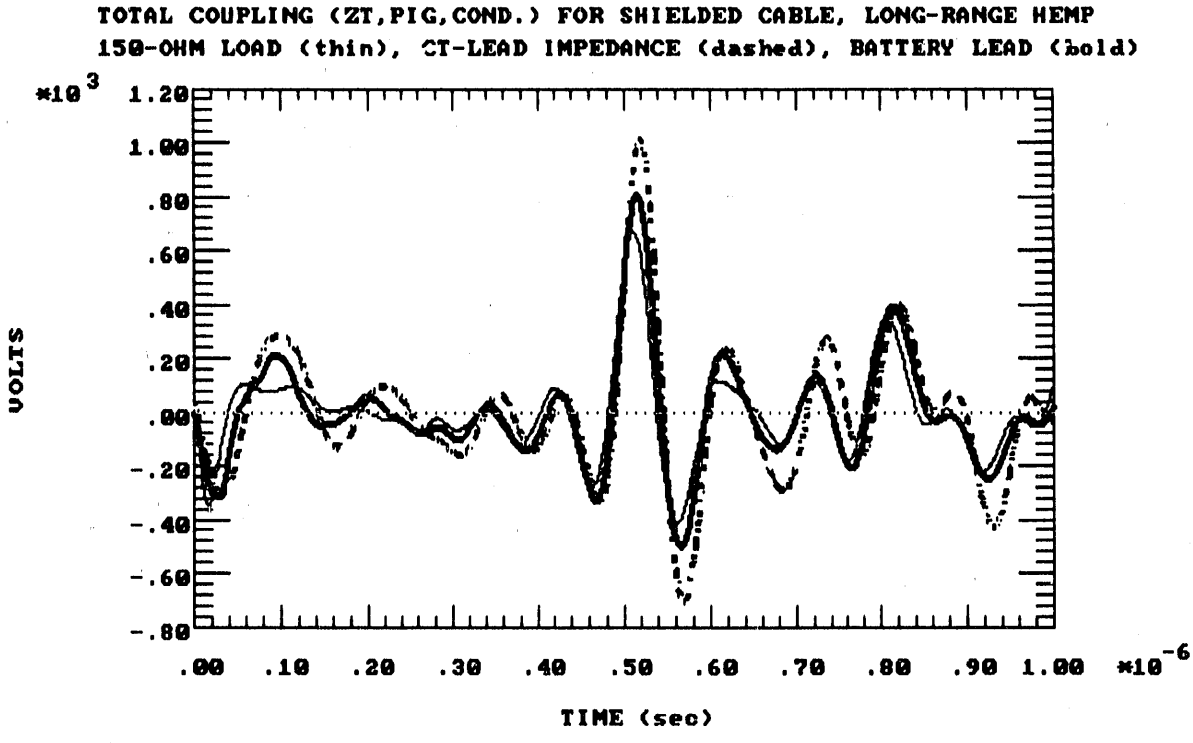

(a) Time-Domain Waveforms

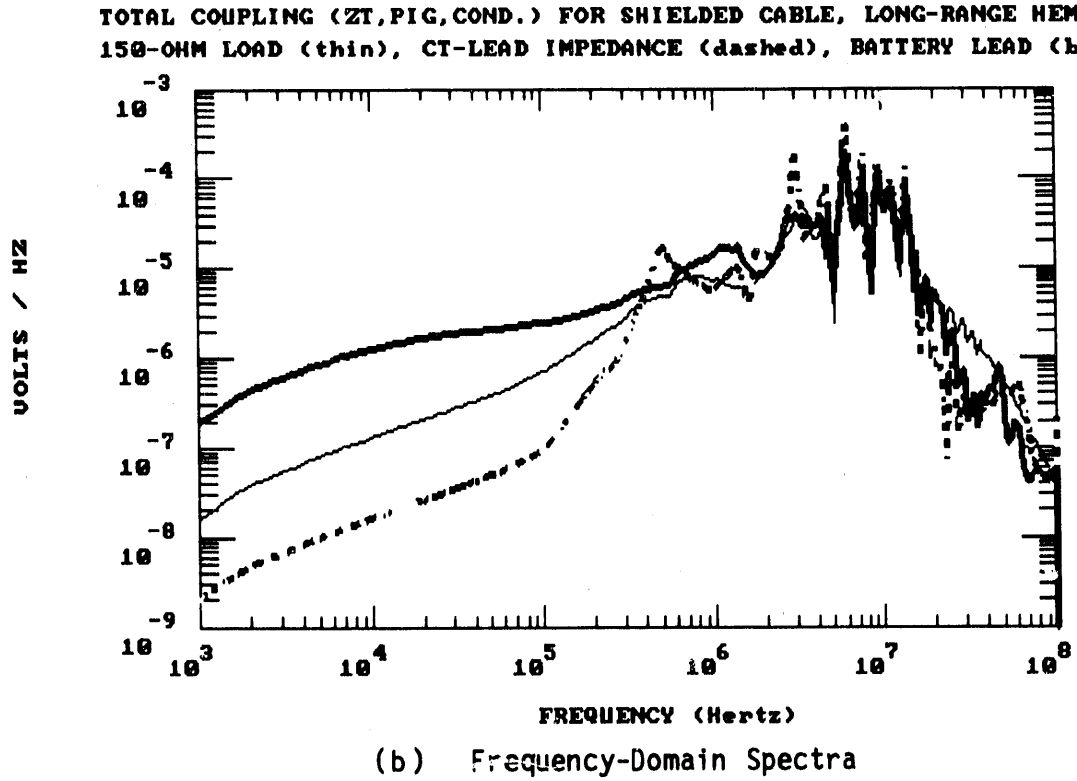

(b) Frequency-Domain Spectra

Figure 4.13. Long-Range HEMP-Induced Voltages for Shielded-Cable Loads: 150 Ω Load (Thin), Measured CT-Lead Impedance (Dotted), Measured DC Batt.-Lead Impedance (Bold)

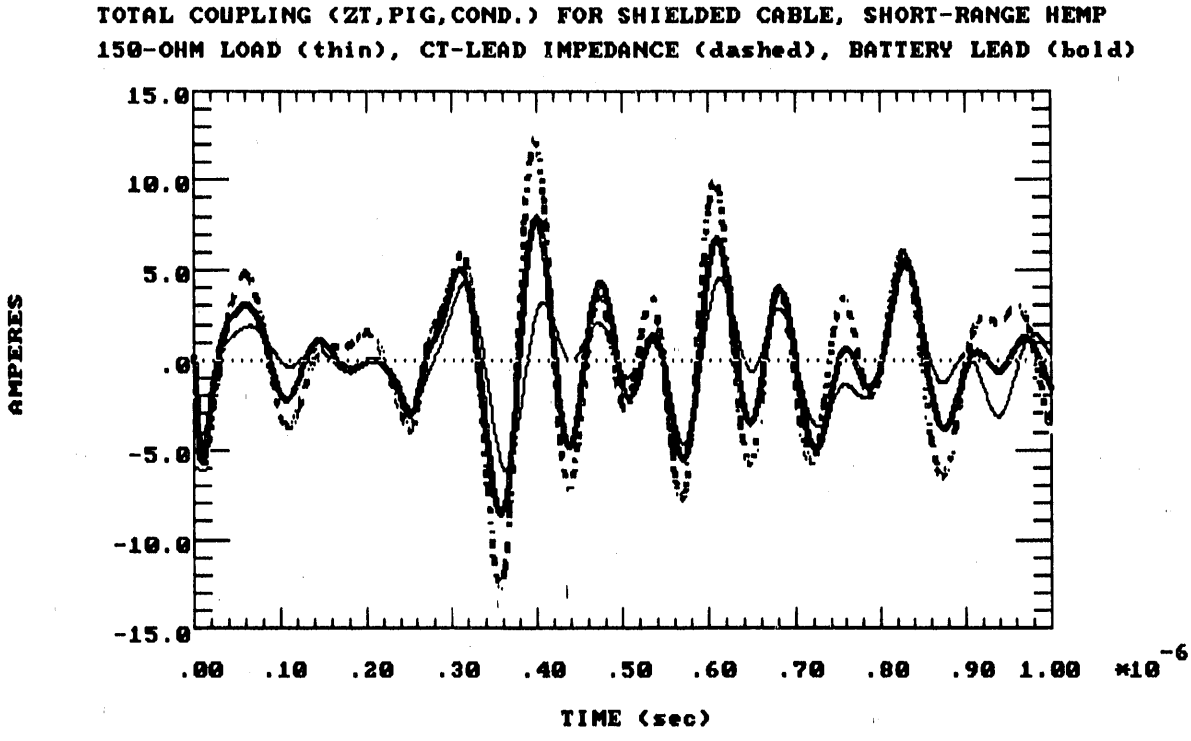

(a) Time-Domain Waveforms

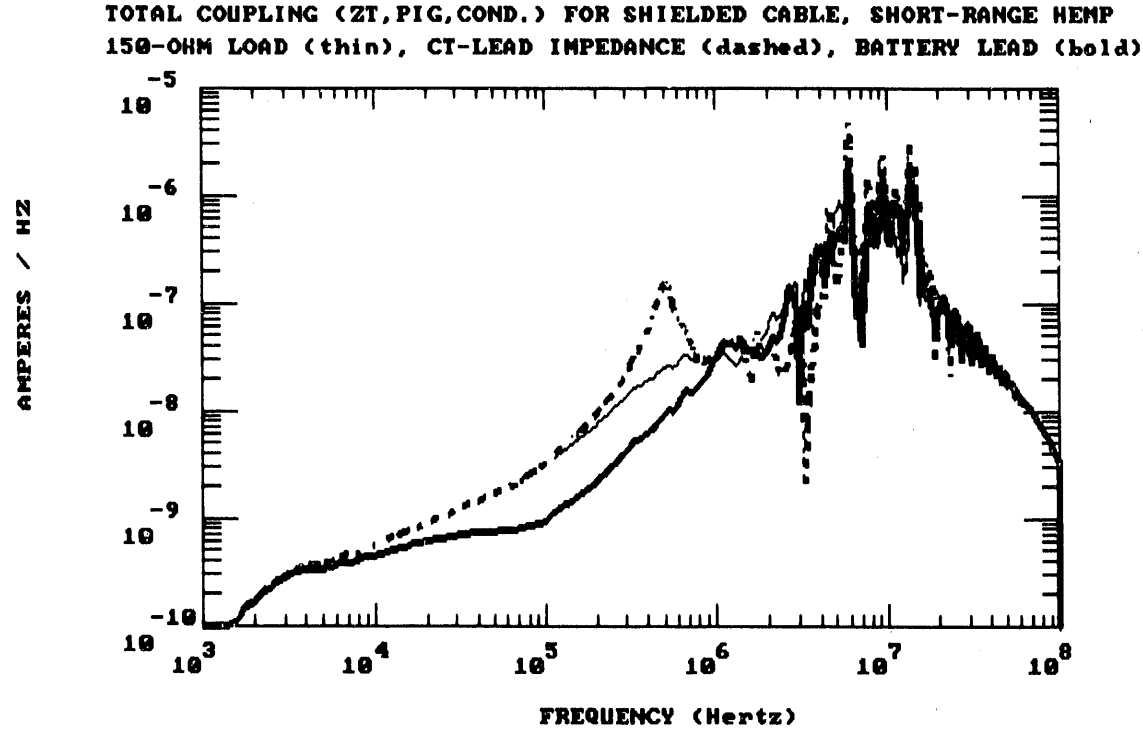

(b) Frequency-Domain Spectra

Figure 4.14. Short-Range HEMP-Induced Currents for Shielded-Cable Loads: 150 Ω Load (Thin), Measured CT-Lead Impedance (Dotted), Measured DC Batt.-Lead Impedance (Bold)

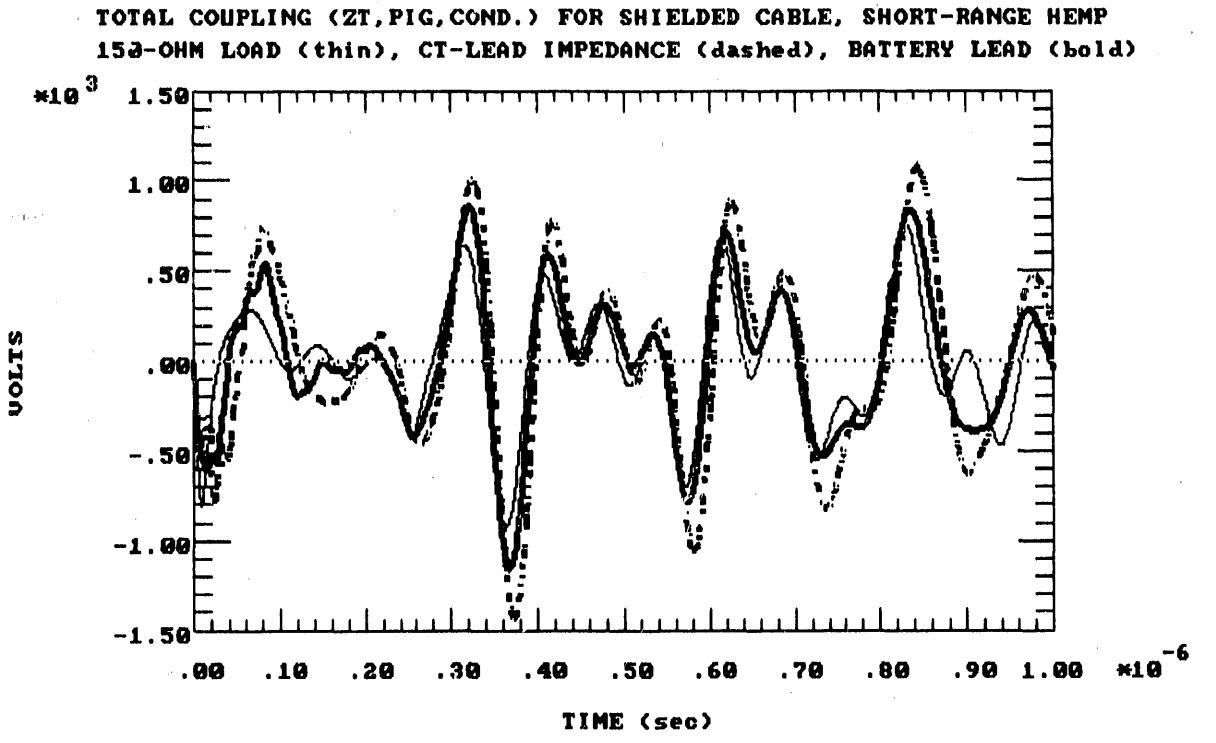

(a) Time-Domain Waveforms

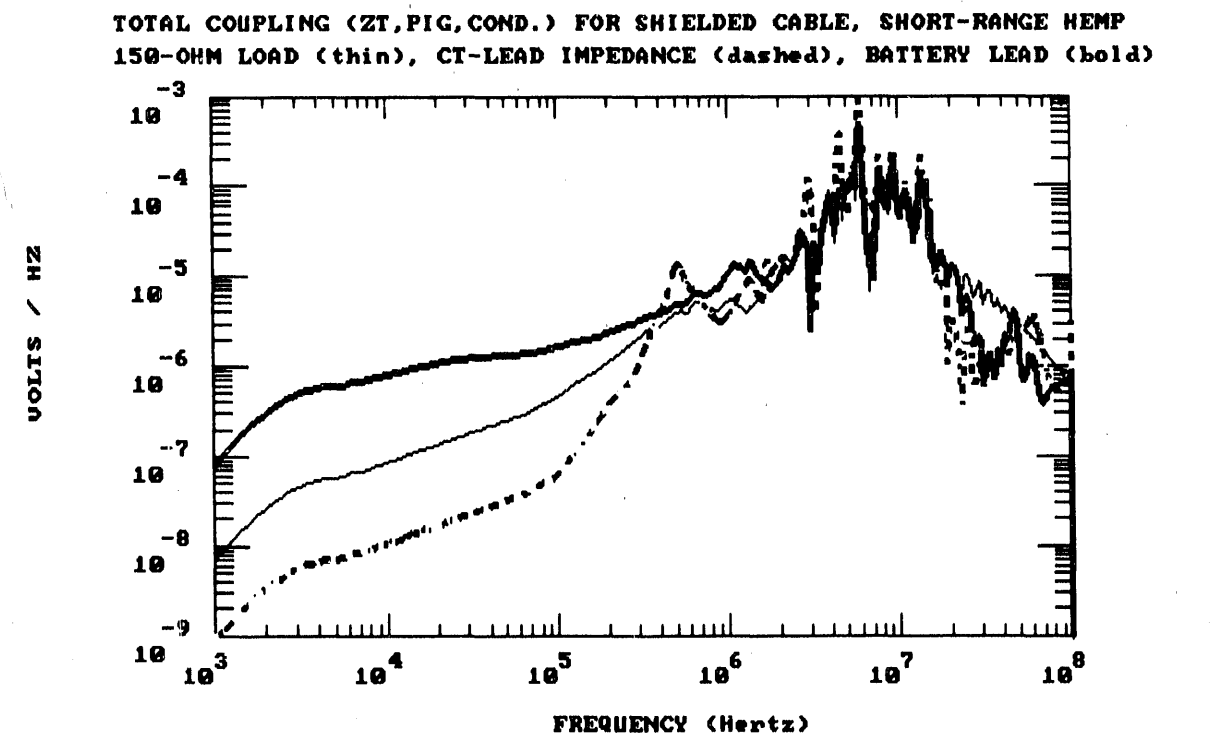

(b) Frequency-Domain Spectra

Figure 4.15. Short-Range HEMP-Induced Voltages for Shielded-Cable Loads: 150 Ω Load (Thin), Measured CT-Lead Impedance (Dotted), Measured DC Batt.-Lead Impedance (Bold)

The norms for all three environments are collected in Table 4.4 for the 150 Ω impedance load. The ST-induced load currents and voltages have the largest peak amplitudes and action integrals; the short-range HEMP-induced load currents and voltages have the largest peak derivatives as well as the shortest local risetimes

Norms for all environments are listed in Table 4.5 for the CT-lead impedance case. Here, the ST-induced currents again have the largest peak amplitudes and action integrals, and the longest local rise times, while the HEMP-induced responses again show the fastest rise times.

The norms for ST and HEMP-induced load responses are listed in Table 4.6 for the relay DC battery-lead impedance. The ST-induced currents again have the highest peak amplitudes and action integrals, and the longest local rise times, while the short range HEMP-induced responses shows the largest peak derivatives and the fastest local rise times.

Zero-peak amplitudes over all environments and all load impedances are summarized in Table 4.7. This table shows that there is some variation in response as a function of the load impedance. Overall, the response is highest for the CT-lead load impedance. Peak amplitude responses of ST are typically 2 - 3 times higher than short range HEMP responses for a given load type.

The open circuit voltage and short circuit current responses of the shielded cable were also determined for the ST and HEMP drives. These responses are given in Figures 16 (switching transient), 17 (long range HEMP), and 18 (short range HEMP). Peak amplitude ST open circuit voltage and short circuit current are about 2 times higher than the maximum response for the CT-lead load impedance. Short range HEMP shows increases of about 30 % in current and 300 % in open circuit voltage over the CT-lead load responses. The open and short circuit responses shown here are used for comparisons to the SWC fast transient later in this section.

Table 4.4. Norms for Transient Control-Wire Currents and Voltages For 150 Ω Load (Summed for All Coupling Modes)

	500 kV 2 PU ST		Long-Range HEMP		Short-Range HEMP	
	Wire Current	Wire Voltage	Wire Current	Wire Voltage	Wire Current	Wire Voltage
Zero-Peak Amplitude	20.8A	3.12kV	4.47 A	0.67 kV	6.14 A	0.92 kV
Local Risetime	16 ns	16 ns	17 ns	17 ns	3.6 ns	3.6 ns
Peak Derivative	4.36E8 $\frac{A}{sec}$	6.53E10 $\frac{V}{sec}$	2.3E8 $\frac{A}{sec}$	3.45E10 $\frac{V}{sec}$	1.09E9 $\frac{A}{sec}$	1.64E11 $\frac{V}{sec}$
Action Integral	1.07E-4 A^2sec	2.40 V^2sec	1.27E-6 A^2sec	0.029 V^2sec	5.04E-6 A^2sec	0.113 V^2sec

Table 4.5. Norms for Transient Control-Wire Currents and Voltages For Measured CT Lead Impedance (Summed for All Coupling Modes)

	500 kV 2 PU ST		Long-Range HEMP		Short-Range HEMP	
	Wire Current	Wire Voltage	Wire Current	Wire Voltage	Wire Current	Wire Voltage
Zero-Peak Amplitude	24.3 A	4.89 kV	7.82 A	1.01 kV	12.7 A	1.43 kV
Local Risetime	20 ns	36 ns	14 ns	17 ns	4.0 ns	2.3 ns
Peak Derivative	5.11E8 $\frac{A}{sec}$	1.35E11 $\frac{V}{sec}$	5.31E8 $\frac{A}{sec}$	5.50E10 $\frac{V}{sec}$	1.13E9 $\frac{A}{sec}$	1.45E11 $\frac{V}{sec}$
Action Integral	8.90E-4 A^2sec	13.2 V^2sec	4.90E-6 A^2sec	0.067 V^2sec	1.85E-5 A^2sec	0.261 V^2sec

Table 4.6. Norms for Transient Control-Wire Currents and Voltages For Measured DC Battery Lead Impedance (Summed for All Coupling Modes)

	500 kV 2 PU ST		Long-Range HEMP		Short-Range HEMP	
	Wire Current	Wire Voltage	Wire Current	Wire Voltage	Wire Current	Wire Voltage
Zero-Peak Amplitude	16.6 A	4.05 kV	5.74 A	0.803 kV	8.56 A	1.16 kV
Local Risetime	13 ns	20 ns	15 ns	17 ns	3.9 ns	3.9 ns
Peak Derivative	4.69E8 $\frac{A}{sec}$	8.09E10 $\frac{V}{sec}$	3.76E8 $\frac{A}{sec}$	4.07E10 $\frac{V}{sec}$	1.10E9 $\frac{A}{sec}$	1.11E11 $\frac{V}{sec}$
Action Integral	4.89E-5 A^2sec	4.31 V^2sec	2.50E-6 A^2sec	0.041 V^2sec	9.28E-6 A^2sec	0.159 V^2sec

Table 4.7. Zero-Peak Amplitudes for Transient Control-Wire Currents and Voltages For 150 Ω, CT, and DC Battery Impedances (Summed for All Coupling Modes)

	500 kV 2 PU ST		Long-Range HEMP		Short-Range HEMP	
	Wire Current	Wire Voltage	Wire Current	Wire Voltage	Wire Current	Wire Voltage
150Ω Lead	20.8A	3.12kV	4.47 A	0.67 kV	6.14 A	0.92 kV
Measd CT Lead	24.3 A	4.89 kV	7.82 A	1.01 kV	12.7 A	1.43 kV
Measd DC Lead	16.6 A	4.05 kV	5.74 A	0.803 kV	8.56 A	1.16 kV

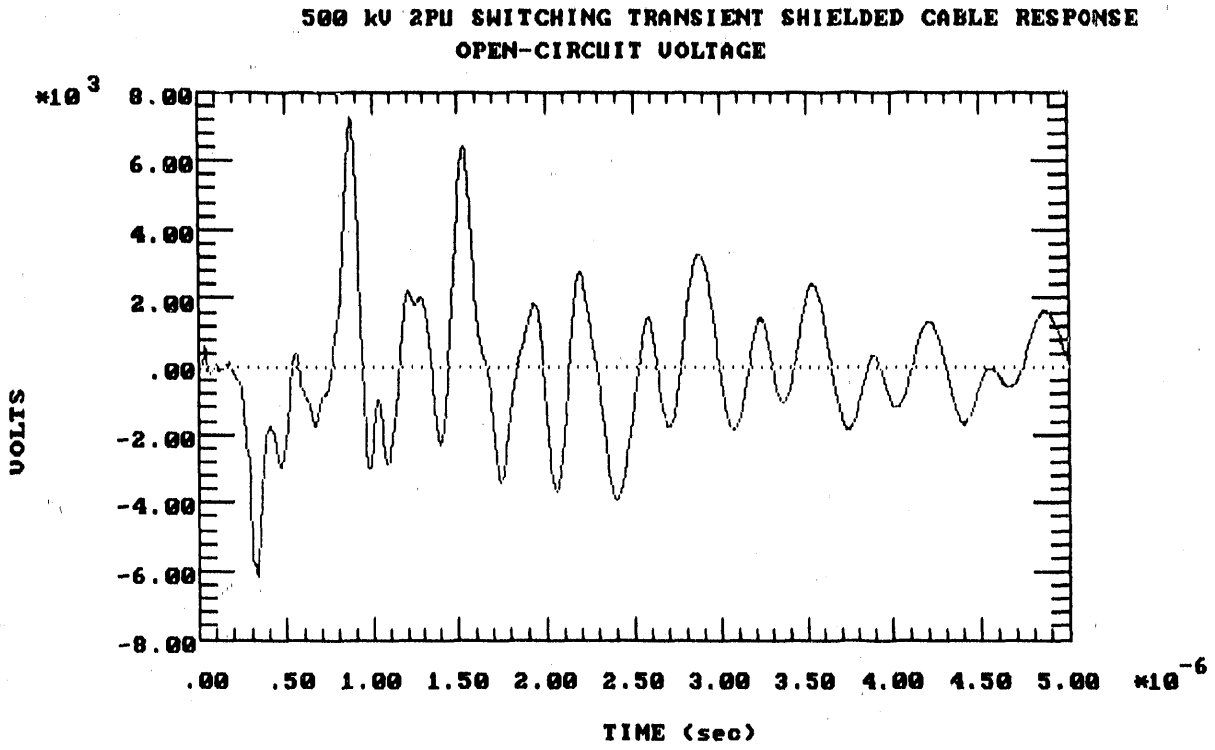

(a) Open Circuit Voltage

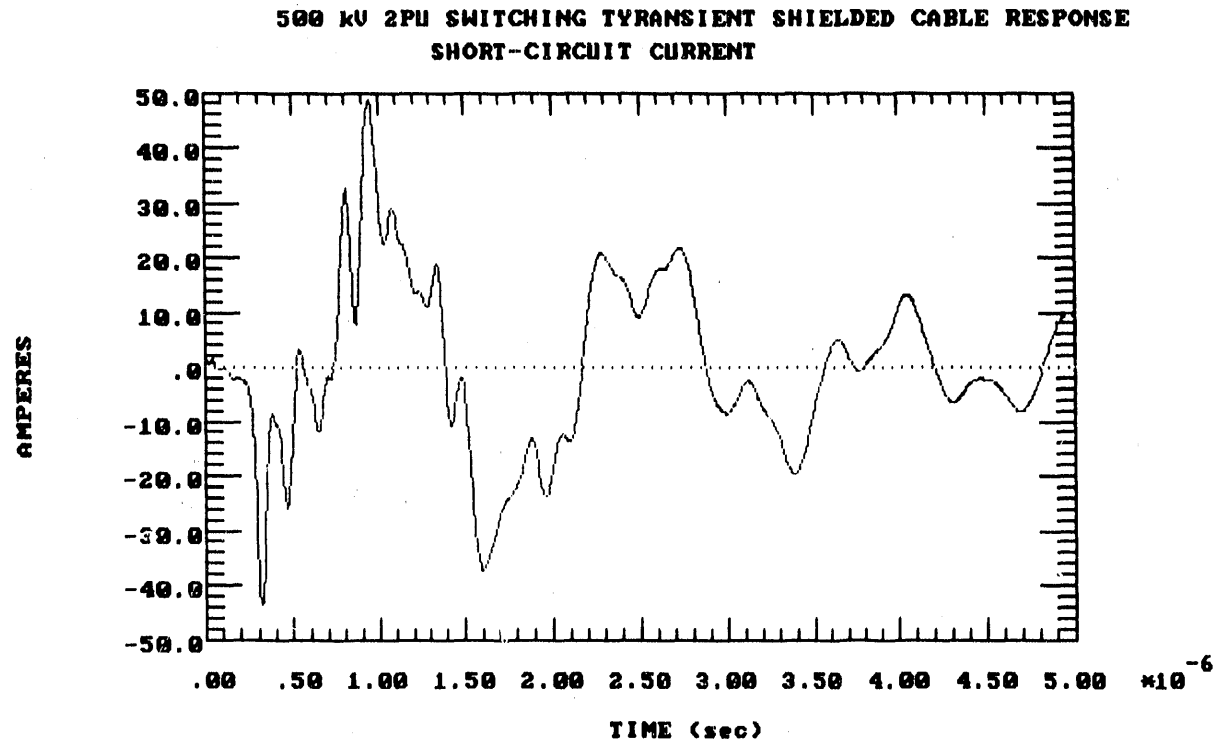

(b) Short Circuit Current

Figure 4.16. 500 kV 2PU Switching Transient Shielded Cable Open and Short Circuit Load Response

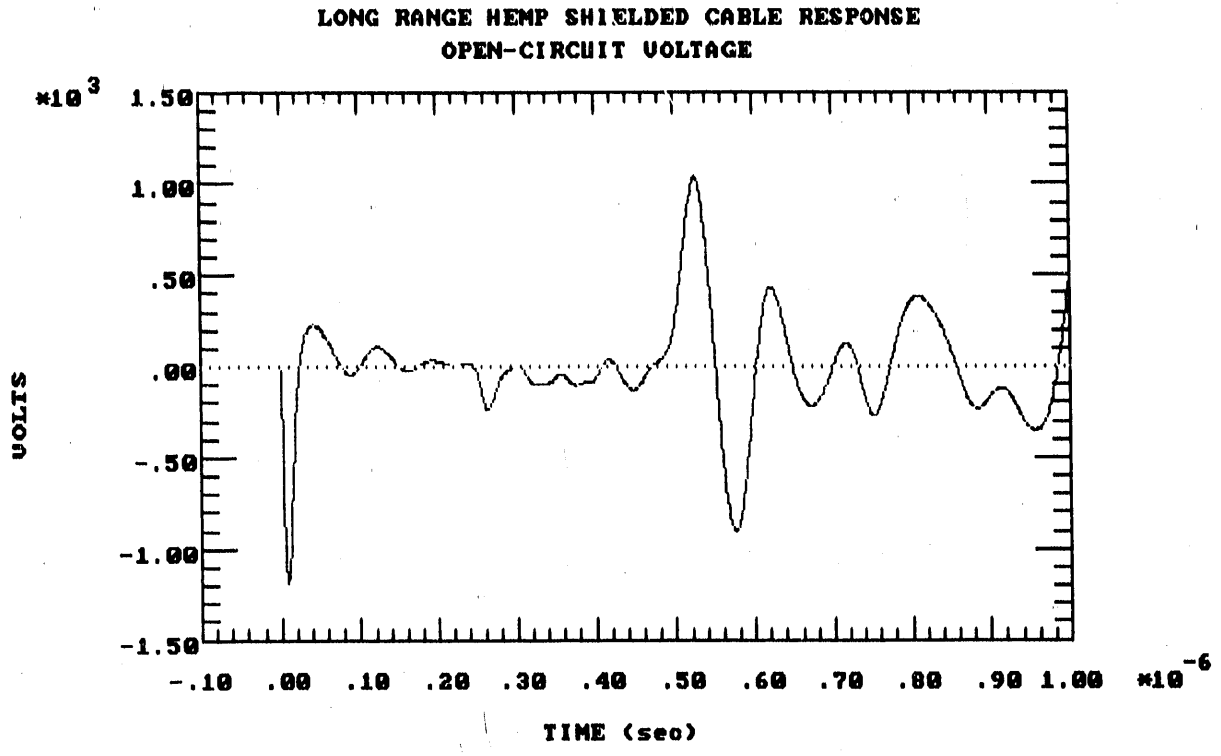

(a) Open Circuit Voltage

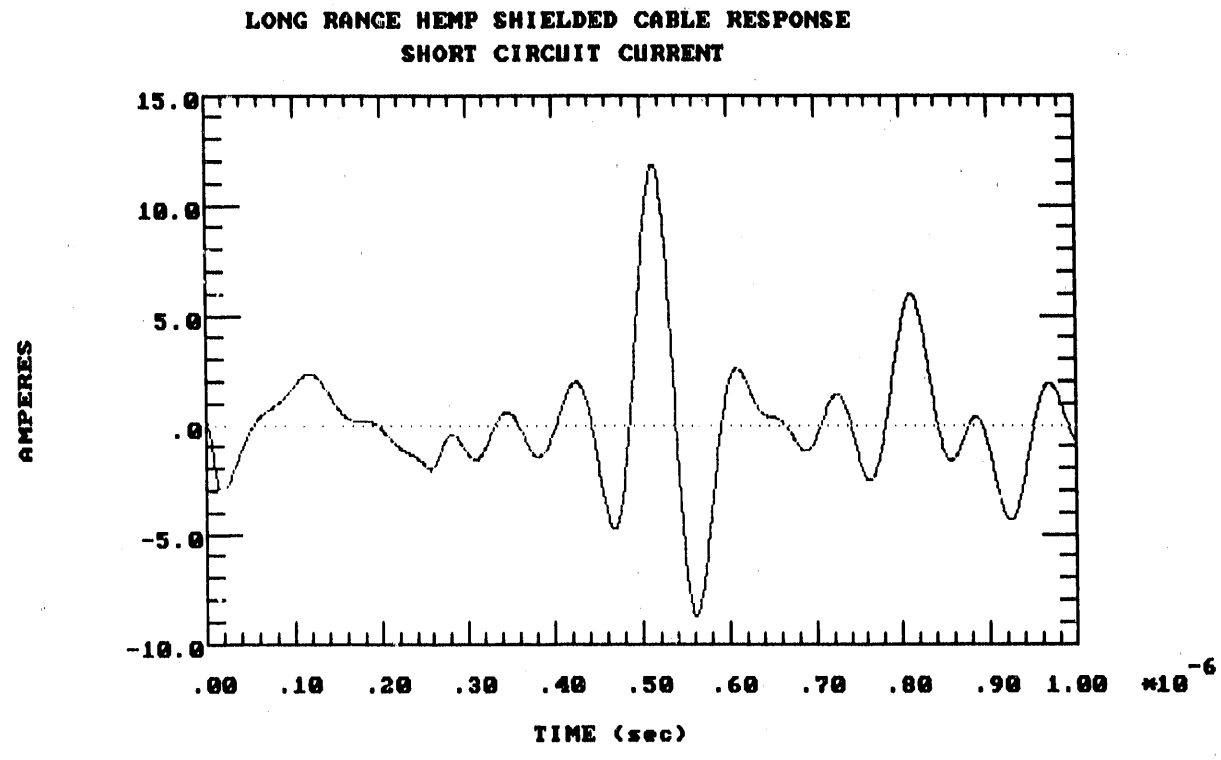

(b) Short Circuit Current

Figure 4.17. Long Range HEMP Shielded Cable Open and Short Circuit Load Response

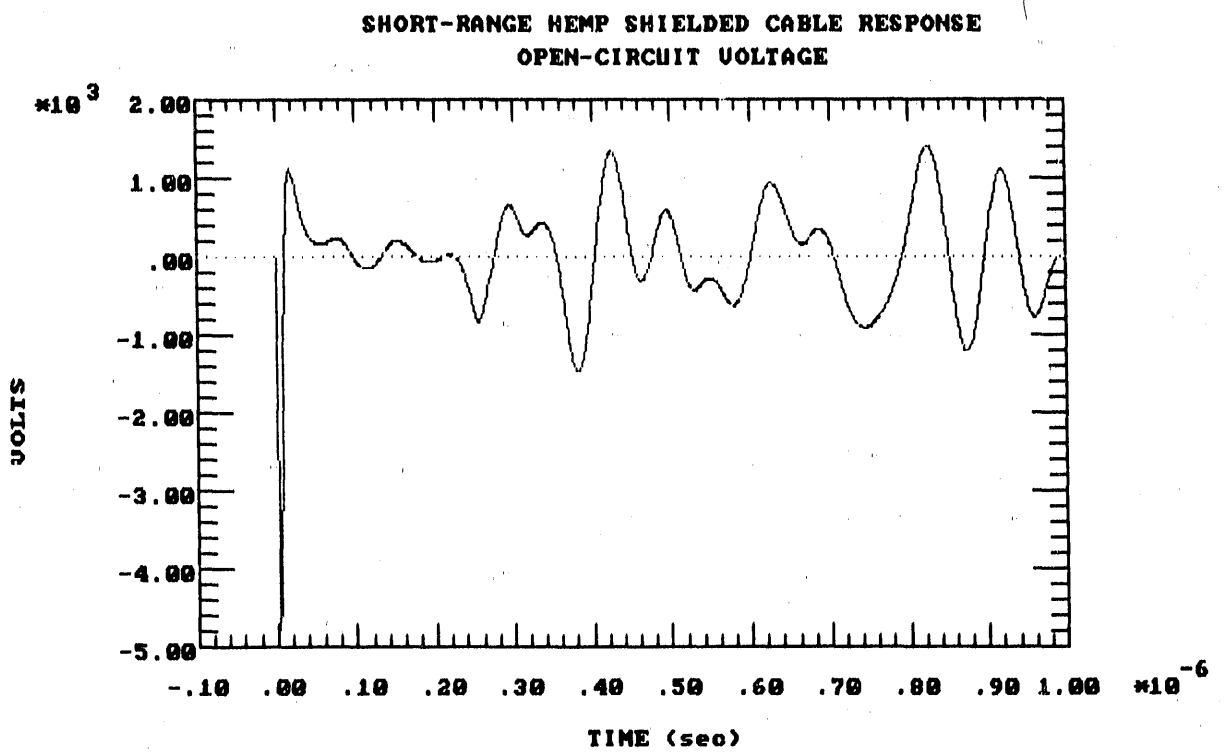

(a) Open Circuit Voltage

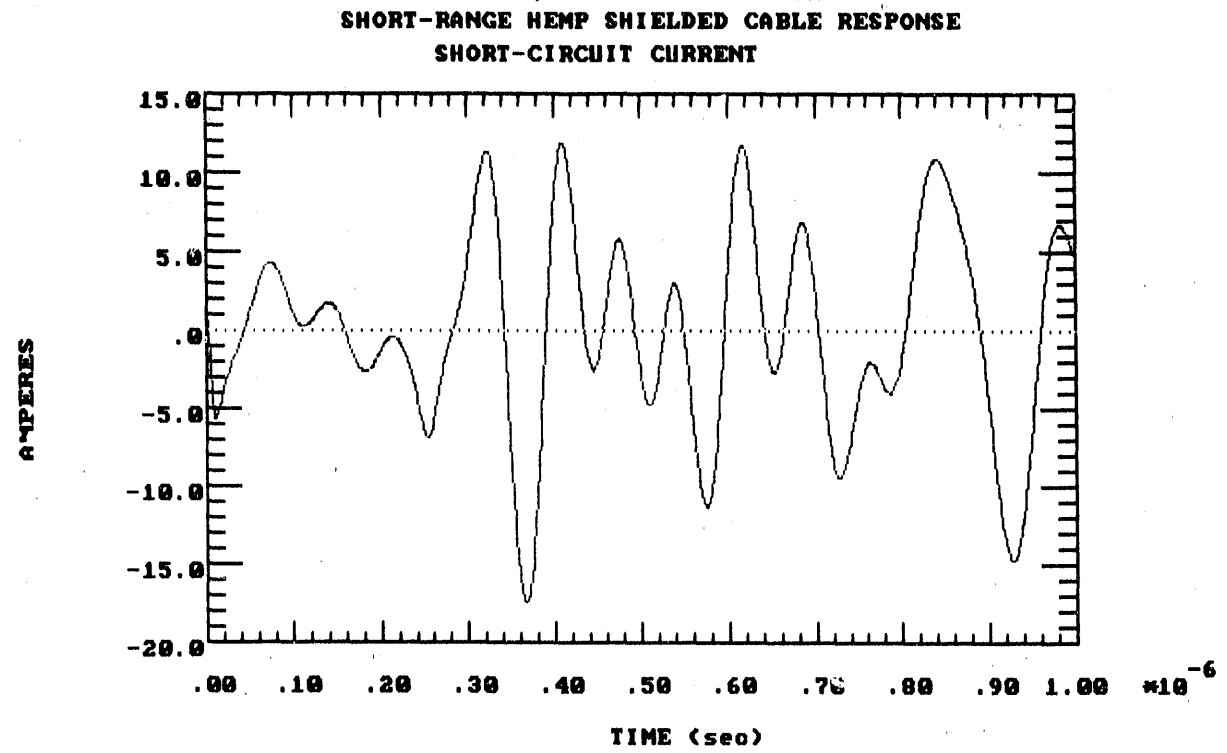

(b) Short Circuit Current

Figure 4.18. Short Range HEMP Shielded Cable Open and Short Circuit Load Response

The induced load currents for the 500 kV 2 PU ST environment, with the CT-lead relay load impedance, and with separate curves overlaid for each of the coupling modes (transfer impedance, pigtail, and conducted coupling), are displayed in Figure 4.19(a) (waveforms) and 4.19(b) (spectra). The transfer impedance and pigtail curves give the net responses for the sum of electric and magnetic field coupling. These plots show that for ST environments, the conducted coupling mode produces the highest peak amplitude, 3 - 4 times greater than pigtail coupling. Conducted coupling dominates at all frequencies below 2 MHz, but at high frequencies (above 50 MHz) pigtail coupling dominates. Both modes contribute much more to the total load response than does the transfer impedance coupling mode. Similar results are seen in the voltage responses, Figure 4.19(c) (waveforms) and 4.19(d) (spectra).

Induced load currents for the long-range HEMP environment, again with the CT-lead relay load impedance, and with separate curves overlaid for each coupling mode, are displayed in Figure 4.20(a) (time-domain) and 4.20(b) (frequency-domain). Examination of these figures reveals that for the long-range HEMP scenario, the conducted coupling mode produces the largest peak amplitude, now about 1.5 times greater than pigtail coupling. At frequencies below 1 MHz, transfer impedance coupling dominates, while pigtail coupling dominates at frequencies above 30 MHz. Both conducted and pigtail coupling contribute much higher peak amplitudes than transfer impedance coupling. Induced load voltages for these modes are given in Figure 4.20(c) (waveforms) and 4.20(d) (spectra).

Induced load currents for the short-range HEMP environment, for the CT-lead relay load impedance, and with separate curves overlaid for each coupling mode, are displayed in Figure 4.21(a) (time-domain) and 4.21(b) (frequency-domain). These plots indicate that for the short-range HEMP case, conducted and pigtail coupling produce similar peak amplitudes, the former being slightly larger. As before, transfer impedance coupling dominates at low frequencies, while pigtail coupling dominates at high frequencies. But in the region from 4 - 15 MHz, which includes the peak spectral responses, conducted coupling dominates. Figure 4.21(c) and (d) provide similar results for the short-range HEMP induced load voltages.

Load current norms for all three environments, with the CT-lead relay load impedance, and for each coupling mode, are gathered together in Table 4.8. It is evident that the largest transfer-impedance coupling peak amplitudes occur for the short-range HEMP case, although all peaks are comparatively small for this mode. Conducted coupling is responsible for the large peak amplitudes of induced currents for both ST and HEMP.

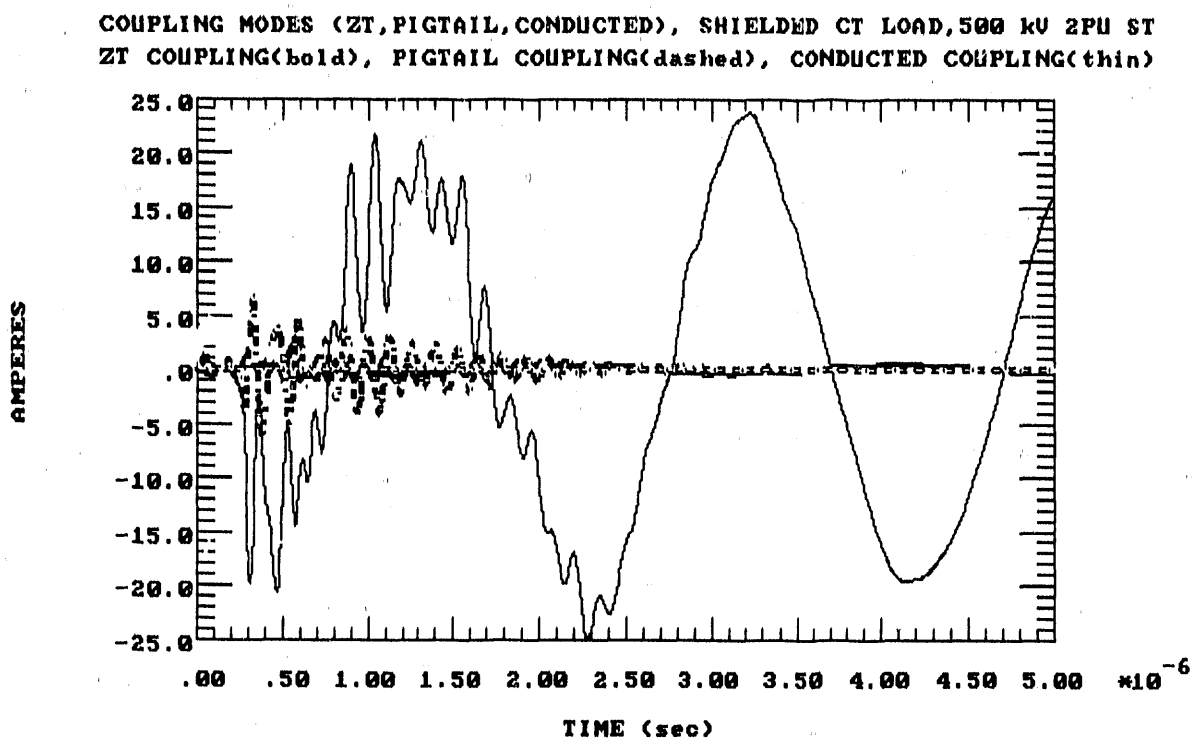

(a) Time-Domain Current Waveforms

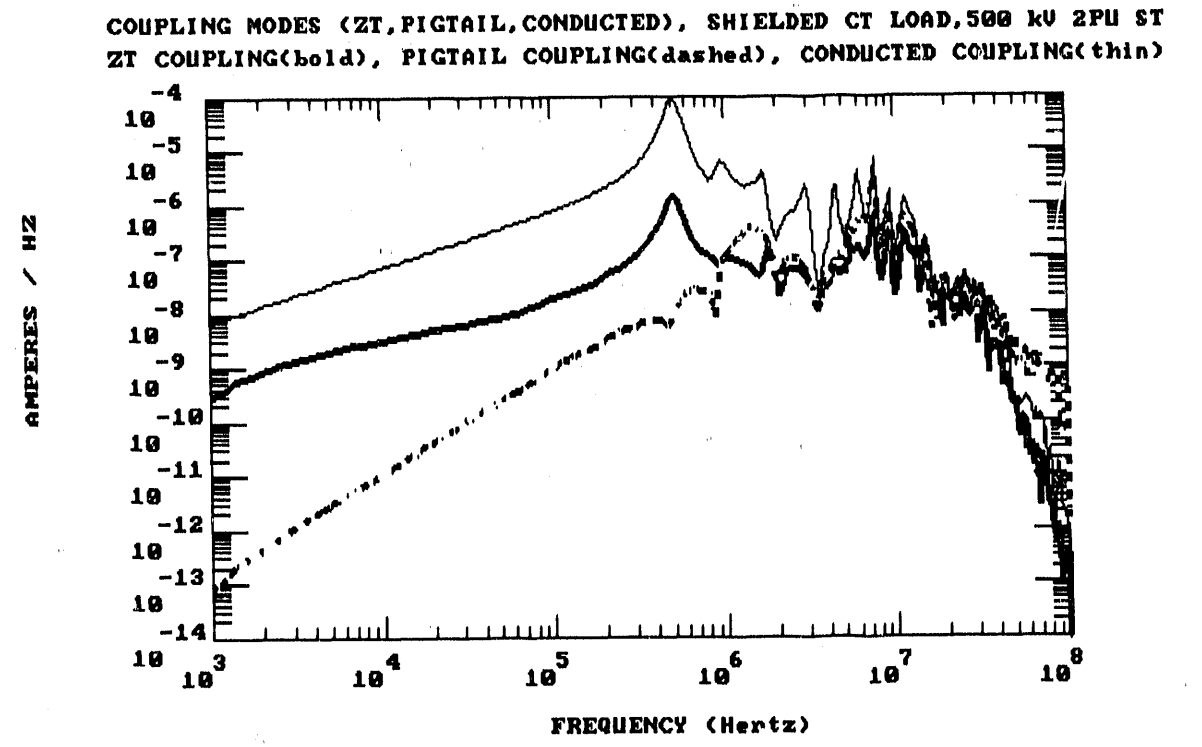

(b) Frequency-Domain Current Spectra

Figure 4.19. Coupling Modes for 500 kV 2 PU ST-Induced Transients, Shielded-Cable Loads, Measured CT Load Impedance: Transfer-Impedance Mode (Bold), Pigtail Mode (Dotted), Conducted Mode (Thin)

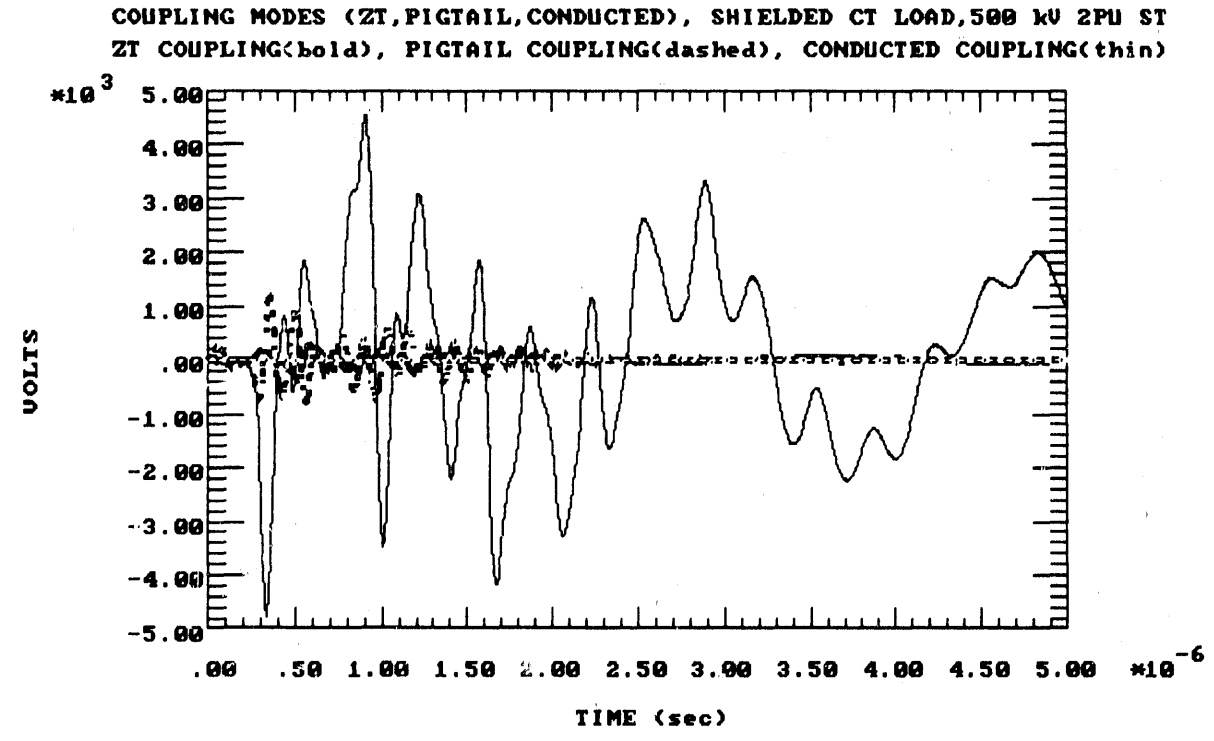

(c) Time-Domain Voltage Waveforms

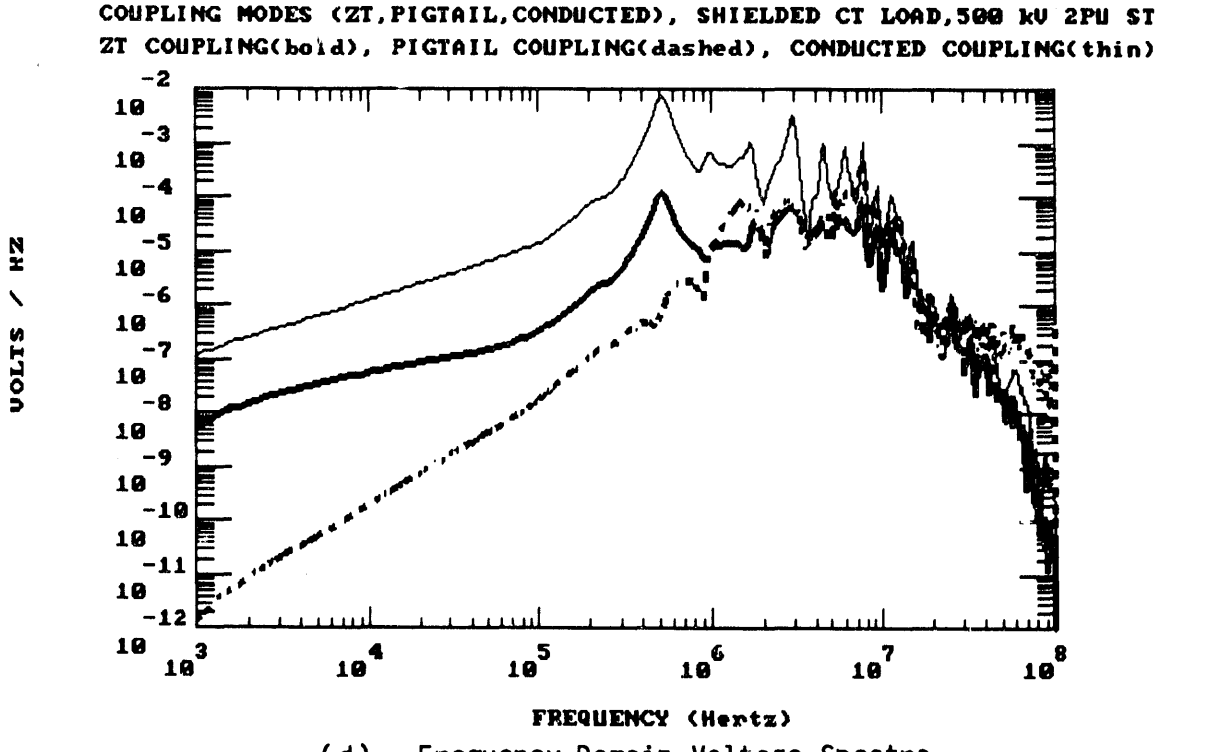

(d) Frequency-Domain Voltage Spectra

Figure 4.19 (Concluded). Coupling Modes for 500 kV 2 PU ST-Induced Transients, Shielded-Cable Loads, Measured CT Load Impedance: Transfer-Impedance Mode (Bold), Pigtail Mode (Dotted), Conducted Mode (Thin)

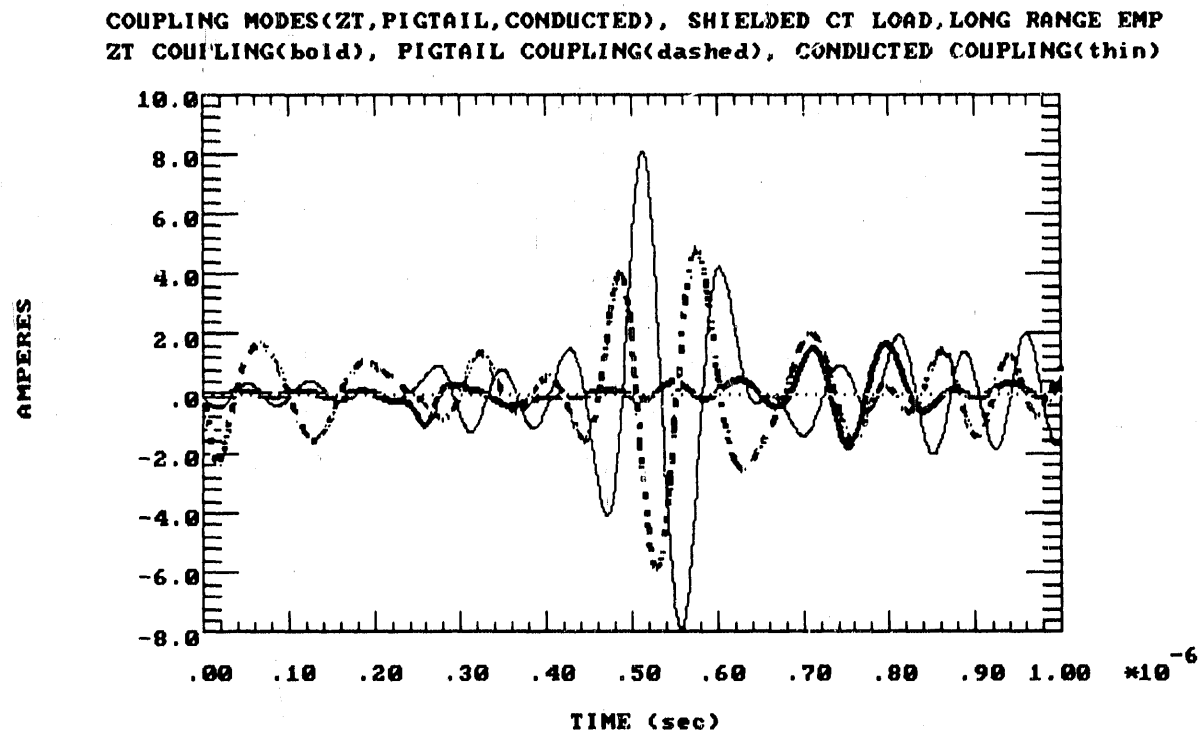

(a) Time-Domain Current Waveforms

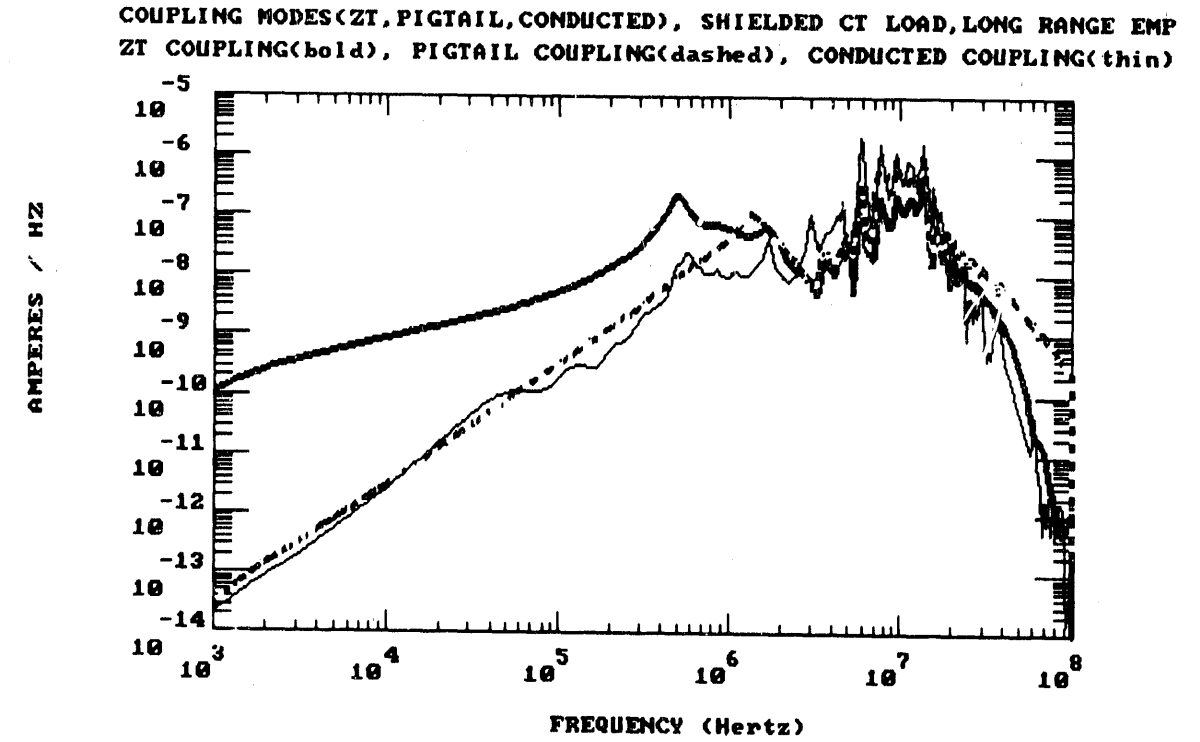

(b) Frequency-Domain Current Spectra

Figure 4.20. Coupling Modes for Long-Range HEMP-Induced Transients, Shielded-Cable Loads, Measured CT Load Impedance: Transfer-Impedance Mode (Bold), Pigtail Mode (Dotted), Conducted Mode (Thin)

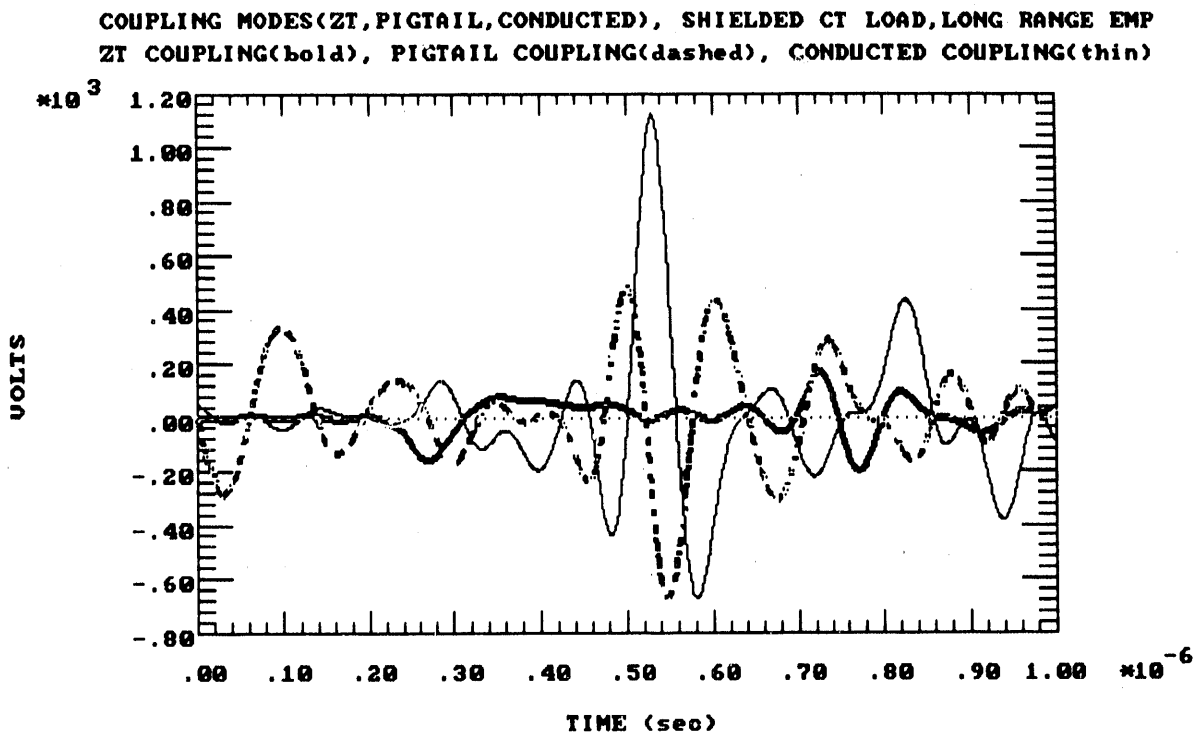

(c) Time-Domain Voltage Waveforms

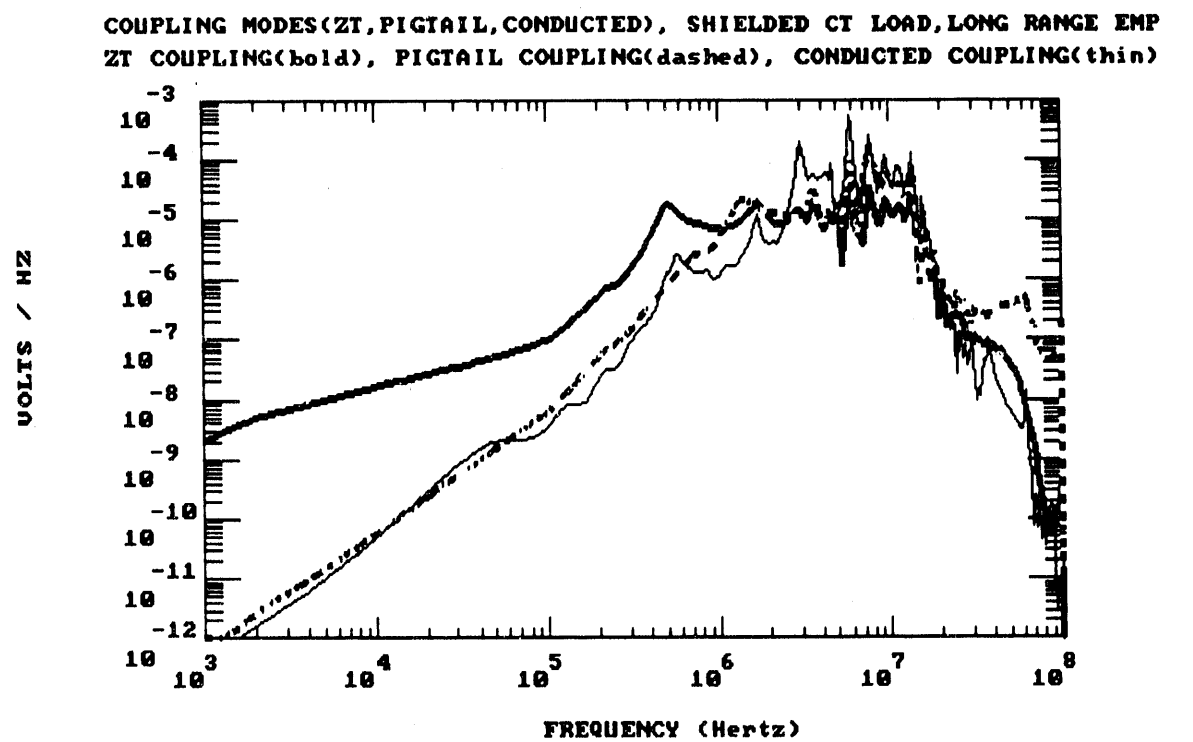

(d) Frequency-Domain Voltage Spectra

Figure 4.20 (Concluded). Coupling Modes for Long-Range HEMP-Induced Transients, Shielded-Cable Loads, Measured CT Load Impedance: Transfer-Impedance Mode (Bold), Pigtail Mode (Dotted), Conducted Mode (Thin)

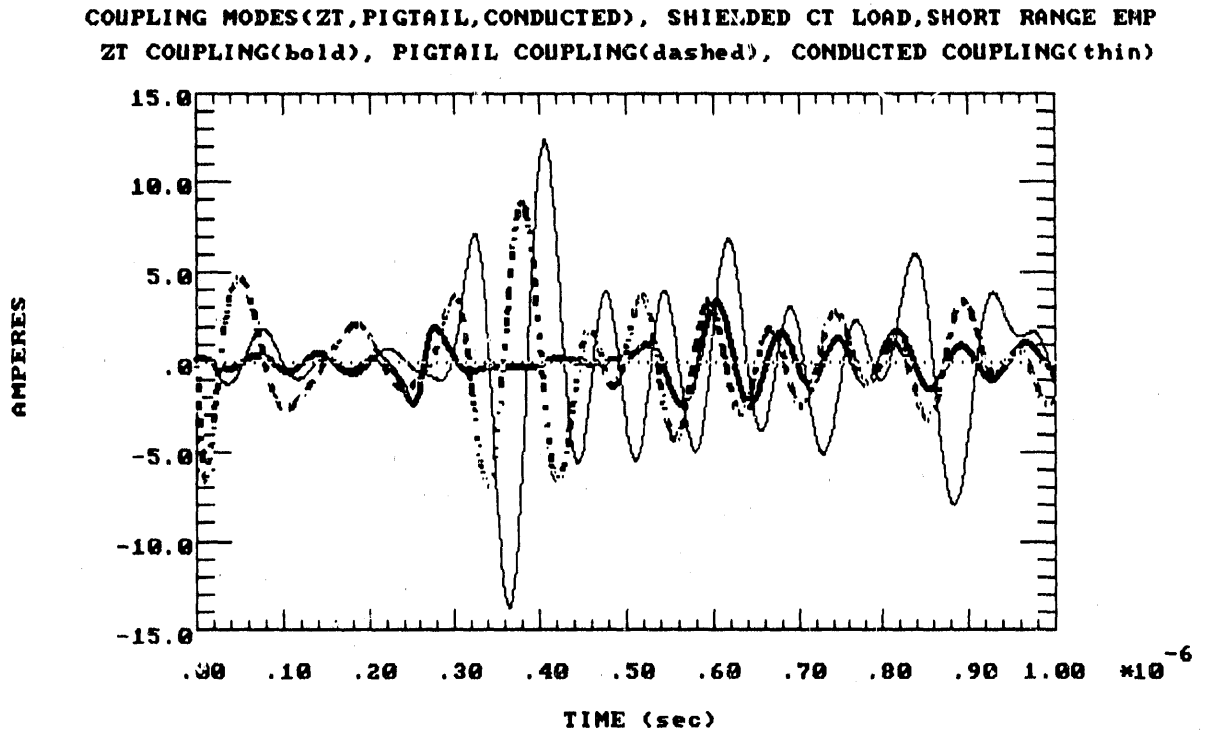

(a) Time-Domain Current Waveforms

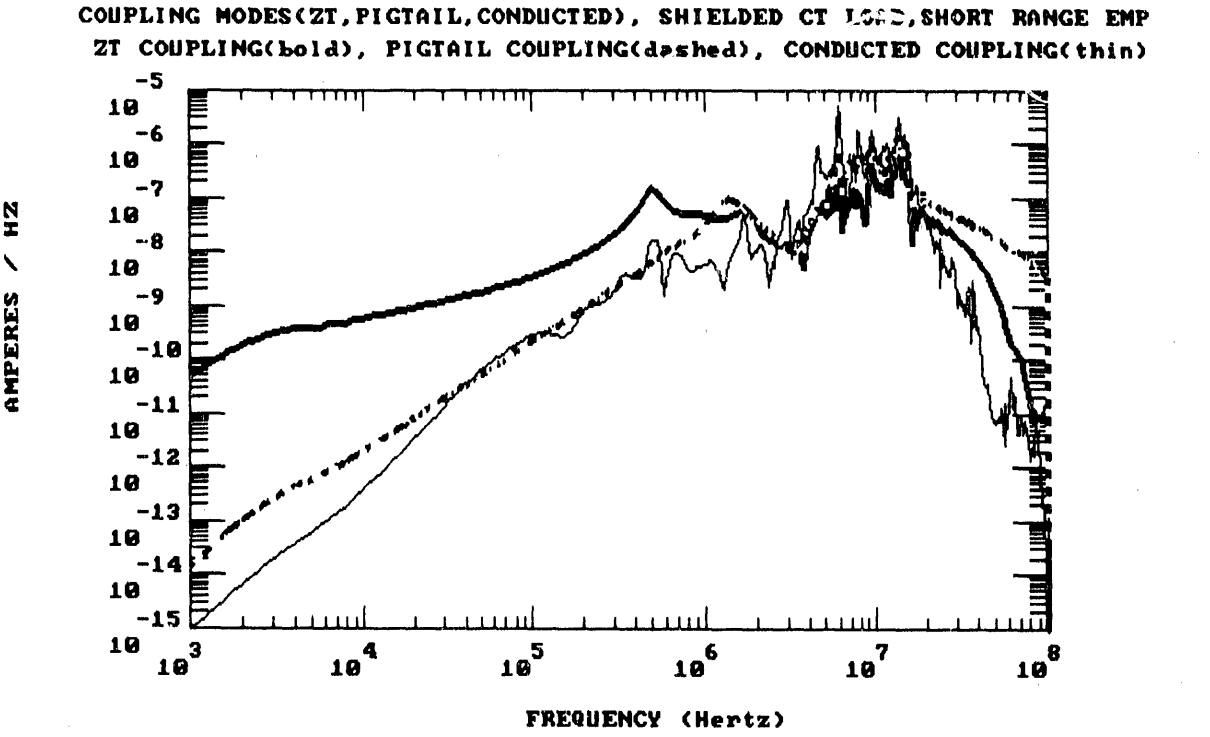

(b) Frequency-Domain Current Spectra

Figure 4.21. Coupling Modes for Short-Range HEMP-Induced Transients, Shielded-Cable Loads, Measured CT Load Impedance: Transfer-Impedance Mode (Bold), Pigtail Mode (Dotted), Conducted Mode (Thin)

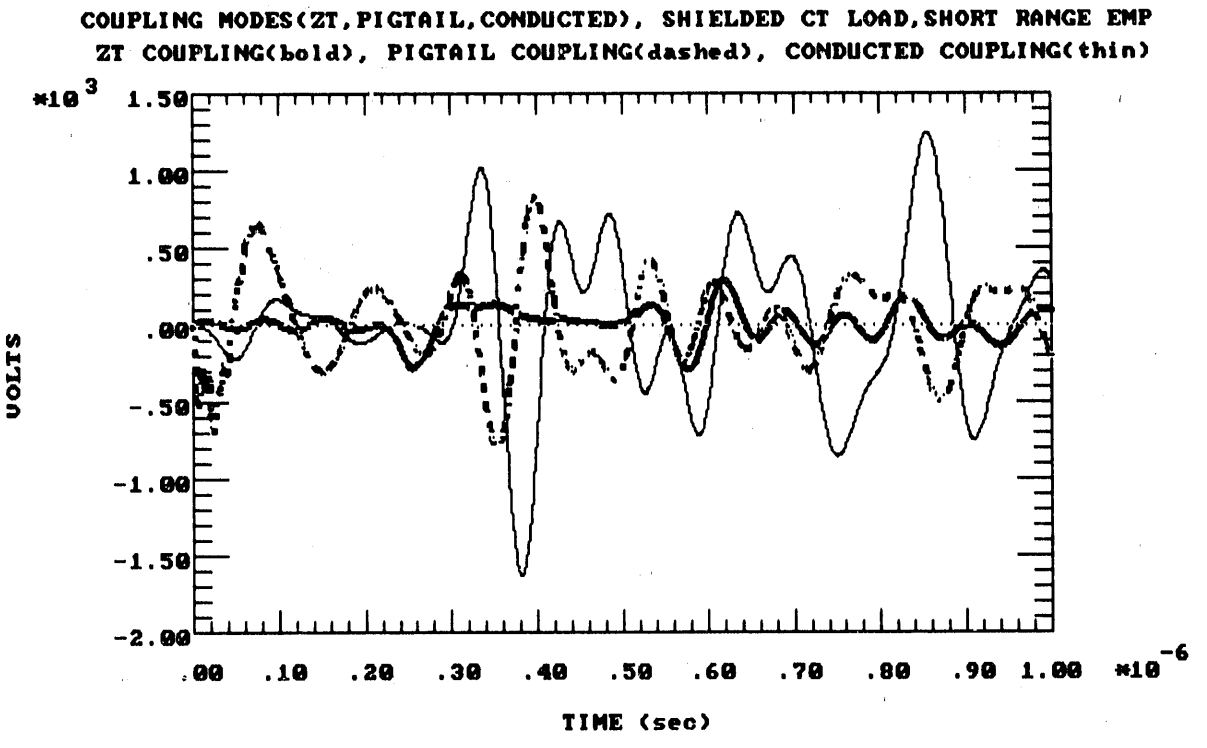

(c) Time-Domain Voltage Waveforms

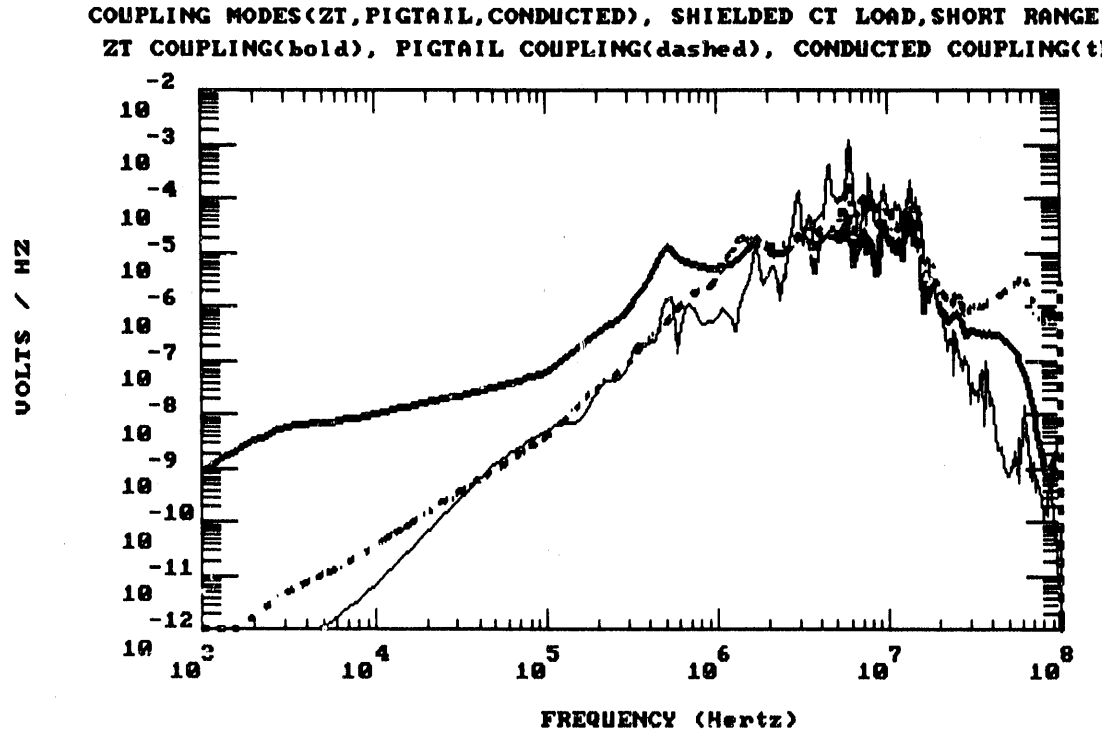

(d) Frequency-Domain Voltage Spectra

Figure 4.21 (Concluded). Coupling Modes for Short-Range HEMP-Induced Transients, Shielded-Cable Loads, Measured CT Load Impedance: Transfer-Impedance Mode (Bold), Pigtail Mode (Dotted), Conducted Mode (Thin)

Table 4.8. Norms for Transient Control-Wire Currents For Measured CT Lead Impedance, by Individual Coupling Modes

	500 kV 2 PU ST			Long-Range HEMP			Short-Range HEMP		
	Z_T Coupling	Pigtail Coupling	Conductd Coupling	Z_T Coupling	Pigtail Coupling	Conductd Coupling	Z_T Coupling	Pigtail Coupling	Conductd Coupling
0-Peak Amplitd.	1.99 A	6.44 A	25.0 A	1.79 A	5.84 A	8.07 A	3.38 A	8.90 A	13.7 A
Local Risetime	14 ns	20 ns	16 ns	13 ns	14 ns	15 ns	8.2 ns	3.8 ns	14 ns
Peak Deriv.	1.34E8 $\frac{A}{sec}$	3.83E8 $\frac{A}{sec}$	6.47E8 $\frac{A}{sec}$	1.29E8 $\frac{A}{sec}$	3.68E8 $\frac{A}{sec}$	5.79E8 $\frac{A}{sec}$	2.95E8 $\frac{A}{sec}$	1.15E9 $\frac{A}{sec}$	1.01E9 $\frac{A}{sec}$
Action Integral	7.91E-7 A^2sec	8.68E-6 A^2sec	9.26E-4 A^2sec	2.37E-7 A^2sec	2.64E-6 A^2sec	4.30E-6 A^2sec	9.61E-7 A^2sec	7.41E-6 A^2sec	1.55E-5 A^2sec

4.3.3 Unshielded-Cable Load Responses

Unshielded cable load responses were calculated for both ST and HEMP environments; for most of these computations only the measured relay DC battery-lead impedance, open circuit, and short circuit conditions were used for the load. DC lines (such as battery lines) are often unshielded in practice. The results for induced load current are shown in Figure 4.22 for a 500 kV 2 PU ST, a long-range HEMP event, and a short-range HEMP event; the corresponding spectra for all three situations are overlaid in Figure 4.23. The ST creates the largest peak load current, while the long-range HEMP produces the smallest peak current. The spectral plot indicates the ST-induced currents are dominant below about 4 MHz, while short-range HEMP-induced currents are dominant above about 80 MHz. The corresponding unshielded-wire voltage waveforms for all environments appear in Figure 4.24 and their spectra are compared in Figure 4.25; the ST again produces the largest peak amplitude, about 2.5 times that of the short-range HEMP-induced peak.

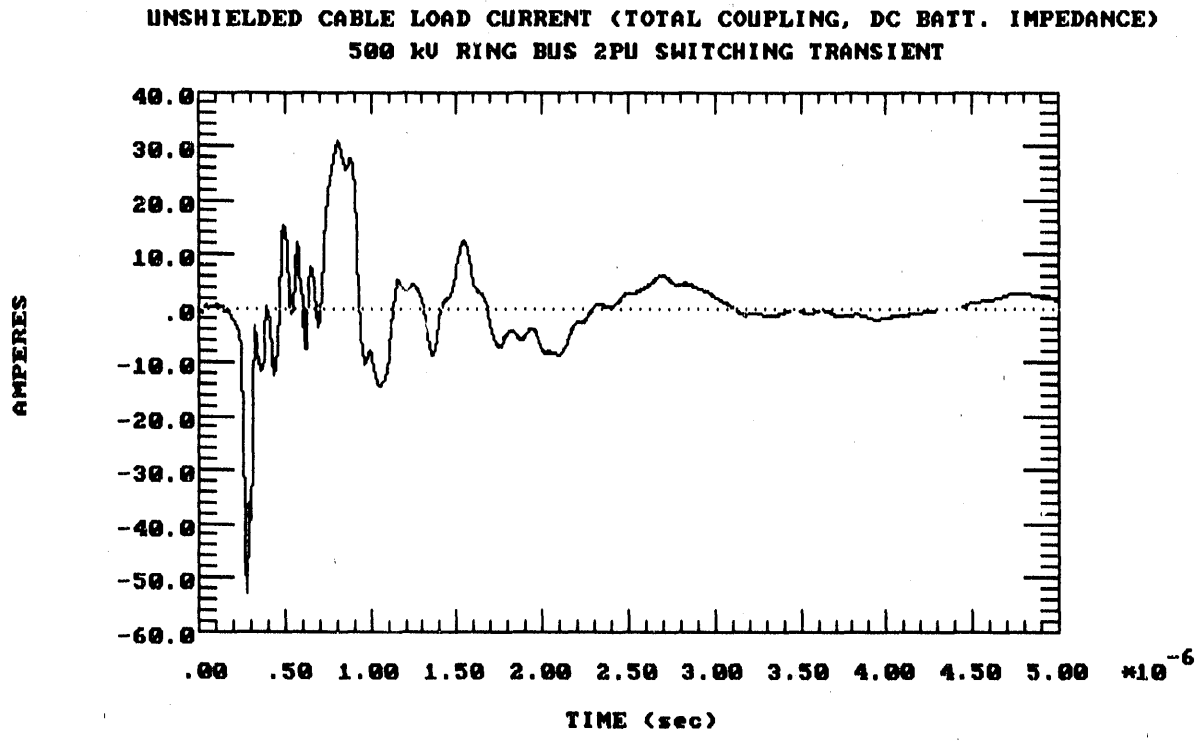

(a) 500 kV 2 PU Switching Transient

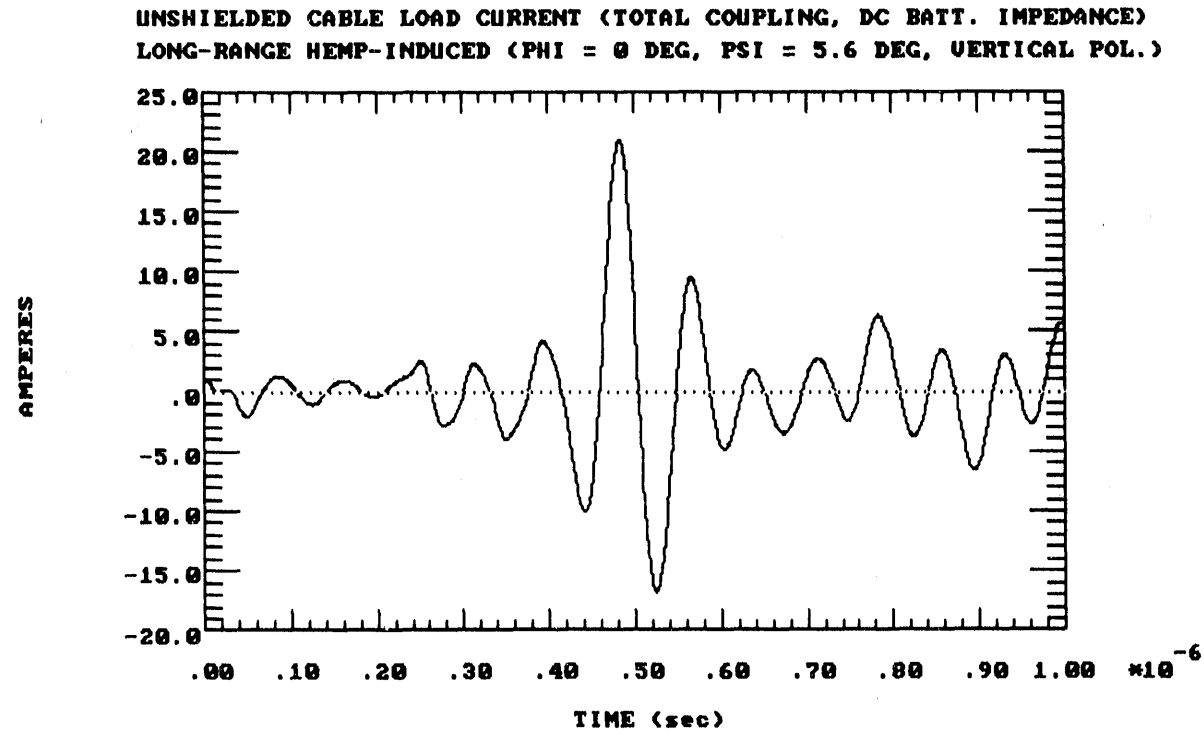

(b) Long-Range HEMP

Figure 4.22. Induced Current Waveforms for Unshielded Cable, Measured DC Batt.Load

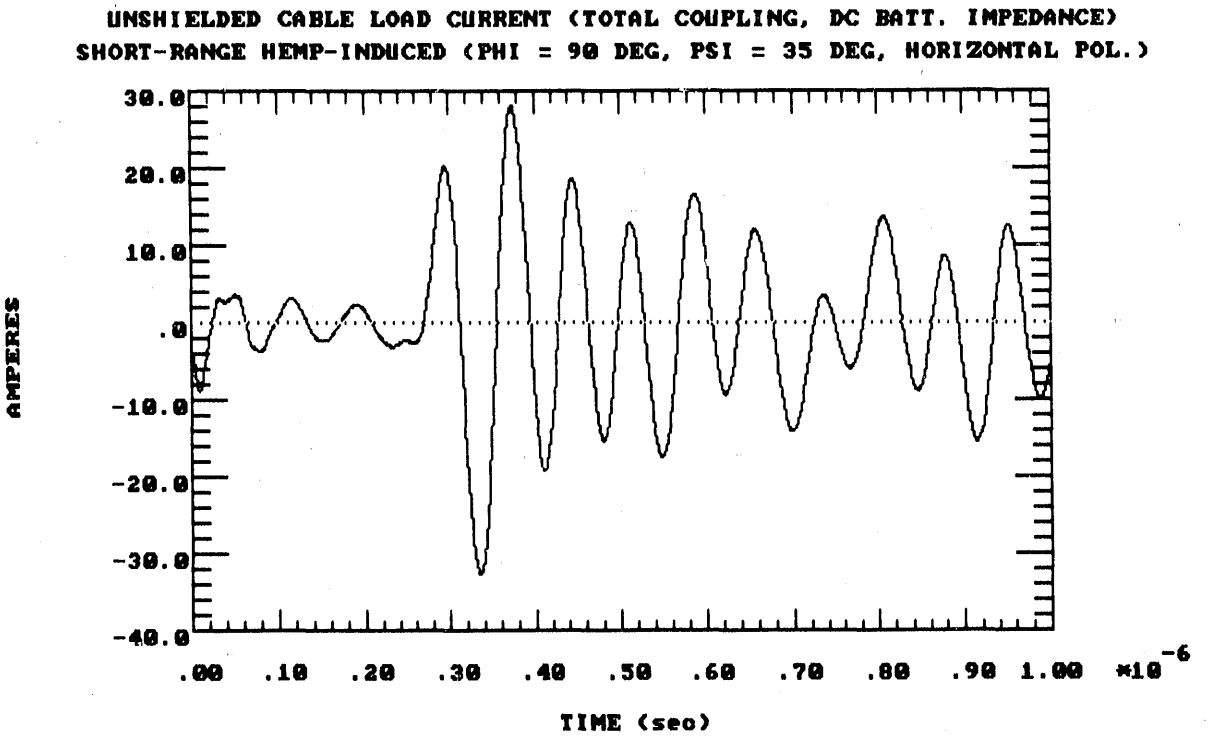

(c) Short-Range HEMP

Figure 4.22 (Concluded). Induced Current Waveforms for Unshielded Cable, Measured DC Batt.Load

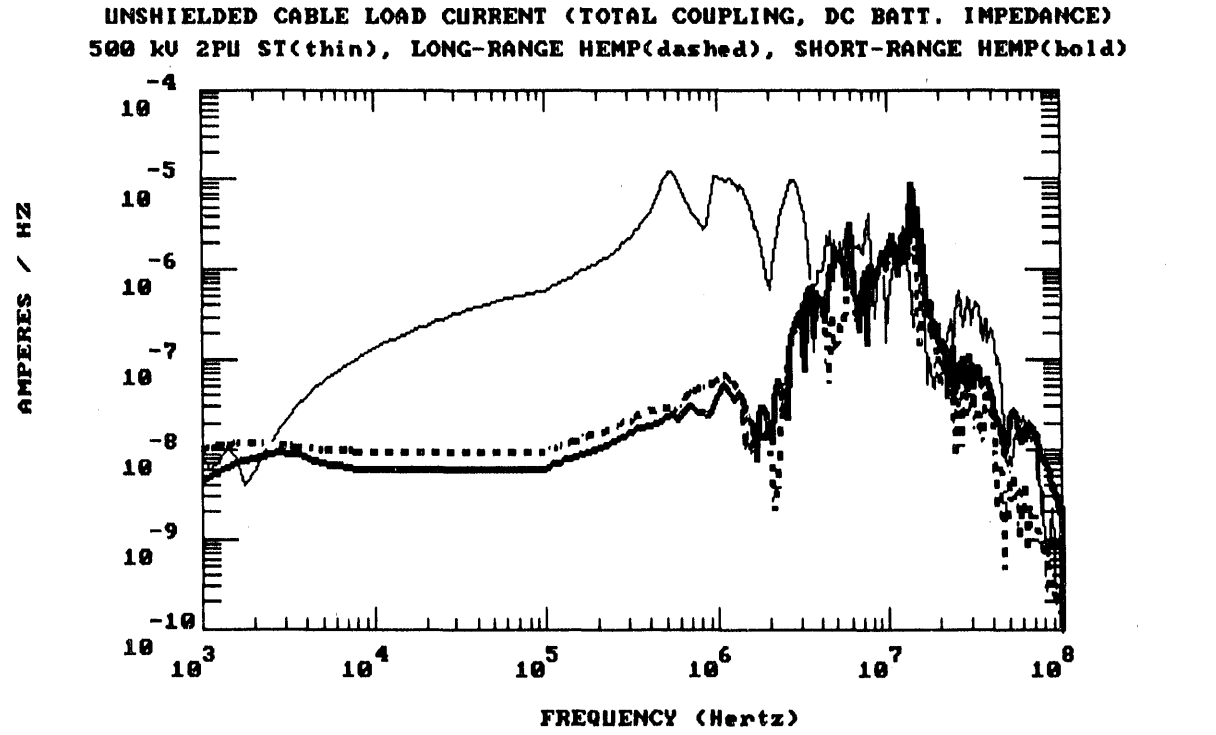

Figure 4.23. Induced Current Spectra for Unshielded Cable, Measured DC Batt.Load: 500 kV 2 PU ST (Thin), Long-Range HEMP (Dotted), Short-Range HEMP (Bold)

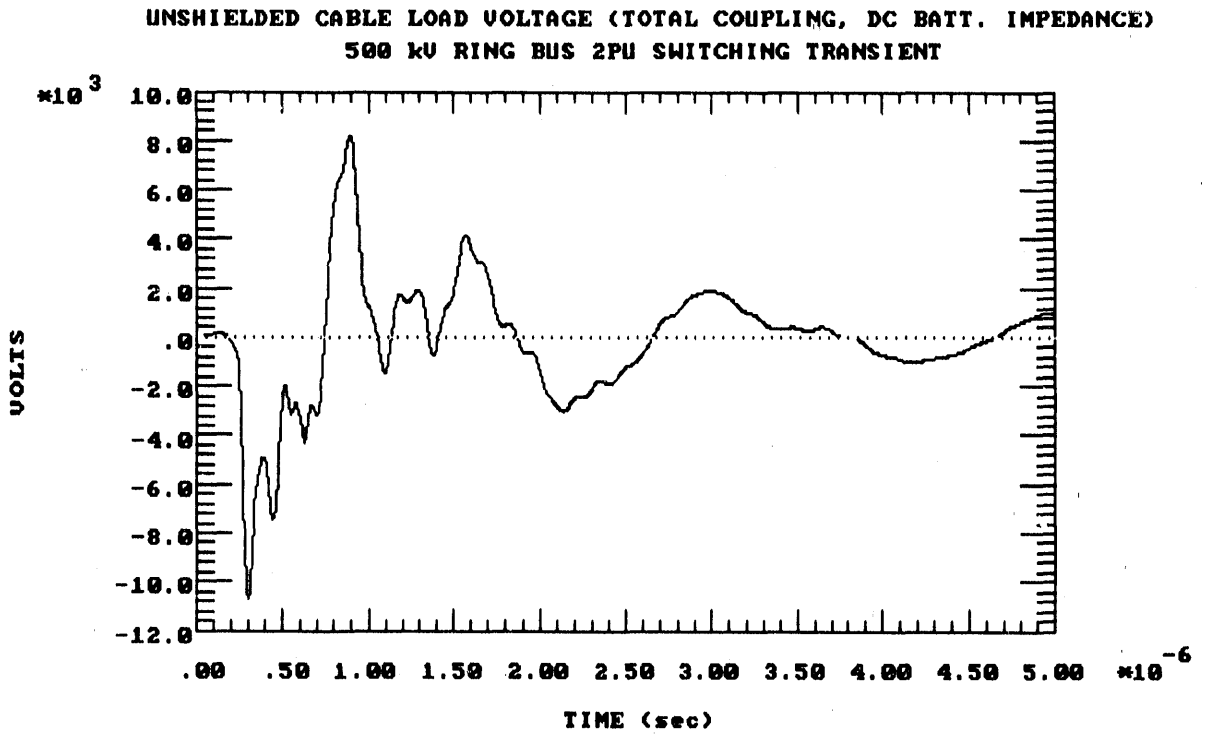

(a) 500 kV 2 PU Switching Transient

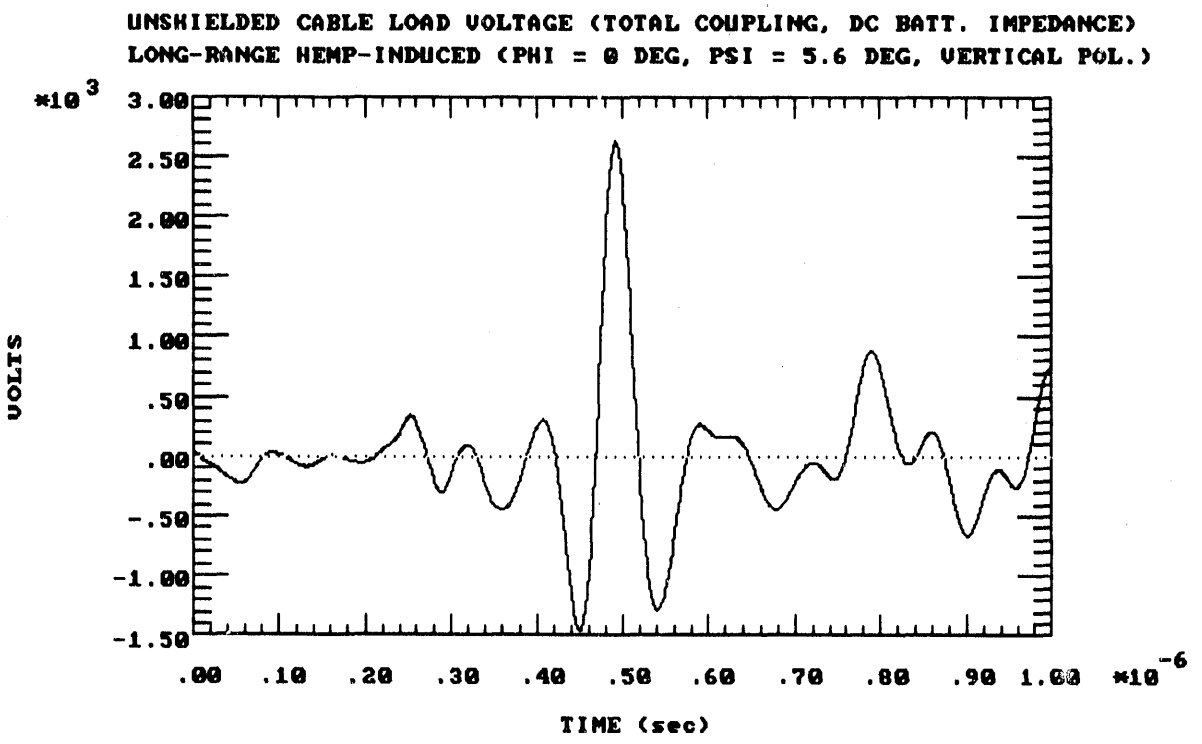

(b) Long-Range HEMP

Figure 4.24. Induced Voltage Waveforms for Unshielded Cable, Measured DC Batt.Load

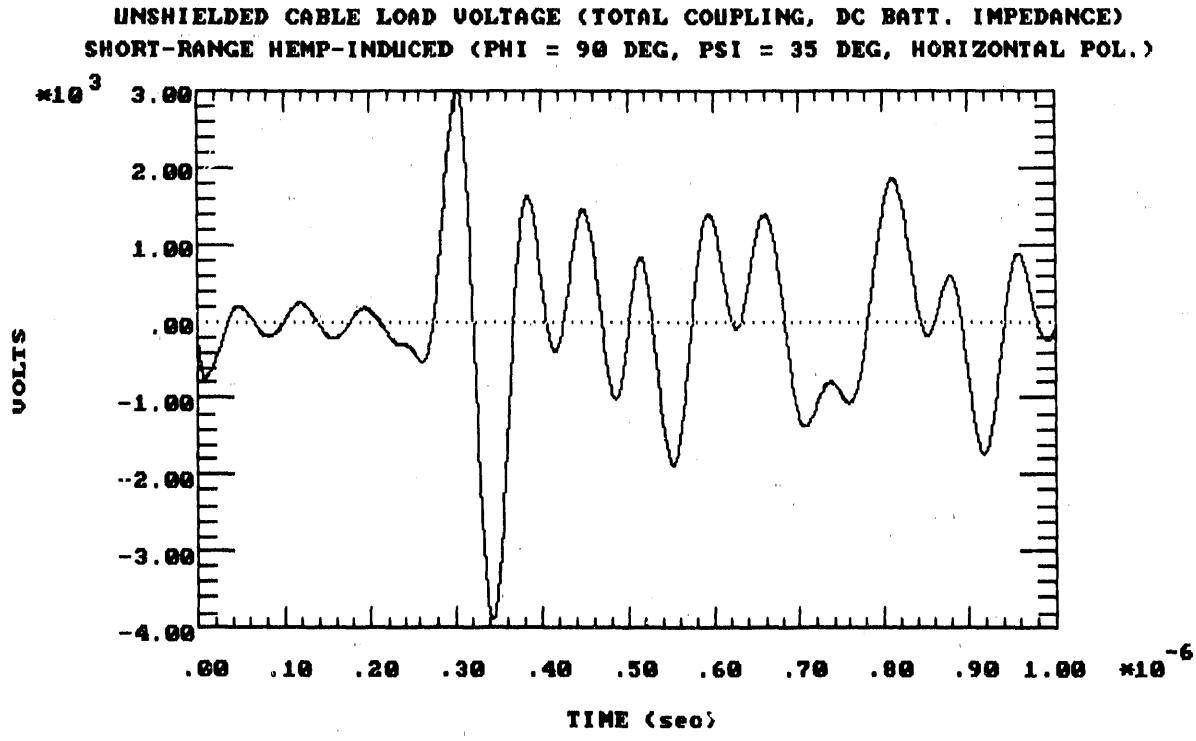

(c) Short-Range HEMP

Figure 4.24 (Concluded). Induced Voltage Waveforms for Unshielded Cable, Measured DC Batt.Load

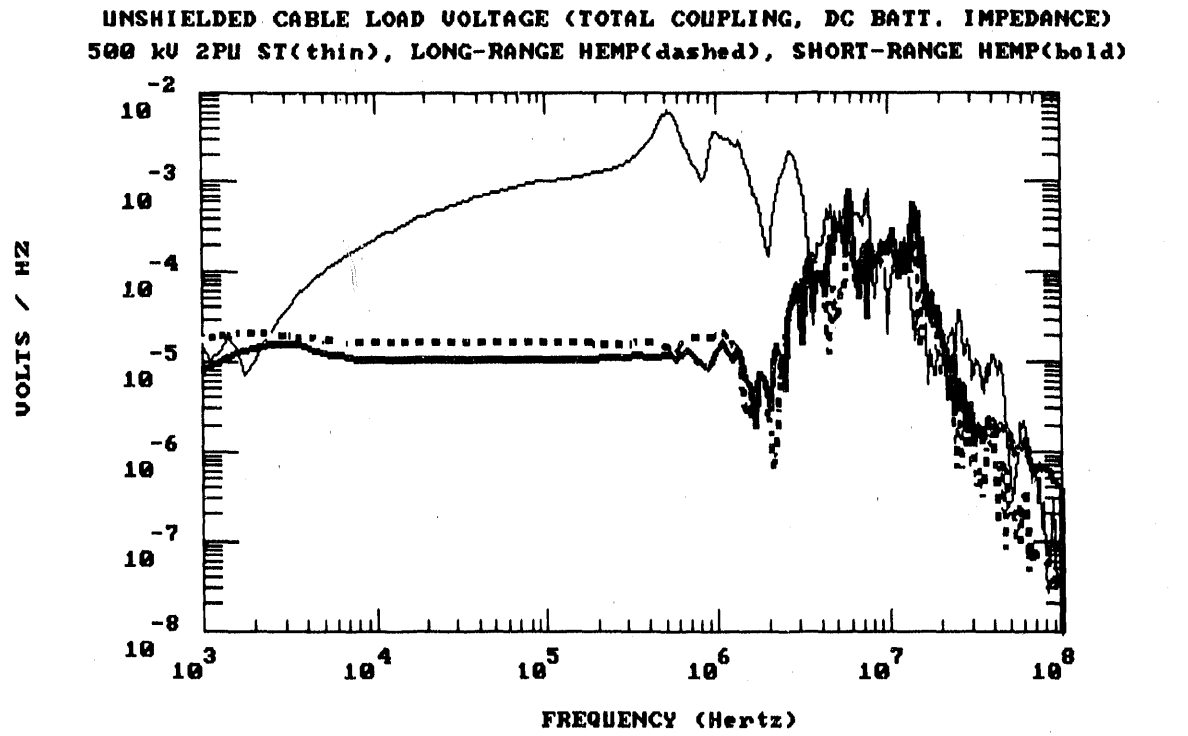

Figure 4.25. Induced Voltage Spectra for Unshielded Cable, Measured DC Batt.Load: 500 kV 2 PU ST (Thin), Long-Range HEMP (Dotted), Short-Range HEMP (Bold)

Norms for unshielded-wire currents and voltages are given in Table 4.9. The ST is responsible for the greatest peak amplitudes, peak derivatives, and action integrals. For all environments, the unshielded cable responses are greater than those for shielded cables, as shown by comparison of Tables 4.9 and 4.6.

Table 4.9. Norms for Unshielded Wire Currents and Voltages For Measured DC Battery Lead Impedance

	500 kV 2 PU ST		Long-Range HEMP		Short-Range HEMP	
	Wire Current	Wire Voltage	Wire Current	Wire Voltage	Wire Current	Wire Voltage
Zero-Peak Amplitude	53.0 A	10.7 kV	20.9 A	2.62 kV	32.5 A	3.88 kV
Local Risetime	9.0 ns	17 ns	13 ns	13 ns	13 ns	13 ns
Peak Derivative	2.76E9 $\frac{A}{sec}$	3.25E11 $\frac{V}{sec}$	1.47E9 $\frac{A}{sec}$	1.54E11 $\frac{V}{sec}$	2.56E9 $\frac{A}{sec}$	2.64E11 $\frac{V}{sec}$
Action Integral	3.13E-4 A^2sec	29.3 V^2sec	2.47E-5 A^2sec	0.32 V^2sec	1.04E-4 A^2sec	1.10 V^2sec

Unshielded cable responses were also calculated for open and short circuit load conditions. Figures 4.26 - 4.28 show the unshielded cable open circuit voltage and short circuit current response for ST and HEMP drives. These responses are compared to the SWC fast transient waveform in subsection 4.3.4.

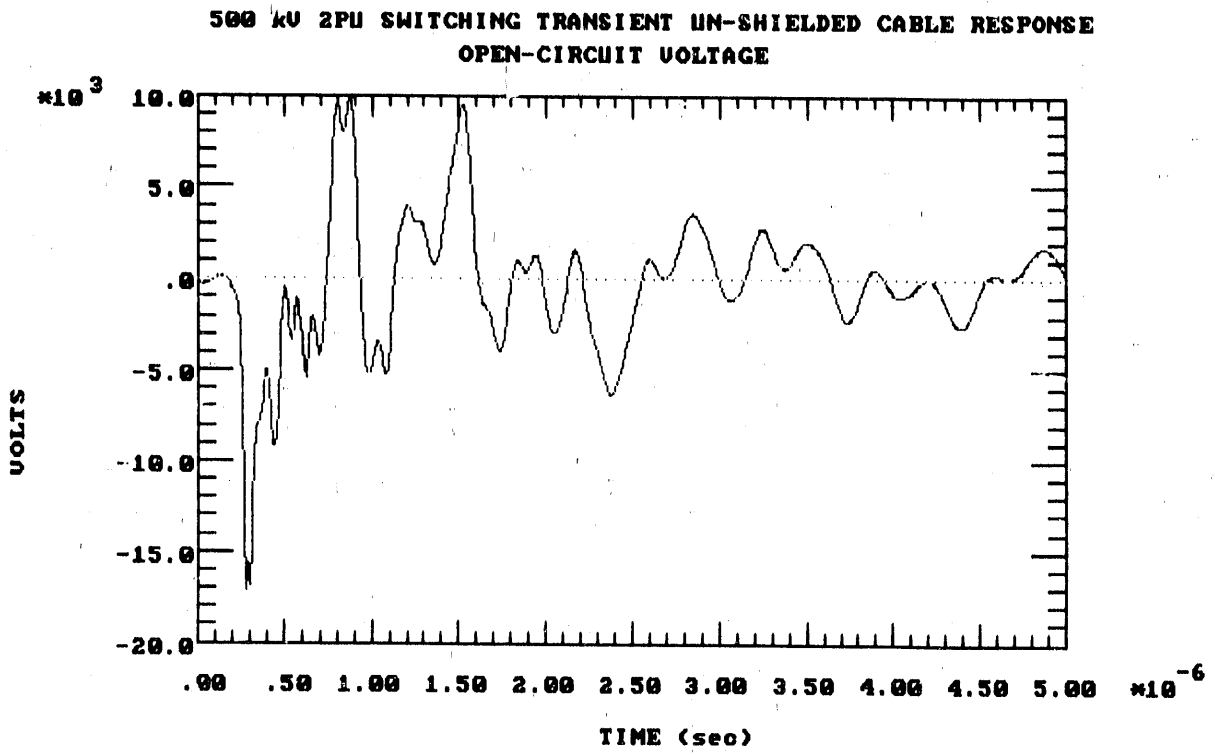

(a) Open Circuit Voltage

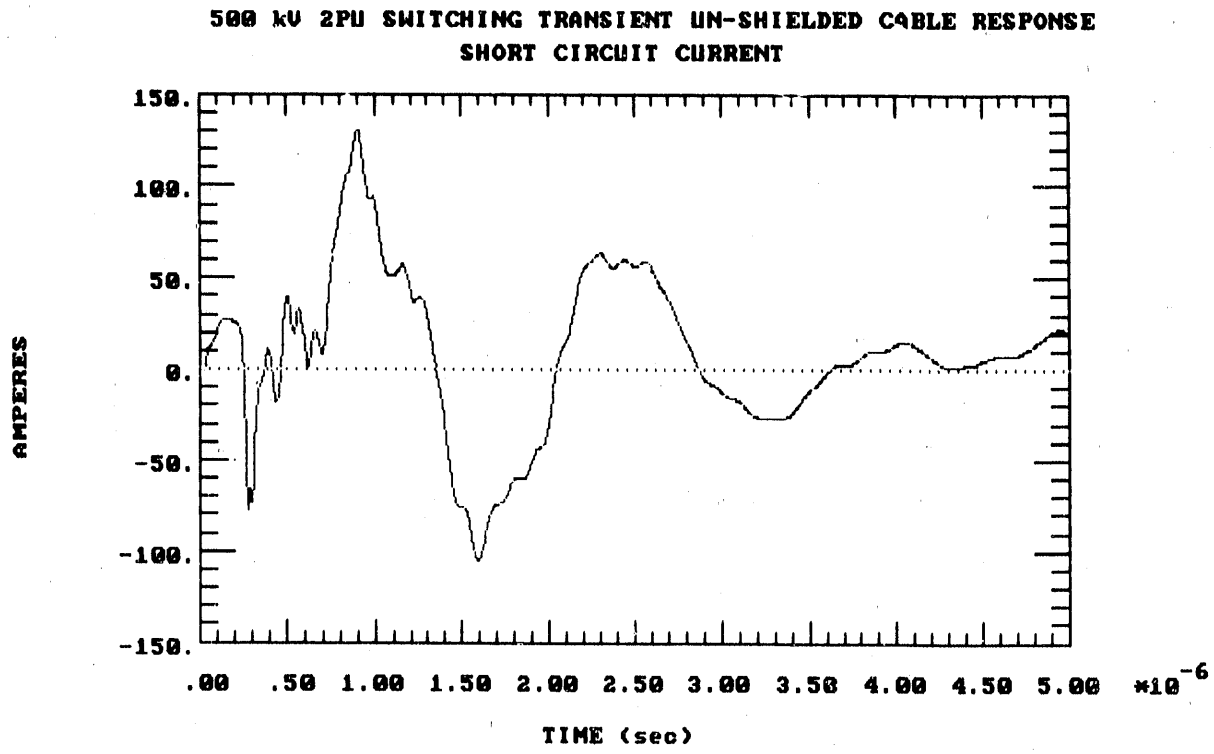

(b) Short Circuit Current

Figure 4.26. 500 kV 2 PU ST Unshielded Cable Open and Short Circuit Load Response

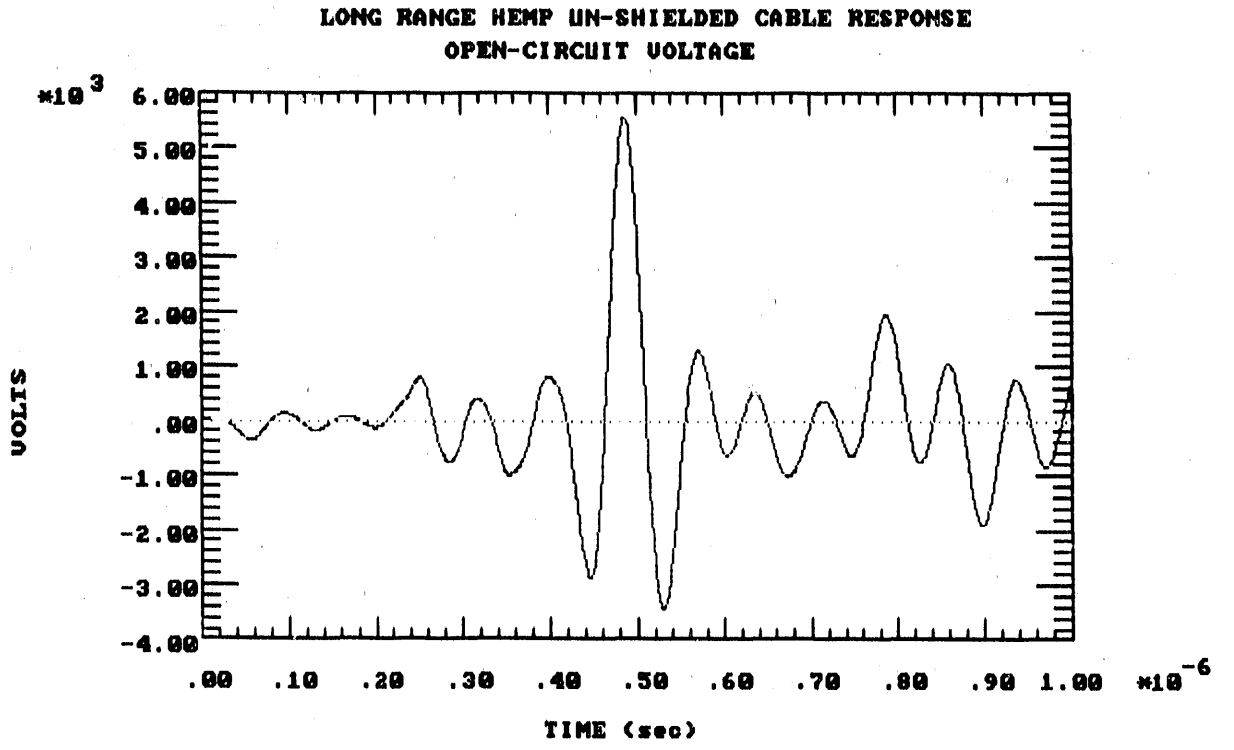

(a) Open Circuit Voltage

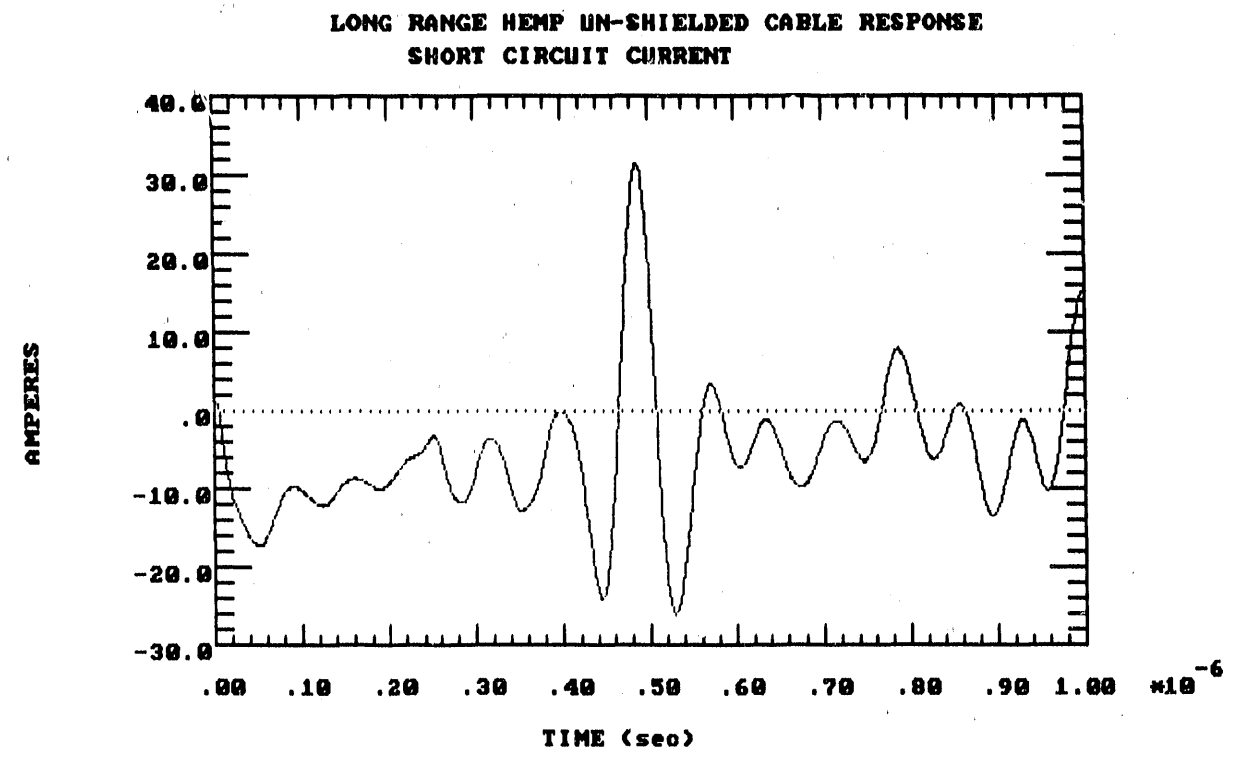

(b) Short Circuit Current

Figure 4.27. Long-Range HEMP Unshielded Cable Open and Short Circuit Load Response

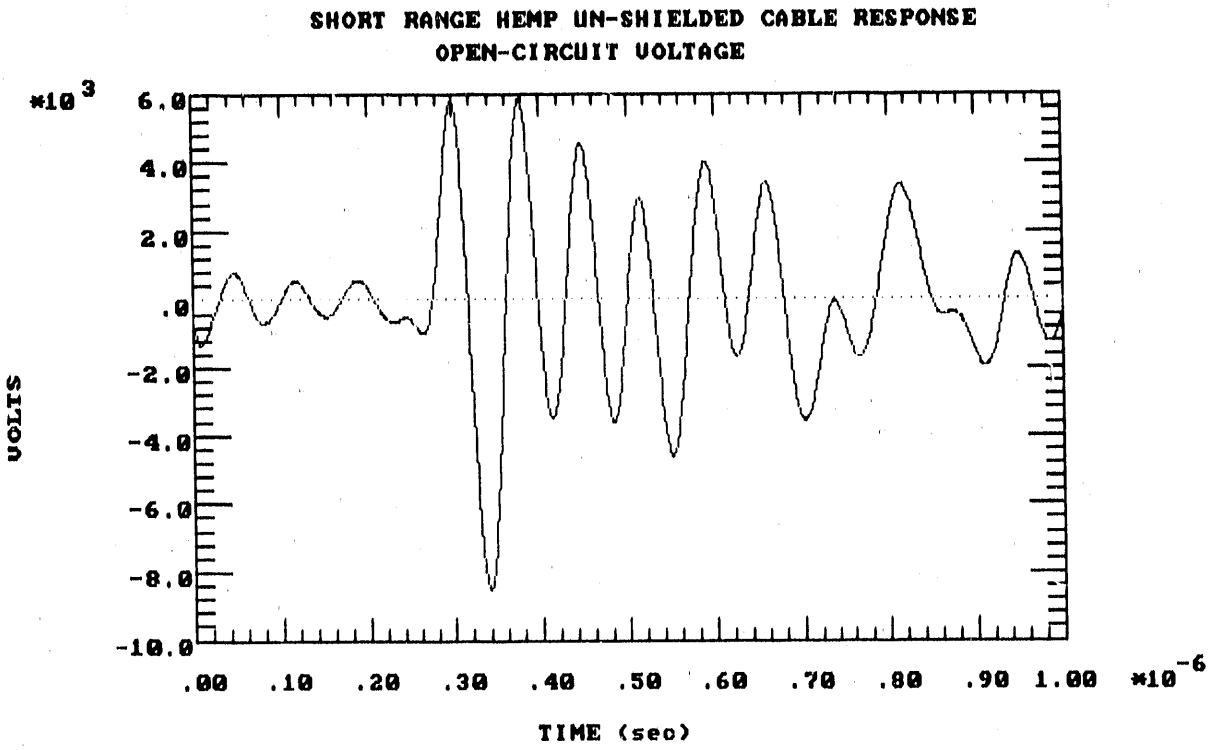

(a) Open Circuit Voltage

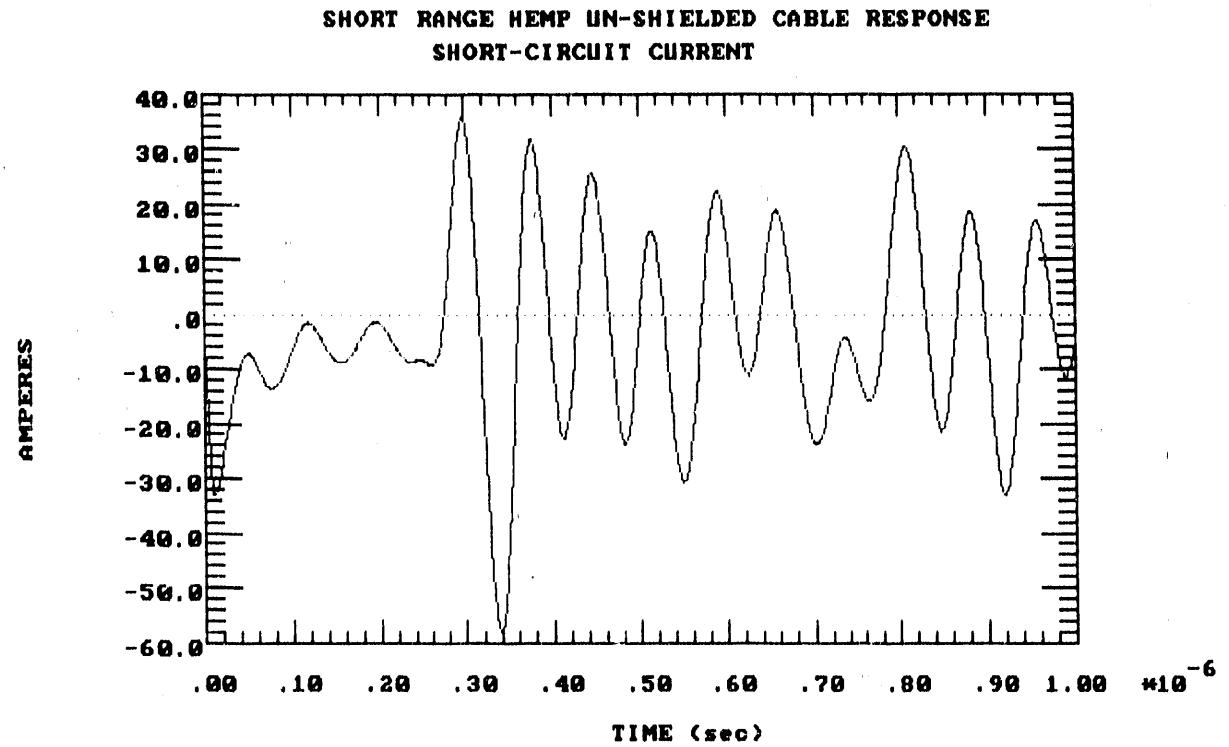

(b) Short Circuit Current

Figure 4.28. Short-Range HEMP Unshielded Cable Open and Short Circuit Load Response

4.3.4 Comparison of Cable Responses With SWC Fast Transient

The open and short circuit load responses of shielded and unshielded cables to ST and HEMP drives were compared with the SWC fast transient test waveform specified by IEEE/ANSI C37.90.1 [10]. The fast transient test waveform is specified in terms of an open circuit voltage as depicted in Figure 4.29(a). The equivalent representation of the fast transient as a short circuit current test waveform is shown in Figure 4.29(b).

Frequency spectra for open circuit voltage responses of shielded cables for 2 PU 500 kV ST, short-range HEMP, and the fast transient SWC are compared in Figure 4.30(a). Corresponding short circuit current comparisons for shielded cables are presented in Figure 4.30(b). As seen from Figure 4.30(a), the fast transient SWC appears to provide an upper bound of both ST and short-range HEMP open circuit voltage below 300 kHz. Between 300 kHz and 10 MHz, the ST open circuit voltage is highest, while short-range HEMP dominates above 10 MHz. In terms of short circuit current on shielded cables, Figure 4.30(b) shows that SWC amplitudes dominate at frequencies below 400 kHz and above 17 MHz. Between these frequencies, ST dominates in the lower range, while short-range HEMP begins to dominate between 10 - 17 MHz.

Comparisons of open circuit voltage and short circuit current responses of unshielded cables to 500 kV 2PU ST and short-range HEMP drives with the fast transient SWC waveform are provided in Figure 4.31. The ST open circuit voltage exceeds the SWC at all frequencies up to 40 MHz; above 40 MHz the fast transient bounds all responses. Between 4 MHz and 20 MHz, the short-range HEMP open circuit voltage response is highest. The fast transient bounds HEMP well at frequencies below 3 MHz. Results are similar when comparing short circuit currents (Figure 4.30(b)).

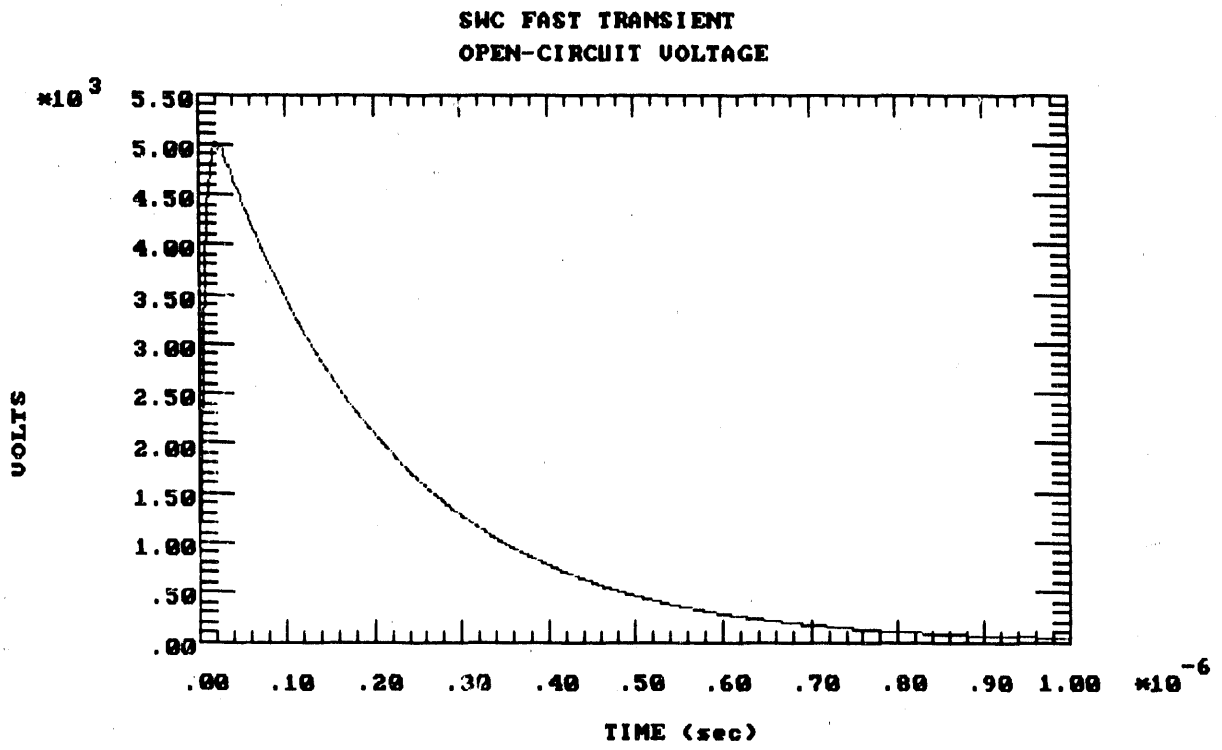

(a) Open Circuit Voltage

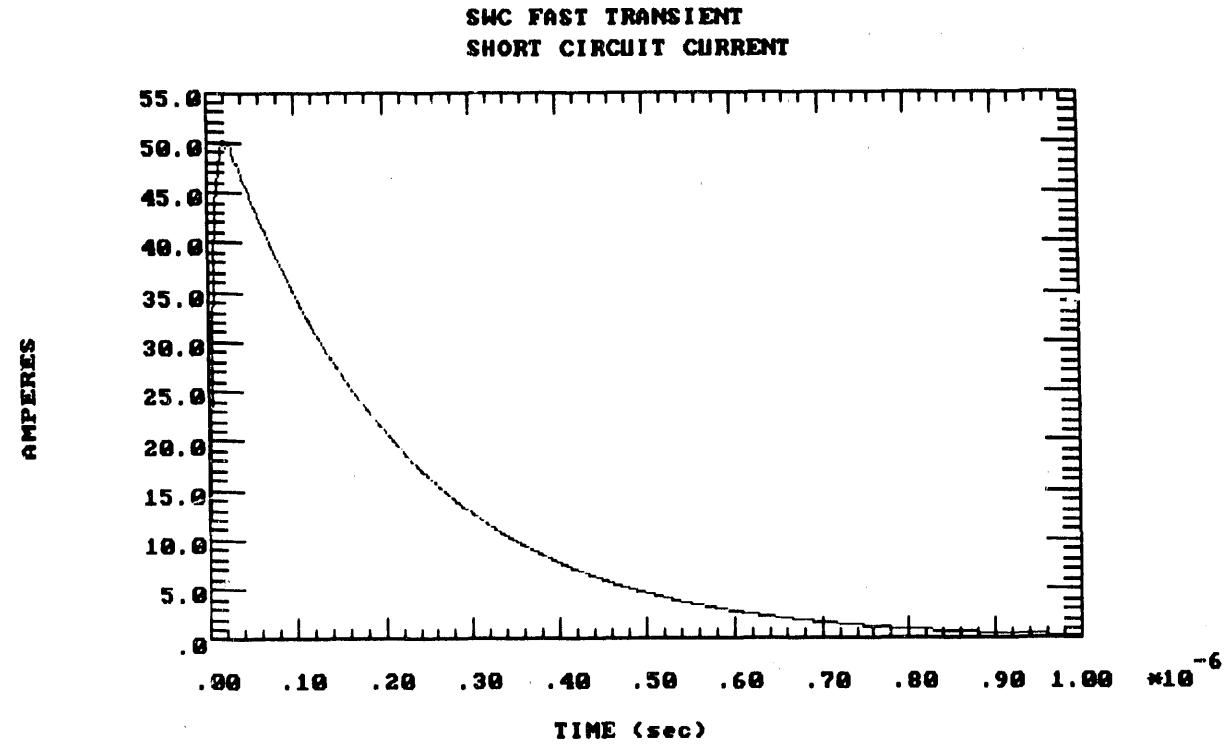

(b) Short Circuit Current

Figure 4.29. Relay Surge Withstand Capability Fast Transient Test Waveform Specified by IEEE/ANSI C37.90.1-1989

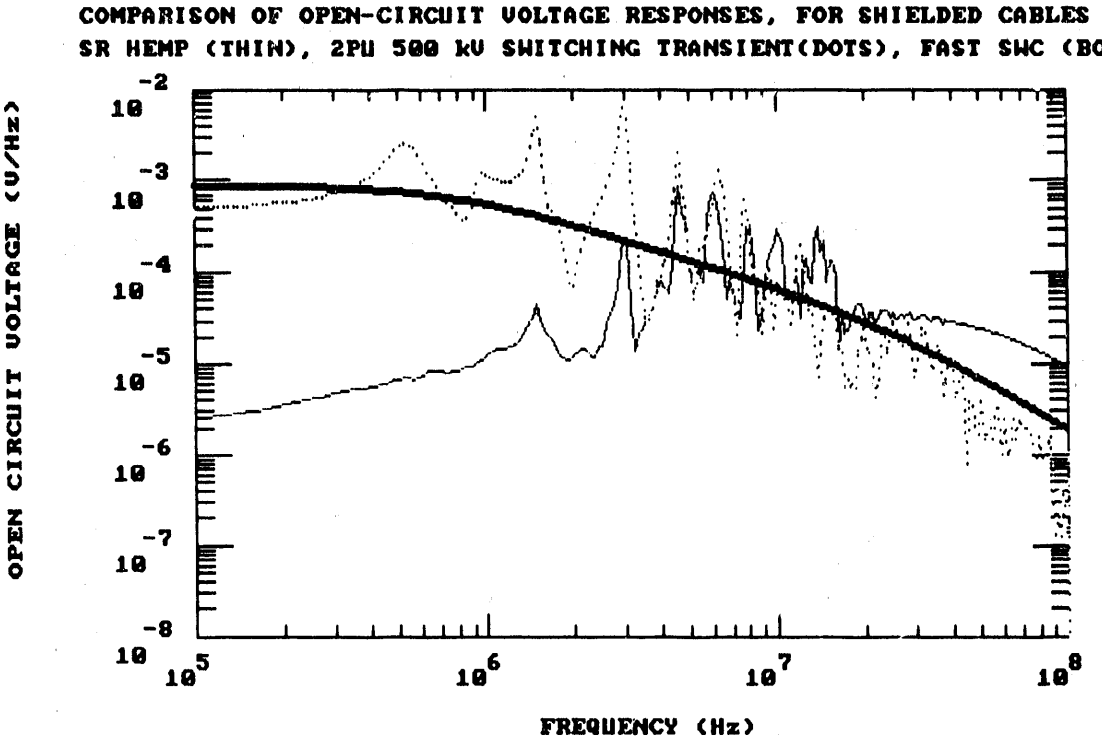

(a) Comparing Open Circuit Voltage Spectra

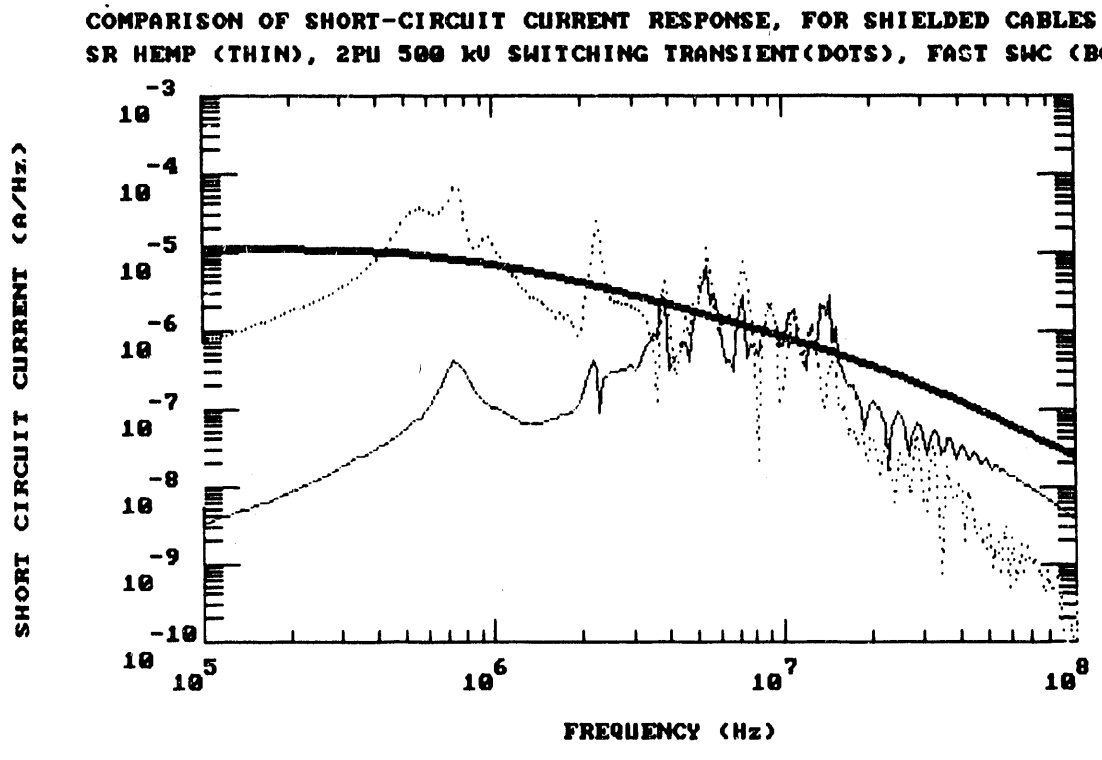

(b) Comparing Short Circuit Current Spectra

Figure 4.30. Comparing Shielded Cable Open and Short Circuit Responses to 500 kV 2 PU ST and Short-Range HEMP Drives with the SWC Fast Transient

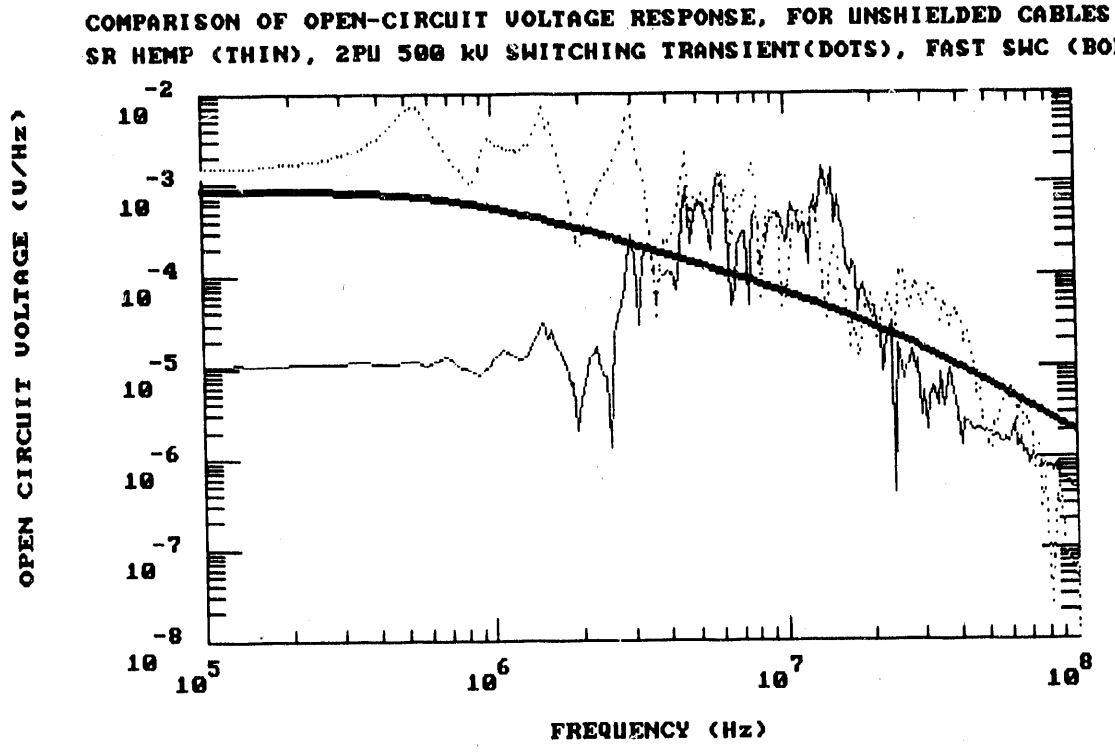

(a) Comparing Open Circuit Voltage Spectra

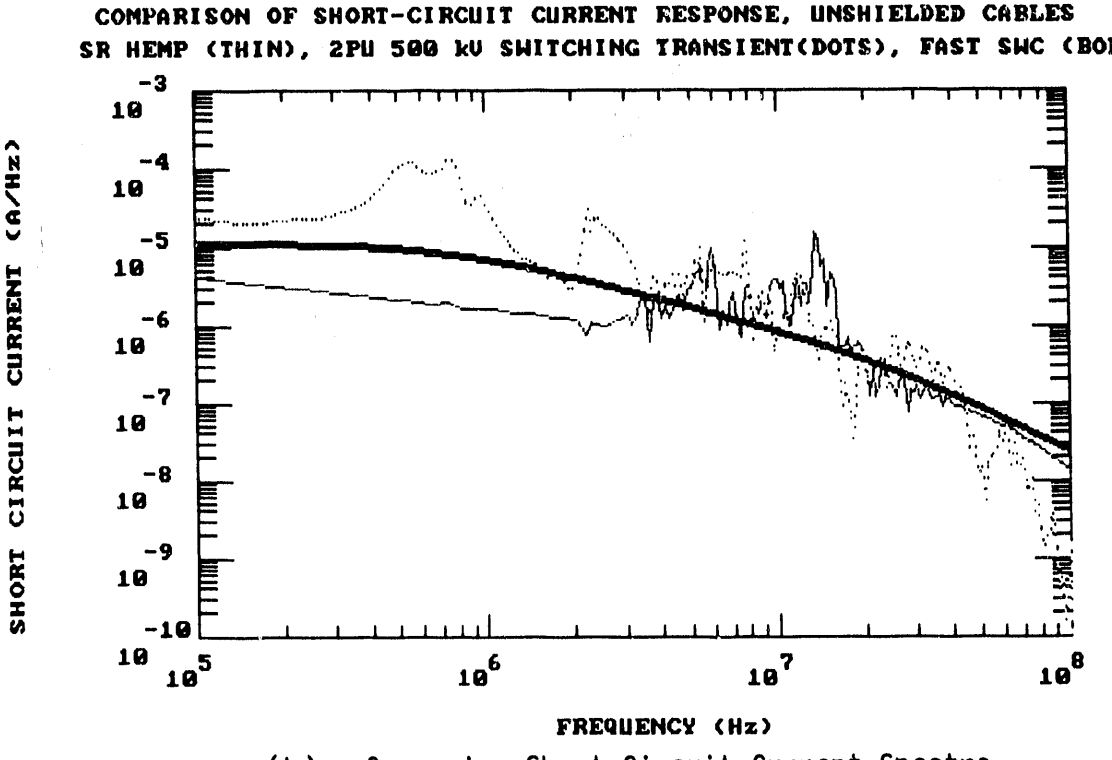

(b) Comparing Short Circuit Current Spectra

Figure 4.31. Comparing Unshielded Cable Open and Short Circuit Responses to 500 kV 2 PU ST and Short-Range HEMP Drives with the SWC Fast Transient

4.3.5. Summary and Comparisons

Table 4.10 summarizes and compares peak load currents and voltages for individual coupling modes for each type of drive and measured cable load impedance condition for shielded and unshielded cables. The relative importance of individual coupling modes and load impedances can be determined from Table 4.10. For example, the conducted coupling mode dominates all other modes (E- and H-field driven transfer impedance and pigtail coupling). Furthermore, conducted coupling is the same for shielded and unshielded cables (i.e, it is not reduced by shielding the cable). The effectiveness of the shield in reducing field-driven coupling can be seen by comparing total currents and voltages for the shielded cable to those of the unshielded cable. Conducted coupling clearly dominates the total coupling to shielded cables, whereas it accounts for about 30 - 40 % of the total coupling to unshielded cables. For shielded cables, the next most important coupling mode is H-field driven pigtail coupling. Pigtail coupling scales directly with the pigtail length, so a pigtail longer than the 12" used here would increase this contribution. Also, in general, the H-field driven coupling modes are more significant than those driven by the E-field. The CT-lead load impedance responses are highest for all drives. Comparing responses to the different environments, conducted coupling is most severe for switching transients. For E-field transfer impedance and pigtail coupling modes, however, the current and voltage responses to short range HEMP are larger than those to 2PU switching transients. For H-field transfer impedance and pigtail coupling modes, the current responses to short range HEMP are larger than those to 2PU switching transients, and the voltage responses are comparable.

Table 4.10. Load Currents and Voltages for Individual Coupling Modes

0-PEAK	2 PU SWITCHING TRANSIENT			LONG RANGE HEMP			SHORT RANGE HEMP		
	150 Ω	CT LEAD	DC BATT	150 Ω	CT LEAD	DC BATT	150 Ω	CT LEAD	DC BATT
COND. COUP.	24.2 A 3.62 kV	25.0 A 4.76 kV	19.0 A 4.62kV	6.66 A 1.00 kV	8.07 A 1.12 kV	7.47 A 1.00 kV	9.98 A 1.50 kV	13.7 A 1.64 kV	11.7 A 1.46 kV
I-SHIELD (H)	<--	116 A	-->	<--	42.1 A	-->	<--	66.8 A	-->
ZT (H)	2.06 A 310 V	1.92 A 354 V	1.95 A 368 V	1.31 A 196 V	1.91 A 194 V	1.64 A 176 V	2.12 A 318 V	3.29 A 296 V	2.73 A 289 V
PIG (H)	4.48 A 672 V	7.22 A 1.27 kV	6.30 A 900 V	3.24 A 487 V	5.65 A 642 V	4.57 A 524 V	5.23 A 784 V	9.49 A 923 V	7.68 A 814 V
ZT+PIG (H)	4.48 A 670 V	7.18 A 1.27 kV	6.28 A 898 V	3.38 A 506 V	5.70 A 645 V	4.77 A 529 V	5.15 A 772 V	9.32 A 911 V	7.56 A 804 V
I-SHIELD (E)	<--	52.4 A	-->	<--	36.8 A	-->	<--	76.5 A	-->
ZT (E)	1.02 A 153 V	1.04 A 180 V	0.954 A 174 V	1.09 A 163 V	1.18 A 167 V	1.07 A 175 V	1.93 A 289 V	2.17 A 258 V	1.96 A 290 V
PIG (E)	1.78 A 268 V	1.99 A 290 V	1.90 A 272 V	2.23 A 335 V	2.53 A 326 V	2.41 A 316 V	5.69 A 853 V	6.05 A 668 V	5.97 A 565 V
ZT+PIG (E)	1.79 A 268 V	1.99 A 290 V	1.90 A 272 V	2.24 A 336 V	2.53 A 325 V	2.41 A 316 V	5.69 A 854 V	6.05 A 668 V	5.97 A 565 V
TOTAL, SHLD	20.8 A 3.12 kV	24.3 A 4.89 kV	15.9 A 4.05 kV	4.47 A 670 V	7.82 A 1.01 kV	5.74 A 803 V	6.14 A 921 V	12.7 A 1.43 kV	8.56 A 1.16 kV
UNSHLD, H	50.2 A 7.54 kV	53.6 A 9.22 kV	48.8 A 8.44 kV	20.4 A 3.06 kV	27.8 A 3.06 kV	23.1 A 2.93 kV	33.0 A 4.94 kV	46.9 A 4.75 kV	38.9 A 4.64 kV
UNSHLD, E	1.38 A 208 V	2.56 A 212 V	1.32 A 212 V	1.25 A 187 V	2.09 A 185 V	1.73 A 186 V	3.05 A 458 V	5.58 A 409 V	4.89 A 415 V
TOTAL, UNSHLD	55.6 A 8.34 kV	64.0 A 11.4 kV	53.0 A 10.7 kV	18.3 A 2.75 kV	22.6 A 2.86 kV	20.9 A 2.62 kV	28.1 A 4.22 kV	38.6 A 4.09 kV	32.5 A 3.88 kV

Table 4.11 compares the total load currents and voltages summed over all coupling modes for shielded and unshielded cables for each drive and measured load impedance. Overall, the 500 kV 2 PU ST gives the highest individual and total current and voltage responses for shielded and unshielded cables when compared to HEMP. Short range HEMP produces about 40 % higher responses than long-range HEMP, but produces only about one-half the peak responses of ST for shielded and unshielded cables. The sums in both Table 4.10 and 4.11 were obtained by adding the complete time domain waveforms (not just the peak amplitudes) since amplitude peaks of different responses may occur at different times.

TABLE 4.11. Load Currents and Voltages for Sum Over All Coupling Modes

0-PEAK	2 PU SWITCHING TRANSIENT			LONG RANGE HEMP			SHORT RANGE HEMP		
	150 Ω	CT LEAD	DC BATT	150 Ω	CT LEAD	DC BATT	150 Ω	CT LEAD	DC BATT
TOTAL, SHLD	20.8 A 3.12 kV	24.3 A 4.89 kV	15.9 A 4.05 kV	4.47 A 670 V	7.82 A 1.01 kV	5.74 A 803 V	6.14 A 921 V	12.7 A 1.43 kV	8.56 A 1.16 kV
TOTAL, UNSHLD	55.6 A 8.34 kV	64.0 A 11.4 kV	53.0 A 10.7 kV	18.3 A 2.75 kV	22.6 A 2.86 kV	20.9 A 2.62 kV	28.1 A 4.22 kV	38.6 A 4.09 kV	32.5 A 3.88 kV

Table 4.12 provides an overall summary of all peak environments investigated in this study for ST and HEMP. This includes the currents and voltages on the substation high voltage bus primary, the incident electric and magnetic fields, and the total response for each coupled mode.

TABLE 4.12. Overall Summary for Environments and Coupling Modes

0-PEAK	2 PU SWITCHING TRANSIENT	LONG RANGE HEMP	SHORT RANGE HEMP
BUS CURRENT	3630 A	575 A	538 A
BUS VOLTAGE	1300 kV	70.3 kV	84.9 kV
INCIDENT E-FIELD	11.9 kV/m	11.2 kV/m	50.0 kV/m
INCIDENT H-FIELD	179 A/m	29.7 A/m	130 A/m
CONDUCTED COUPLING (CT LOAD)	25.0 A, 4.77 kV	8.07 A, 1.12 kV	13.7 A, 1.64 kV
SHIELD CURRENT (E+H) (CT LOAD)	65.2 A	41.2 A	81.8 A
TRANSFER IMPEDANCE COUPLING (E+H) (CT LOAD)	1.99 A, 0.361 kV	1.79 A, 0.199 kV	3.38 A, 0.298 kV
PIGTAIL COUPLING (E+H) (CT LOAD)	6.44 A, 1.20 kV	5.83 A, 0.671 kV	8.90 A, 0.806 kV
TOTAL, SHIELD (E+H) (CT LOAD)	24.3 A, 4.89 kV	7.82 A, 1.01 kV	12.7 A, 1.43 kV
TOTAL, UNSHIELD (E+H) (CT LOAD)	64.0 A, 11.4 kV	22.6 A, 2.86 kV	38.6 A, 4.09 kV

Table 4.13 summarizes the peak open circuit voltages and short circuit currents for the sum of all coupling modes for shielded and unshielded cables for ST and HEMP drives. Open circuit voltages and short circuit current responses are about twice that of the peak responses for the CT-lead load impedance for all drives. These responses can also be compared to those of the fast transient SWC test wave which provides a peak open circuit voltage of 5 kV and a peak short circuit current of 50 A (Figure 4.29). For shielded cables, the fast transient SWC test waveform appears to provide an upper bound

in all cases except 500 kV 2 PU ST open circuit voltage (7.27 kV compared to 5 kV). In the case of unshielded cable responses, both ST and short range HEMP current and voltage levels exceed those of the SWC fast transient.

TABLE 4.13. Open-Circuit Voltages and Short-Circuit Currents for Sum Over All Coupling Modes

0-PEAK	2 PU SWITCHING TRANSIENT		LONG RANGE HEMP		SHORT RANGE HEMP	
	OPEN CIRCUIT VOLTAGE	SHORT CIRCUIT CURRENT	OPEN CIRCUIT VOLTAGE	SHORT CIRCUIT CURRENT	OPEN CIRCUIT VOLTAGE	SHORT CIRCUIT CURRENT
TOTAL, SHIELD	7.27 kV	48.4 A	1.19 kV	11.8 A	4.79 kV	17.4 A
TOTAL, UNSHIELD	17.1 kV	130 A	5.54 kV	31.6 A	8.55 kV	58.2 A

An attempt has been made here to calculate responses for representative drive levels, circuit geometries, coupling modes and coupling levels. In all cases above, responses have been referenced to the load end of a nominal 73 m lossy substation control cable. In cases where there is less loss or cables are shorter than 73 m, the peak responses for all drives may be expected to increase.

4.4 RELAY SUSCEPTIBILITY

In this study, a limited investigation to determine the conducted susceptibilities of a representative relay was performed. Relay conducted susceptibility is defined here as that set of conditions existing when the relay failed to operate correctly when subjected to a transient current and/or voltage stimulus at an input terminal. Generally, susceptibility conditions specify the failure mode and the characteristics of the stimulus, including its location and its levels when failure occurred. Relay failure was defined as any transient or permanent condition resulting from the applied stimulus in which the relay failed to operate as intended. If no relay failure occurs within a given stimulus test space, then no relay susceptibility exists for these test conditions.

Conducted susceptibility tests using HEMP-like injected single pulses were performed on a transformer differential relay as described in Section 3. The zero-to-peak amplitude, HEMP-like stimulus V-I (voltage-current) test

space covered a voltage range from 0 volts to 19 kV and a current range from 0 amps to 150 amps. The potential for relay susceptibilities was explored by injecting pulses with rise times of a few nanoseconds into each relay input (in both differential and common mode) over the V-I test space. As discussed in Section 3, while flashovers occurred routinely inside the relay at voltage levels greater than 2 kV, failures normally did not occur. Thus, flashovers inside the relay usually did not result in a relay susceptibility for most test conditions. However, one relay susceptibility was found at a test level of 12.3 kV and 150 amps, near the maxima for the V-I space explored. As discussed in Section 3, at this level simultaneous arcing to ground on both DC battery circuits can blow fuses or short circuit unprotected batteries. A survey of several utilities indicates that battery circuits are typically protected with circuit breakers or fuses set high to avoid spurious trips. Simultaneous arcing to ground on both DC wires can result in power follow through on either protected or unprotected batteries, preventing relay operation in either case. Furthermore, flashovers can occur at any point along the battery cable, not just at the load end. Figure 4.32 illustrates how the peak voltage decreases along a 73 m battery cable with distance from the source of the disturbance. For this figure, the worst-case short range HEMP drive (at $\phi = 90^{o}$) was assumed. Close to the source, the voltage is more than twice as high as it is near the load.

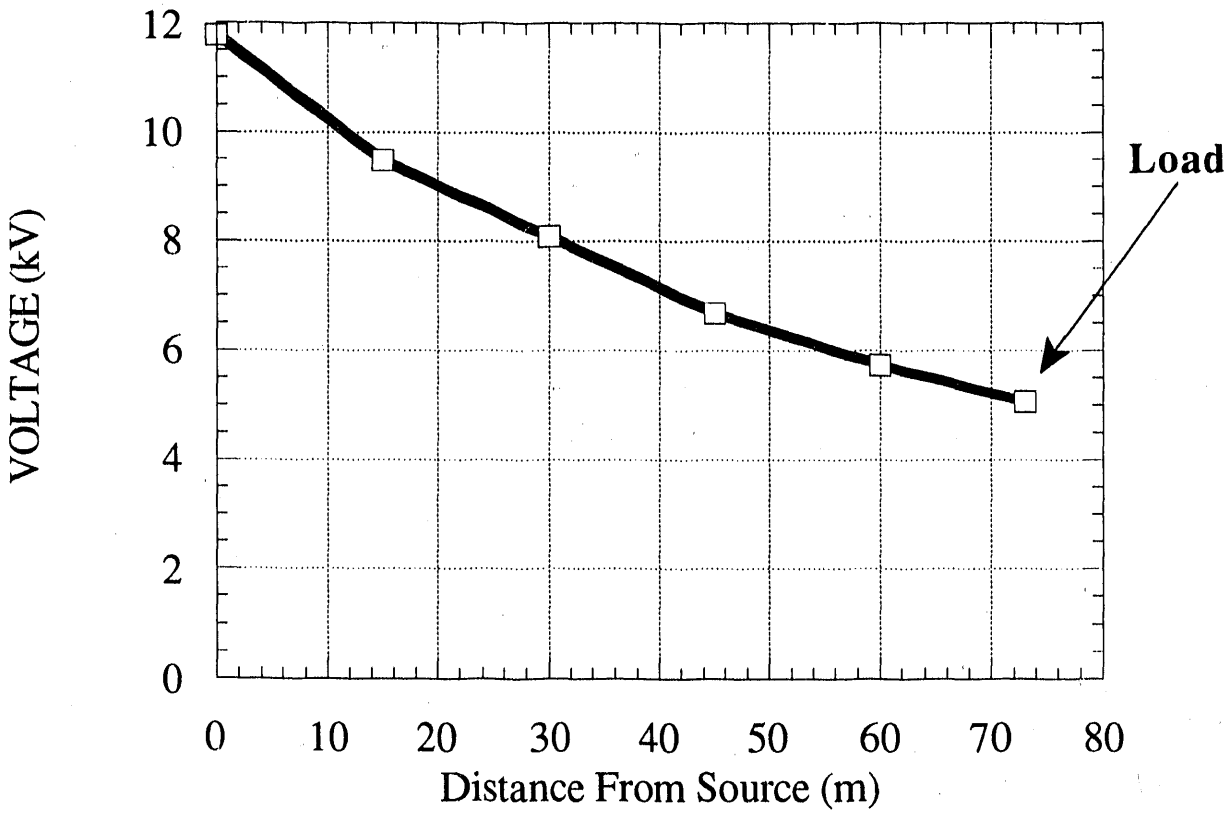

Figure 4.32. Zero-Peak Voltage Along Unshielded Cable to DC Battery As Function of Distance from Source

4.5 RELAY VULNERABILITY

One can define the vulnerability of a system generally as the intersection of the systems' susceptibility state space with that of an achievable threat (stress). Any, or all, norms common to both the system susceptibility and the stress could be used to define their state spaces. Many different norms were calculated earlier in Section 4.3 for the various EMI stresses investigated. Two norms particularly useful for defining state spaces are the peak currents and voltages of susceptibilities and threats referenced to a convenient comparison location.

In this study, a relay is said to possesses a vulnerability to HEMP if it has a HEMP-like susceptibility that falls within the expected conducted

HEMP stress V-I space. If a relay susceptibility falls outside the expected HEMP stress space by a certain amount, then the relay possesses a survivability margin of that amount.

The susceptibility V-I space for a representative relay was calculated in Section 4.4. The susceptibility test space was 0 - 19 kV by 0 - 150 A; however, only a single susceptibility was found, so the relay susceptibility V-I space consists of the single point (12.3 kV, 150 A).

The stress V-I space was determined by the predicted transient peak currents and voltages near the relay equipment resulting from ST and short and long range HEMP coupling to relay control wiring when all cases considered. Thus, the stress V-I space is defined by the shielded and unshielded cable load peak currents and voltages of Section 4.3 when results for both ST and HEMP threats (long and short range), and the three load impedances (150 ohm, measured frequency-dependent CT-lead input, measured frequency-dependent DC-lead input) are all included.

Figures 4.33 and 4.34 show the HEMP stress V-I spaces for unshielded and shielded cables. Stresses from 500 kV 2 PU switching transients have also been included for comparison. Switching transient stresses for the three different wire load impedances are denoted by various sizes of open and filled squares. Similarly, long range and short range HEMP are denoted by diamonds and triangles, respectively. The relay susceptibility <u>test</u> space is also denoted by X symbols in these figures to indicate where relay susceptibility was investigated. The relay susceptibility is also shown as "the X in a circle".

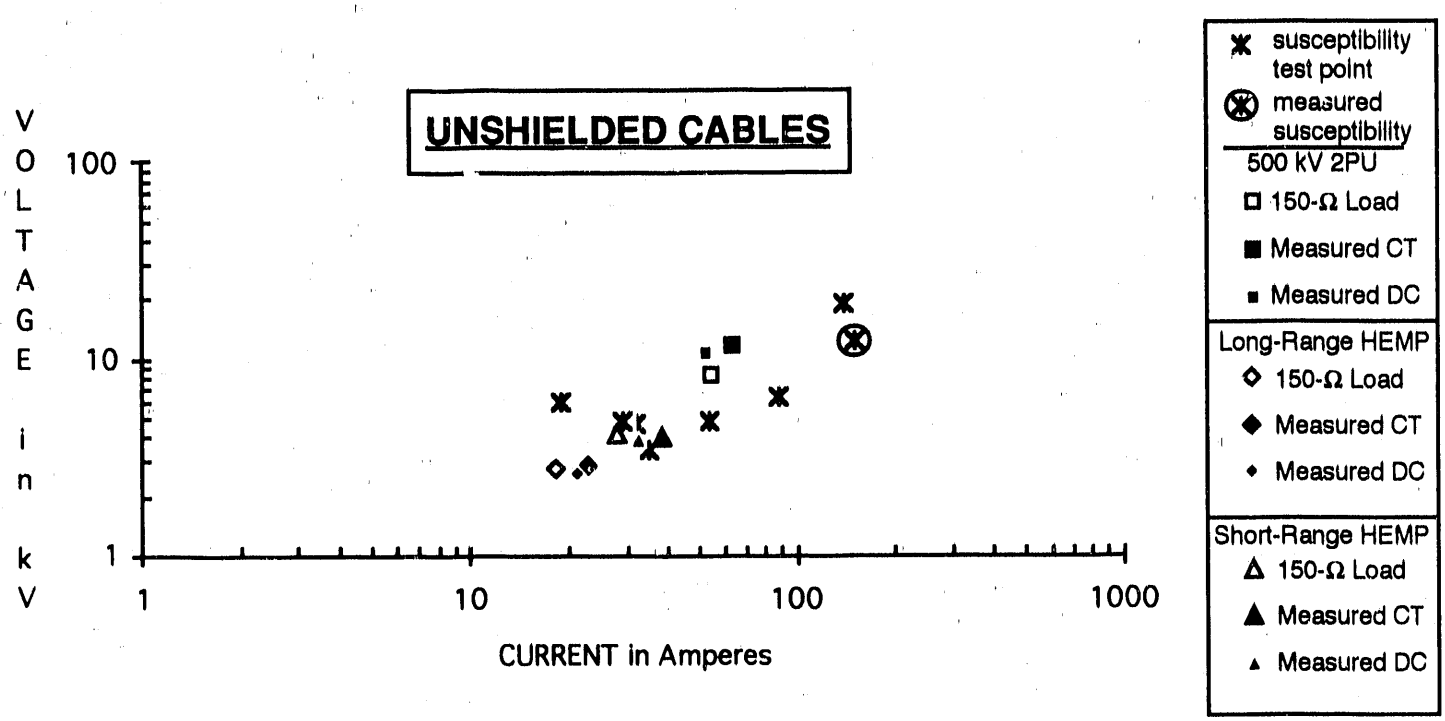

Figure 4.33. Relay Vulnerability V-I Space for Unshielded Cables

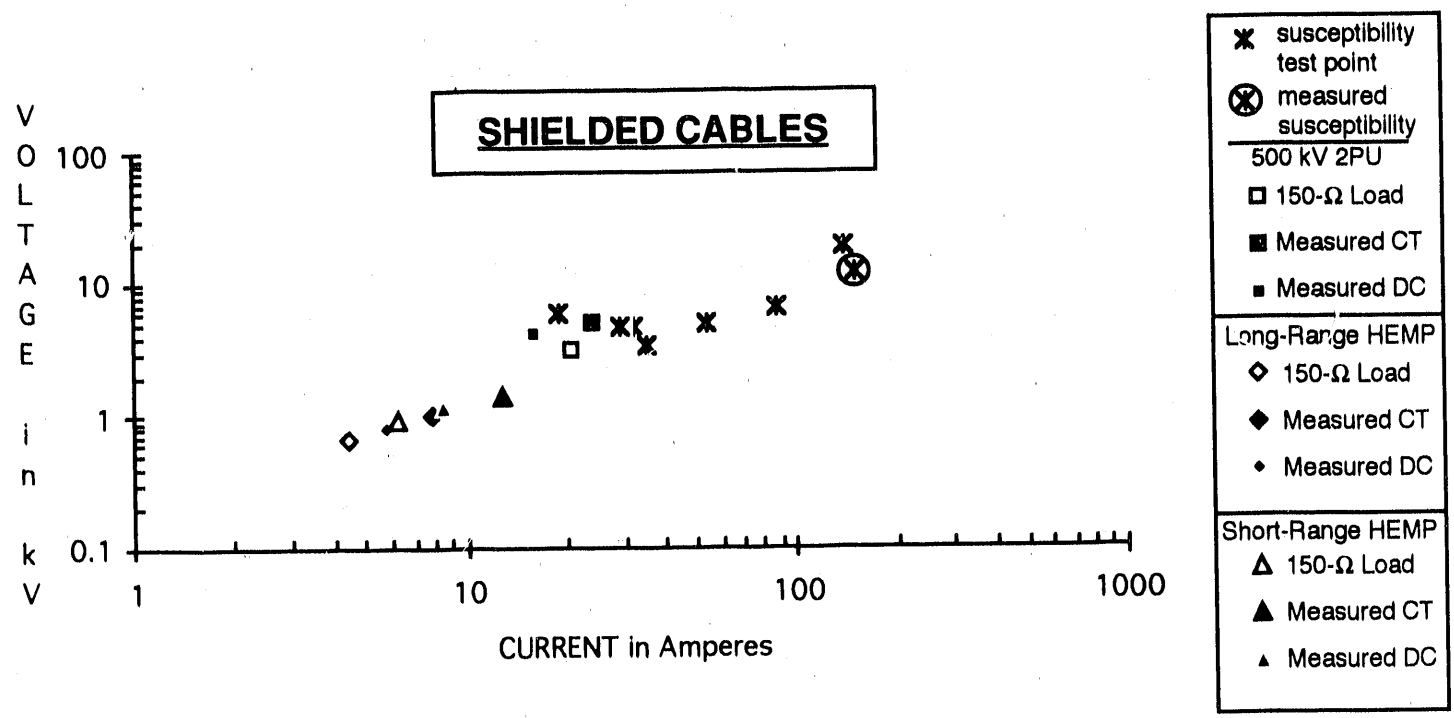

Figure 4.34. Relay Vulnerability V-I Space for Shielded Cables

From the data in Figures 4.33 and 4.34 several observations can be made. First, no relay vulnerability is found. Instead, survivability margins exist for each of the three drives. The margin is least for unshielded cables (Figure 4.33) where it is about (64 A, 11 kV), or about 6 dB, for the highest stress, 500 kV 2 PU ST on the CT-lead input (large, filled rectangle). For short-range HEMP (39 A, 4 kV), the margin is about 9 dB. For shielded cables, the highest stress margins are about 12 - 15 dB for ST and 20 dB for short-range HEMP. The X symbols are scattered about the stresses showing that the relay susceptibility space was adequately sampled during tests for these threats.

4.6 HEMP MITIGATION

Table 4.10 summarizes the peak amplitudes of HEMP current and voltage stresses predicted near the substation control cable loads for all parameter conditions investigated. 500 kV 2 PU ST produces the highest peak amplitude transients over all cable load conditions investigated: currents and voltages from 24 A and 5 kV (shielded cables) to 64 A and 11 kV (unshielded cables). Corresponding short-range HEMP levels are at least a factor of 2 less than this. While these levels are at least 6 dB to 20 dB below those resulting in the susceptibility for the relay tested, whether they exceed susceptibility levels of other relays has not been determined in this study.

As seen in Table 4.13, short-range HEMP and 500 kV 2 PU ST stress levels on unshielded cables are higher, however, than allowed by IEEE/ANSI C37.90.1-1989, the standard for substation relay surge withstand capability (SWC) tests [10], for both the oscillatory and fast transient test waveforms. For unshielded cables ST stresses exceed the fast transient SWC test levels by about a factor of three (current and voltage), while short-range HEMP levels are about 20 - 30 % higher. The fast transient test waveform does appear to provide a sufficient upper bound to predicted ST and HEMP stress levels on shielded control cables. The fast transient test wave generator produces maximum outputs of 50 A and 5 kV under short and open circuit conditions of the generator.

Since both shielded and unshielded cables are common in substations, the discussions in the preceding paragraph suggests that, on average, there may be

little or no margin between relay SWC test levels and expected short range HEMP and 500 kV 2 PU ST stresses. Therefore the use of transient suppression devices to protect relay equipment from HEMP and ST would seem prudent, particularly on unshielded cables. Some newer relays may already provide this type of protection in the form of limiters, filters, isolators, etc. A simple shunt capacitor from a relay wire to ground placed near the relay may be an effective HEMP mitigation technique.

In Section 3.4.6, the effectiveness of a typical surge suppression package (SPP) (Westinghouse 6299D27G02) for increasing the margin of a relay's DC power line was investigated. Arcing caused by a 5 kV steep front impulse was effectively eliminated by the SPP, a 0.5 μf shunt capacitor. Moreover, the SPP provided protection against arcing by HEMP-like impulses as high as 12 kV, near the DC wire susceptibility level measured on the transformer differential relay.

5.0 CONCLUSIONS AND RECOMMENDATIONS

5.1 LIMITATIONS AND CAVEATS

This study has calculated the strength of optimized CHAP-fit HEMP fields incident on high voltage transmission substations and has estimated the current and voltage transients resulting from HEMP coupling to the substation primary bus and to the control wiring of relay circuits protecting substation equipment. Since estimates of relay vulnerability or margins to HEMP are made which may not be valid in general, assumptions and limitations of the present study are emphasized below.

HEMP sources have been based on unclassified CHAP-fit data. The peak CHAP-fit fields have been scaled to 50 kV/m. Only effects due to high-altitude electromagnetic pulse (HEMP) have been considered. Thus, no effects due to either the magnetohydrodynamic (MHD) tail that occurs in the late-time EMP, or to ionizing radiation from neutron, gamma- and x-ray EMP components have been included in this analysis.

HEMP is a single pulse event, whereas up to 10,000 switching transients of varying amplitudes are produced during a single substation disconnect switching operation. In this study HEMP is compared to a single disconnect switching transient representative of the nominal worst case known to occur. However, in a typical switching operation 20 to 40 of these nominal worst case switching transients are often produced [1].

HEMP comparisons are only made with switching transient data for air-insulated substations (AIS). Switching transients in gas-insulated substations (GIS) occur with much higher frequencies than those of (AIS) [1]. While peak GIS switching transient field amplitudes between the gas enclosure and ground are somewhat lower than those between the primary bus and ground in AIS, the dominant spectral components of GIS fields can be more than 100 MHz. Thus, GIS spectral components may be closer to those of HEMP.

The amplitudes of control wire current and voltage stresses near the relay equipment are the result of summing contributions from multiple conducted and radiated coupling pathways. While all of these coupling models are broadband and have been either measured directly or validated against substation switching transient measurements, and have been extended in high frequency response by virtue of the simple analytical fits employed, they have not necessarily been validated over the entire HEMP bandwidth. Parameter values used in the models were based on actual substation measurements, manufacturer's data, and on data found in the literature [12].

Current and voltage stresses near relay equipment depend on the relay loads. In limited measurements on all common and differential mode inputs to a single relay, this project has shown that relay load impedances vary greatly with frequency. Also, load versus frequency response curves vary greatly as a function of the relay input selected. In addition to fixed load impedances of 150 ohms, actual measured relay load frequency responses were used in calculating HEMP stresses in order to show the effect of such variations. However, the results for only a single relay were used. The generality of these results is not known.

Only current and voltage stresses driven into relay loads from wiring circuits external to the relay house were calculated. Direct field coupling to relay equipment racks by HEMP fields penetrating the house was not considered. Based on limited relay house shielding effectiveness measurements reported in [1] for switching transient fields, a typical metal relay house may provide about 16 dB or less of shielding.

Upset and failure susceptibilities were only measured for a single relay in this study. An attempt was made to select a relay that might be considered to have nominal susceptibilities, however the minimum and maximum susceptibilities that could occur for all relays was not determined and is unknown. Thus it is not known if the susceptibilities measured are in fact nominal. The relay DC circuit failure threshold susceptibility was determined only at a battery voltage of 48 V. Relay systems commonly operate at much higher DC voltages. It is possible that the failure threshold could be lower at these higher voltages; however this was not investigated. Only single, HEMP-like pulses were injected for measuring relay susceptibilities. These

susceptibility levels may not be representative of those of switching transients which occur in quasi-random bursts of up to 10,000 transients.

Relay vulnerability and protection margin estimates are the result of comparing EMI stresses with relay susceptibilities. If a stress exceeds a susceptibility, a vulnerability is said to exist. If a stress is less than a susceptibility by a certain amount, then a margin of this amount is said to exist. Comments made in the paragraphs above illustrate the uncertainties and variabilities both in the levels of the EMI stresses at relay equipment inputs and in the relay susceptibilities themselves. Thus, these same uncertainties will be reflected in vulnerability estimates and margins. While this study has attempted to use worst case fields and nominal coupling parameter and susceptibility values, calculated vulnerabilities or margins should probably exceed factors of 2 or so in order to be considered significant.

5.2 CONCLUSIONS

5.2.1 Maximum HEMP Fields on a Substation

For a 400-km altitude burst over the central CONUS, there are two substation locations relative to ground zero where near-worst-case HEMP stresses are produced. The HEMPs at these two locations have been defined in this report as "short-range HEMP" and "long-range HEMP". The nominal maximum HEMP electric field strength is 39 kV/m and occurs at a ground range 500 km south of ground zero. This horizontally polarized electric field is incident on the substation at an elevation angle of 35.4 degrees measured from the horizontal and is termed short-range HEMP. In this study, HEMP electric fields have been scaled to a peak of 50 kV/m. A maximum induced current stress on the substation occurs when HEMP electric fields are incident at grazing angles on long transmission lines connected to the substation. In this case the peak HEMP electric field drive occurs at a ground range of 1660 km west-northwest of ground zero and is incident at an elevation angle of 5.6 degrees and at an amplitude of 32 kV/m (after scaling). These conditions are termed long-range HEMP.

5.2.2 Comparing Incident HEMP and Switching Transient Fields in Substations

The short-range HEMP horizontal incident electric field rises to a maximum of 50 kV/m in 4 ns and falls to 1/e of maximum in about 20 ns. Because long range HEMP coupling depends strongly on polarization and grazing angle incidence, and because the lower amplitude, vertical component couples more strongly, two components are important. The long-range HEMP vertical incident electric field rises to a maximum of about 11.2 kV/m in 9 ns (10%-90% risetime), and falls to 1/e of maximum in about 70 ns. The long-range HEMP horizontal incident electric field rises to a maximum of 32 kV/m in 9 ns, and falls to 1/e of maximum in about 65 ns. HEMP fields all exhibit unipolar waveforms; the horizontally polarized switching transient electric and magnetic fields are bipolar. The 2 PU switching transient horizontal incident electric field in a 500 kV air-insulated substation rises to a maximum of 12 kV/m in about 500 ns and falls to 1/e of maximum in about 4 μs. The corresponding maximum zero-peak magnetic fields incident to ground are 130 A/m for short-range HEMP, 30 A/m (vertical) and 85 A/m (horizontal) for long-range HEMP, and 179 A/m for 2 PU switching transients in a 500 kV substation. The rise times and durations for the HEMP magnetic fields are similar to their electric fields. Disconnect switching transient magnetic fields rise to peak amplitude in about 250 ns and decay to zero amplitude in about 10 μs, whereas ST electric fields decay to a relatively high non-zero value for times up to 8 milliseconds.

Other norms, summarized in Table 4.2, show that HEMP fields have higher peak derivatives and faster local risetimes (HEMP 10 - 90 % peak risetimes are also much faster), while switching transient fields have greater total energy. Thus, the short-range HEMP electric field rises 100 times faster and is about 5 times higher amplitude, but decays 80,000 times faster and contains 3 times less energy than those of 2 PU disconnect switching transient electric field in 500 kV substations. On the other hand, the 2 PU ST magnetic field amplitude is somewhat greater than that of short-range HEMP and also has much more energy.

5.2.3 Comparing HEMP and Switching Transients Induced on the Primary Bus

Short-range HEMP produces maximum zero - peak currents and voltages of 538 A and 85 kV on the substation primary bus. When including contributions from both vertical and horizontal field polarizations, long-range HEMP produces 575 A and 70 kV on the primary bus. Disconnect switching

under 2 PU initial conditions across the switch gap in 500 kV air substations produces 3,600 A and 1,300 kV on the primary bus. Thus, 500 kV substation 2 PU switching transients produce peak amplitude bus transients 15 - 19 times higher in voltage and 6 - 7 times higher in current than those produced by HEMP.

5.2.4 Comparing Relative Importance of Coupling Modes to Total Wire Coupling

Substation control wiring installation guidelines allow cables to be shielded or unshielded [11]; therefore, coupling to both types was investigated.

Two shielded control cable configurations having different coupling pathways to the EMI environment in the switchyard were studied. One cable configuration is representative of CT and PT wiring where one end of the cable physically connects directly to the high voltage bus through a transformer or capacitors and includes both conducted and radiated field coupling mechanisms. In the other cable configuration, such as characterized by trip coil circuits, only radiative field coupling is important since there is no direct connection to the primary bus. Coupling via the conducted pathway is from transients on the high voltage primary directly through either the instrument transformer or its parasitic capacitance to a control wire inside the shielded cable. Radiation field coupling to shielded control wires near relay equipment involves multiple parallel and sequential pathways. In the case of shielded cables, fields first couple to the cable shield. Shield current and voltage transients then couple to a control wire two ways. One way is via the cables' transfer impedance, the other way is through the mutual inductance between the shield and a wire that occurs at the pigtail shield termination near the relay equipment.

Using nominal parameter values for relay load impedances, cable diameter, and pigtail length, dominant modes for coupling each type of EMI to the relay equipment control wiring were found. The dominant mode for coupling for all HEMP and ST drives into control wiring was found to be conducted coupling, with significant contributions also from magnetic field-driven pigtail coupling in the case of shielded cables. Coupling via cable transfer impedance was found to contribute the least to the total coupling in all cases.

5.2.5 Comparing HEMP and Switching Transients Induced on Control Wiring

All conducted and radiated coupling mode contributions are summed to produce total current and voltage coupling responses in the following comparisons. Response comparisons are made at the ends of shielded and unshielded lossy 73-m control cables (where relay equipment would be connected) for three different relay load impedance conditions.

For shielded cables, with the shield grounded in a 12" pigtail at the load end and the cable load impedance represented by a constant 150-ohm value, short-range HEMP produced 6.1 A and 0.9 kV, long-range HEMP produced 4.5 A and 0.7 kV, and disconnect switching produced 21 A and 3.1 kV (all zero-peak amplitude) near the relay equipment. In this case, short-range HEMP currents and voltages are about 2 times those of long-range HEMP and about one-half that of 2 PU switching transients. In the case of unshielded cables, short-range and long-range HEMP current and voltage responses increased by about a factor of 4 over their values on shielded cables, while ST responses increased by a factor of about 2.5.

For shielded cables, with the shield grounded in 12" pigtail at the load end and the cable load impedance represented by the measured frequency dependent CT-lead impedance of the test relay, short-range HEMP produced 12.7 A and 1.4 kV, long-range HEMP produced 7.8 A and 1.0 kV, and 2 PU disconnect switching produced 24.3 A and 4.9 kV near the relay equipment. In this case, the short-range HEMP stress is about 1.5 times that of long-range HEMP, and about half that of switching transients. Unshielded cable responses are almost 3 times higher those for shielded cables for all drives. The CT-lead impedance gave the highest overall response among the measured relay load impedances considered.

For shielded cables, with the shield grounded in 12" pigtail at the load end and the cable load impedance represented by the measured frequency dependent DC battery lead impedance of the test relay, short-range HEMP produced 8.6 A and 1.2 kV, long-range HEMP produced 5.7 A and 0.8 kV, and 2 PU disconnect switching produced 15.9 A and 4.1 kV near the relay equipment. In this case, the short-range HEMP wire current stress is 1.5 times that of long-range HEMP and about half that of 2 PU switching transients. Unshielded cable responses are 3 - 4 times higher than those for shielded cables for all drives.

5.2.6 Relay Susceptibility to HEMP

A solid state transformer differential relay was subjected to HEMP-like impulses over 0-to-peak ranges of 0 - 150 A and 0 - 19 kV. Only one susceptibility was found at (150 A, 12.3 kV). The susceptibility can occur when both DC wires flash over to ground simultaneously causing failure of the relay battery circuit. Susceptibilities for other relays, and for other conditions of the test relay, were not investigated. Therefore no conclusions regarding relay susceptibility in general were reached as a result of this limited study.

5.2.7 Relay Vulnerability to HEMP

When the single measured relay susceptibility was compared with all predicted HEMP voltage and current stresses, no HEMP vulnerability was found. HEMP survivability margins ranging from 9 dB for unshielded and 20 dB for shielded control cables were found for this relay susceptibility. However, these vulnerability conclusions apply only to the test relay, as tested, and are not general. HEMP margins were found to be greater than those for 2 PU ST which were 6 dB (unshielded cables) and 12-15 dB (shielded cables). These margins are calculated at the end of a nominal 73-m control cable where relay equipment would be attached. It has been noted in Section 4.3 that voltages on unshielded cables can be much higher on shorter cables or nearer the source end on long ones, and could cause short circuits - particularly on DC cables; this could reduce the margins cited above.

5.2.8 HEMP Mitigation in Substations

On unshielded control cables, no margins against the levels of HEMP predicted here are provided by the current SWC fast transient (or damped sine) test specifications for substation relay equipment [10]. At frequencies where short-range HEMP amplitudes are highest (4 MHz to 20 MHz), expected HEMP stress levels were found to exceed SWC test levels by than a factor of 10 on unshielded cables and up to a factor 10 on shielded cables. Simple shunt capacitors placed on relay wiring near the relay equipment were found to mitigate HEMP effects such as arcing and provide margins to 12 kV for the test relay.

5.3 RECOMMENDATIONS

A wider range of relay susceptibility data is needed before general conclusions regarding relay vulnerabilities and margins to HEMP can be drawn. Susceptibilities should be measured under HEMP-like pulses injected at levels up to 20 kV and 150 A for both protected and unprotected relays including electromechanical, solid state, and microprocessor types. Relays and relay systems should be tested in operational status as normally installed in substations. Susceptibilities should also be determined for other equipment used for substation communication and control.

Since predicted HEMP stress levels exceed SWC test standards in some cases, the use of mitigation techniques may be warranted on relay equipment even though vulnerabilities or margins have not yet been clearly established.

REFERENCES

[1] C. M. Wiggins et. al., "Electromagnetic Transients in Substations", EPRI RP2674-1 Draft Final Report, Electric Power Research Institute, Palo Alto, CA 94304, June 1990

[2] C. L. Longmire, et. al., "A Nominal Set of High-Altitude EMP Environments", ORNL/Sub/86-18417/1, Martin Marietta Energy Systems, Inc., Oak Ridge National Laboratory, Oak Ridge, TN 37831, February 1987.

[3] F. M. Tesche and P. R. Barnes, "Development of a New High Altitude Electromagnetic Pulse (HEMP) Environment and Resulting Overhead Line Responses", Hemisphere Publish. Corp.,Electromagnetics 8:213-239, 1988.

[4] G. E. J. Bridges and L. Shafai, "Plane Wave Coupling to Multiple Conductor Transmission Lines Above a Lossy Earth", IEEE Transactions on Electromagnetic Compatibility, Vol. 31, No. 1, February 1989.

[5] D. E. Thomas, et. al., "Comparison of Transients on the High Voltage Bus", BDM/ABQ-89-0285-TR, BDM Corp., Albuquerque, NM 87106, March 1989.

[6] D. E. Thomas et. al., "Prediction of Electromagnetic Field and Current Transients in Power Transmission and Distribution Systems", IEEE Transactions on Power Delivery, Vol. 4,pp. 744-755, January 1989.

[7] E. F. Vance, Coupling to Shielded Cables, Wiley- Interscience, New York, 1978.

[8] C. R. Paul. "Effect of Pigtails on Crosstalk to Braided-Shield Cables" IEEE Transactions on Electromagnetic Compatibility, Vol. EMC-22, No. 3, August 1980, pp. 161 - 172.

[9] C. M. Wiggins et. al., "Measurement of Switching Transients in a 115 kV Substation", IEEE Transactions on Power Delivery, Vol. 4, No. 1, pp. 756-769, January 1989.

[10] ANSI/IEEE C37.90.1-1989 "Standard Surge Withstand Capability (SWC) Tests for Protective Relays and Relay Systems", (P472/D9), January, 1987).

[11] "IEEE Guide for Selection and Installation of Control and Low Voltage Cable Systems in Substations," IEEE 525-1978.

[12] A. Greenwood, Electrical Transients in Power Systems, Wiley-Interscience, New York, 1971.

[13] L. Scott, et. al.,"Electromagnetic Pulse Technology Development Program: Bounding of EMP-Induced Cable Currents on Aircraft", EMPTD-3-MRC-014, Mission Research Corporation, Albuquerque, NM, January 1982. See also EMPTD-3-MRC-011 or AFWL-TR-82-41, January, 1982.

APPENDIX A

This appendix contains 15 plots of the voltage waveforms resulting from the relay flashover tests discussed in Sections 3.4.4 and 3.4.5. Each waveform is identified by the listing below which includes its filename and page number referenced in the text, and other descriptors. Waveforms plots are presented in the order discussed in Section 3.

The tests were conducted as described in Figure 3.4, that is, different EMP-like pulse types were injected through a pair of wires in a 100-ft, 4-conductor, #10 insulated wire, standard 600V control cable. The pulse injection wire pair was connected through a shorting block to different pairs of the six relay inputs (1,2,4,5,6, and 10) identified in Figures 3.3 and 3.1. Pins 5 and 6 are one of the CT inputs; note pin 5 is grounded. In the first 6 waveforms presented below, pulses are injected on pins 5 and 6. In waveforms 7 and 8, pulses are injected through pins 2 and 5, the relay (common mode) output. In waveforms 9, 10, and 11, pulses are injected through pins 2 and 10, the relay trip coil (differential mode) output. In waveforms 12 and 13, pulses are injected between pins 1 and 5, the (+) battery and ground. In waveforms 14 and 15, the pulses are injected between pins 10 and 5, the (-) battery lead and ground. The pins driven by the pulse are identified in the headers of each plot shown below. Waveform voltages are monitored with the oscilloscope and recorded on the digitizing camera system (DCS) at a point near the shorting block as illustrated in Figure 3.3. Three different types of EMP-like pulses were injected at several different pulser charge levels in some of the tests. These waveforms are identified in Figure 3.3 as the Square Pulse Generator (SPG) 130ns charge line pulse, the SPG 800ns charge line pulse, and the capacitor network pulse generator (CAP) pulse. The type of pulse injected and the pulser charge level are indicated in the header of each of the waveforms presented below. Current taps on the Type STD15C relay are selectable from 2.9 to 8.7 A using a current tap plug. The current tap was varied to study its effect on CT tests; the tap plug used is noted in first 6 plot headers.

Waveform No.	Filename	Page	Description
1	(RL15.DTL)	52	CT Voltage, SPG@11kV, 130ns
2	(RL51.DTL)	52	CT Voltage, SPG@6kV, 130ns
3	(RL73.DTL)	53	CT Voltage, SPG@6kV, 800ns
4	(RL76.DTL)	53	CT Voltage, SPG@8kV, 800ns
5	(ORL8.DTL)	53	CT Voltage, CAP@5kV
6	(ORL14.DTL)	53	CT Voltage, CAP@10kV
7	(OPG2.DTL)	54	Trip Coil Voltage, CAP@3kV
8	(OPG9.DTL)	54	Trip Coil Voltage, CAP@10kV
9	(OP18.DTL)	54	DC Output Volts, SPG@5kV,130ns
10	(OP45.DTL)	54	DC Ouput Volts,SPG@2.5kV,800ns
11	(OOP2.DTL)	54	DC Output Voltage, CAP@2kV
12	(DCG12.DTL)	54	+DC to Grd Voltage, CAP@6kV
13	(DCG26.DTL)	55	+DC to Grd Voltage, CAP@20kV
14	(DCG34.DTL)	55	-DC to Grd Voltage, CAP@10kV
15	(DCG40.DTL)	55	-DC to Grd Voltage, CAP@15kV

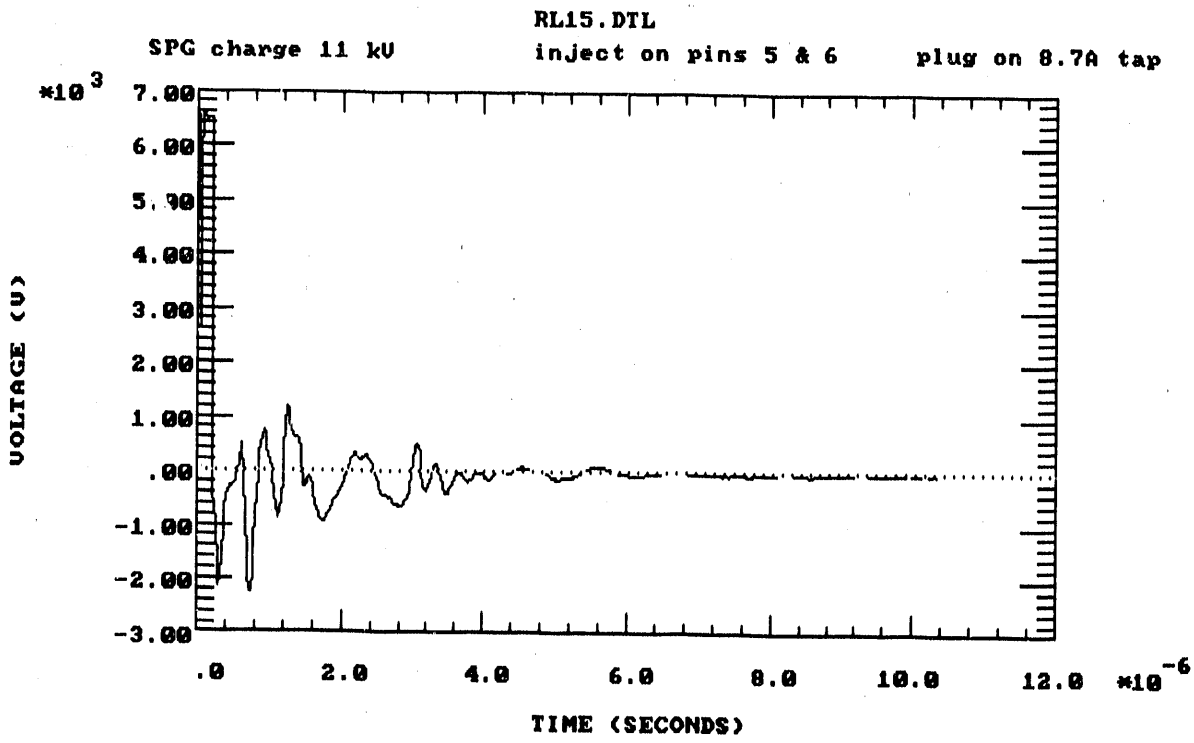

Waveform 1

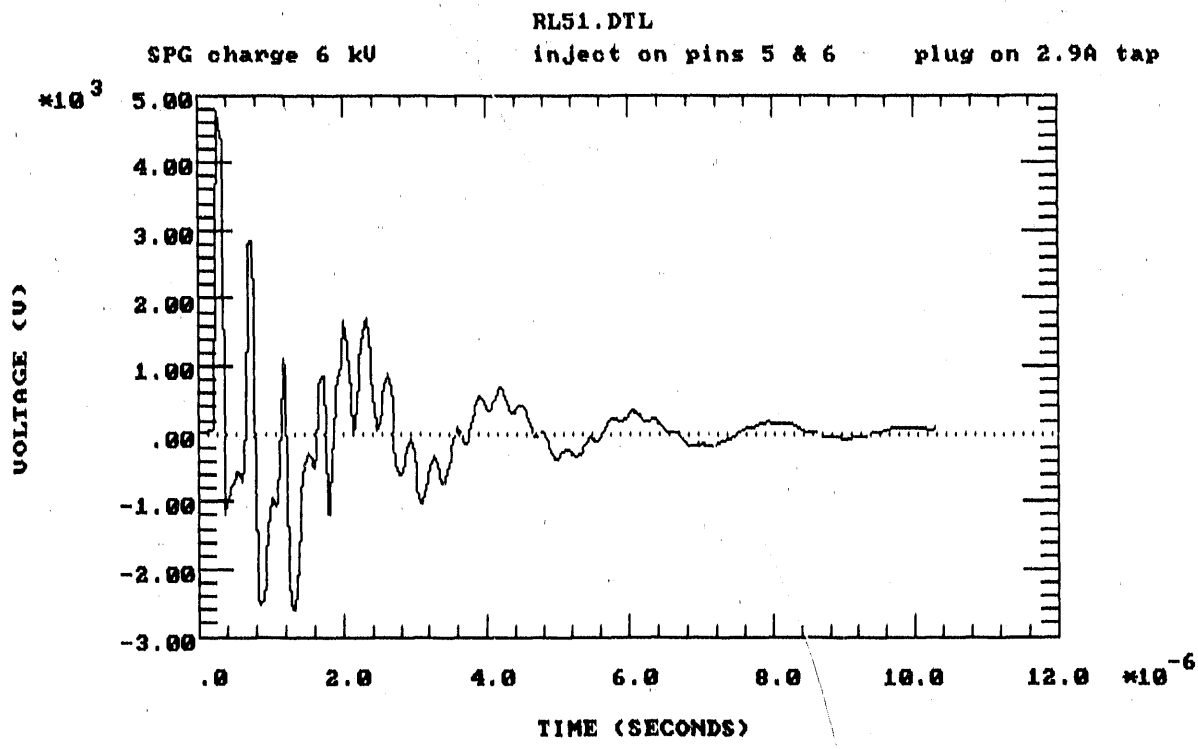

Waveform 2

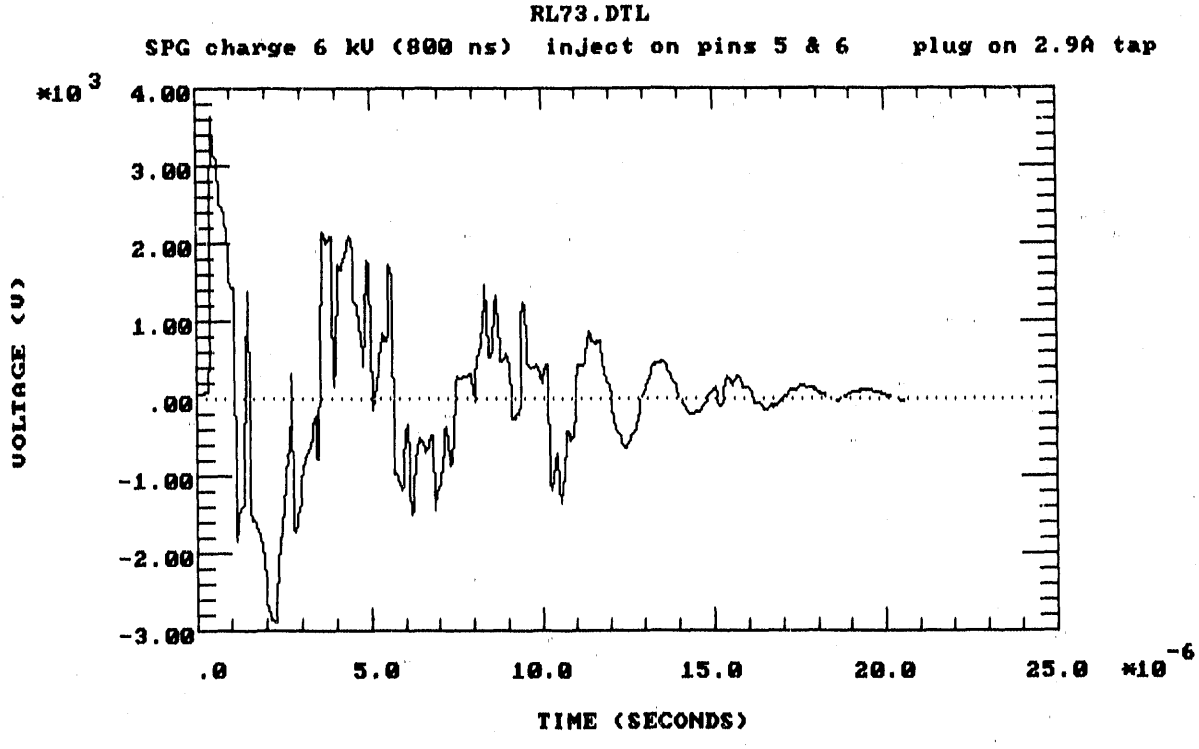

Waveform 3

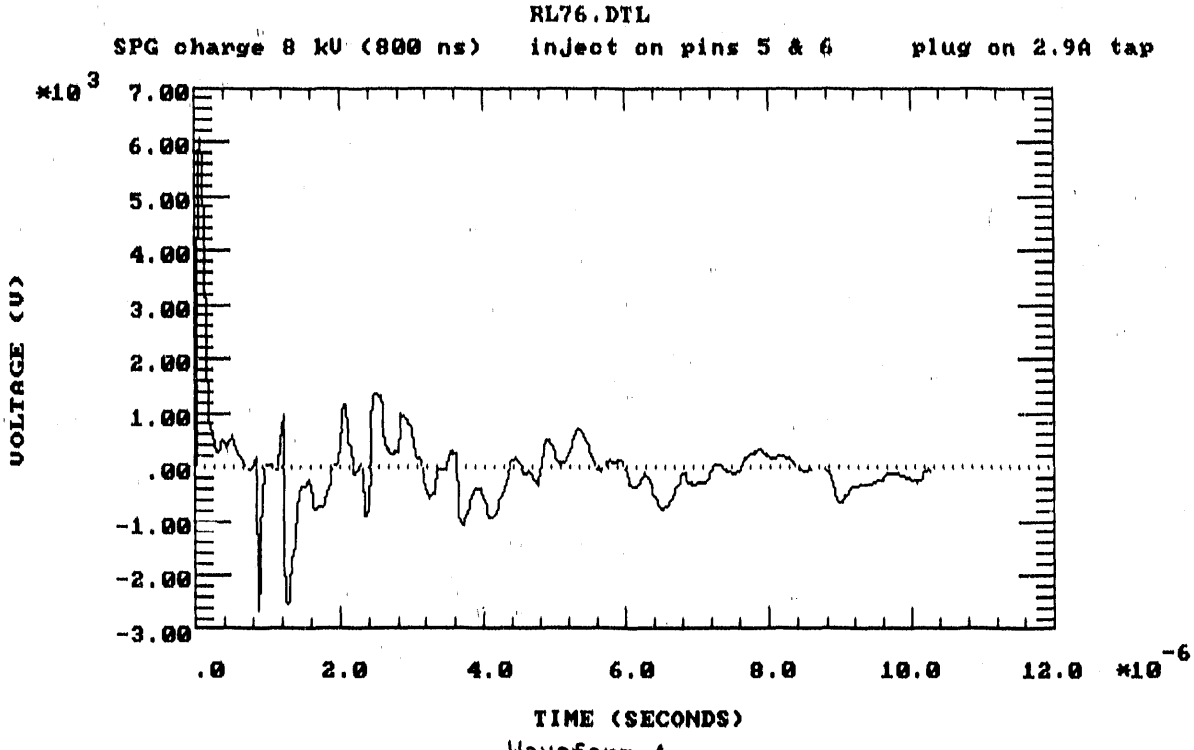

Waveform 4

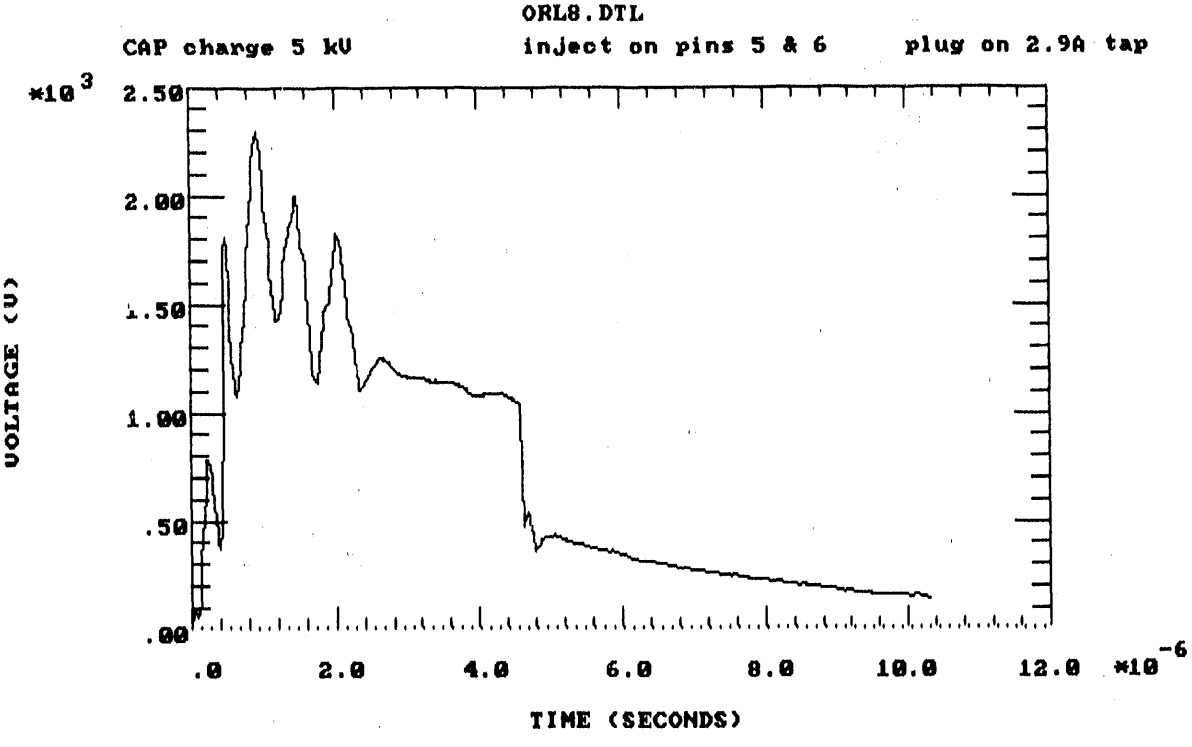

Waveform 5

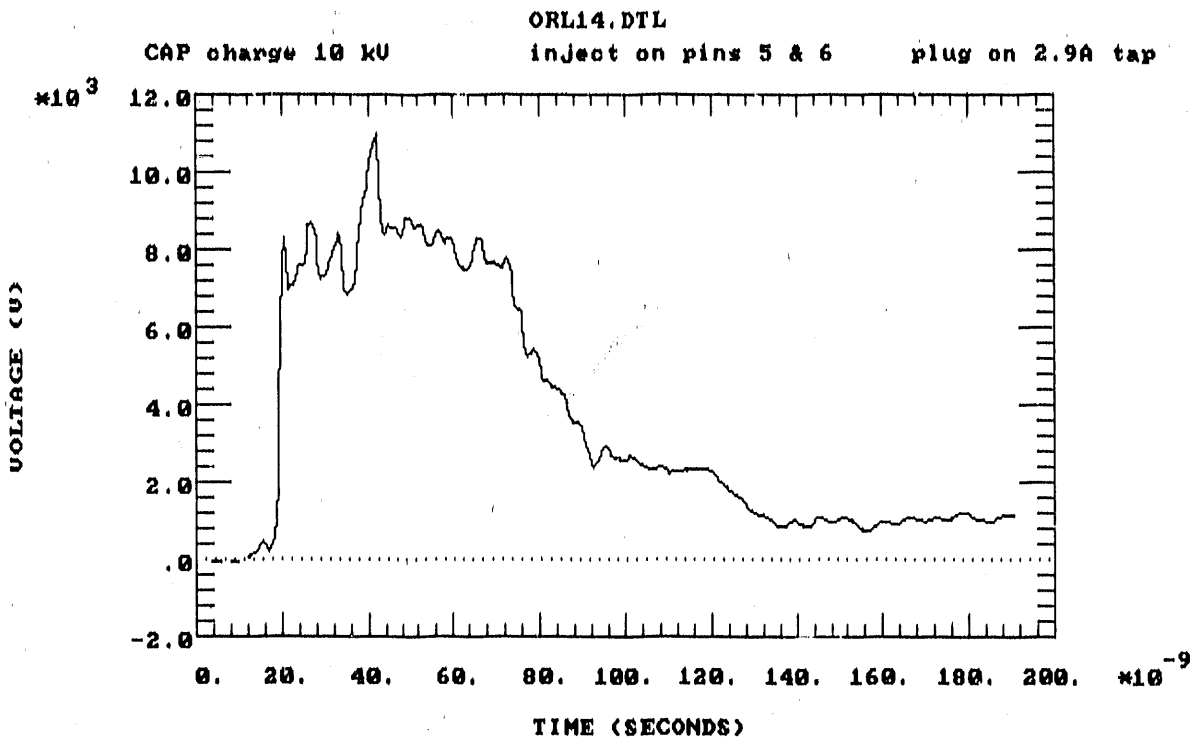

Waveform 6

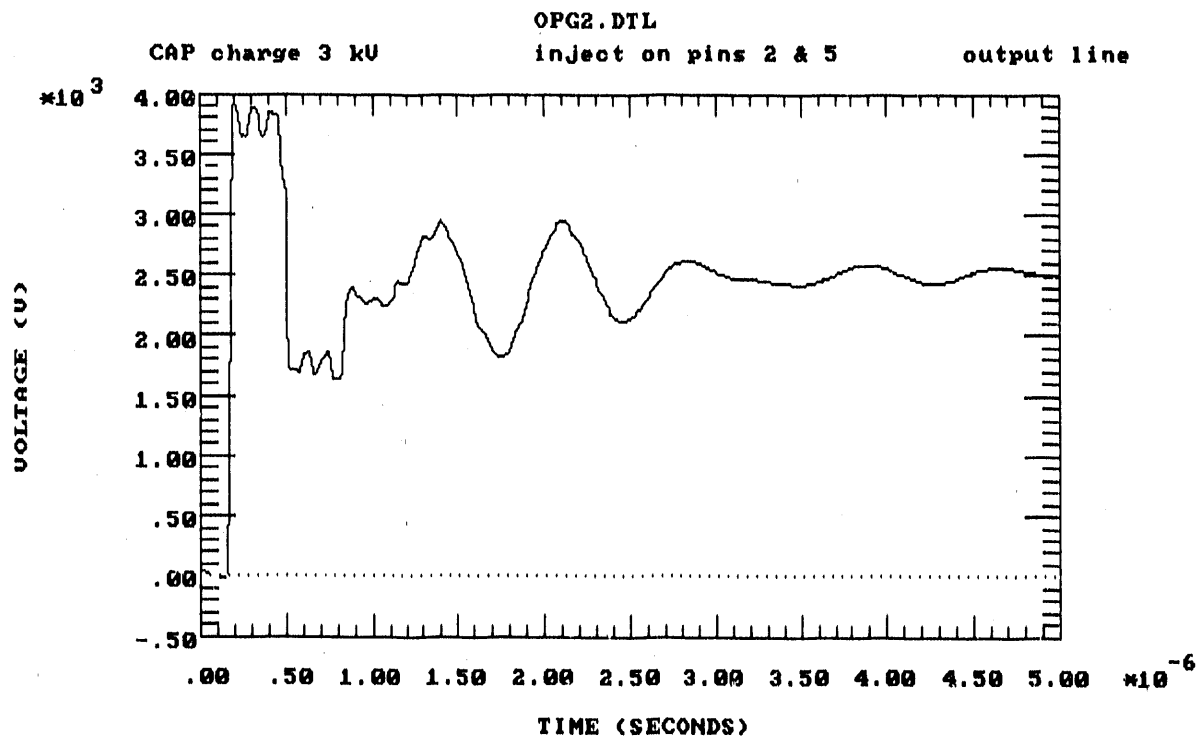

Waveform 7

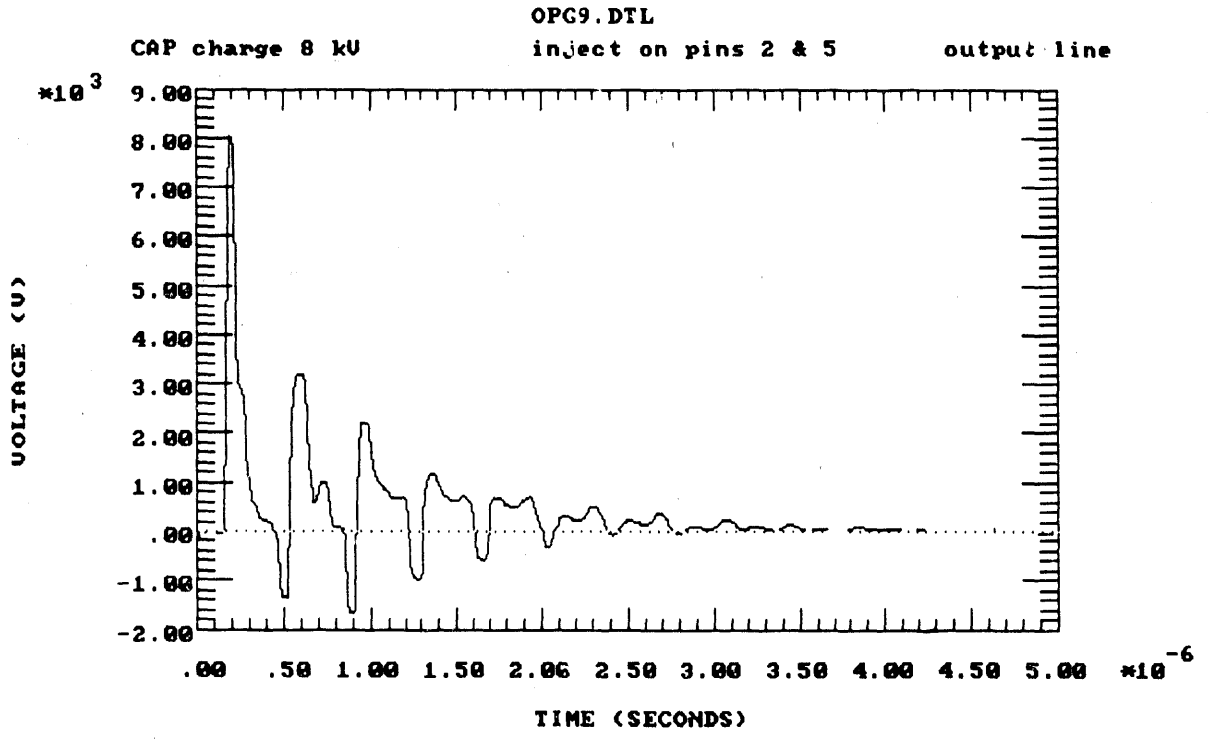

Waveform 8

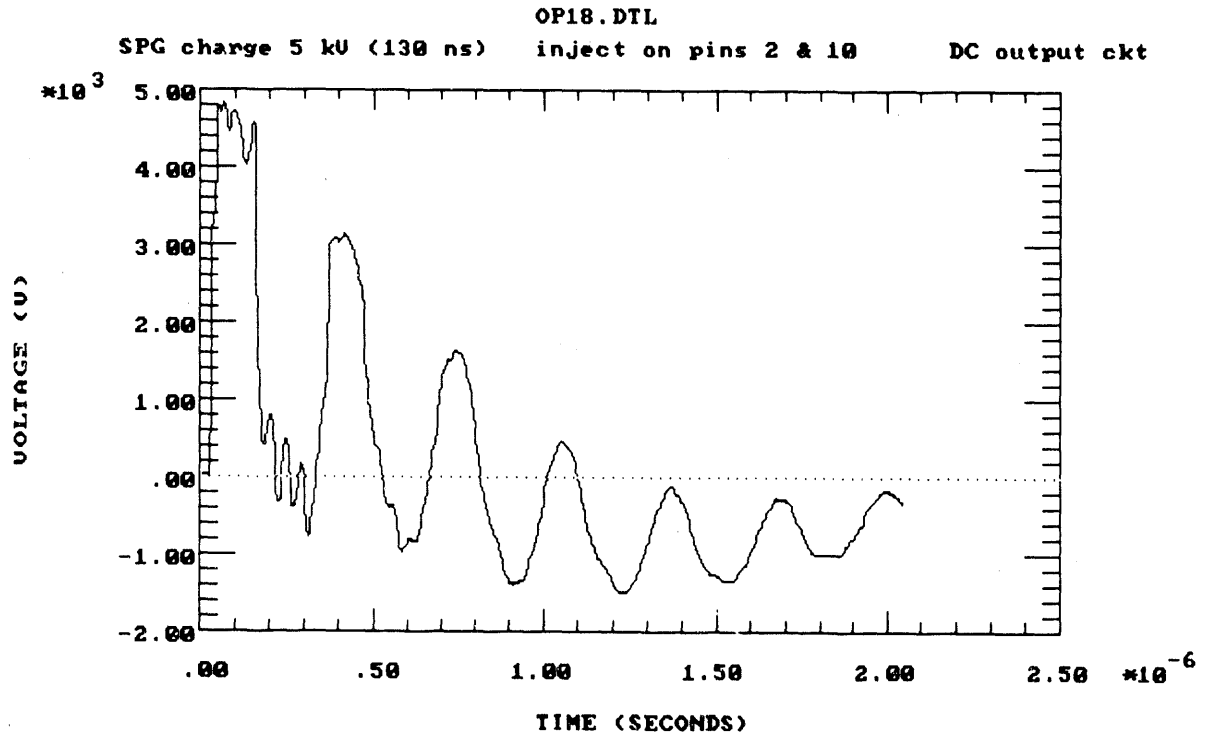

Waveform 9

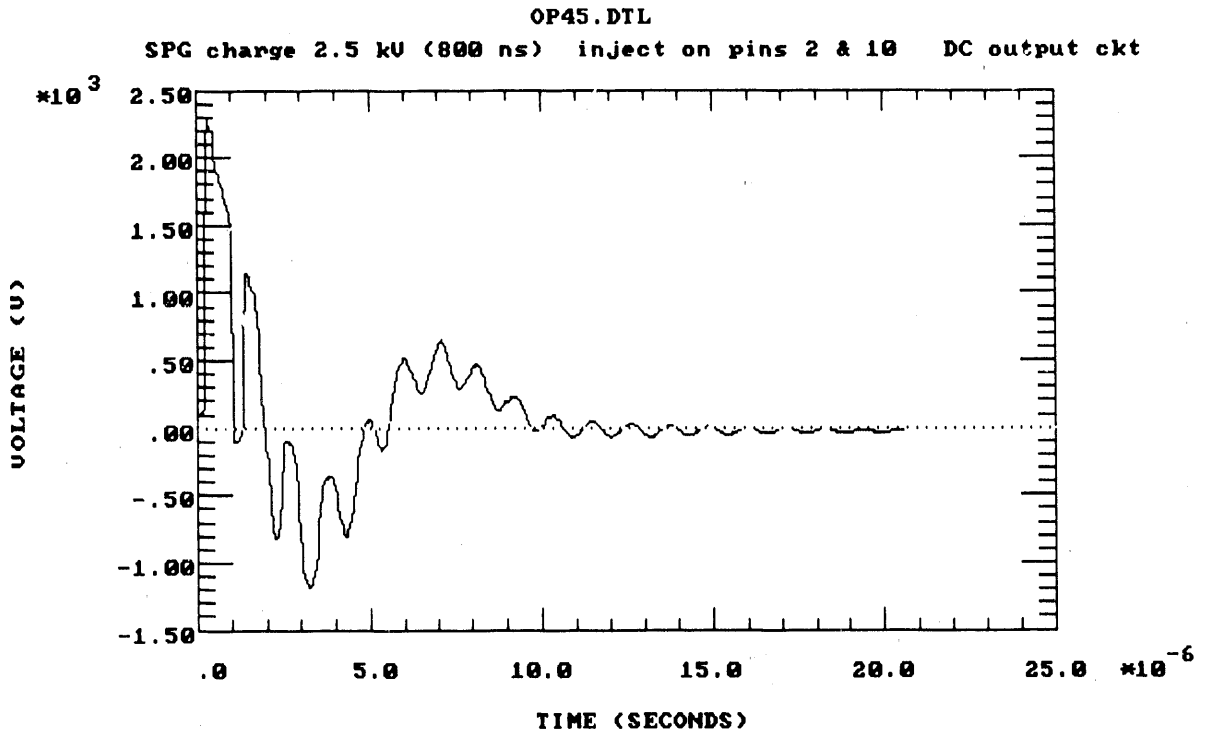

Waveform 10

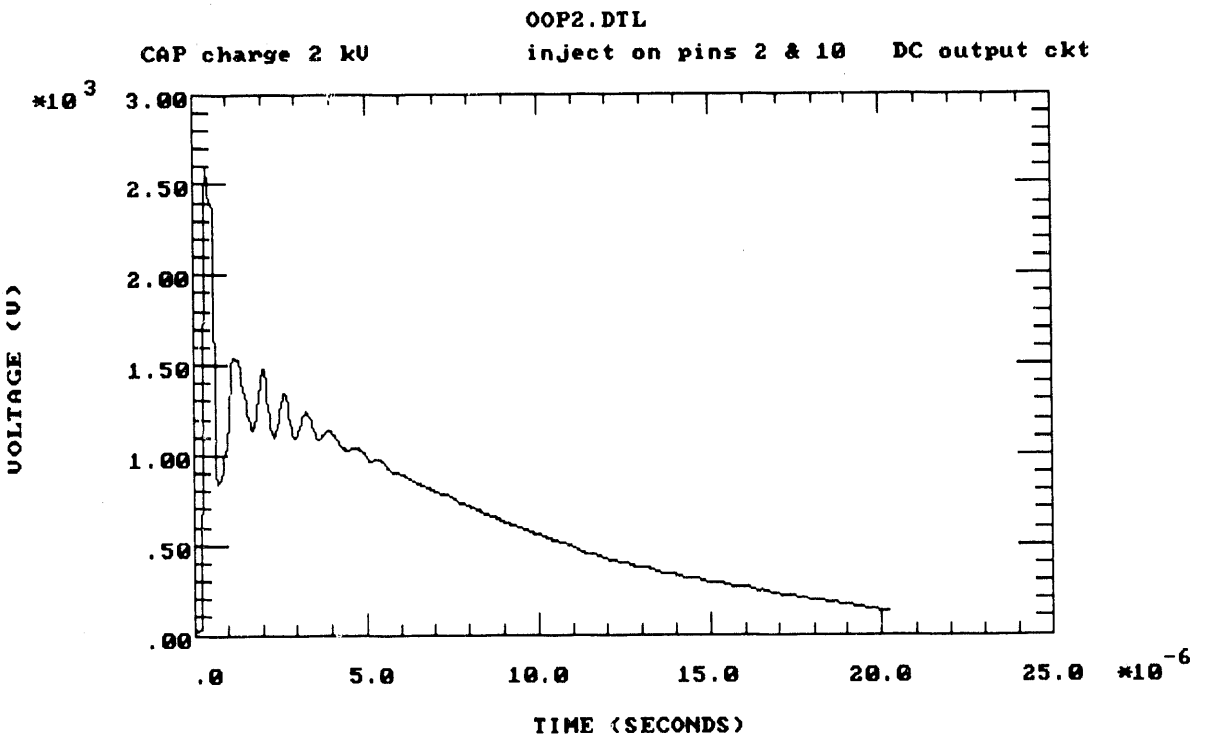

Waveform 11

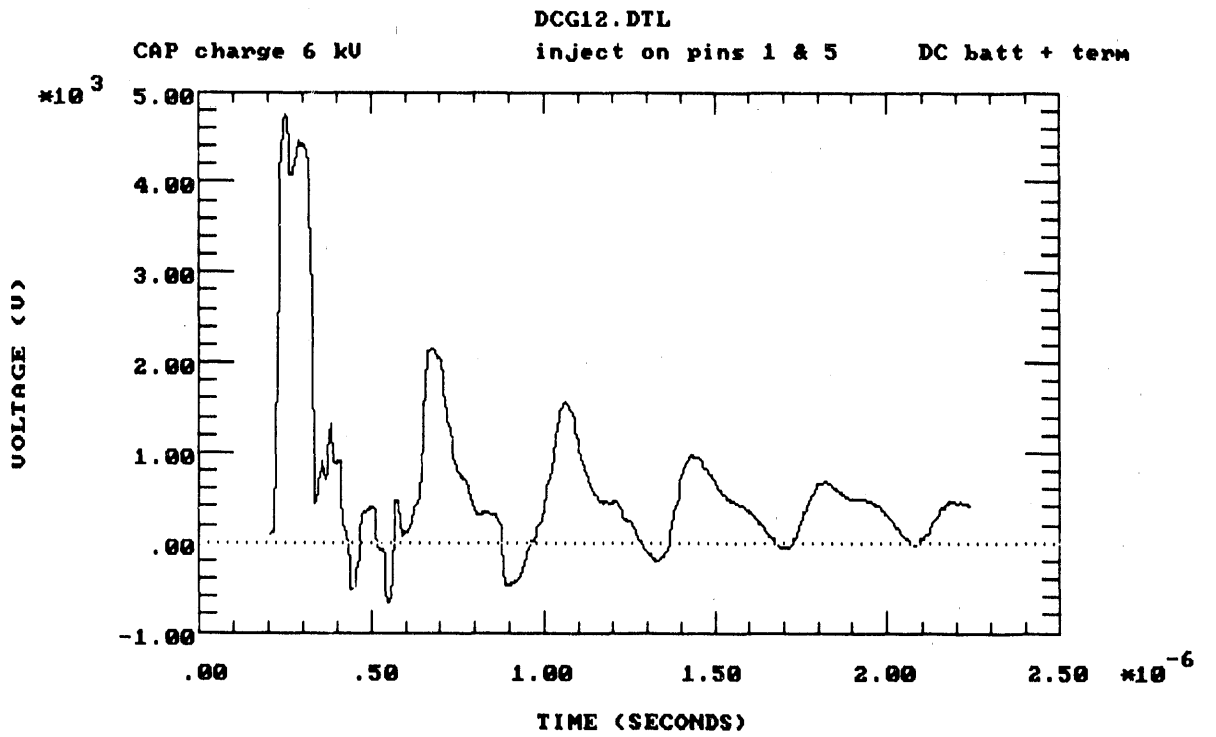

Waveform 12

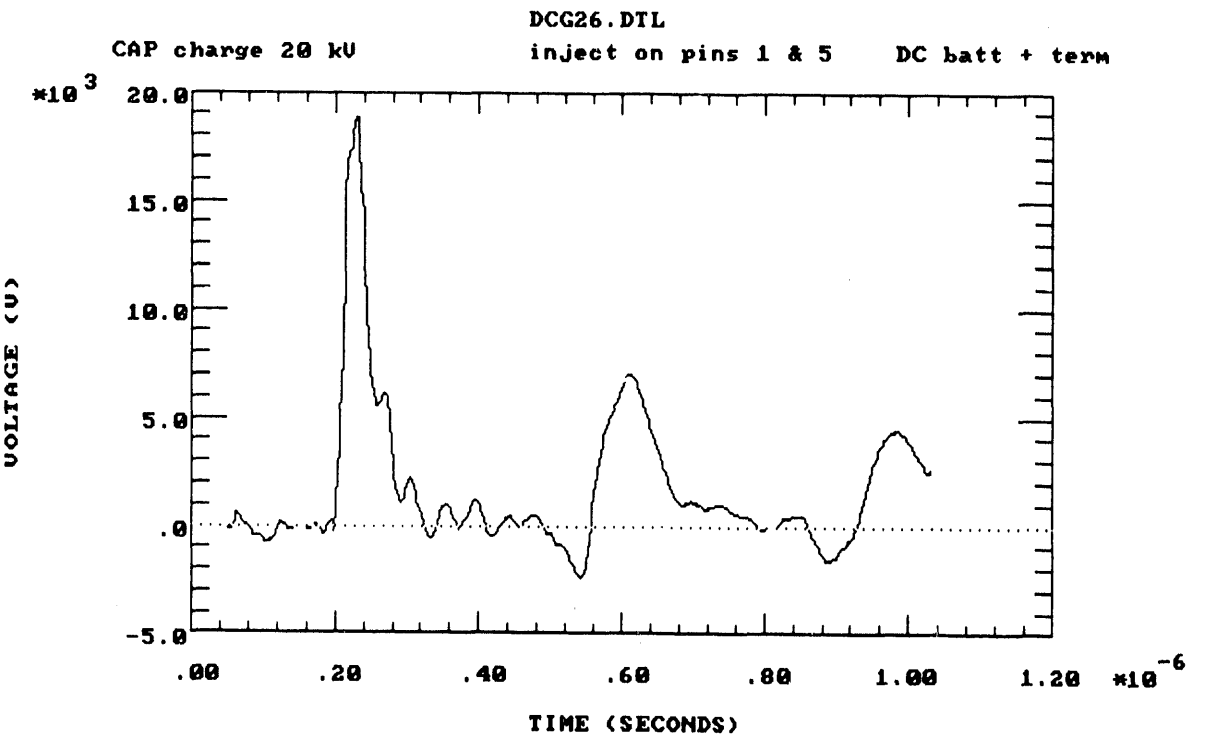

Waveform 13

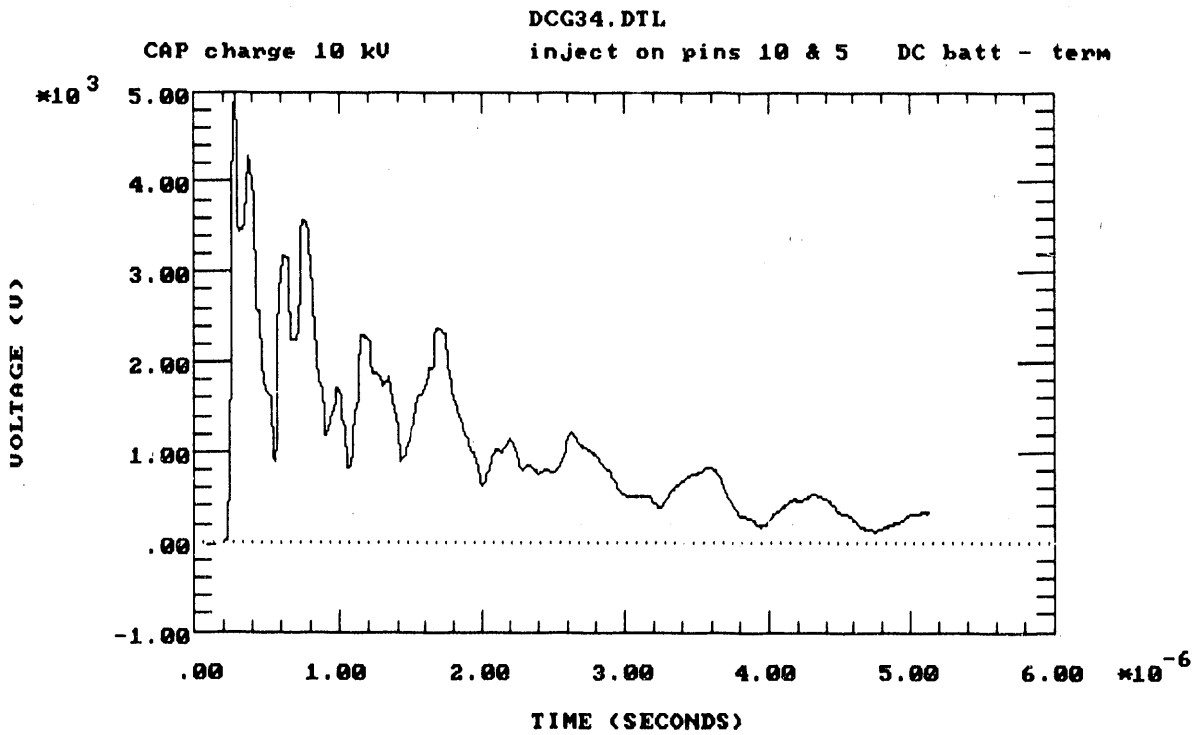

Waveform 14

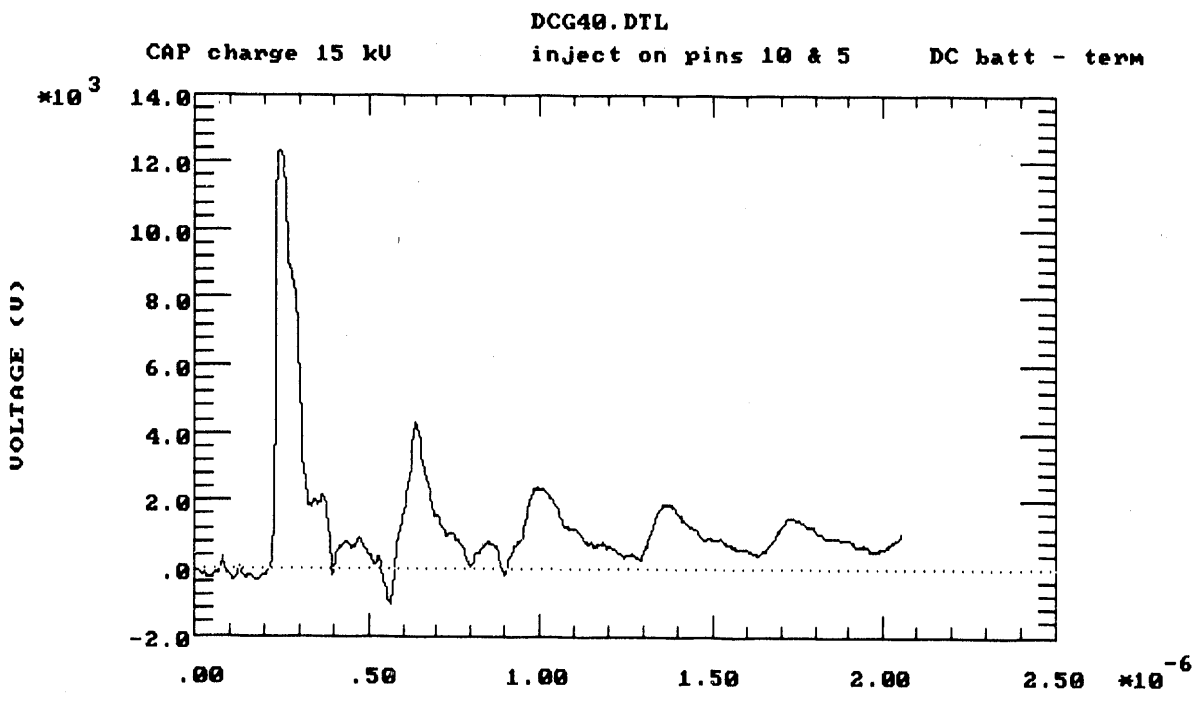

Waveform 15

APPENDIX B

This appendix contains individual plots of 56 predicted waveforms developed in the analysis for field and bus drives, and for bus primary and secondary circuit responses, for both switching transients and HEMP. These plots are included again here because the overlay plots used in Section 4.0 sometimes obscured some of the smaller response waveforms. Each graph presented below is identified by its header, and is referenced to the figure number where it appears in the Section 4.0. In the following plot listing, descriptive titles are shortened as follows: 2 PU switching transients are denoted ST; short-range HEMP is SR; long-range HEMP is LR.

Waveform No.	Fig. No.	Description
1	4.1(a)	ST Bus Current on 500 kV Primary
2	4.1(b)	LR Bus Current Coupled to 500 kV Bus
3	4.1(c)	SR Bus Current Coupled to 500 kV Bus
4	4.3(a)	ST Bus Voltage on 500 kV Primary
5	4.3(b)	LR Bus Voltage Coupled to 500 kV Bus
6	4 3(c)	SR Bus Voltage Coupled to 500 kV Bus
7	4.5(a)	Incident ST E-Field at Ground under Bus
8	4.5(b)	Incident LR E-Field at Ground under Bus
9	4.5(c)	Incident SR E-Field at Ground under Bus
10	4.7(a)	Incident ST H-Field at Ground under Bus
11	4.8(a)	ST E & H Field-Coupled Control Cable Shield Current
12	4.8(b)	LR E & H Field-Coupled Control Cable Shield Current (First Peak)
13	--	LR E & H Field-Coupled Control Cable Shield Current (Second Peak)
14	4.8(c)	SR E & H Field-Coupled Control Cable Shield Current
15	4.10(a) (thin)	ST Total Current Coupling (All Modes) to Shielded Control Cable with 150-ohm Load
16	4.11(a) (thin)	ST Total Voltage Coupling (All Modes) to Shielded Control Cable with 150-ohm Load

Waveform No.	Fig. No.	Description
17	4.12(a) (thin)	LR Total Current Coupling (All Modes) to Shielded Control Cable with 150-ohm Load
18	4.13(a) (thin)	LR Total Voltage Coupling (All Modes) to Shielded Control Cable with 150-ohm Load
19	4.14(a) (thin)	SR Total Current Coupling (All Modes) to Shielded Control Cable with 150-ohm Load
20	4.15(a) (thin)	SR Total Voltage Coupling (All Modes) to Shielded Control Cable with 150-ohm Load
21	4.10(a) (dashed)	ST Total Current Coupling (All Modes) to Shielded Control Cable with CT-Lead Load
22	4.11(a) (dashed)	ST Total Voltage Coupling (All Modes) to Shielded Control Cable with CT-Lead Load
23	4.12(a) (dashed)	LR Total Current Coupling (All Modes) to Shielded Control Cable with CT-Lead Load
24	4.13(a) (dashed)	LR Total Voltage Coupling (All Modes) to Shielded Control Cable with CT-Lead Load
25	4.14(a) (dashed)	SR Total Current Coupling (All Modes) to Shielded Control Cable with CT-Lead Load
26	4.15(a) (dashed)	SR Total Voltage Coupling (All Modes) to Shielded Control Cable with CT-Lead Load
27	4.10(a) (bold)	ST Total Current Coupling (All Modes) to Shielded Control Cable w/Battery-Lead Load
28	4.11(a) (bold)	ST Total Voltage Coupling (All Modes) to Shielded Control Cable w/Battery-Lead Load
29	4.12(a) (bold)	LR Total Current Coupling (All Modes) to Shielded Control Cable w/Battery-Lead Load
30	4.13(a) (bold)	LR Total Voltage Coupling (All Modes) to Shielded Control Cable w/Battery-Lead Load
31	4.14(a) (bold)	SR Total Current Coupling (All Modes) to Shielded Control Cable w/Battery-Lead Load
32	4.15(a) (bold)	SR Total Voltage Coupling (All Modes) to Shielded Control Cable w/Battery-Lead Load
33	4.19(a) (bold)	ST Z_T Mode Current Coupled to Shielded Control Cable with CT Load
34	4.19(c) (bold)	ST Z_T Mode Voltage Coupled to Shielded Control Cable with CT Load
35	4.20(a) (bold)	LR Z_T Mode Current Coupled to Shielded Control Cable with CT Load
36	4.20(c) (bold)	LR Z_T Mode Voltage Coupled to Shielded Control Cable with CT Load

Waveform No.	Fig. No.	Description
37	4.21(a) (bold)	SR Z_T Mode Current Coupled to Shielded Control Cable with CT Load
38	4.21(c) (bold)	SR Z_T Mode Voltage Coupled to Shielded Control Cable with CT Load
39	4.19(a) (dashed)	ST Pigtail Mode Current Coupled to Shielded Control Cable with CT Load
40	4.19(c) (dashed)	ST Pigtail Mode Voltage Coupled to Shielded Control Cable with CT Load
41	4.20(a) (dashed)	LR Pigtail Mode Current Coupled to Shielded Control Cable with CT Load
42	4.20(c) (dashed)	LR Pigtail Mode Voltage Coupled to Shielded Control Cable with CT Load
43	4.21(a) (dashed)	SR Pigtail Mode Current Coupled to Shielded Control Cable with CT Load
44	4.21(c) (dashed)	SR Pigtail Mode Voltage Coupled to Shielded Control Cable with CT Load
45	4.19(a) (thin)	ST Conducted Mode Current Coupled to Shielded Control Cable with CT Load
46	4.19(c) (thin)	ST Conducted Mode Voltage Coupled to Shielded Control Cable with CT Load
47	4.20(a) (thin)	LR Conducted Mode Current Coupled to Shielded Control Cable with CT Load
48	4.20(c) (thin)	LR Conducted Mode Voltage Coupled to Shielded Control Cable with CT Load
49	4.21(a) (thin)	SR Conducted Mode Current Coupled to Shielded Control Cable with CT Load
50	4.21(c) (thin)	SR Conducted Mode Voltage Coupled to Shielded Control Cable with CT Load
51	4.22(a)	ST Total Current Coupling (All Modes) to Unshielded Control Cable w/Batt.-Lead Load
52	4.24(a)	ST Total Voltage Coupling (All Modes) to Unshielded Control Cable w/Batt.-Lead Load
53	4.22(b)	LR Total Current Coupling (All Modes) to Unshielded Control Cable w/Batt.-Lead Load
54	4.24(b)	LR Total Voltage Coupling (All Modes) to Unshielded Control Cable w/Batt.-Lead Load
55	4.22(c)	SR Total Current Coupling (All Modes) to Unshielded Control Cable w/Batt.-Lead Load
56	4.24(c)	SR Total Voltage Coupling (All Modes) to Unshielded Control Cable w/Batt.-Lead Load

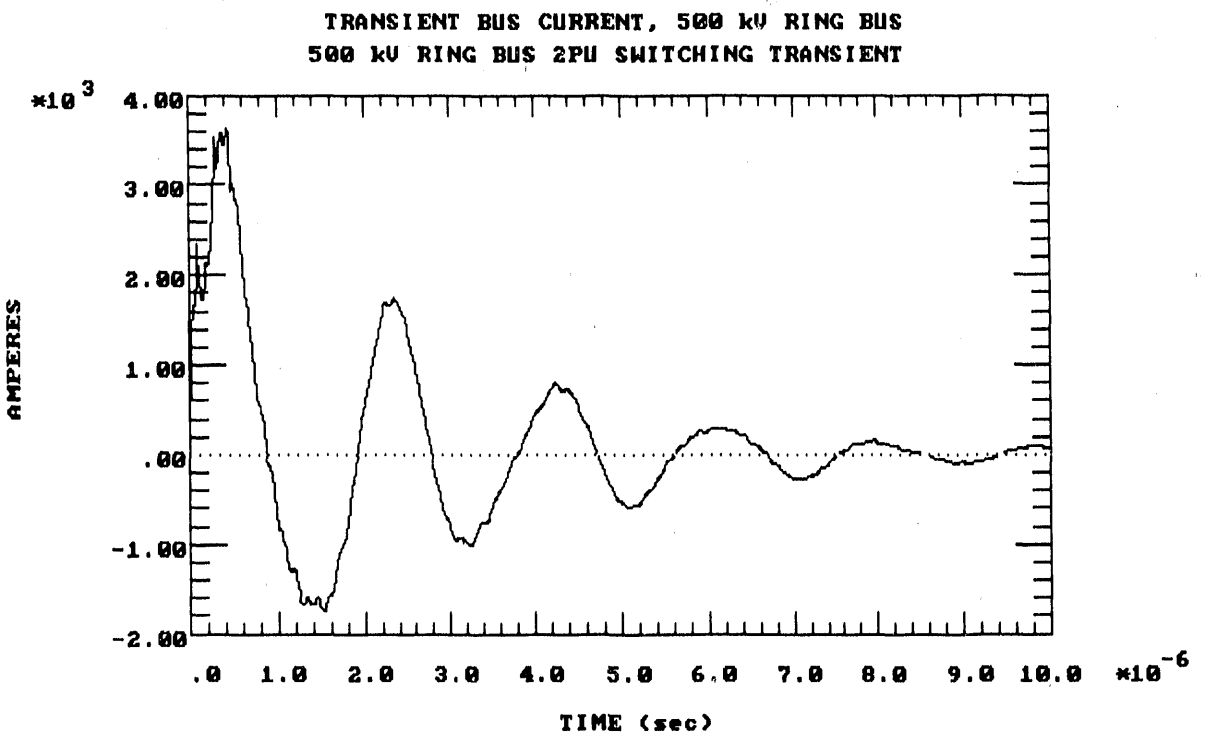

Waveform 1

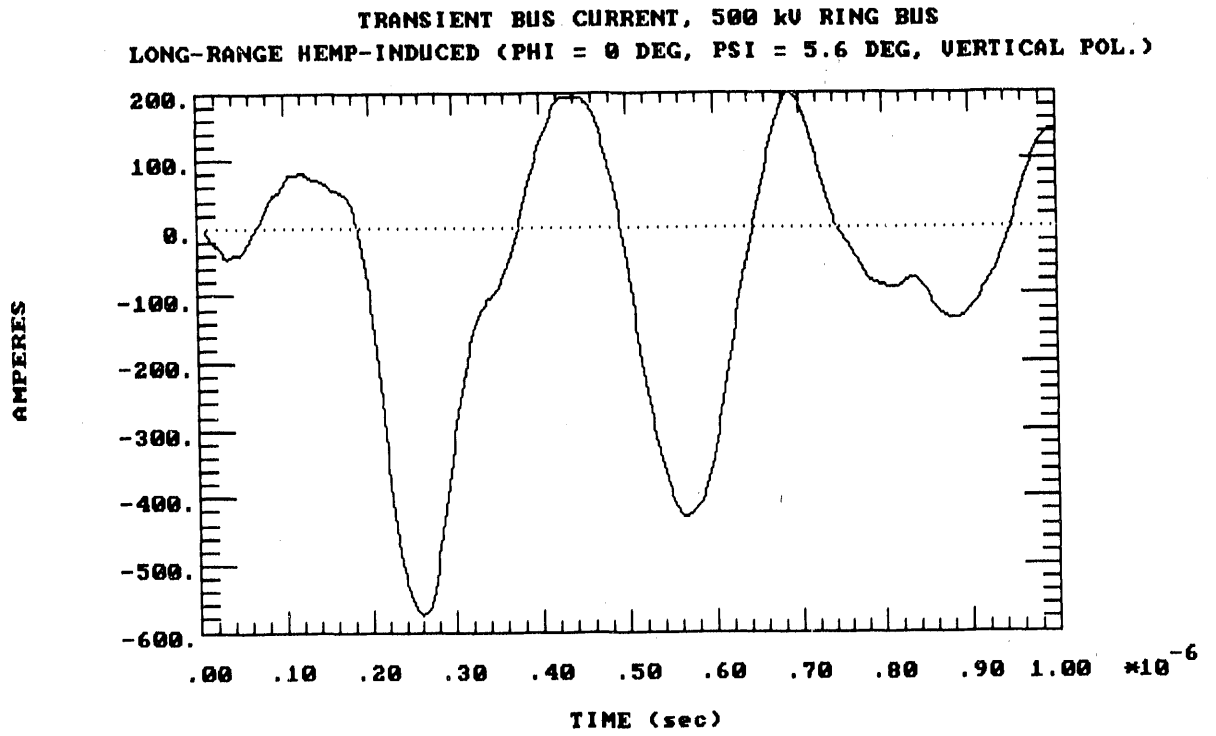

Waveform 2

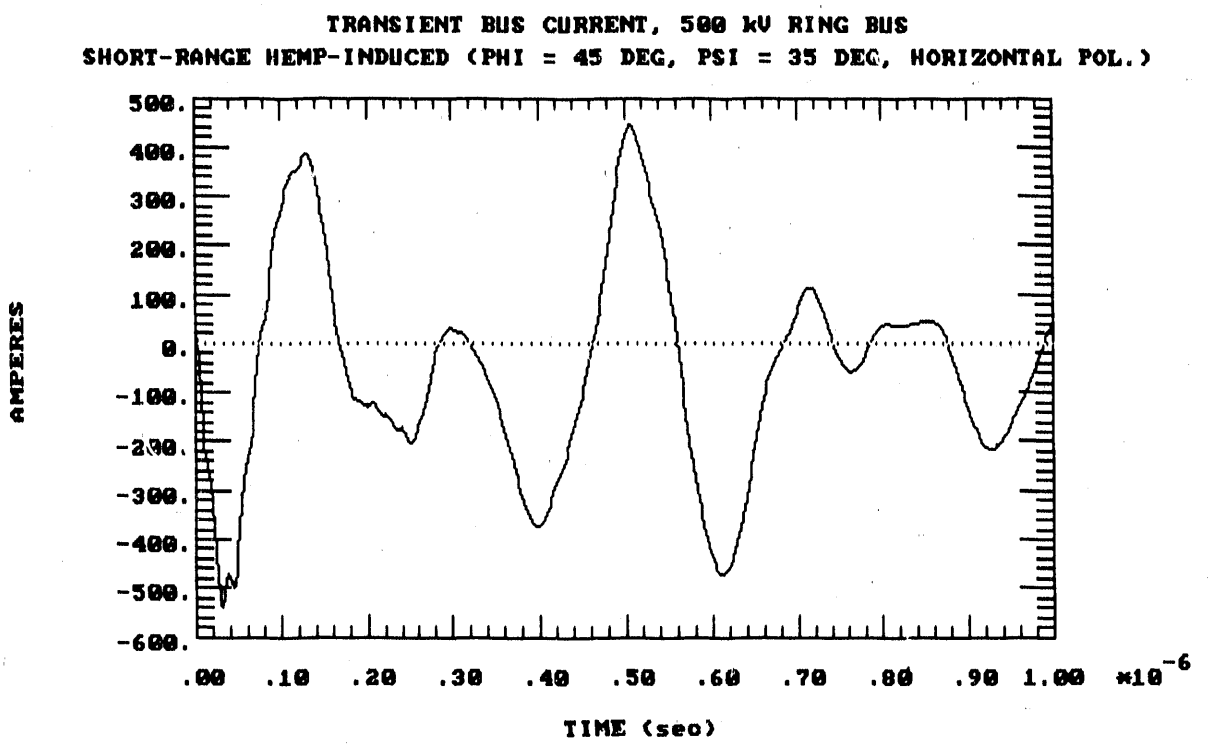

Waveform 3

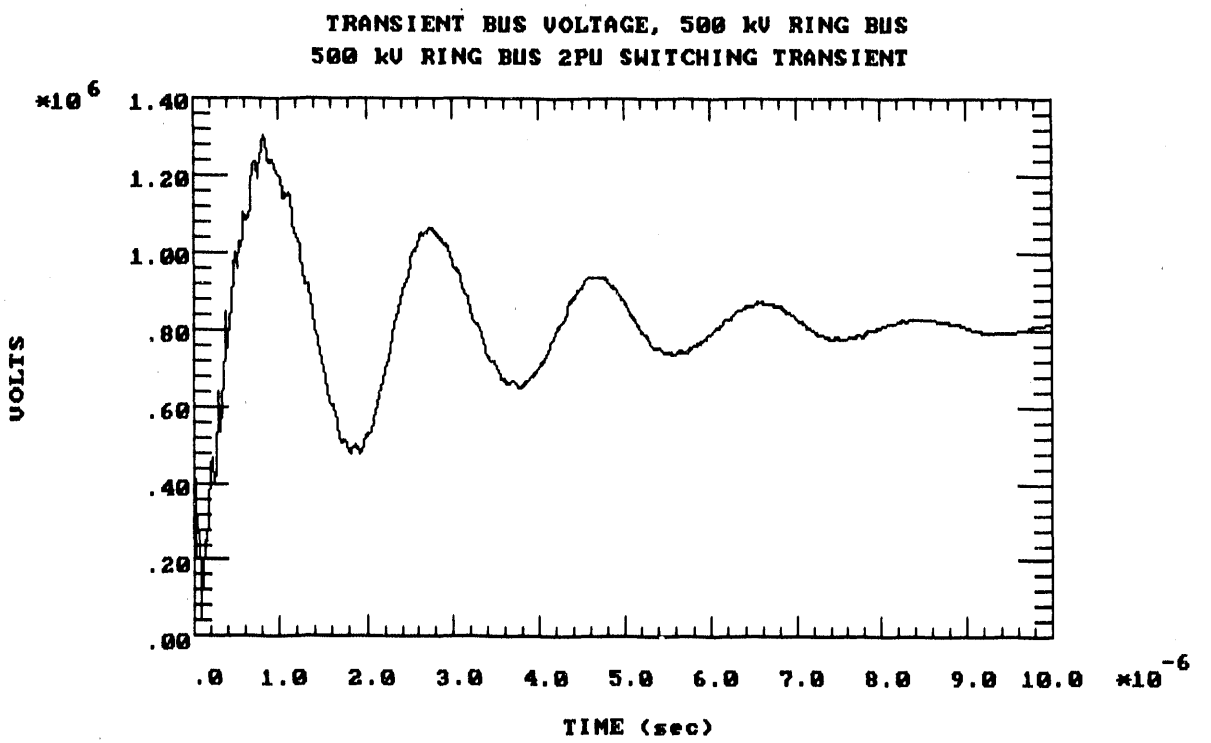

Waveform 4

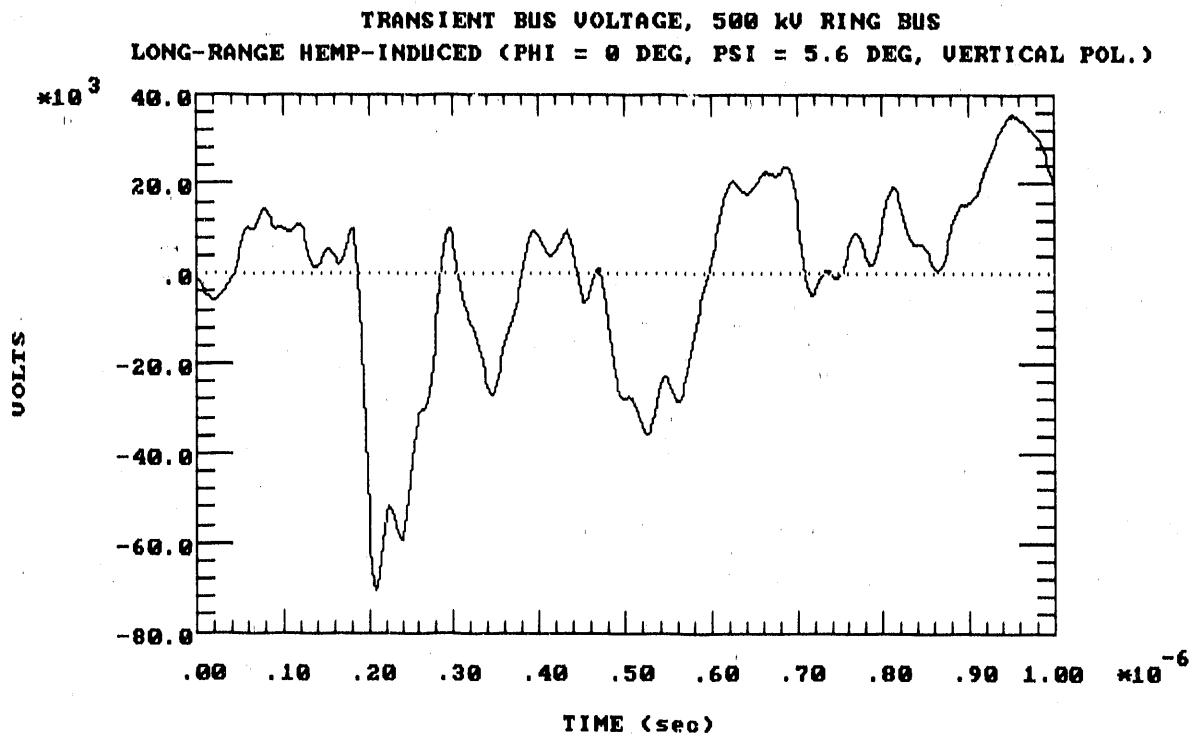

Waveform 5

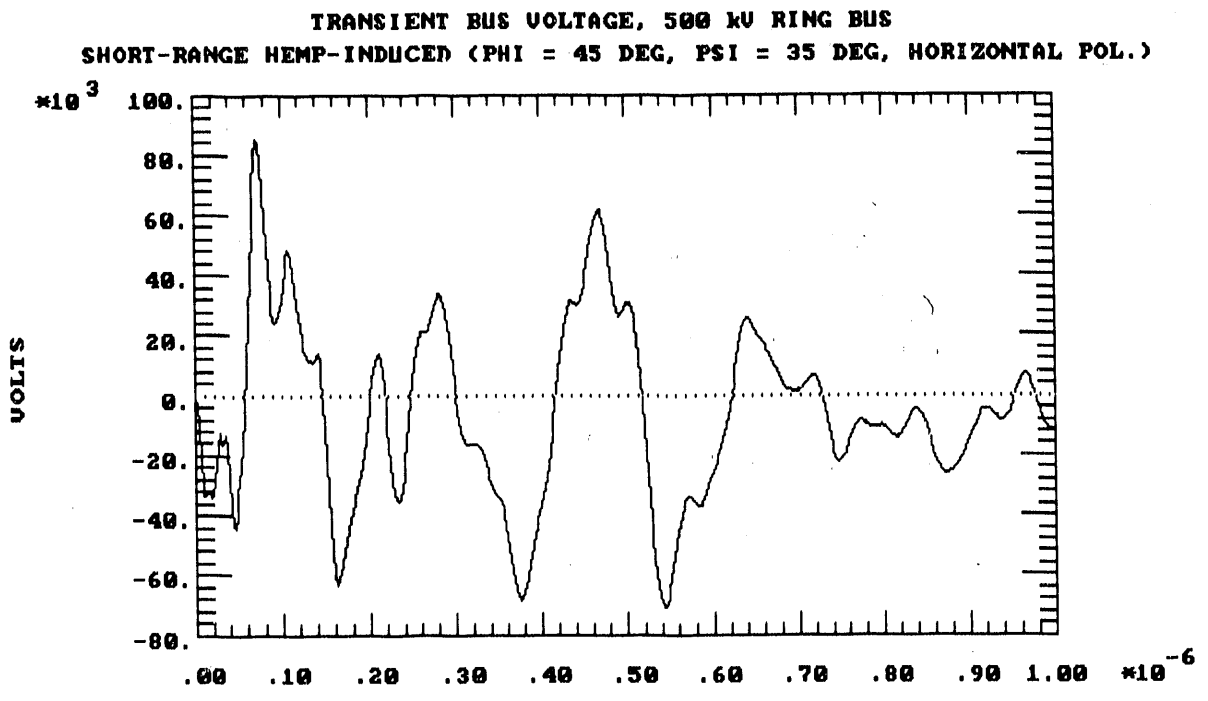

Waveform 6

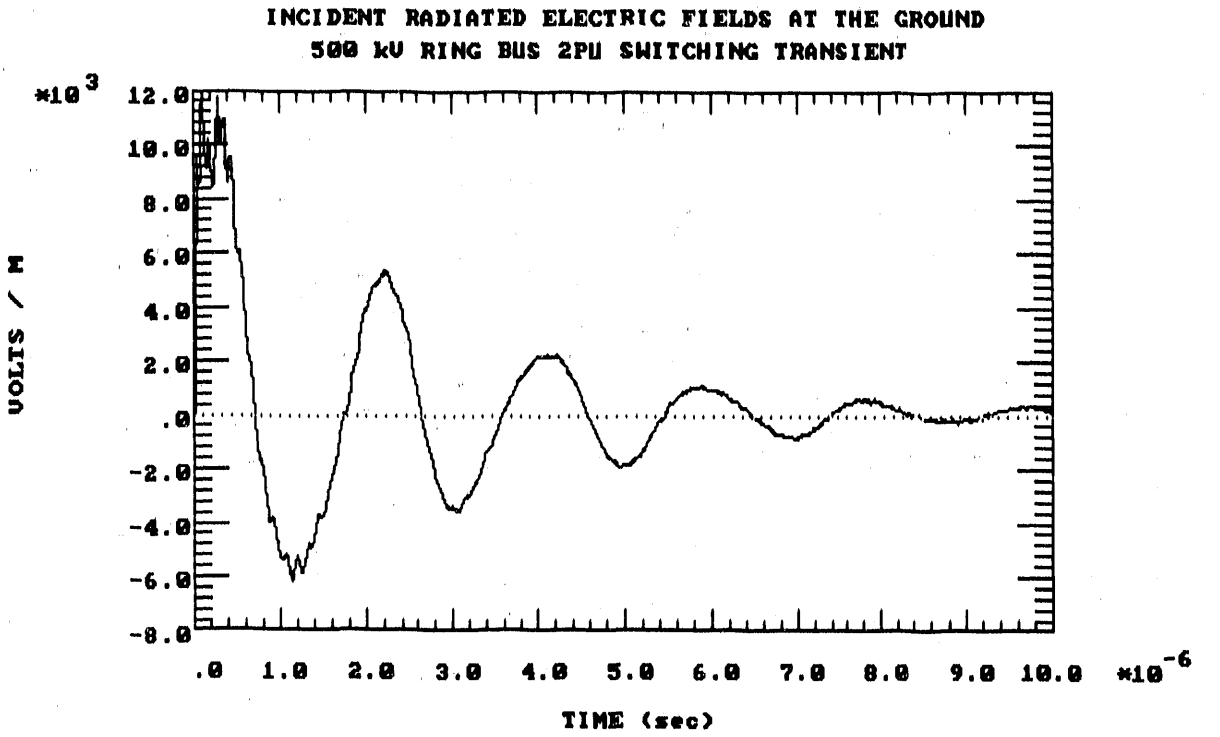

Waveform 7

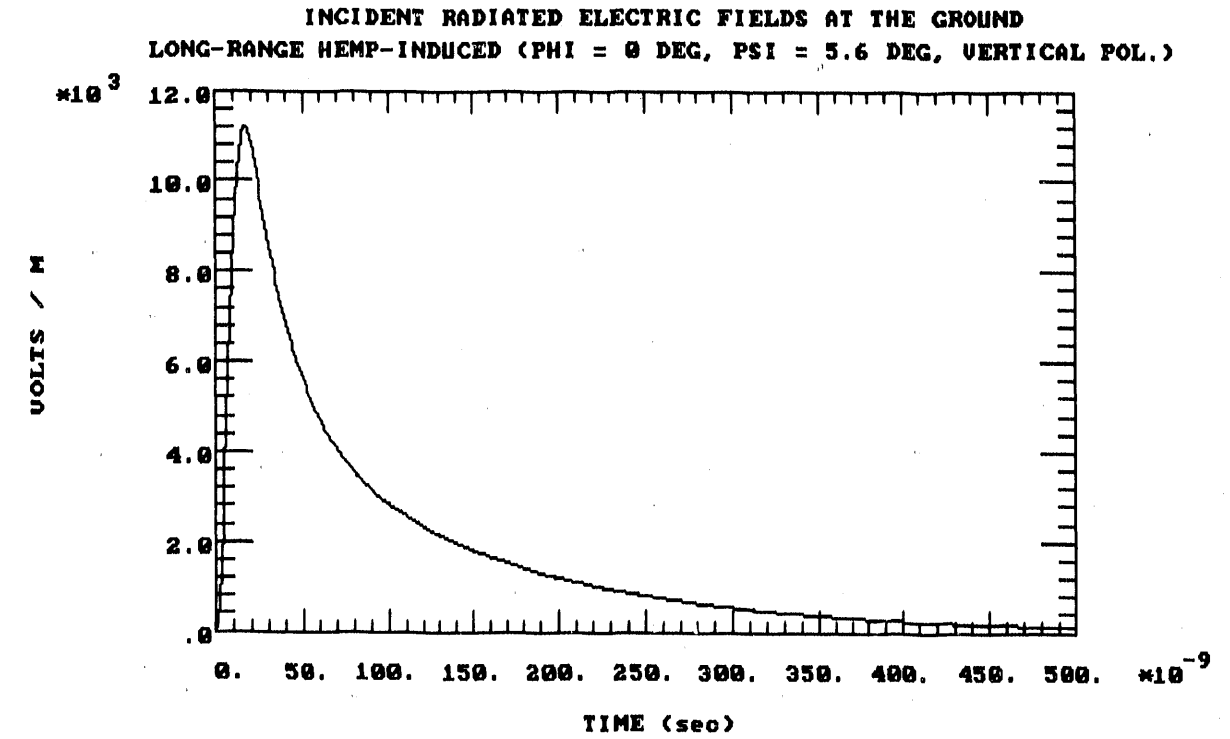

Waveform 8

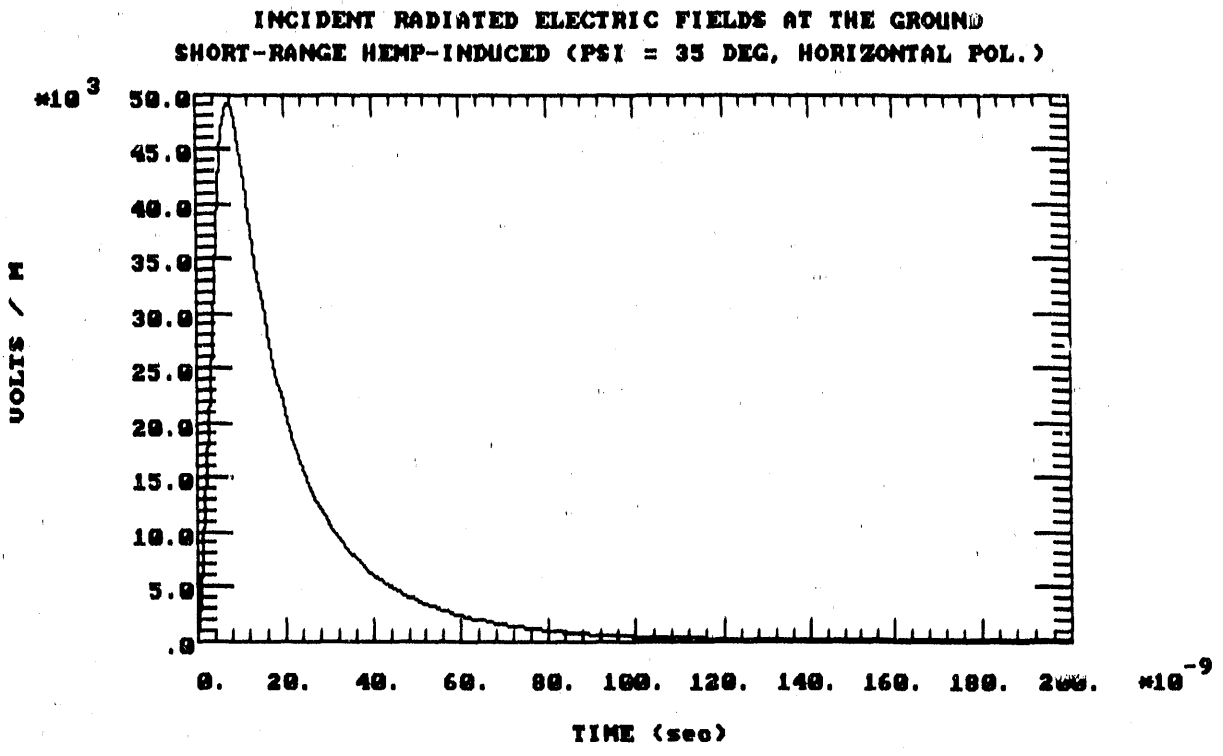

Waveform 9

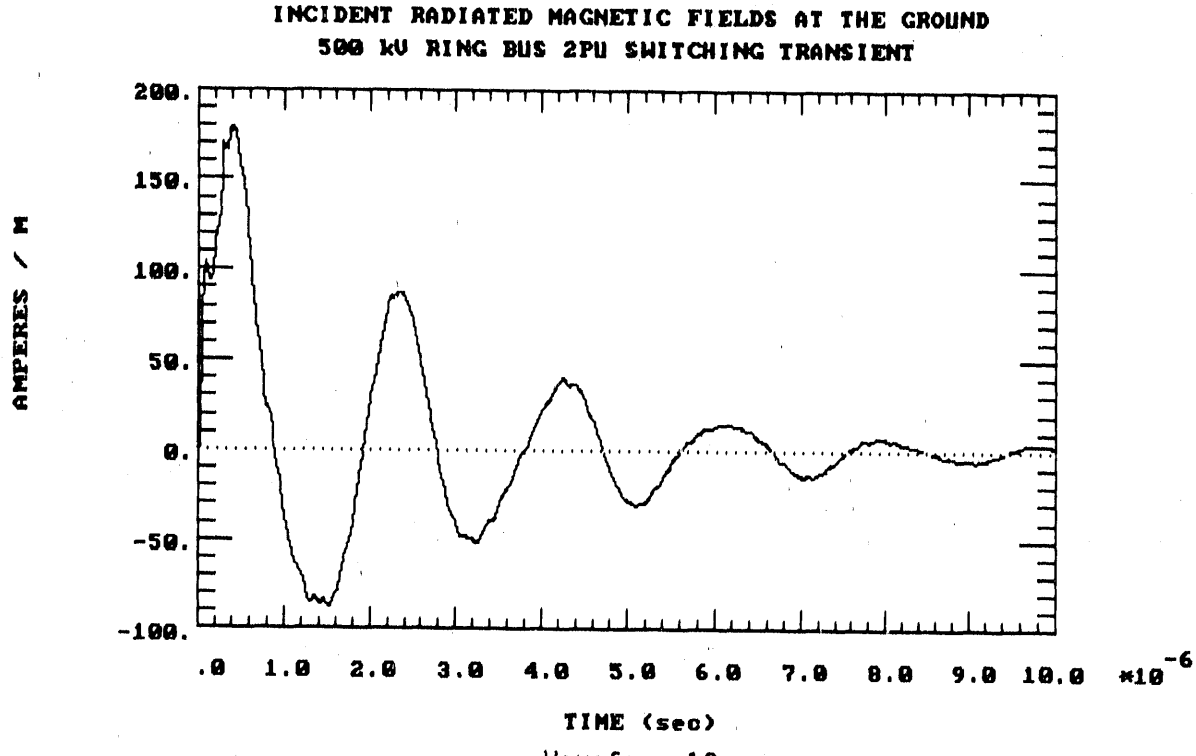

Waveform 10

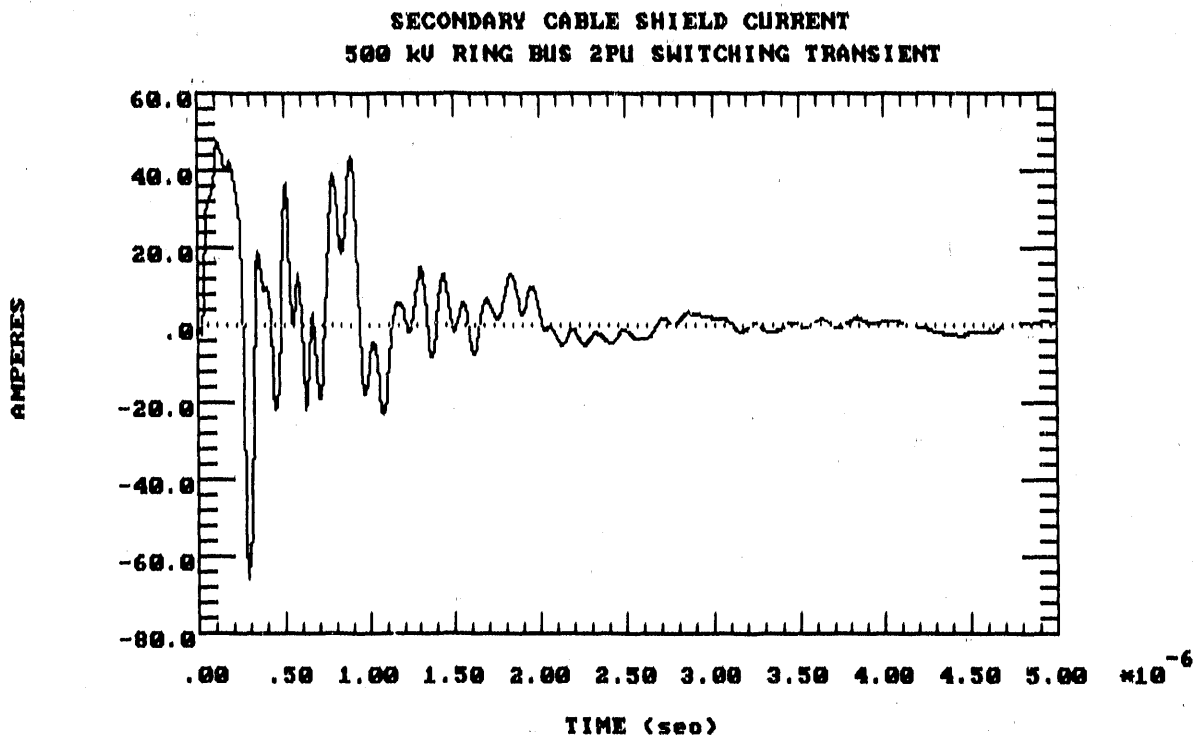

Waveform 11

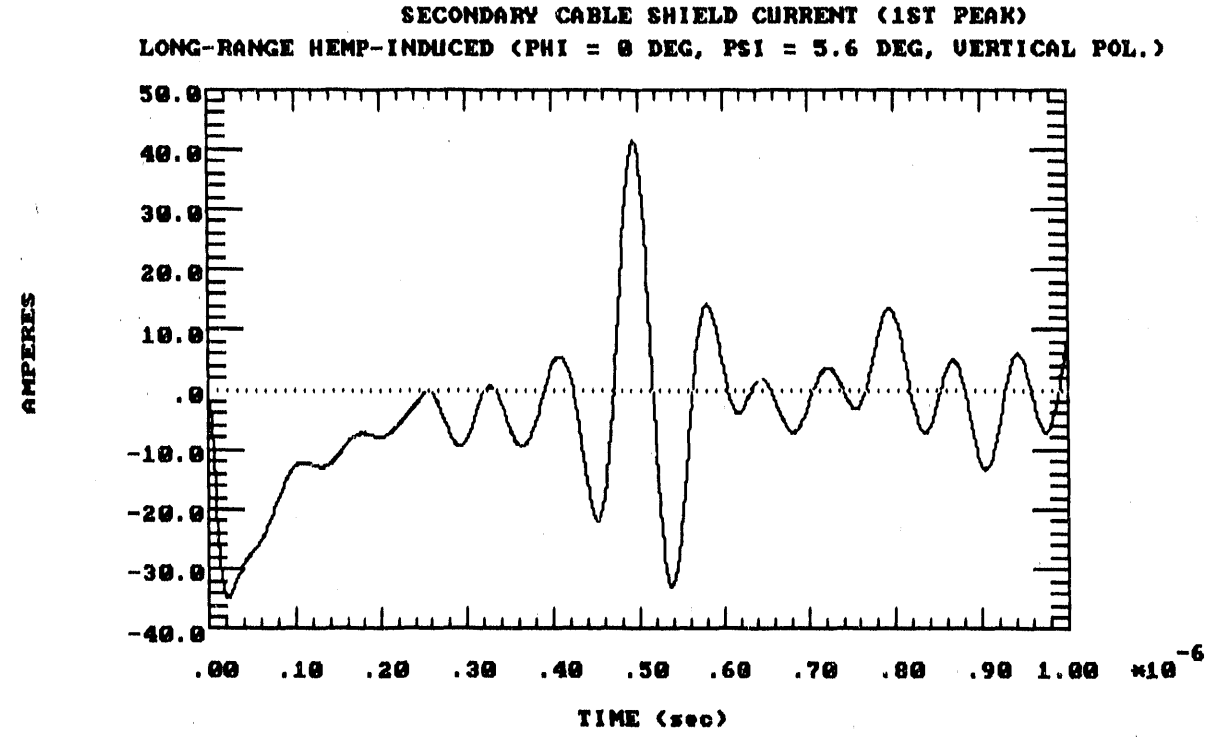

Waveform 12

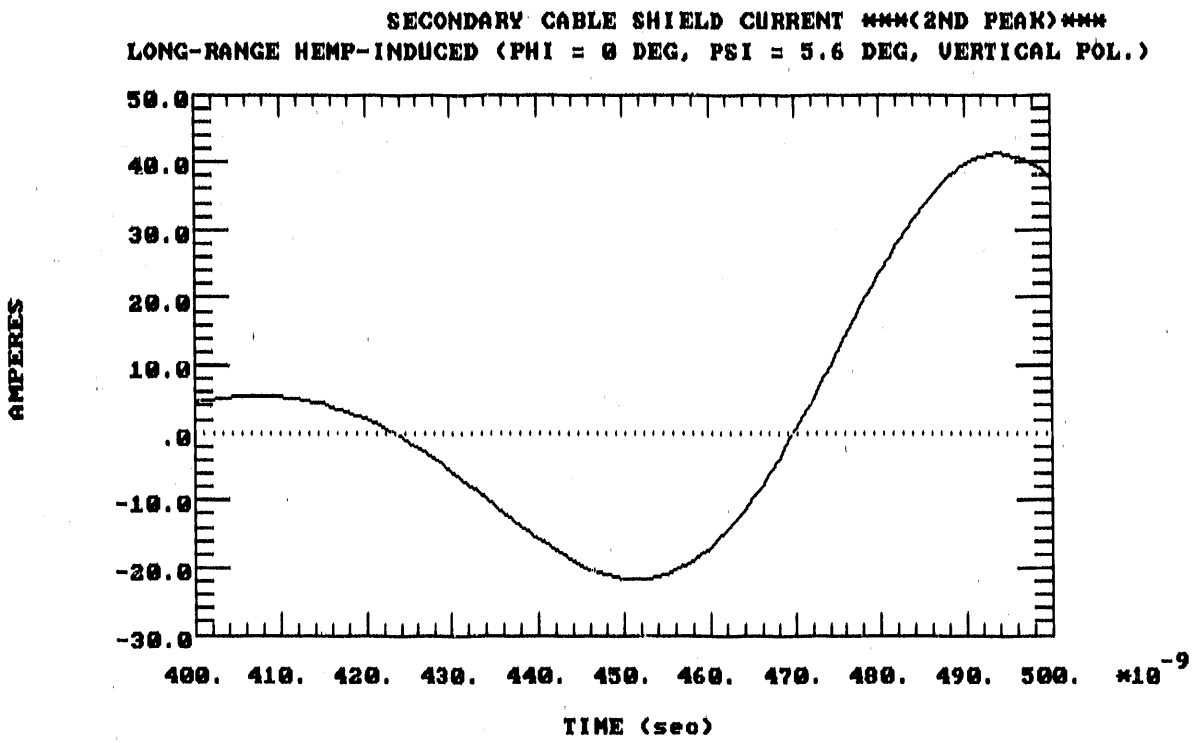

Waveform 13

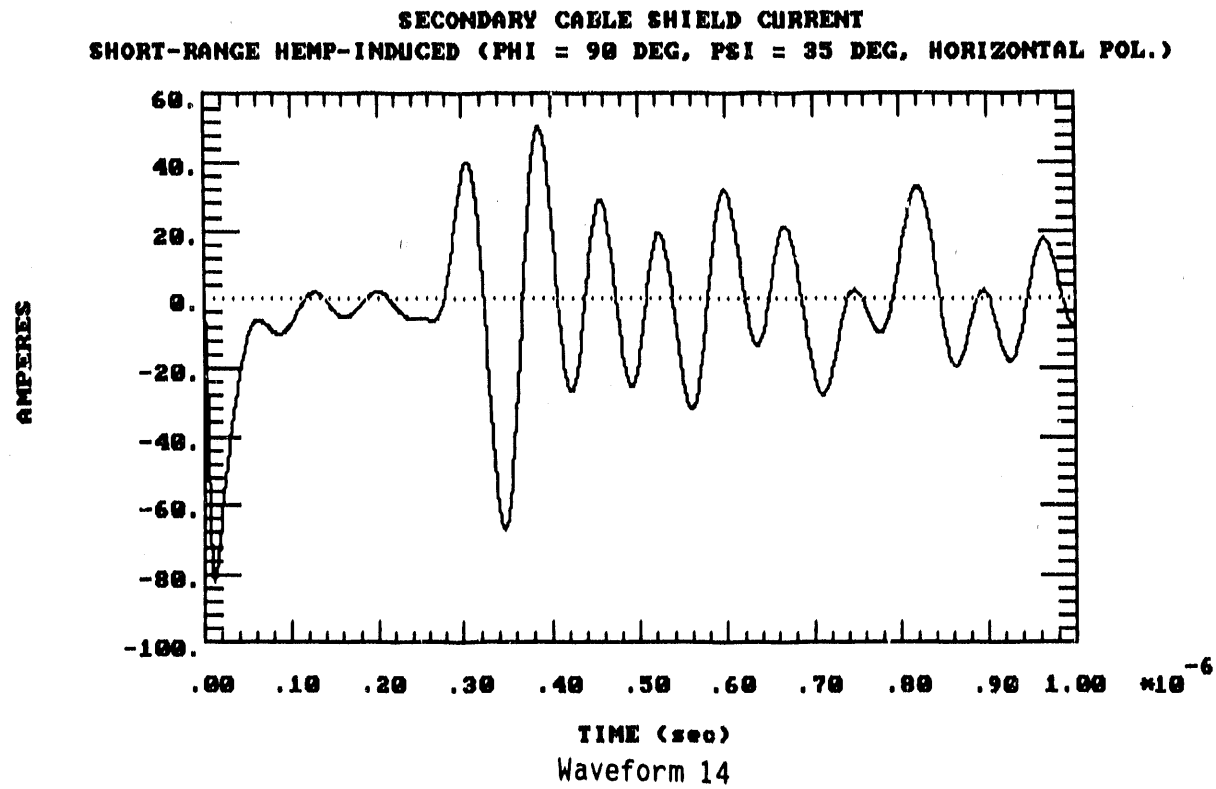

Waveform 14

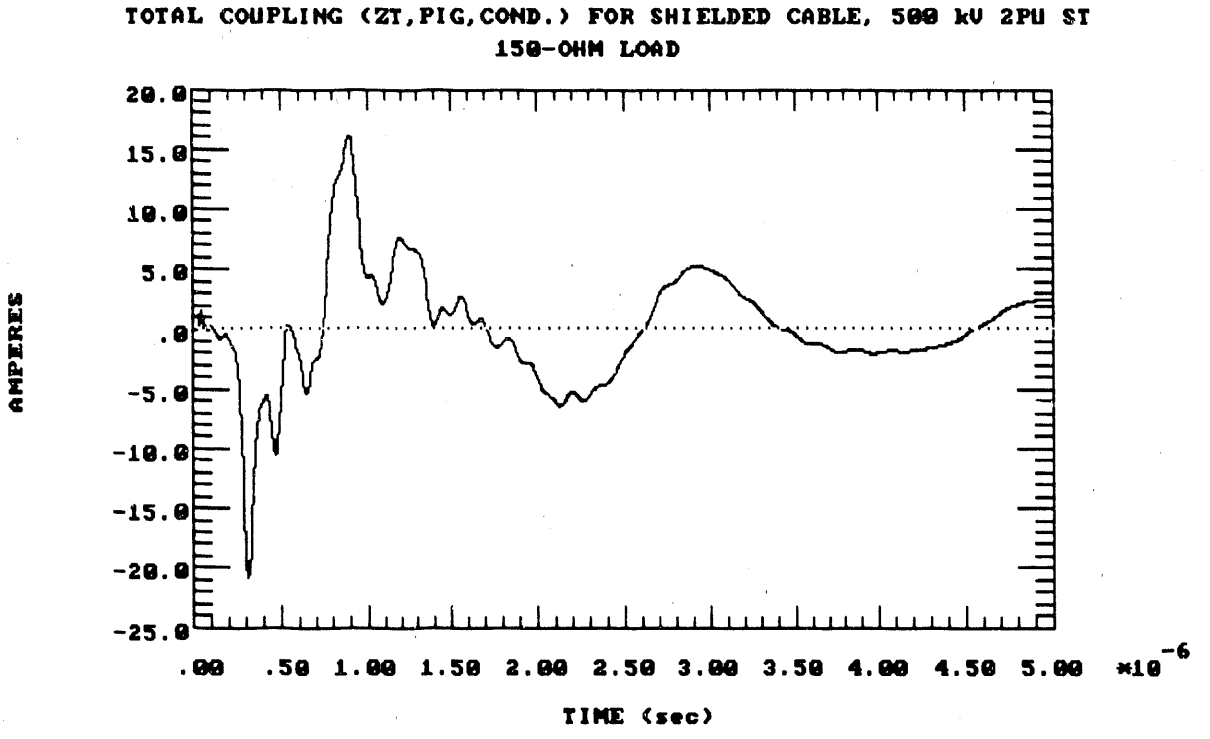

Waveform 15

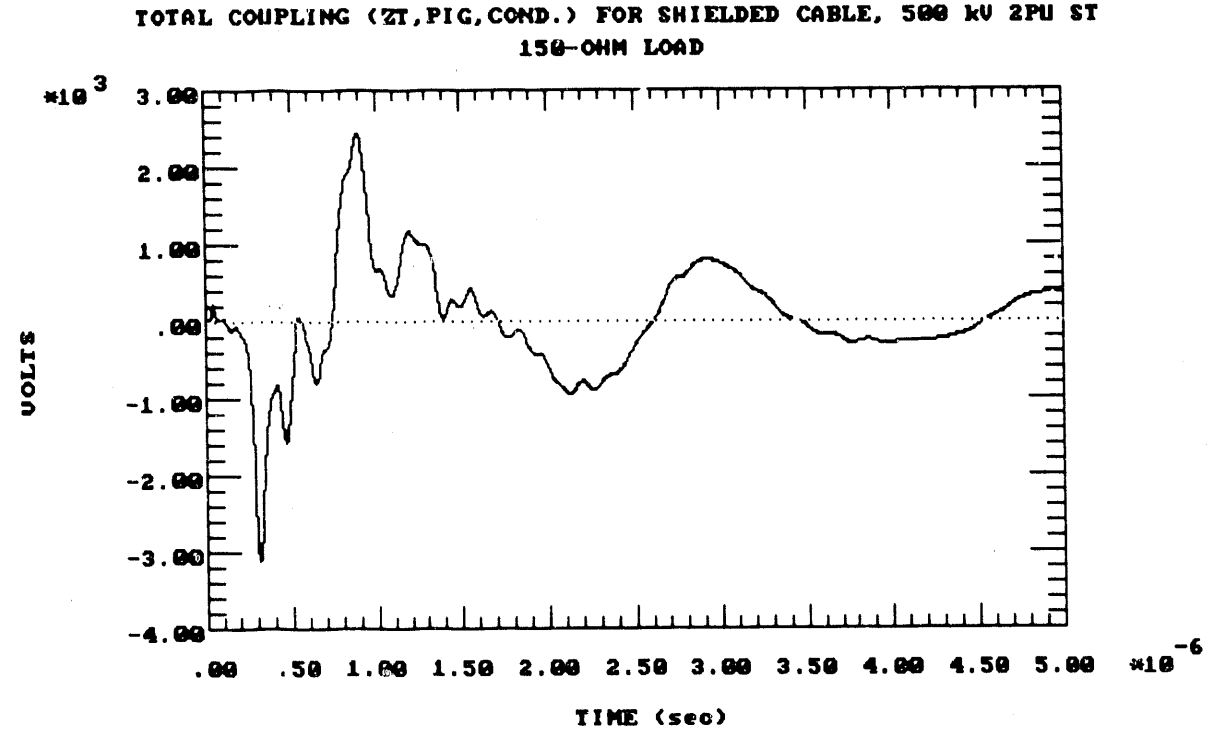

Waveform 16

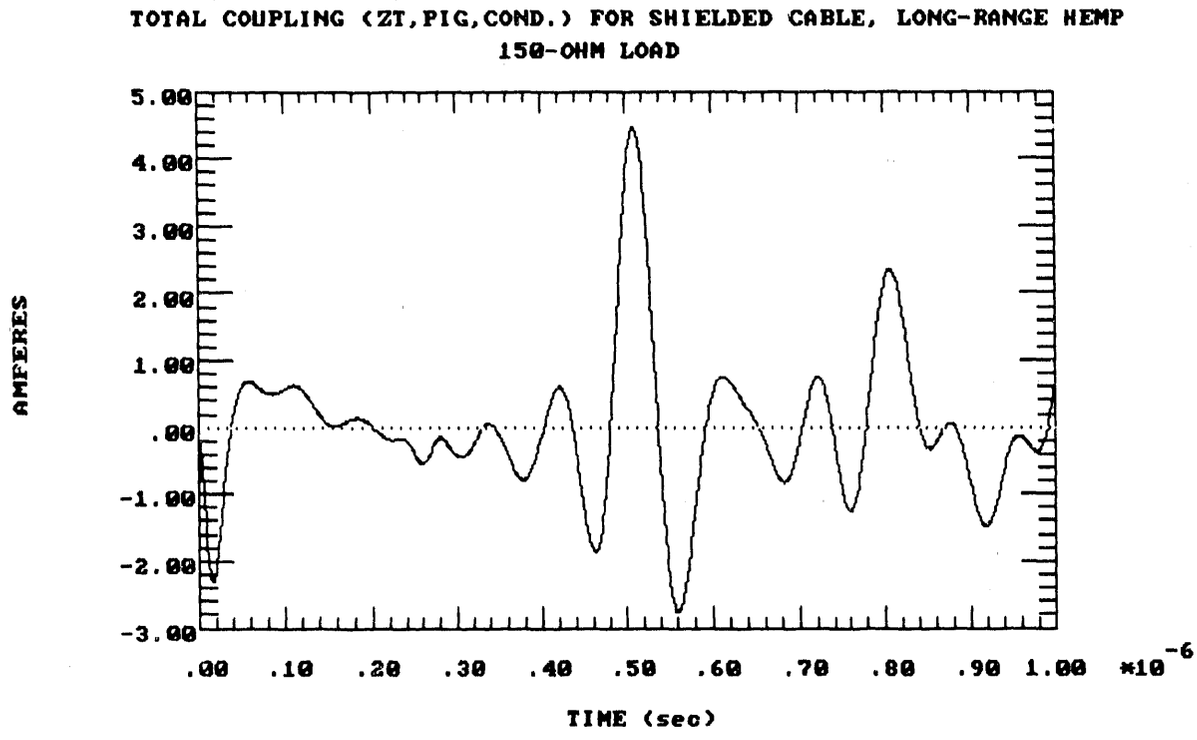

Waveform 17

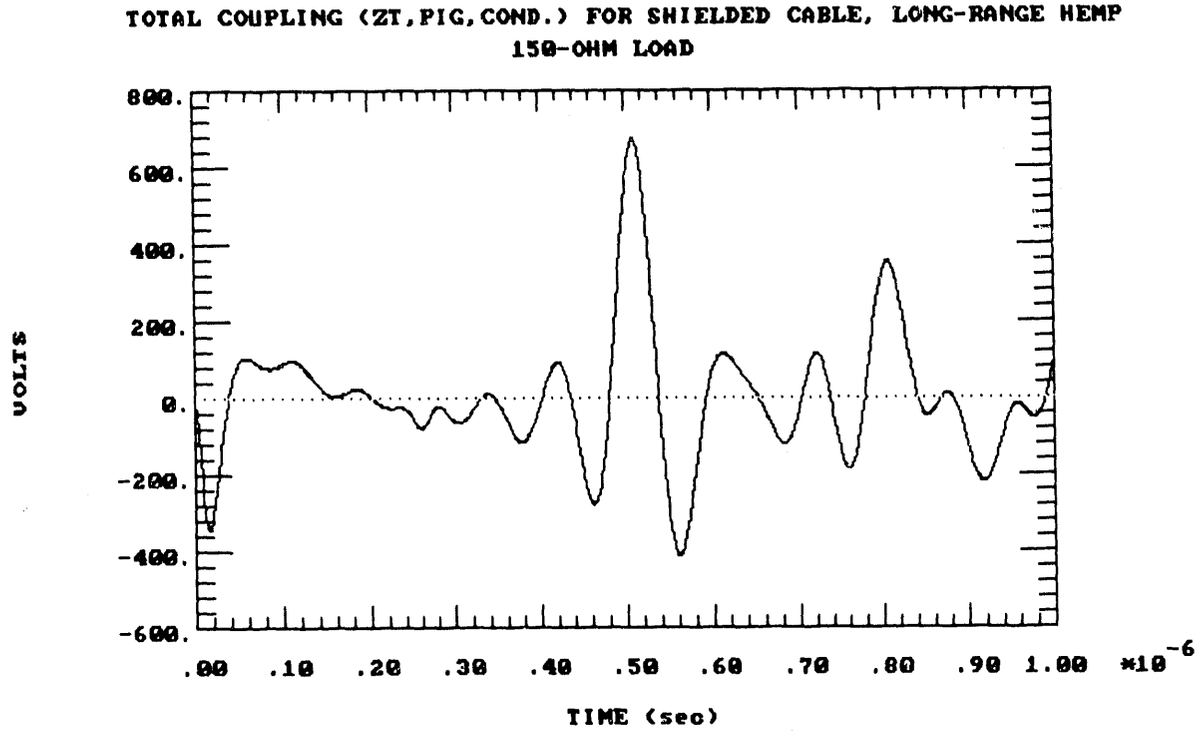

Waveform 18

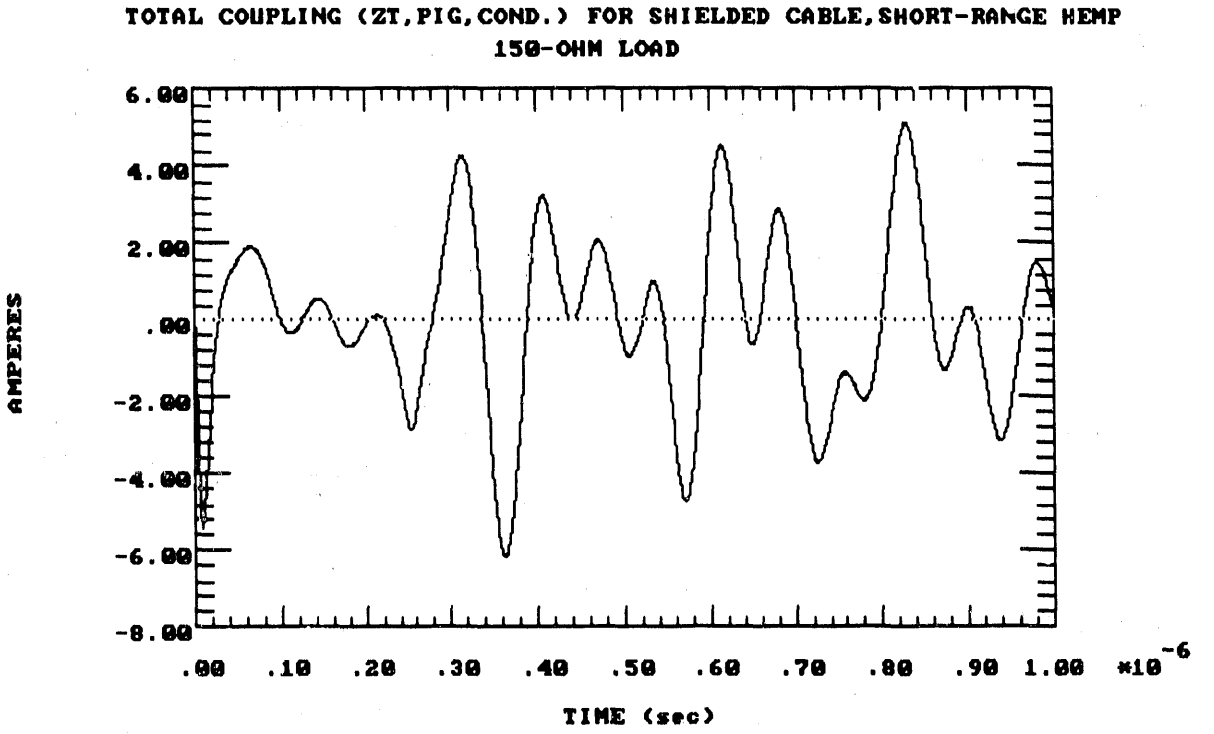

Waveform 19

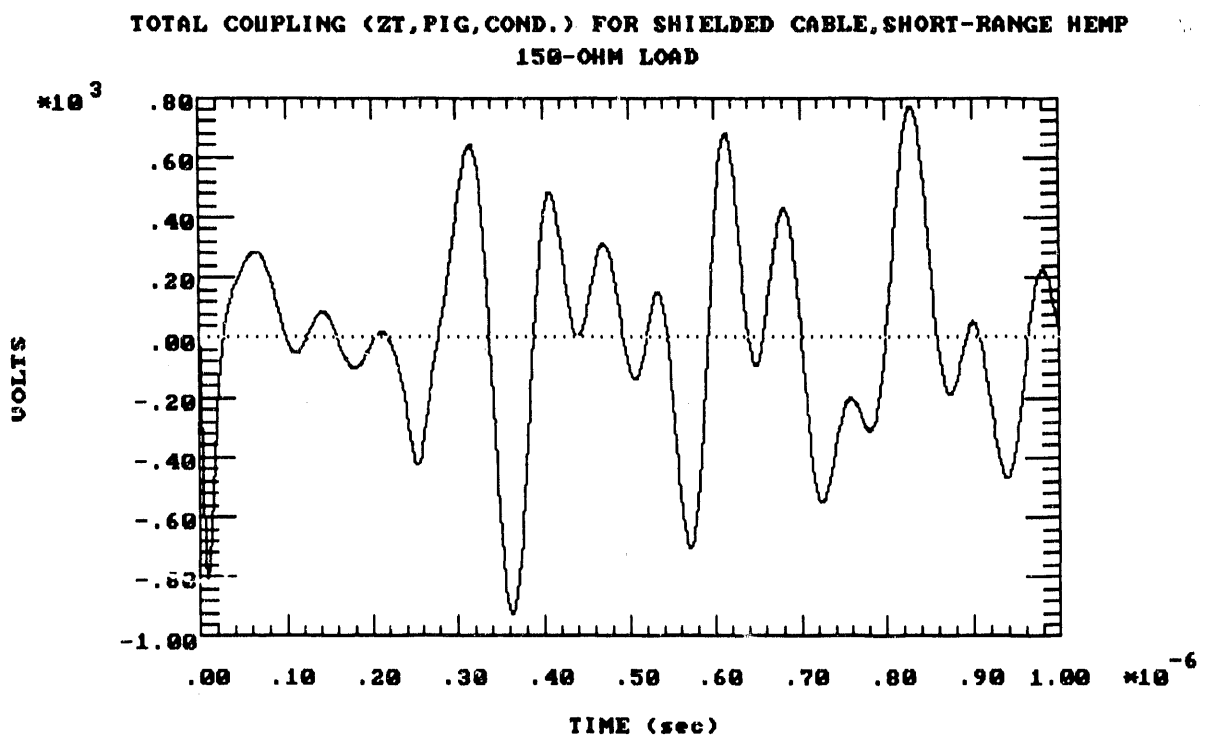

Waveform 20

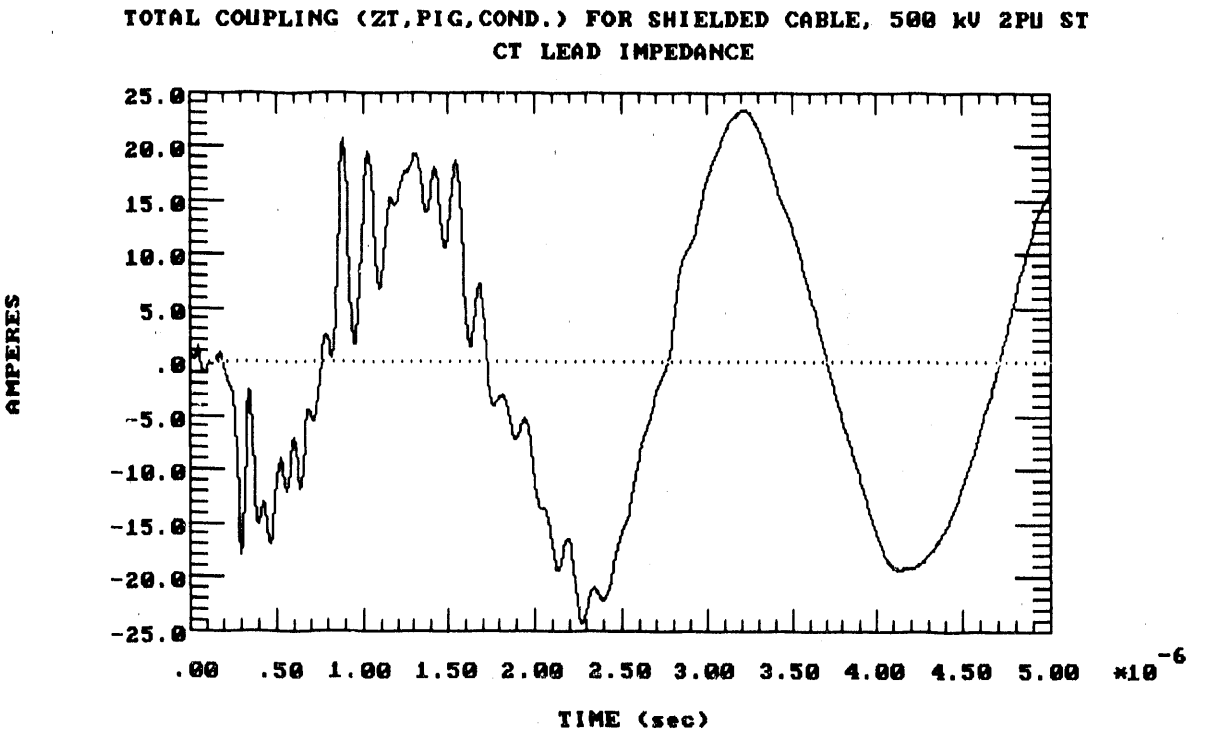

Waveform 21

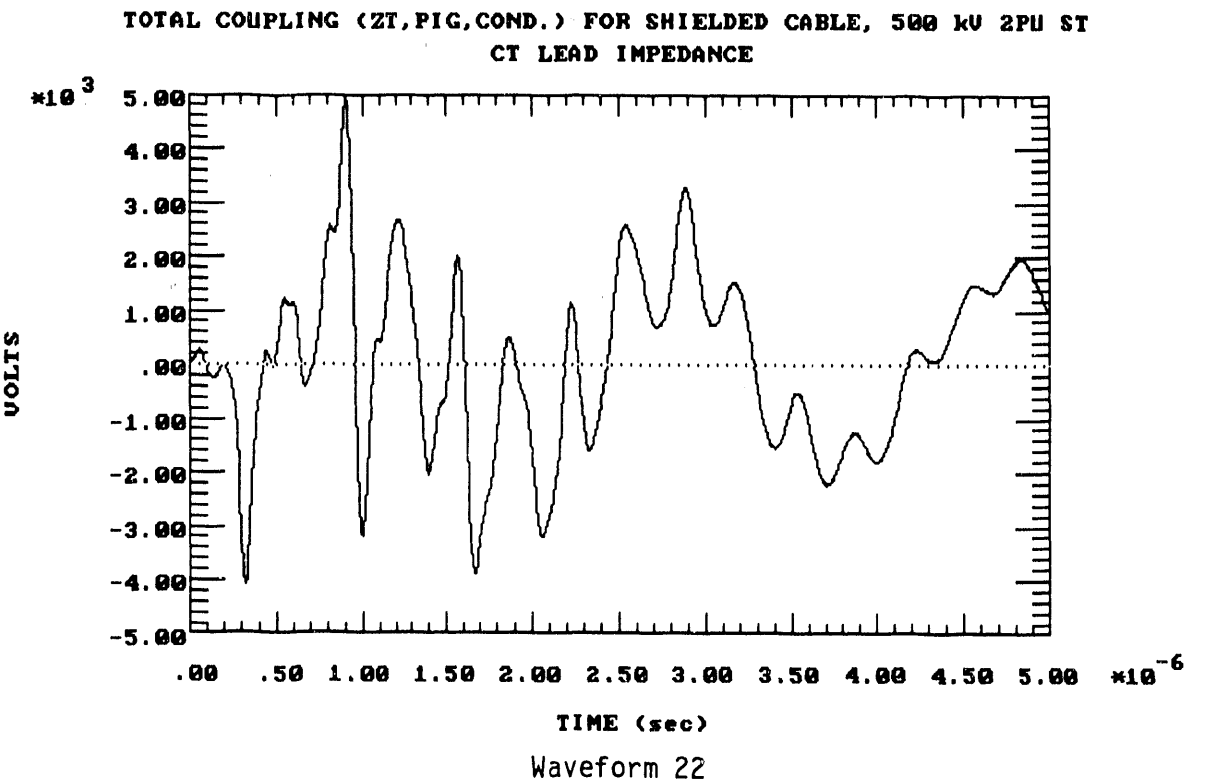

Waveform 22

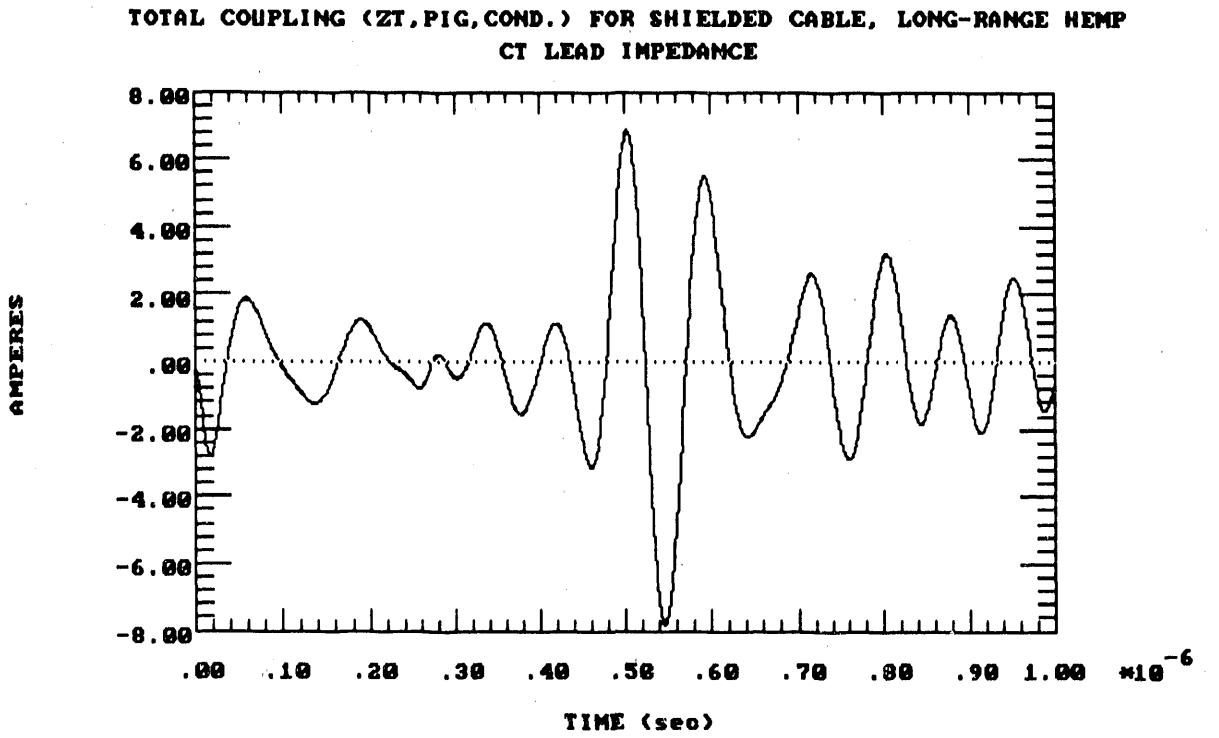

Waveform 23

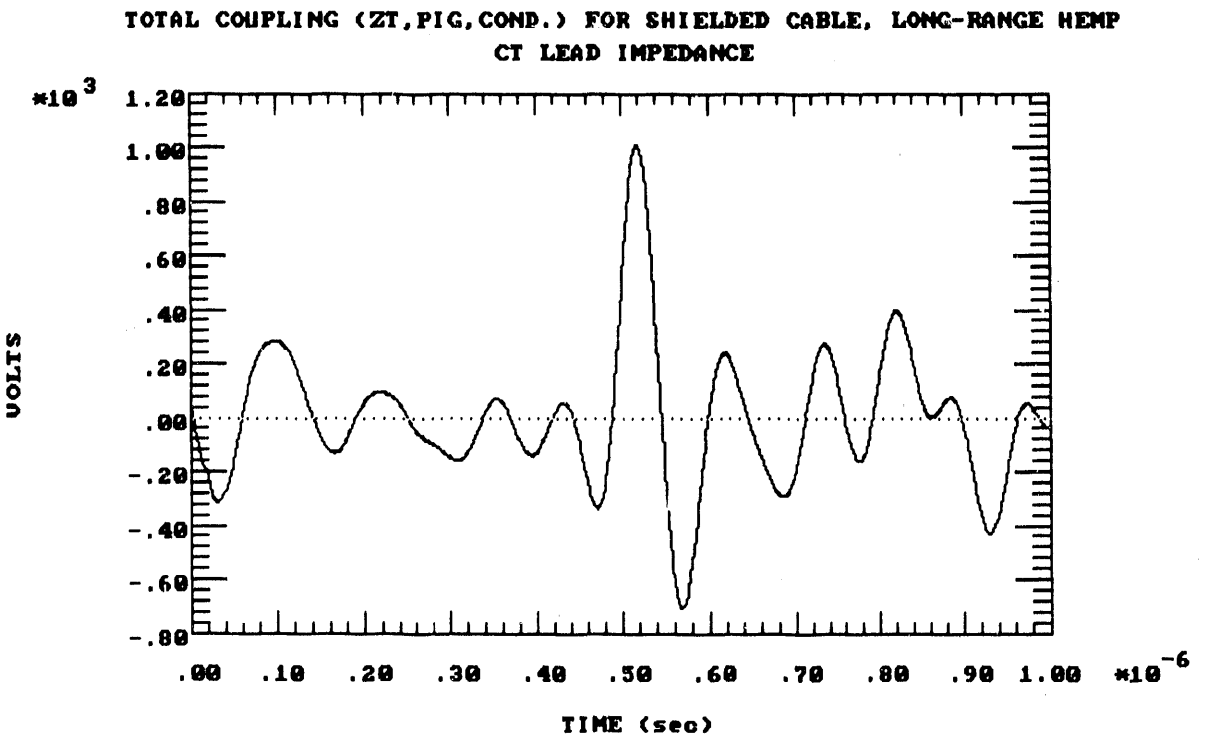

Waveform 24

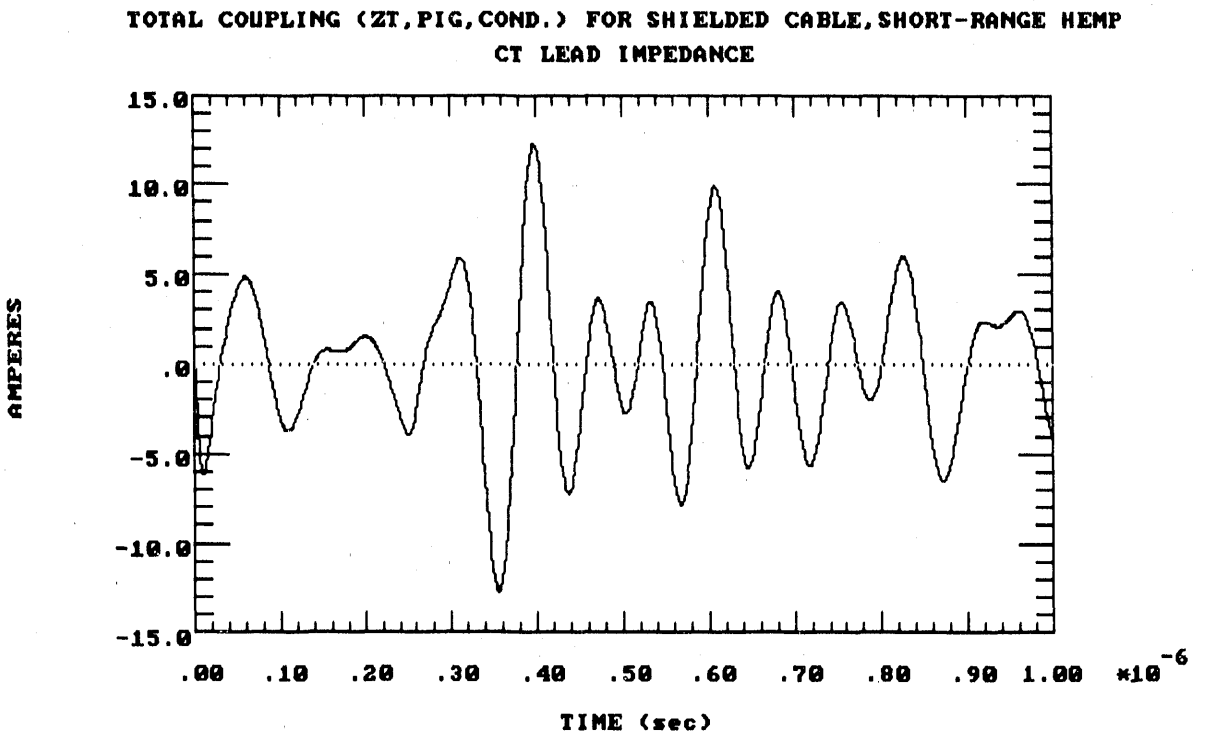

Waveform 25

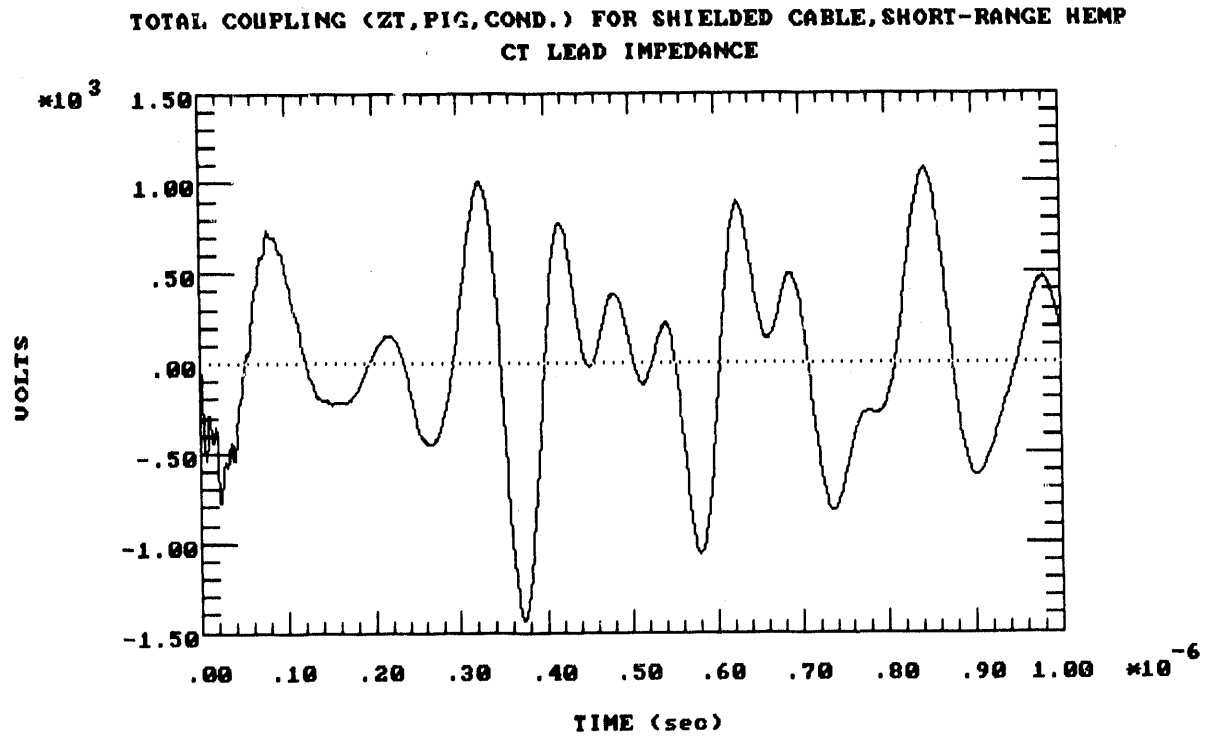

Waveform 26

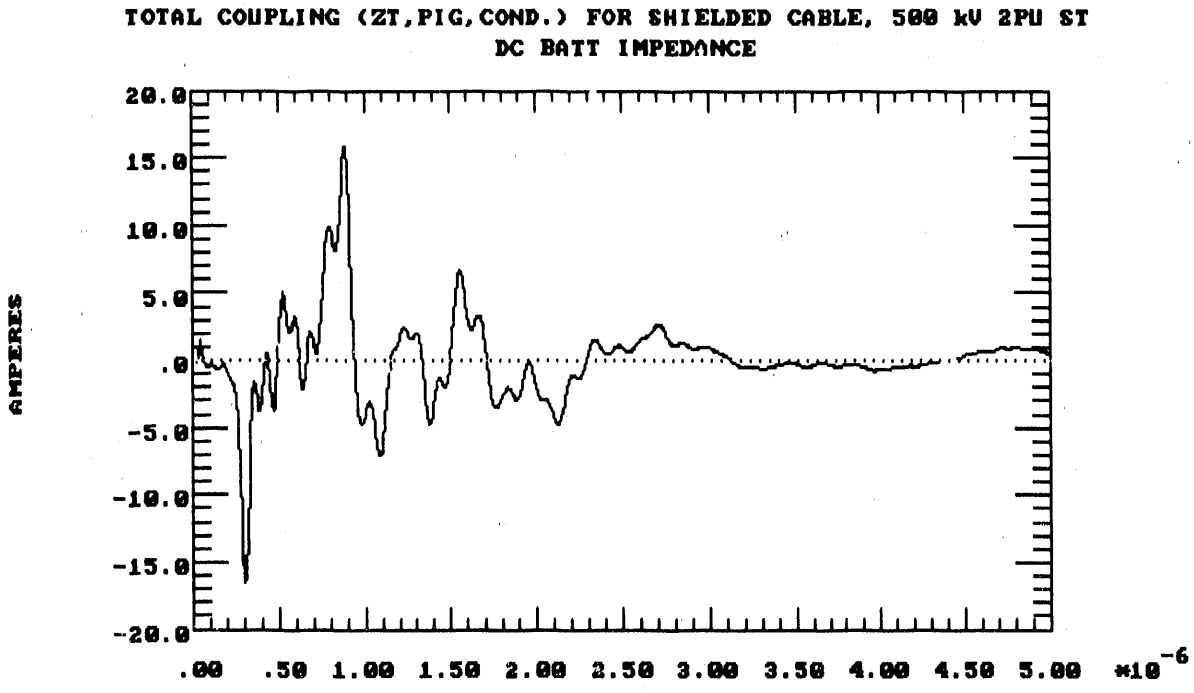

Waveform 27

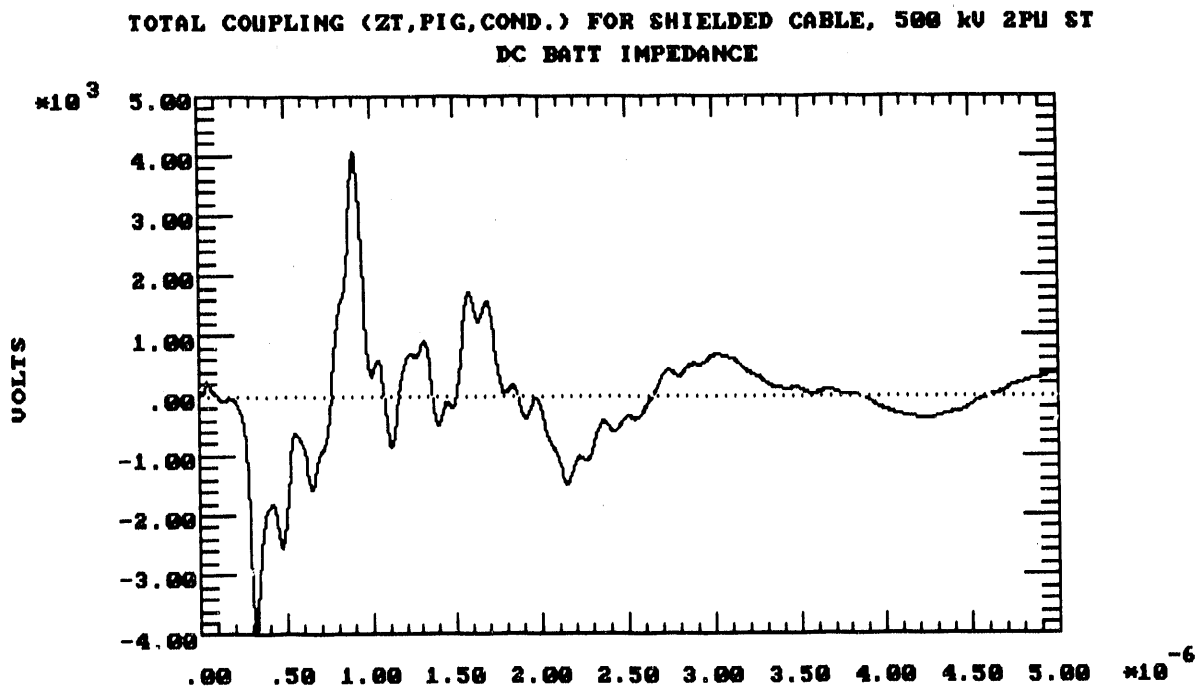

Waveform 28

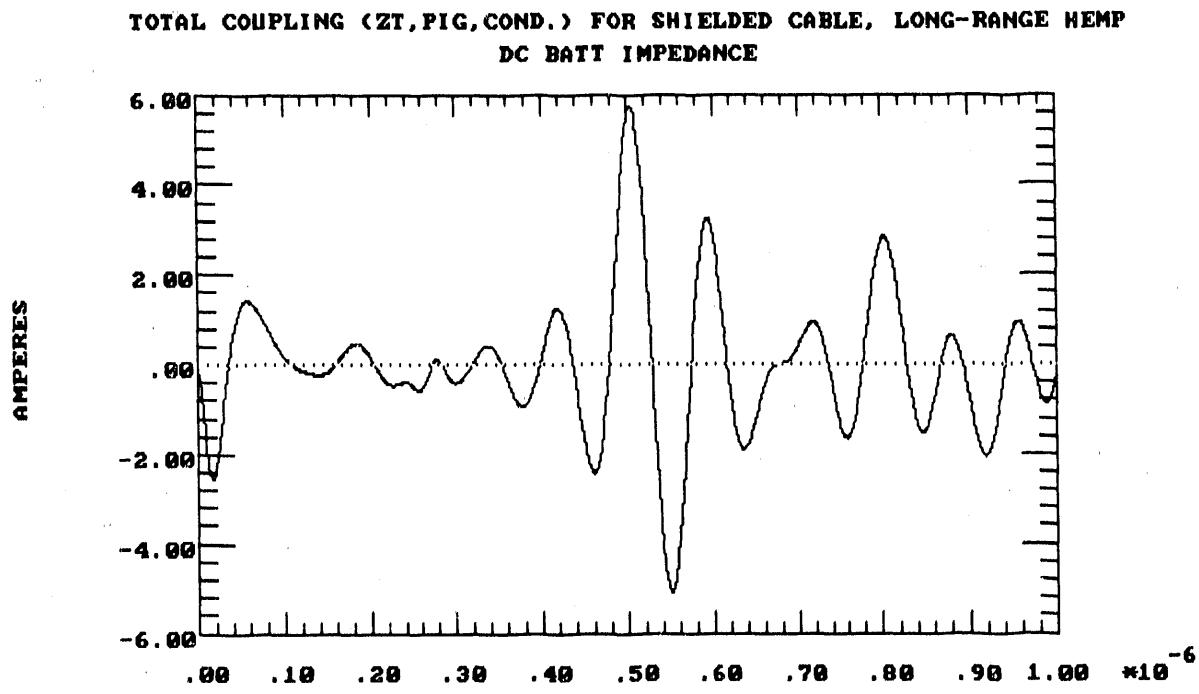

Waveform 29

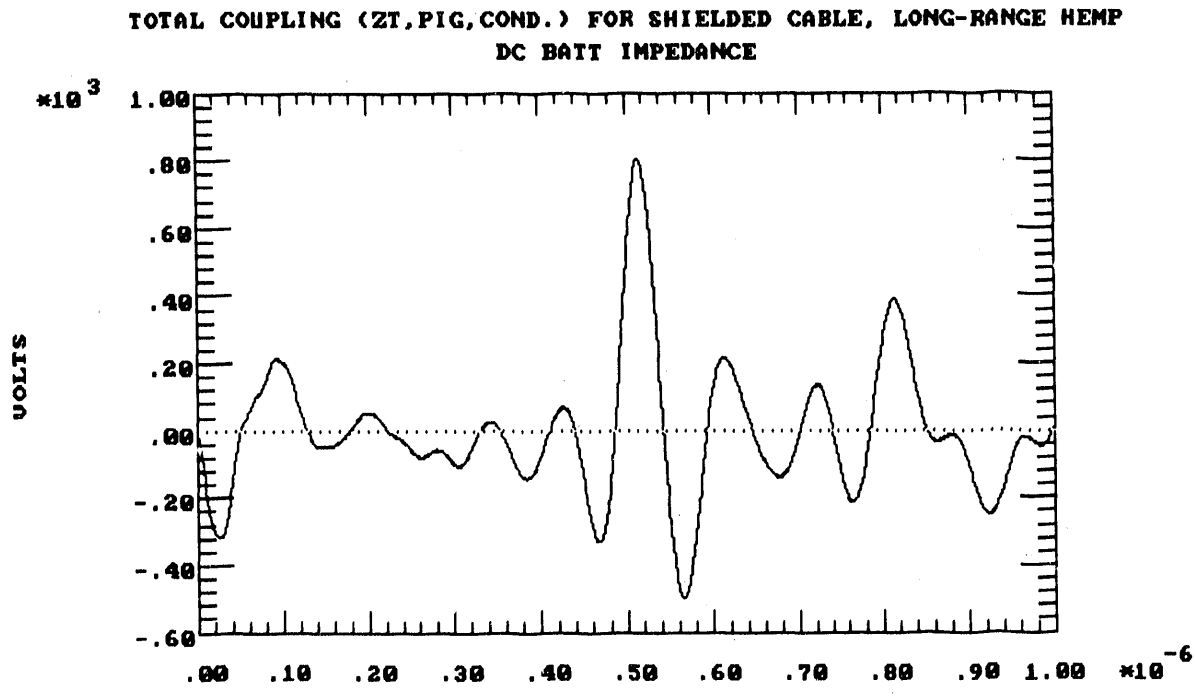

Waveform 30

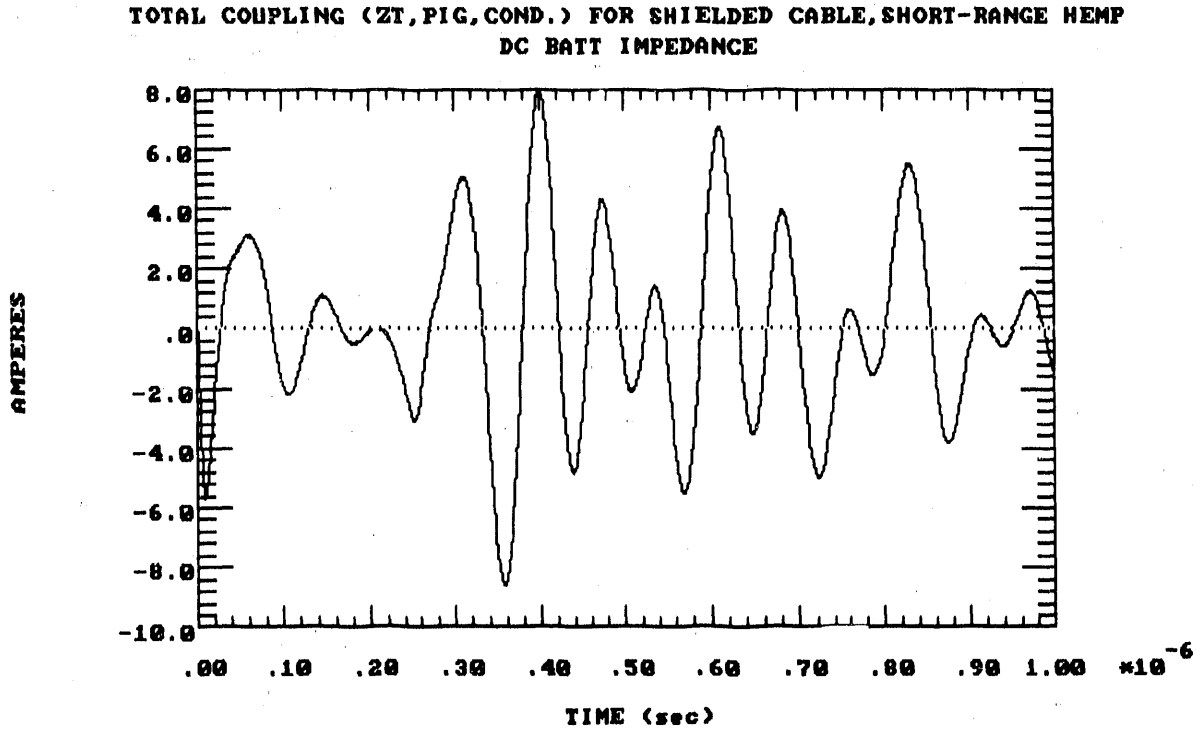

Waveform 31

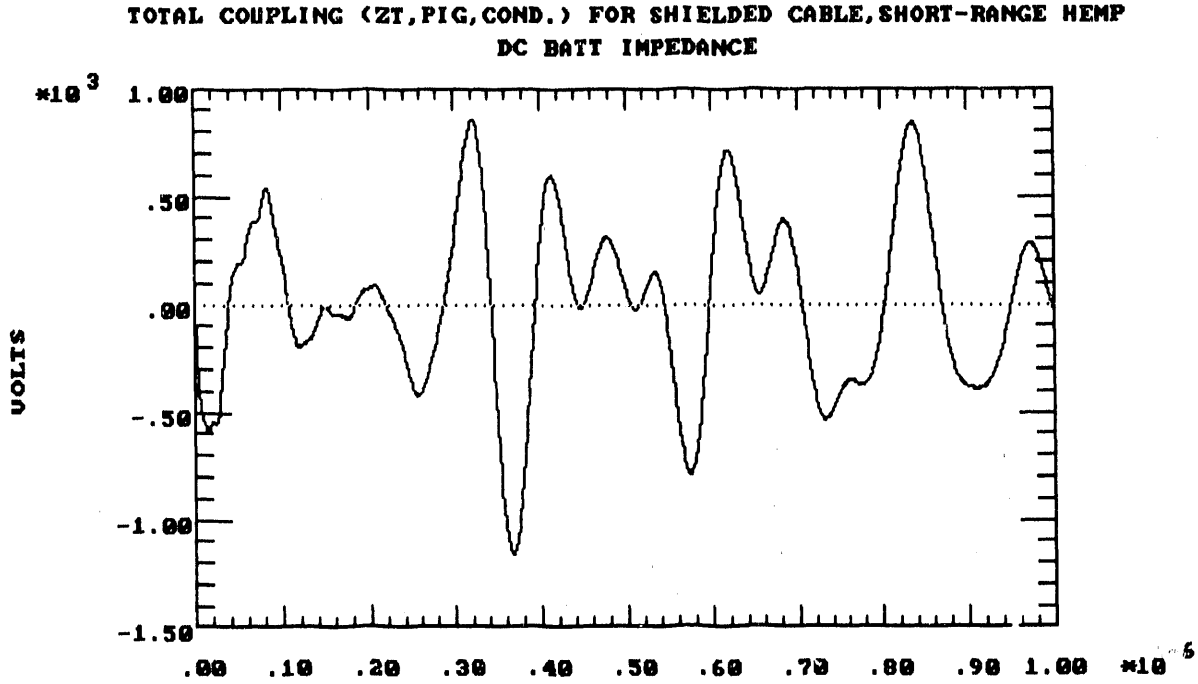

Waveform 32

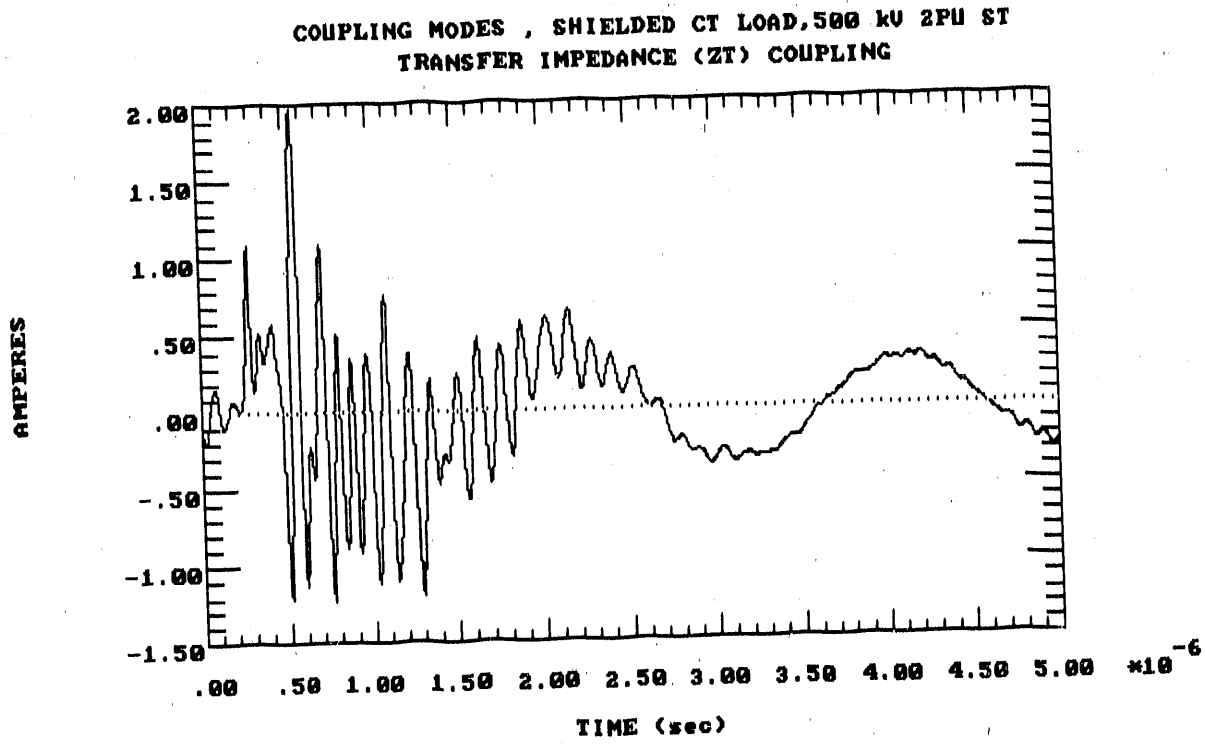

Waveform 33

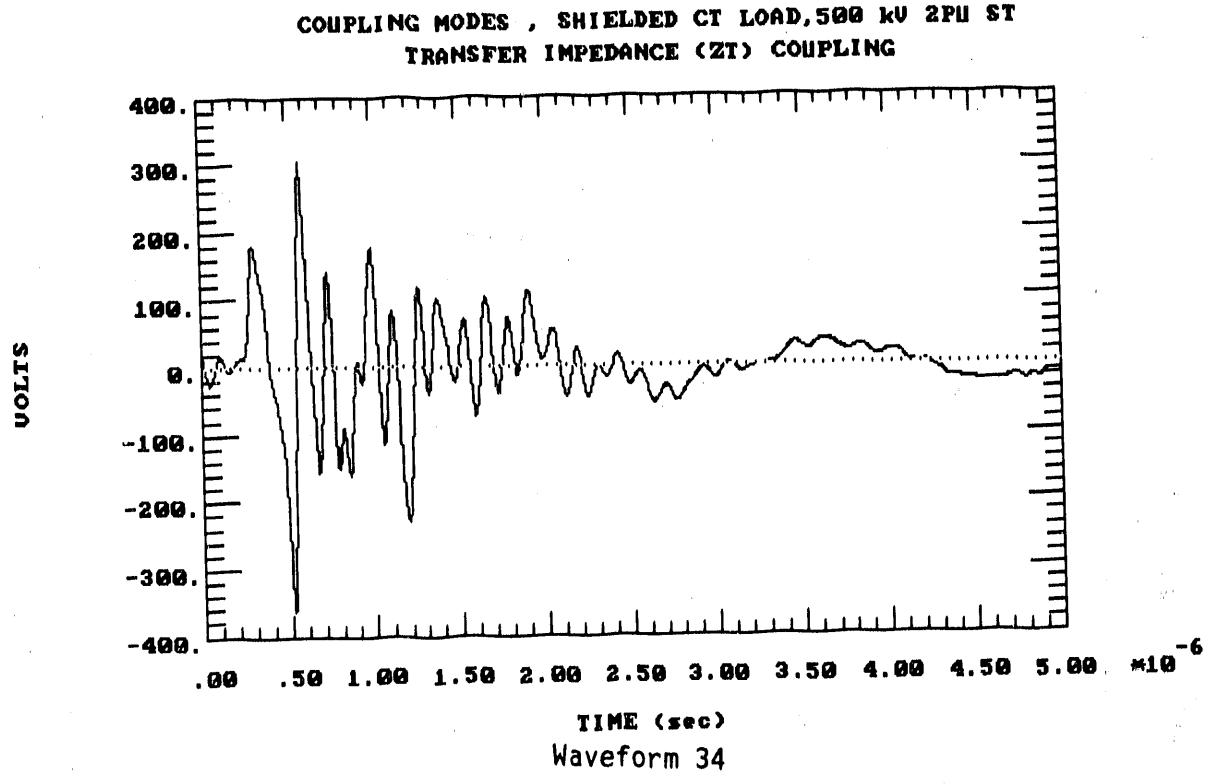

Waveform 34

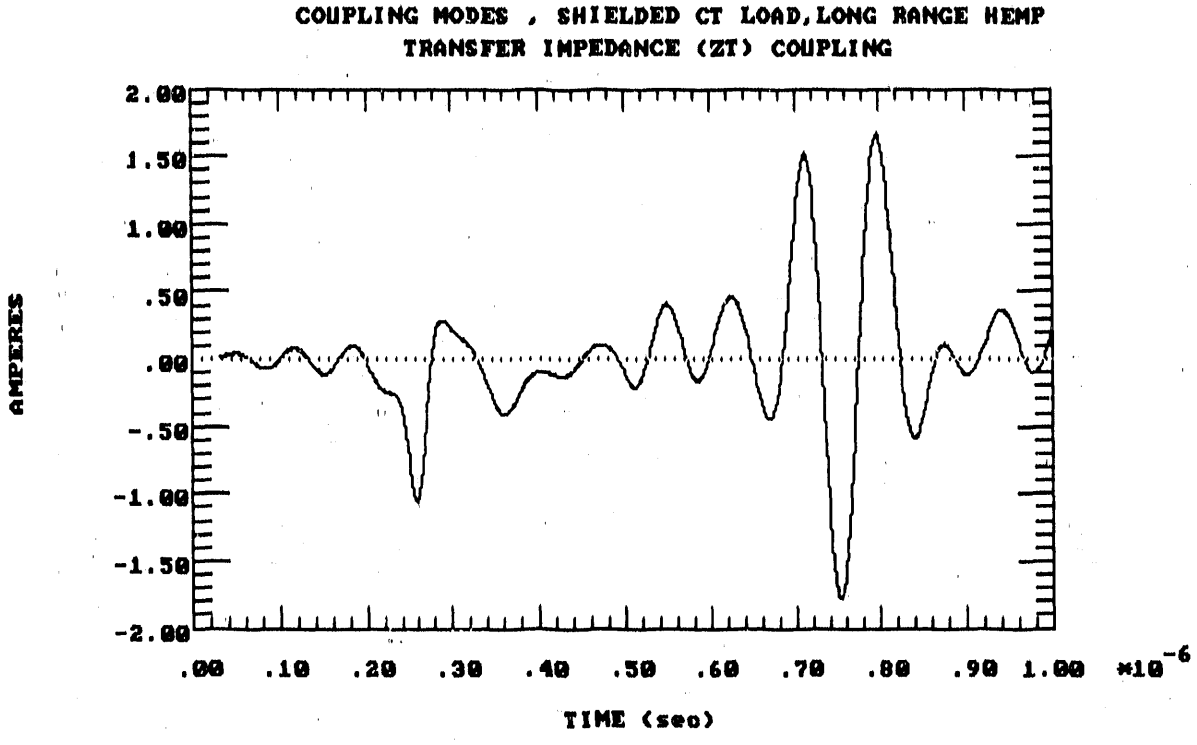

Waveform 35

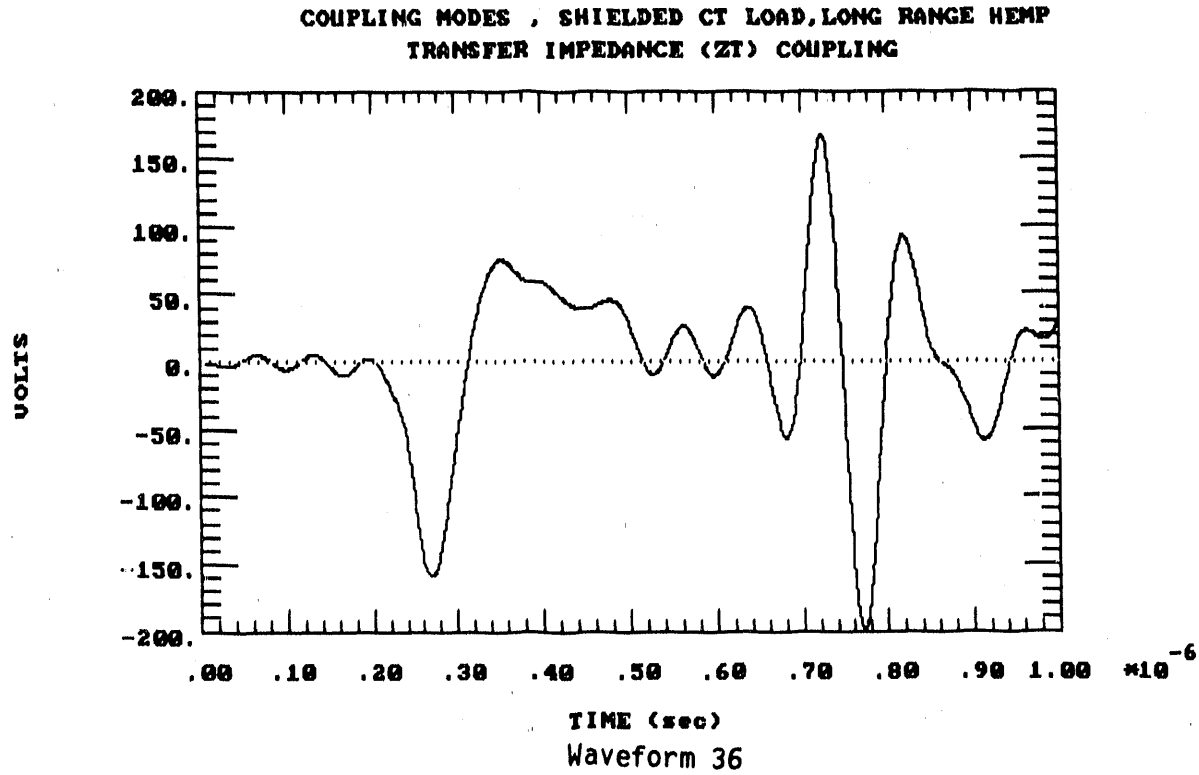

Waveform 36

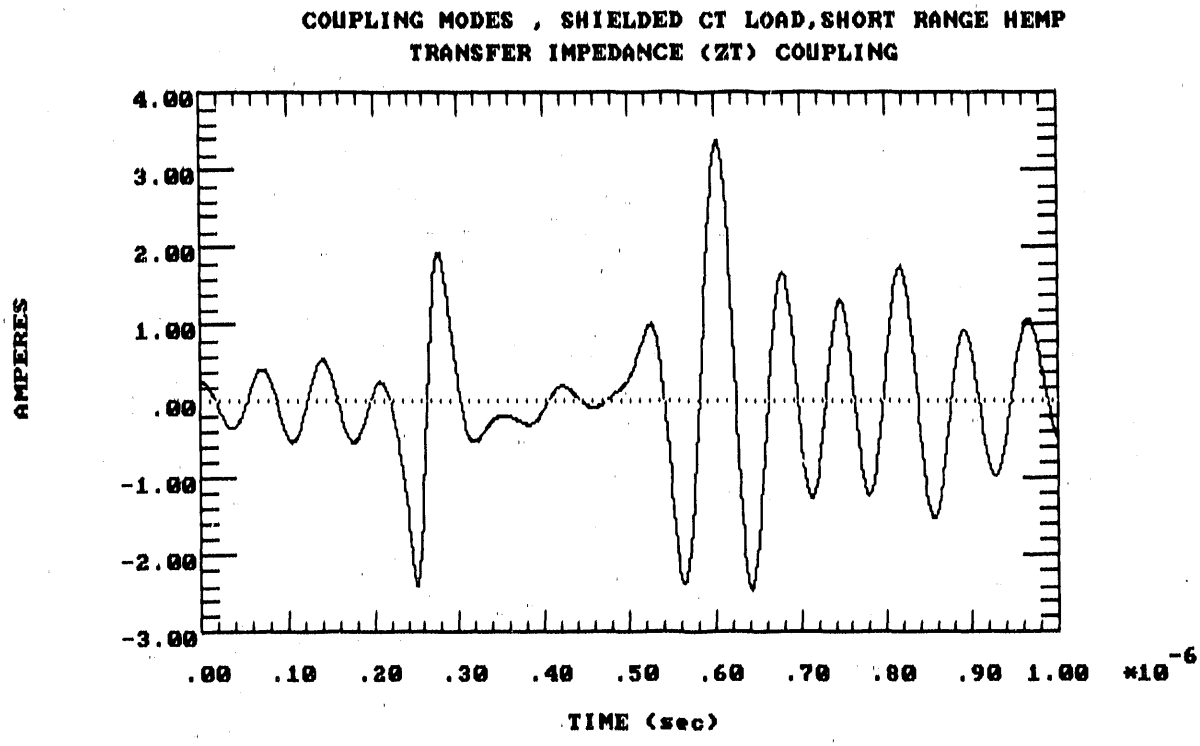

Waveform 37

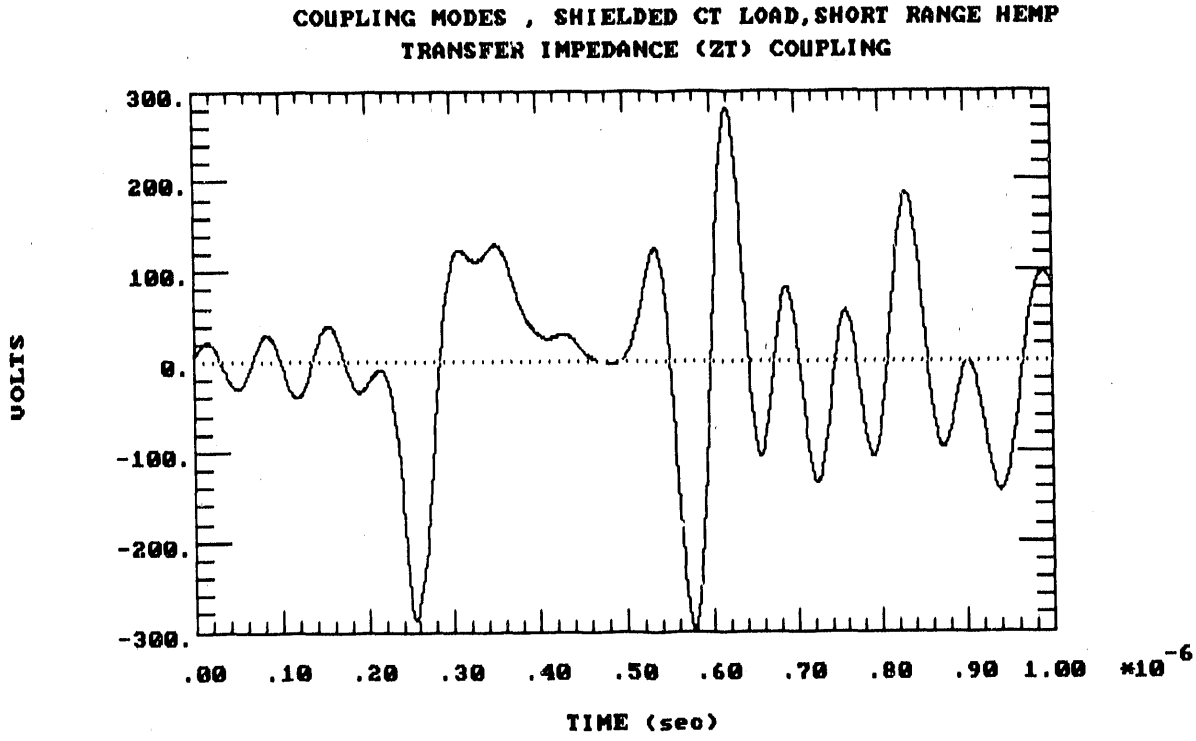

Waveform 38

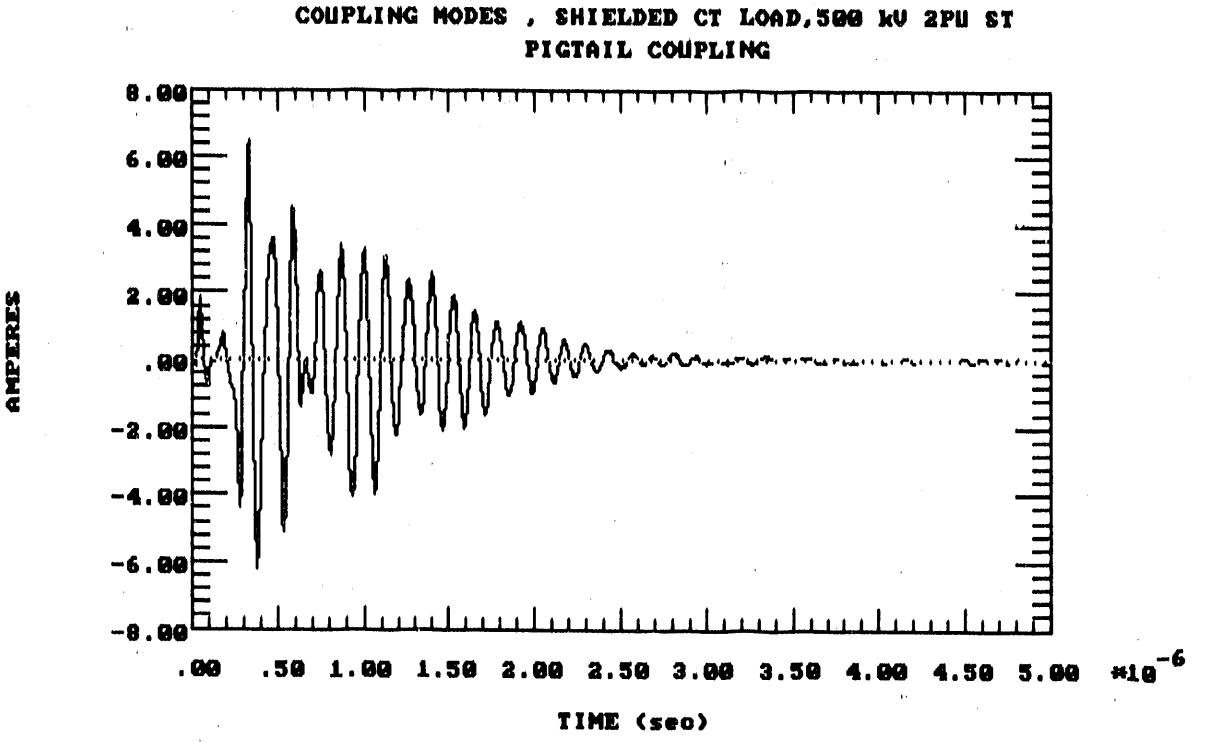

Waveform 39

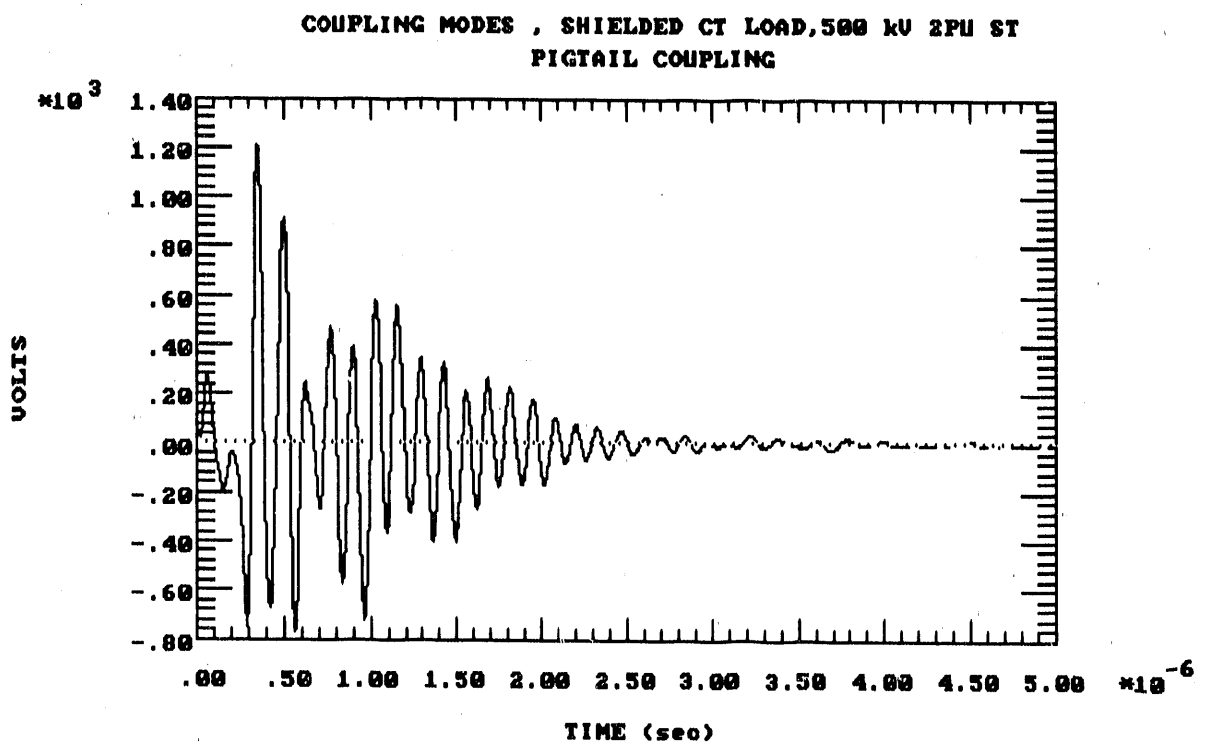

Waveform 40

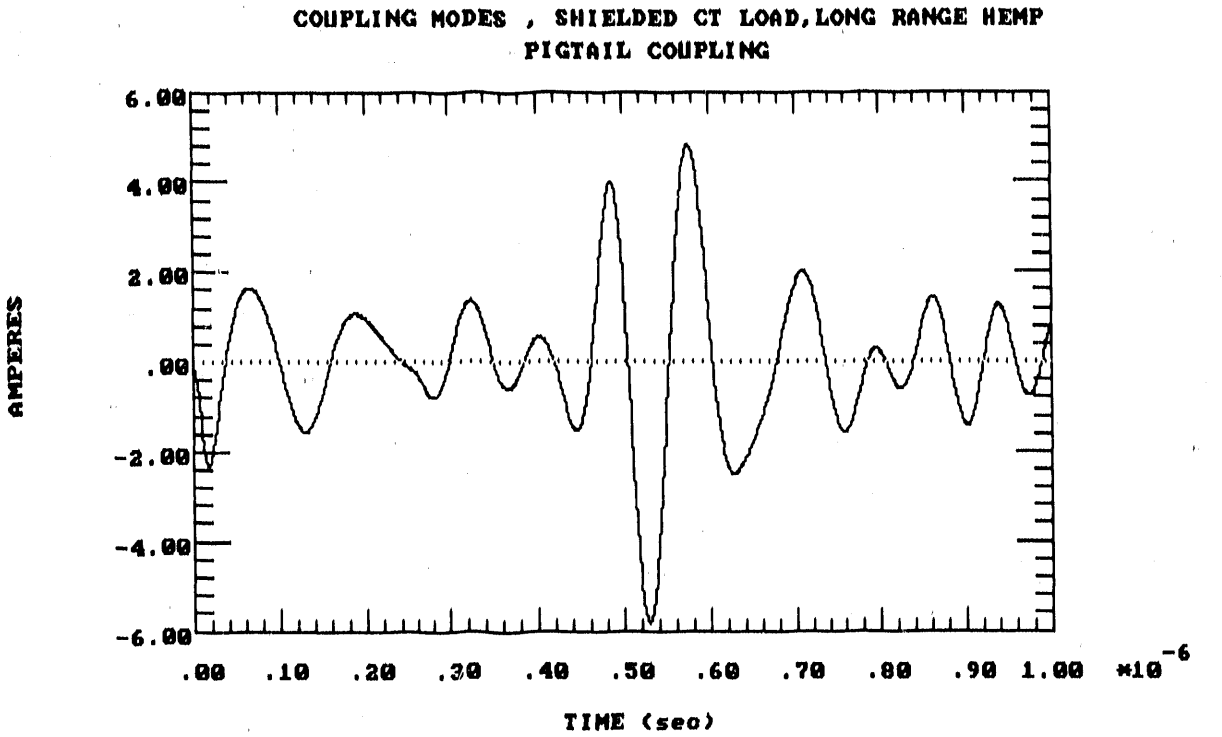

Waveform 41

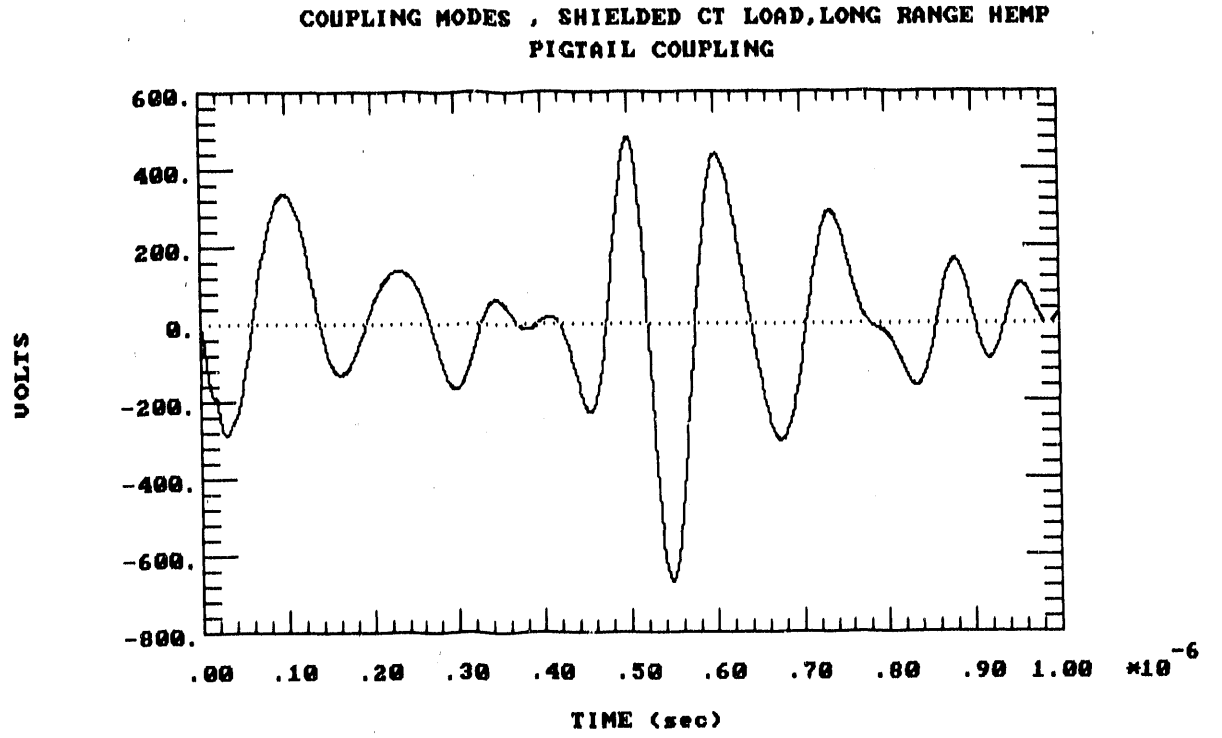

Waveform 42

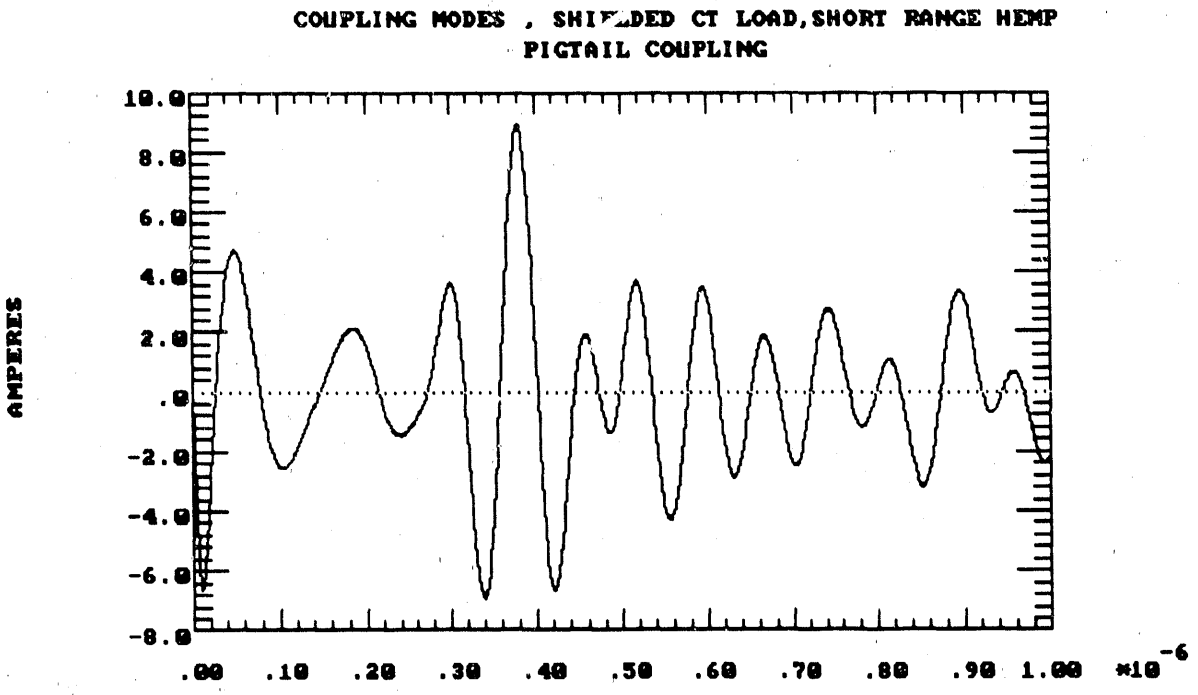

Waveform 43

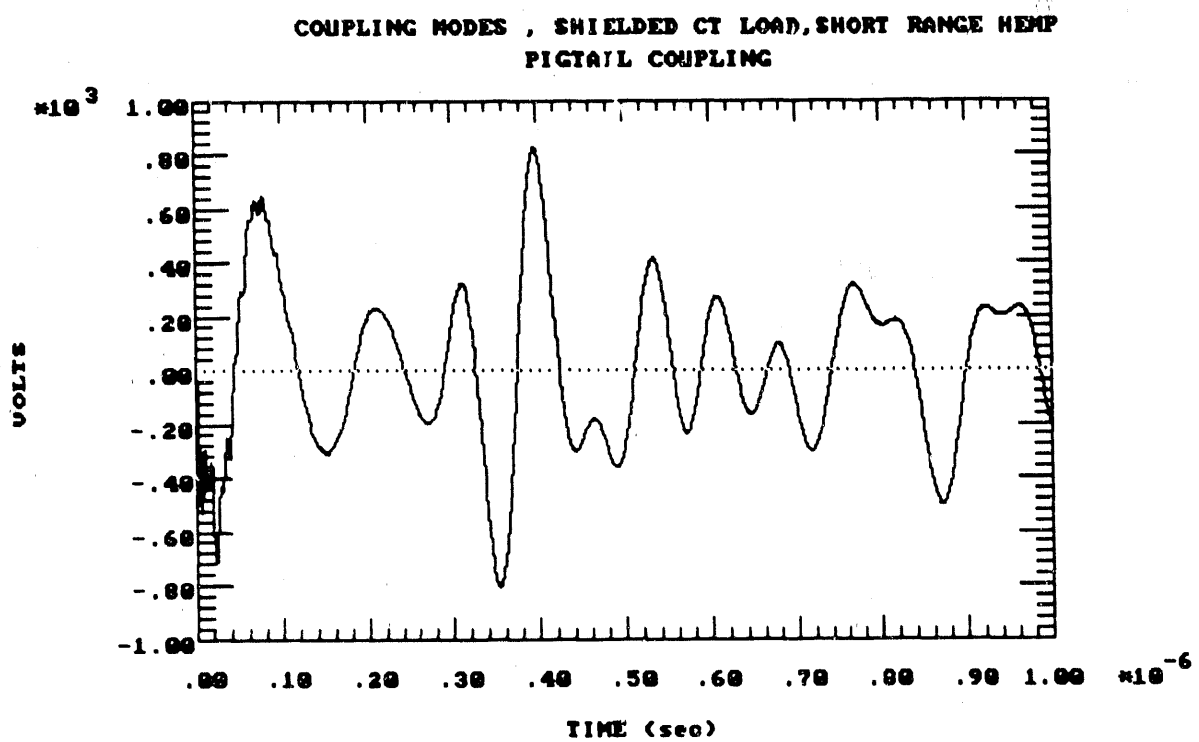

Waveform 44

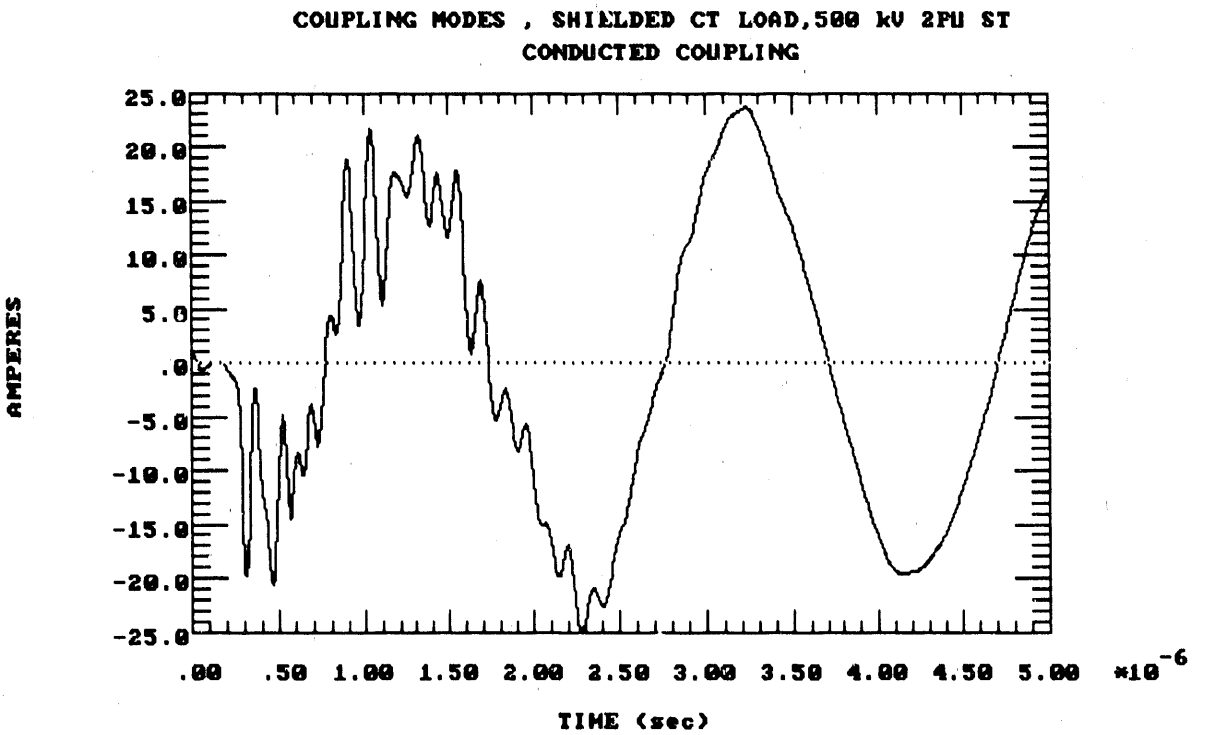

Waveform 45

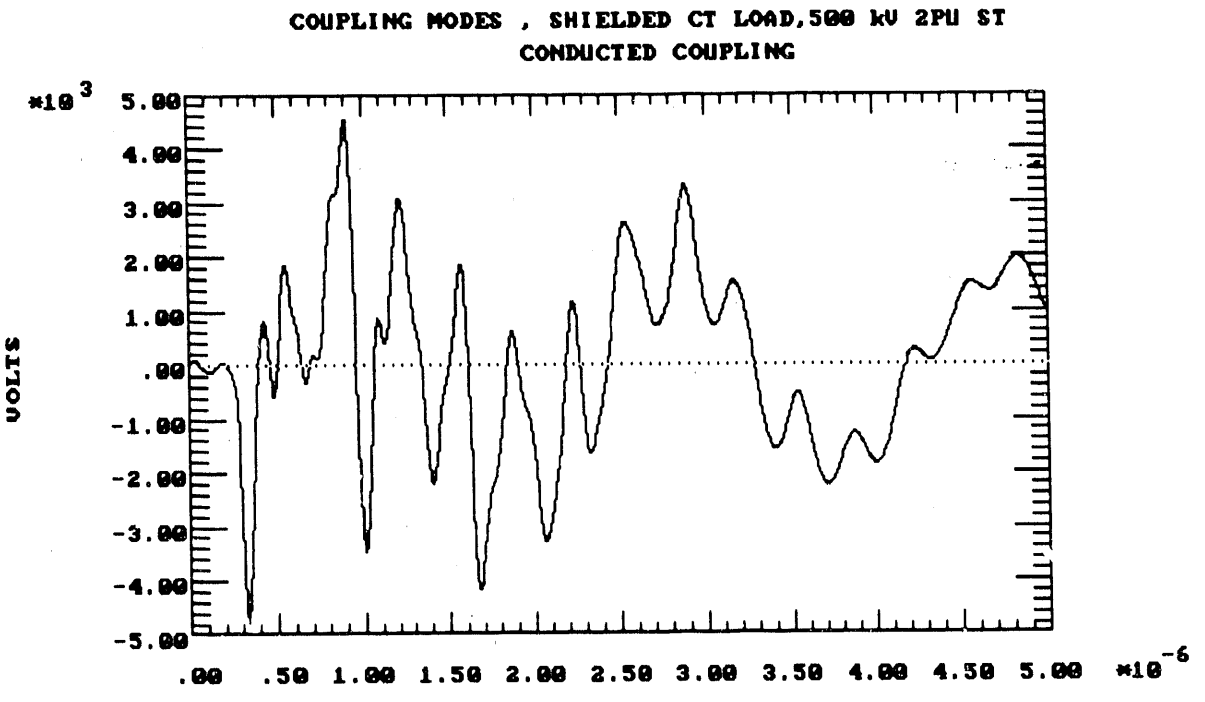

Waveform 46

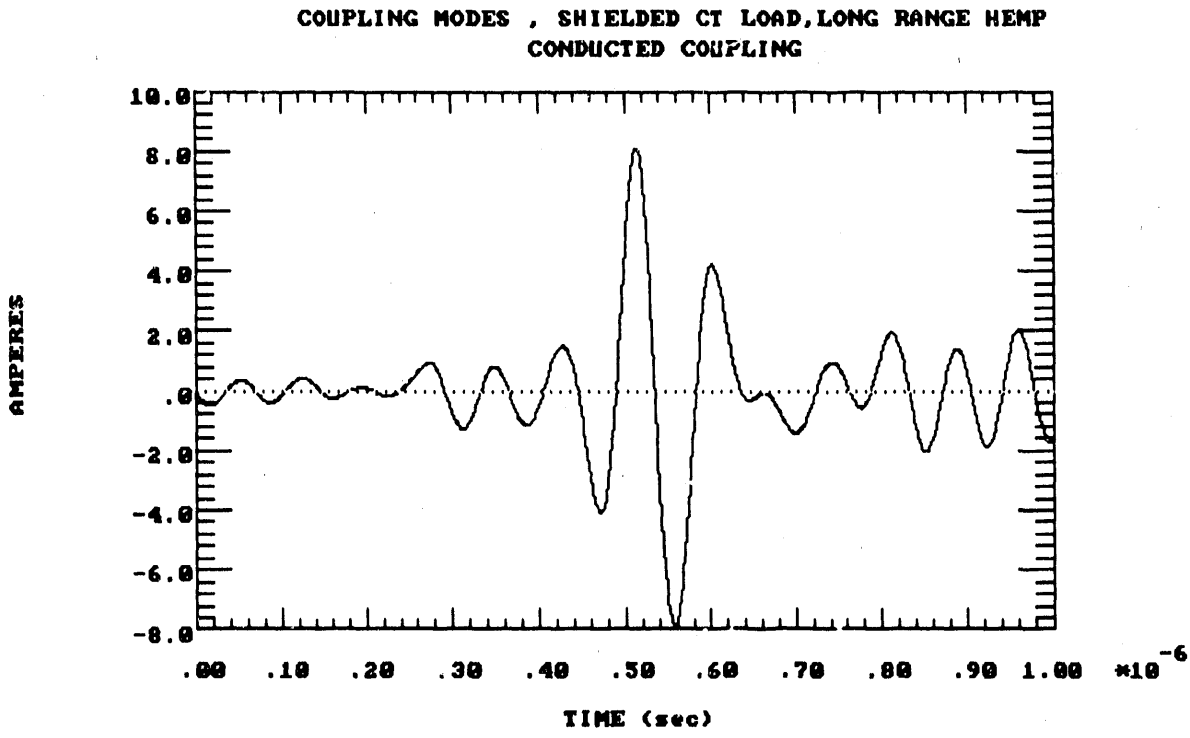

Waveform 47

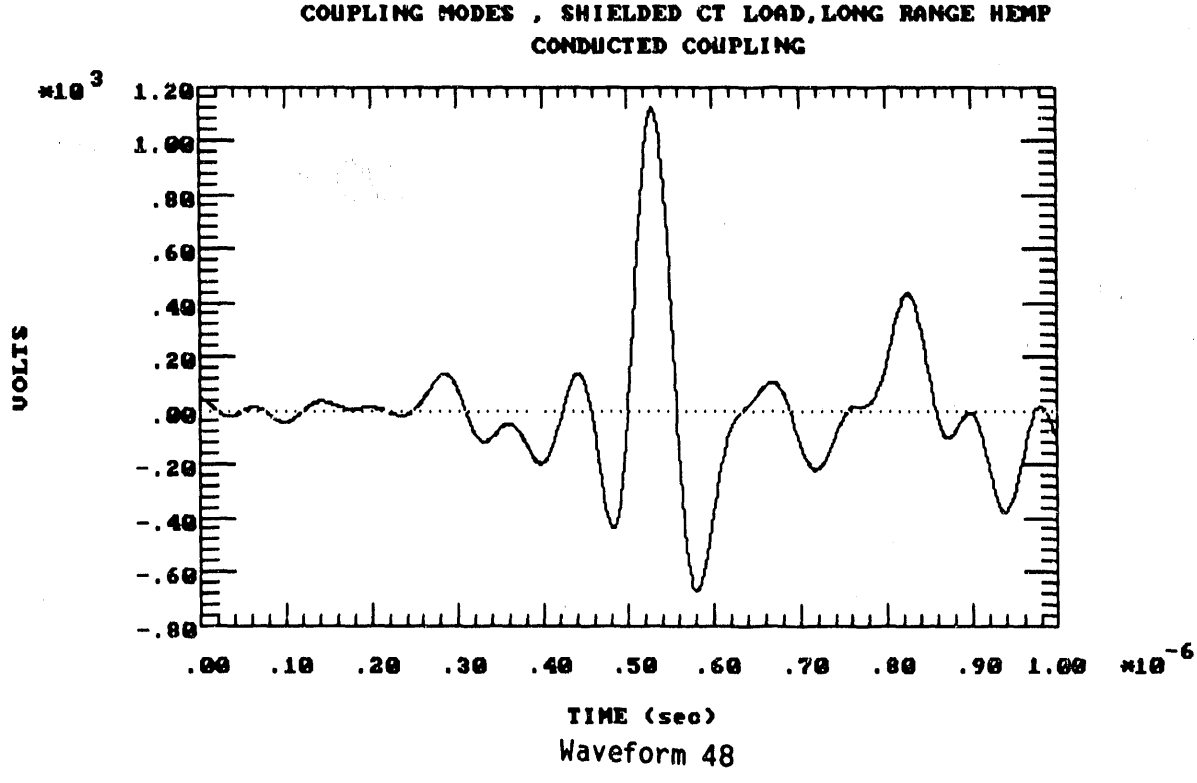

Waveform 48

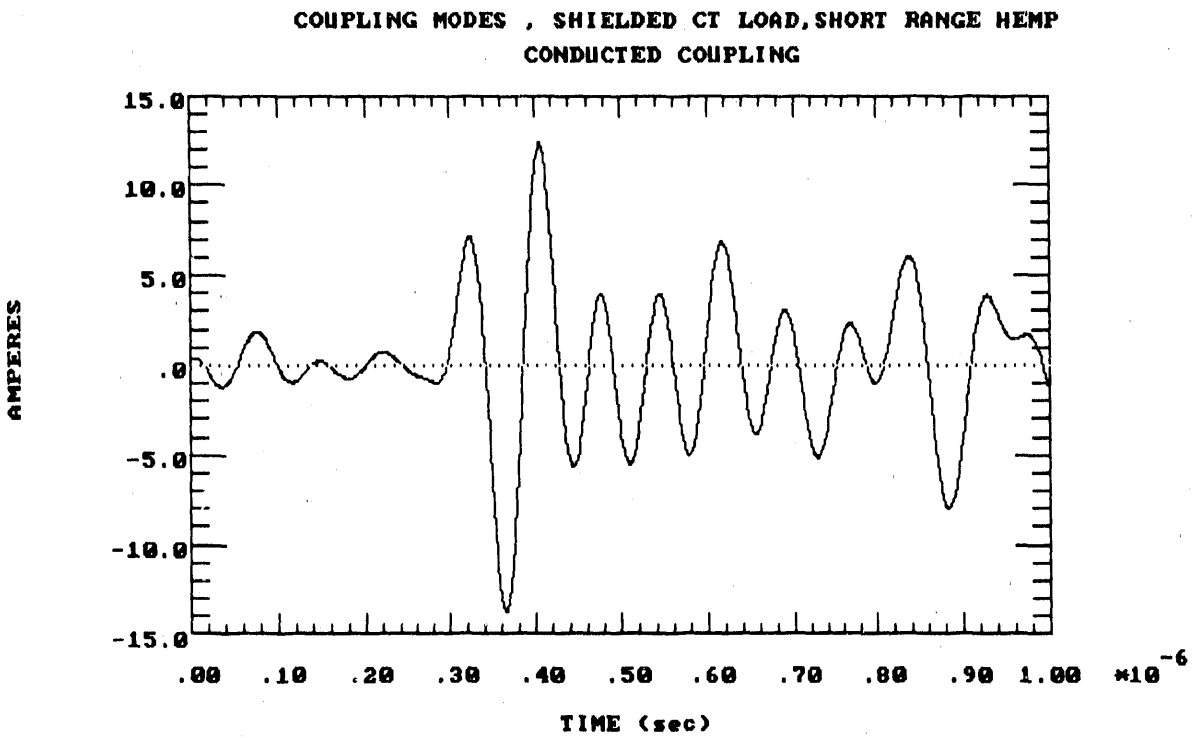

Waveform 49

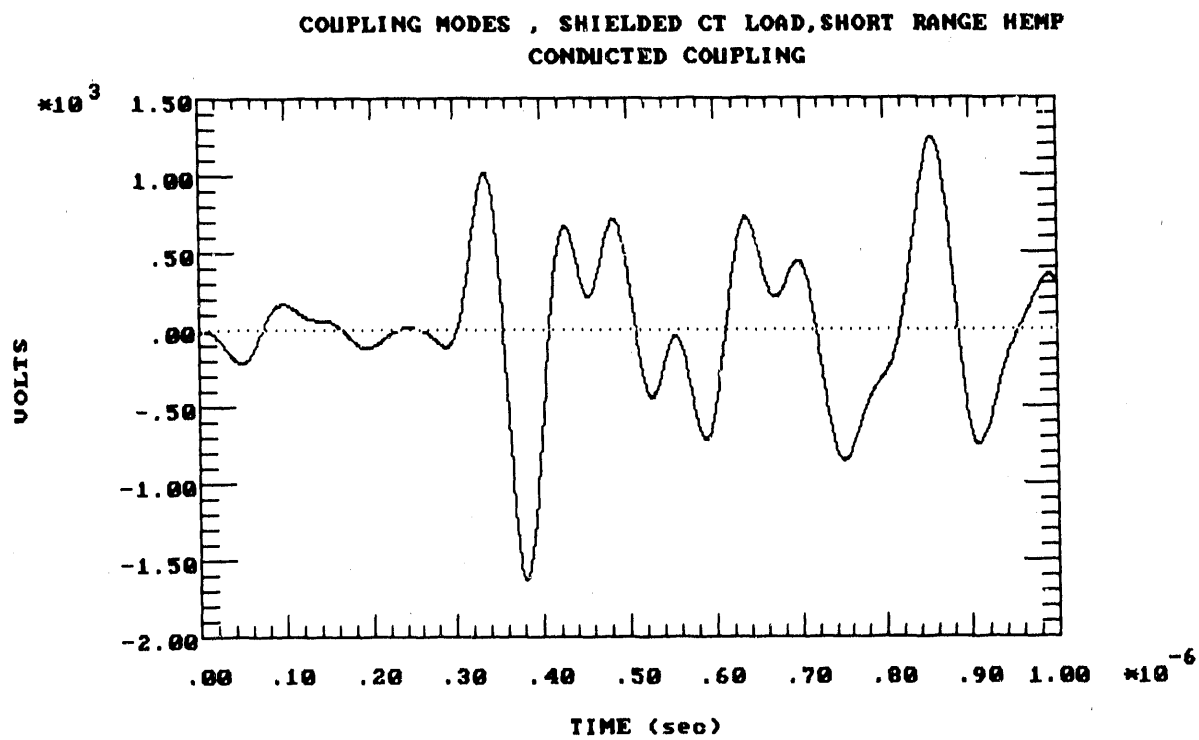

Waveform 50

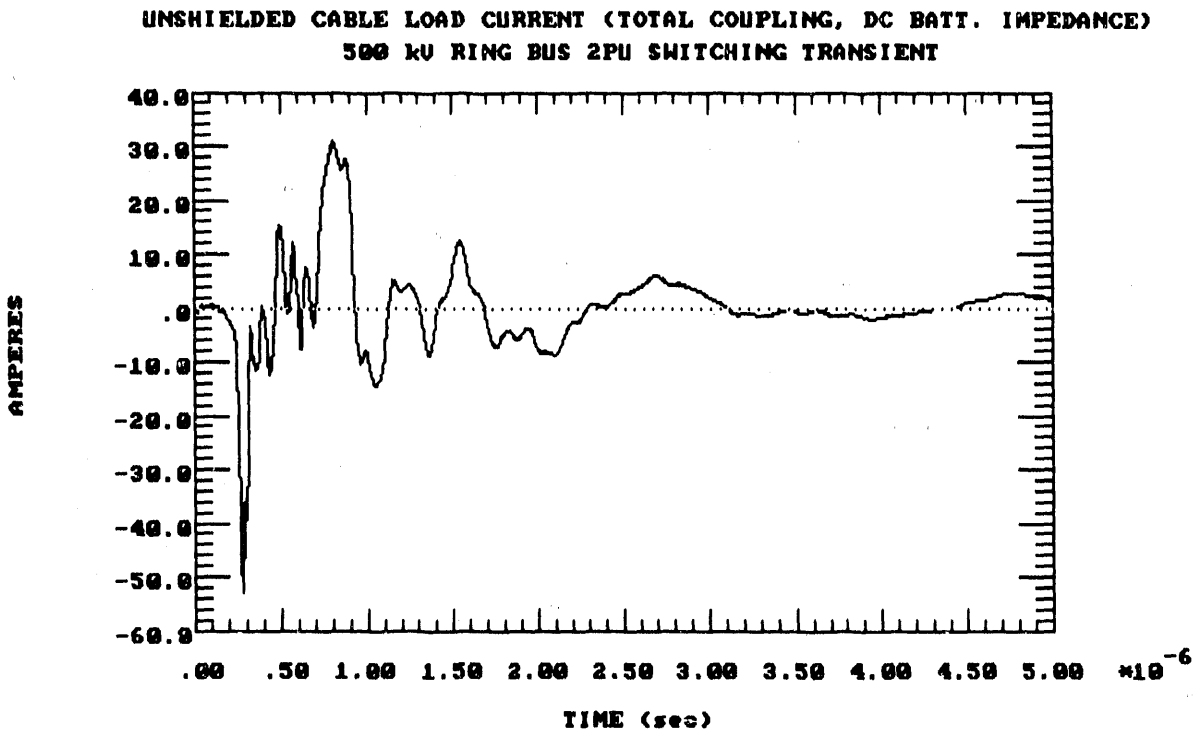

Waveform 51

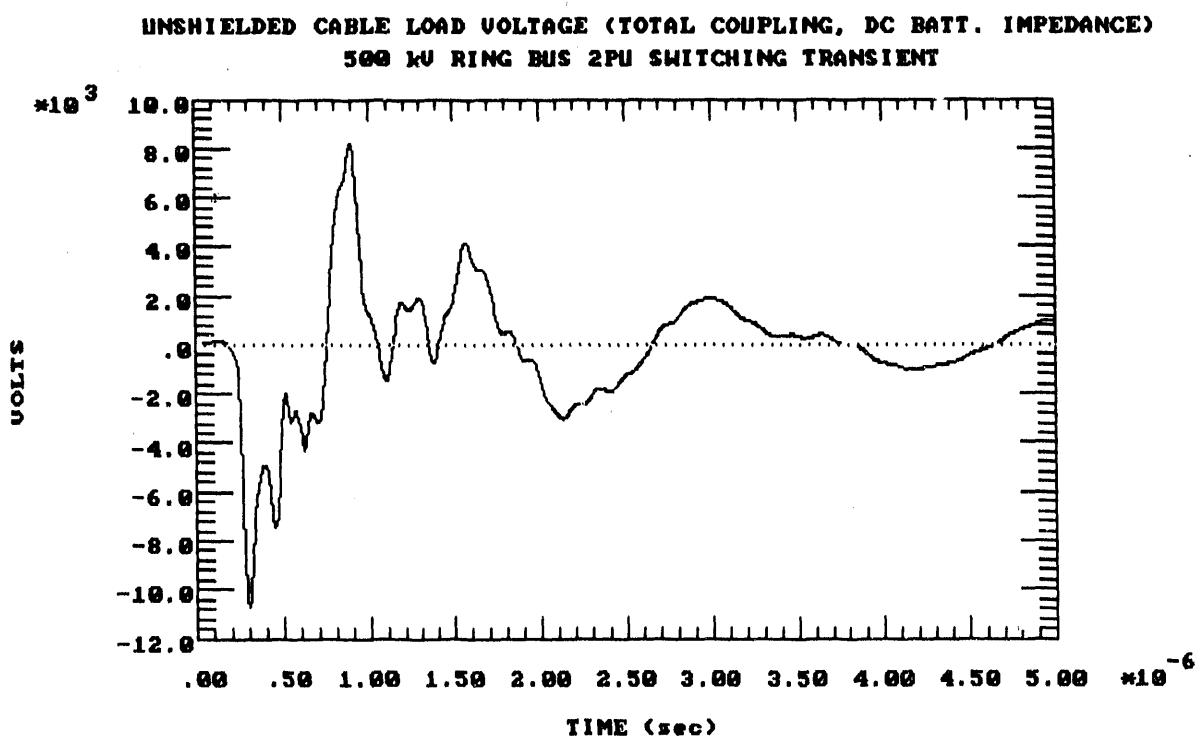

Waveform 52

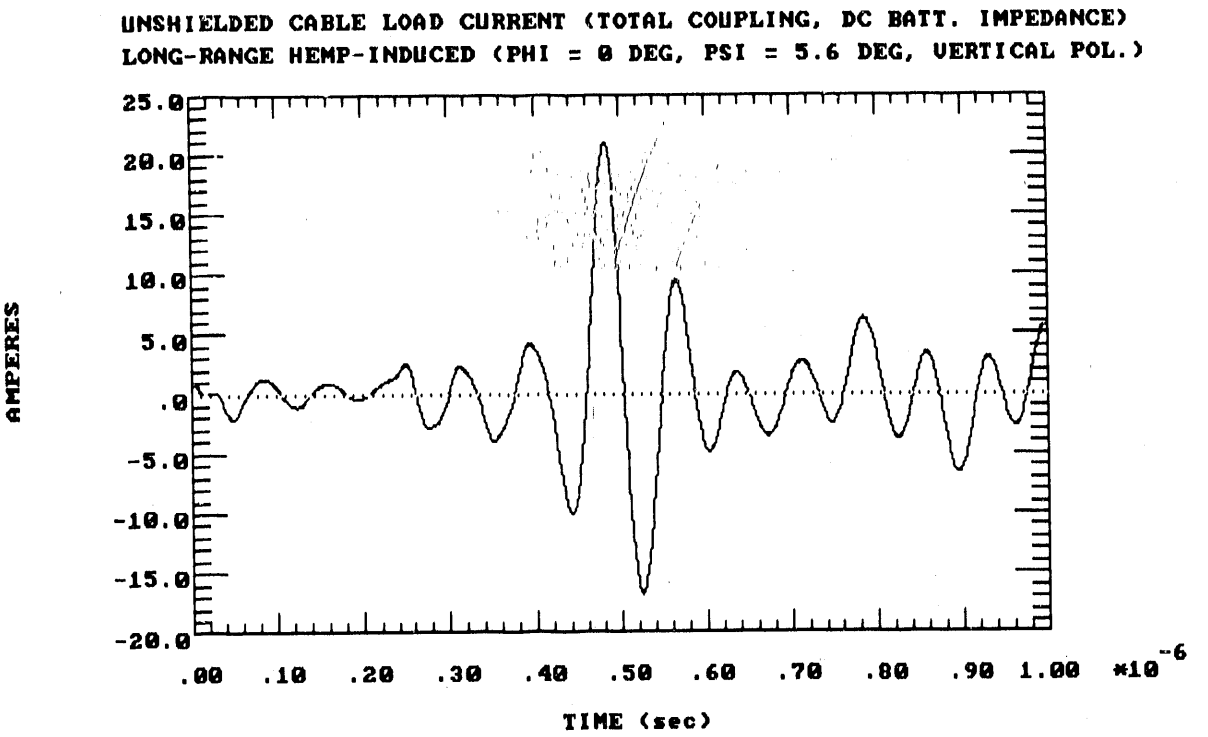

Waveform 53

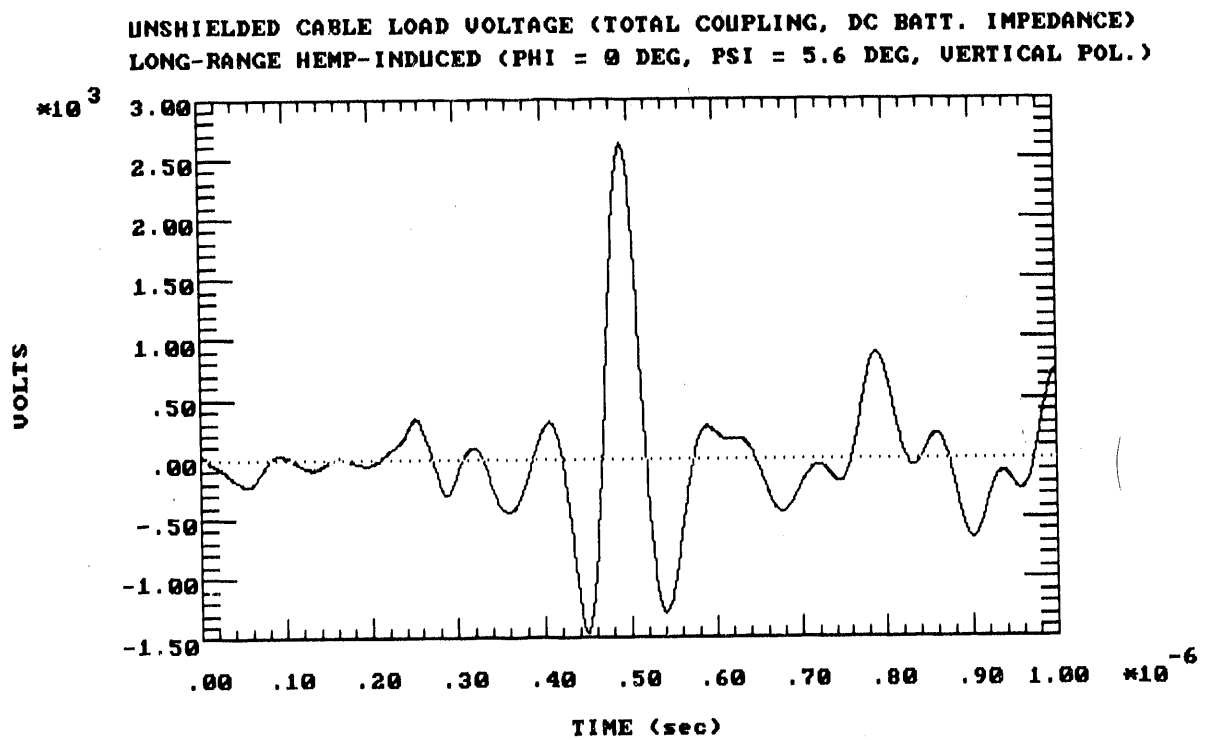

Waveform 54

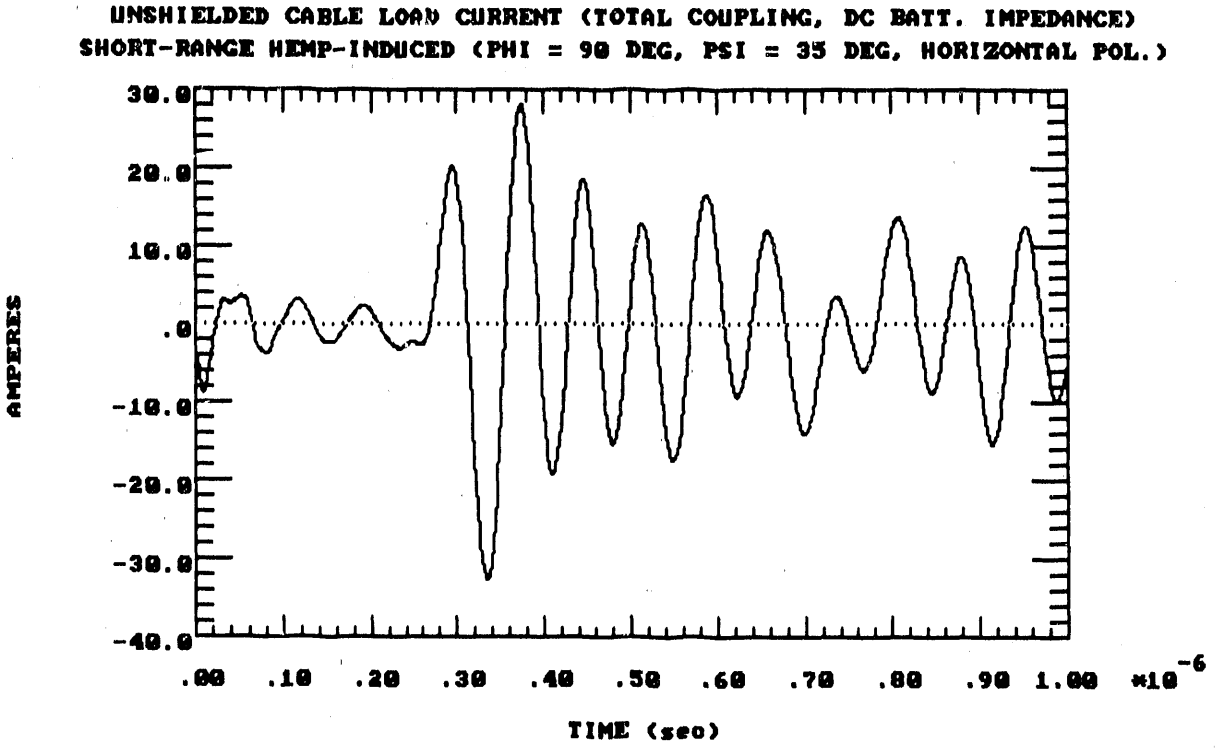

Waveform 55

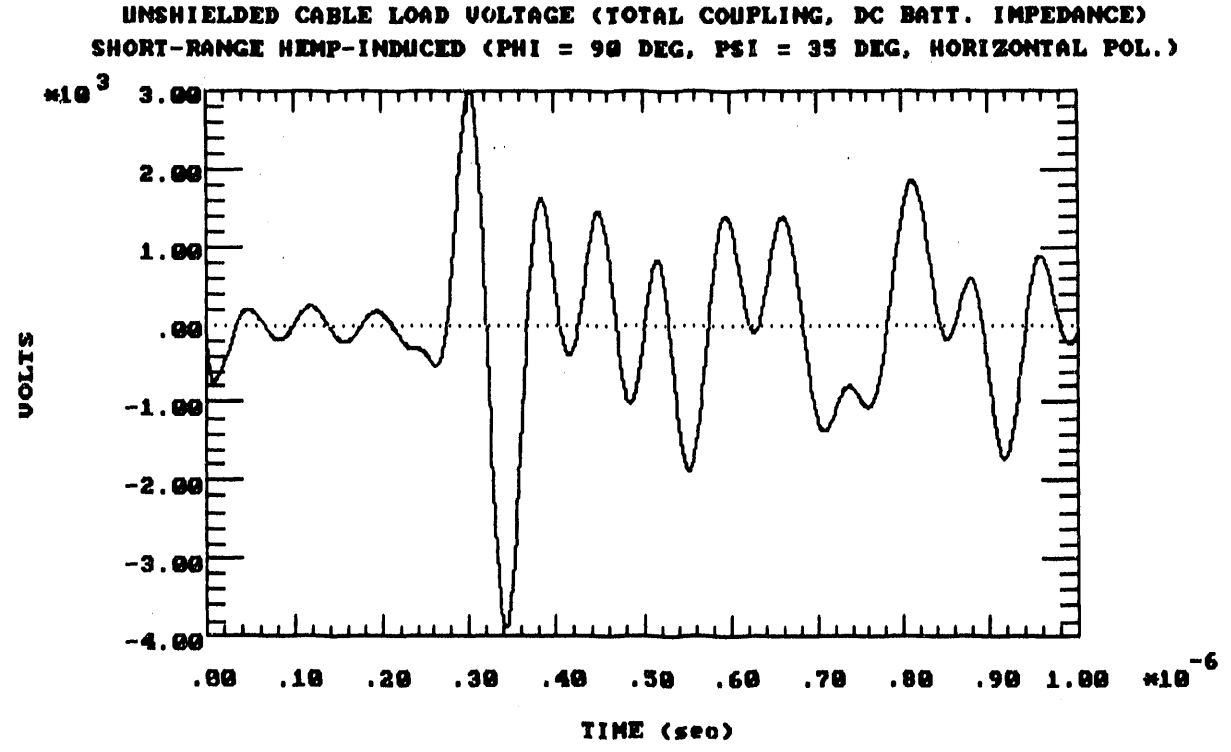

Waveform 56

INTERNAL DISTRIBUTION

1-10. P. R. Barnes
11. G. E. Courville
12. S. J. Dale
13. P. S. Gillis
14. M. A. Kuliasha
15. D. T. Rizy
16. R. B. Shelton
17. J. N. Stone
18. J. P. Stovall
19. ORNL Patent Office
20. Central Research Library
21. Document Reference Section
22. Y-12 Technical Library
23-32. Laboratory Records
33. Laboratory Records-RC

EXTERNAL DISTRIBUTION

34. V. D. Albertson, Dept. of Electrical Engineering, University Of Minnesota, 123 Church Street, S.W., Minneapolis, MN 55455.

35. J. C. Allen, Southwestern Electric Power co., P. O. Box 21106, Shreveport, LA 71156.

36. R. W. Allen, New England Power Service Co., 25 Research Drive, Westboro, MA 01582.

37. G. Applegren, Main Coordination Center, 1n301 Swift Road, P.O. Box 278, Lombard, Illinois 60148.

38. M. R. Apprill, Engineering & System Operations, Missouri Public Service, 10700 East 350 Highway, Kansas City, MO 64138.

39. G. H. Baker, HQ DNA/RAEE, 6801 Telegraph Road, Alexandria, VA 22310-3398.

40. P. Balma, Public Service Electric, 80 Park Plaza, Newark, NH 07101.

41. D. L. Bartel, Wisconsin Power & Light Co., 222 West Washington Ave., P. O. Box 192, Madison, WI 53701-0192.

42. J. E. Benning, Power System Engineering/Operations, PSI Energy, 1000 East Main Street, Plainfield, IN 46168.

43. Robert E. Benson, Chief Electrical Engineer, New York State Electric & Gas Corp., 4500 Vestal Parkway East, Binghamton, NY 13903.

44. G. D. Birney, Western Area Power Administration, P. O. Box 3402, Golden, CO 80401.

45. P. D. Blair, Energy and Materials Program, Congress of the United States, Office of Technology Assessment, Washington, DC 20510.

46. L. Bolduc, Hydro Quebec, 1800 Montee Ste Julie, Varennes, QC, Canada, J3X 1S1.

47. W. T. Boston, Tennessee Valley Authority, 6N 31B Signal Place, 1101 Market Street, Chattanooga, TN 37402-2801.

48. Larry Bressler, Western Area Power Administration, P. O. Box 3402, Golden, CO 80401.

49. B. G. Buchanan, Computer Science Department, University of Pittsburgh, 206 Mineral Industries Building, Pittsburgh, Pennsylvania 15260.

50. W. J. Budney, Distribution Systems, Public Service Electric & Gas Co., 80 Park Plaza, Newark, NJ 07101.

51. C. K. Bush, Atlanta Electric, P.O. Box 1264, Pleasantville, NJ 08232.

52. R. F. Campbell, Transmission & Electrical Projects, Tennessee Valley Authority, 3N 53A Missionary Ridge Place, Chattanooga, TN 37402-2801.

53. H. S. Cabayan, Lawrence Livermore National Laboratory, P.O. Box 5504, L-81, Livermore, CA 94550.

54. J. Chadwick, 902 Glamis Circle, Signal Mountain, TN 37377.

55. D. J. Christofersen, Manager, Electrical Engineering Division, United Power Association, P. O. Box 800, Elk River, MN 55330-0800.

56. P. Chrzanowski, Evaluation & Planning Program, Lawrence Livermore National Lab, P.O. Box 808, L-81, Livermore, CA 94550.

57. R. F. Chu, Research Engineer, Philadelphia Electric Co., Research Division (S10-1), 2301 Market Street, Philadelphia, PA 19101.

58. C. F. Clark, Bonneville Power Administration, P. O. Box 3621, Portland, OR 97208.

59. Lynn Coles, Principal Policy Advisor, SERI, 1617 Cole Boulevard, Golden, CO 80401.

60. R. Coles, Geological Survey of Canada, Geophysics Division, One Observator Crescent, Ottawa, CANADA K1A OY3.

61. O. R. Compton, Richmond Plaza, P. O. Box 26666, Richmond, Virginia 23261.

62. T. B. Cook, 80 Castlewood Dr., Pleasanton, CA 94566.

63. G. H. Coplon, U.S. Department Of Energy, Rm. 8F089, 1000 Independence Avenue, S.W., Washington, DC 20585.

64. G. Cucchi, PJM - Valley Forge Corporate Ctr., 955 Jefferson Avenue, Norristown, PA 19403.

65. J. J. Cuttica, Research and Development, Gas Research Institute, 8600 W. Bryn Mawr Avenue, Chicago, Illinois 60631.

66. G. Dahlen, Royal Institute of Technology, Tds, P.O. Box 70043, S-10044, Stockholm, Sweden.

67. L. W. DeJong, Iowa Public Service Co., P. O. Box 778, Sioux City, IA 51102.

68. A. R. Donnell, Northwestern Public Service Co., 3rd St. & Dakota Ave., S.E., Huron, SD 57350.

69. Raymond Dunlop, Director of Research, New England Power Service Co., 25 Research Drive, Westborough, MA 01582.

70. H. Elbadaly, Underground T&D Research Manager, Consolidated Edison Company, 4 Irving Place, New York, NY 10003.

71. D. Fagnan, Philadelphia Electric Co., 2301 Market Street, Philadelphia, PA 19101.

72. W. E. Ferro, Electric Research and Management, Inc., P.O. Box 165, State College, PA 16804.

73. N. Fraser, Ontario-Hydro (HH A25), 700 University Avenue, Toronto, Ontario, M5G 1X6, CANADA.

74. R. Gates, EMP Program Manager, FEMA, RM 606, 500 C Street, S.W., Washington, DC 20472.

75. P. R. Gattens, Allegheny Power, 800 Cabin Hill Dr., Greensburg, PA 15601.

76. M. R. Gent, President, North American Electric Reliability Council, 101 College Road East, Princeton, New Jersey 08540-8060.

77. C. R. Gordon, HQ DNA/RAEE, 6801 Telegraph Road, Alexandria, VA 22310-3398.

78. M. Granger, Hydro-Quebec, Planning Systems Division, 855 East Ste-Catherine, 20 ieme etage, Montreal Quebec, Canada, H2L 4PS.

79. J. D. Gregory, Southern Company Services, Inc., P. O. Box 2625, Birmingham, AL 35202-2625.

80. V. Guten, National Security Agency (M-352), Fort Mead, MD 20755.

81. I. Gyuk, Program Manager, U.S. Department of Energy, 1000 Independence Ave., S.W., Washington, DC 20585.

82. Wayne Hilson, Manager, Transmission and Electrical Systems Department, Missionary Ridge, 3 North 41, 1101 Market Street, Chattanooga, TN 37402-2801, .

83. E. R. Holcomb, Texas Utilities Electric Co., 1506 Commerce Street, Dallas, TX 75201.

84. M. B. Hunter, Puget Sound Power & Light Co., 13635 N.E. 80th Street, Redmond, WA 98052-4098.

85. Joe Iannucci, Pacific Gas & Electric, 3400 Crow Canyon, San Ramon, CA 94583.

86. J. Kappenman, Minnesota Power, 30 W. Superior St., Duluth, Minnesota 55802.

87. S. Kashyap, Defense Research Establishment — Ottawa, Electronics Division, 3701 Carling Ave., Ottawa, Ontario K1A0Z4, Canada.

88. J. L. King, System Executive Operations, Entergy Corporation, P. O. Box 61005, 225 Baronne St., New Orleans, LA 70161.

89. Joseph L. Koepfinger, Director, Systems Studies and Research, Duquesne Light Company, One Oxford Center, 301 Grant Street (19-5), Pittsburgh, PA 15279.

90. J. L. Koepfinger, Director, Sys. Studies & Research, Duquesne Light Co., 301 Grant St. (19-5), Pittsburgh, PA 15279.

91. B. Korbutiak, Alberta Power, Ltd., 10035 195th St., Edmondton, Alberta T5J 2V6, CANADA.

92. R. A. Kramer, Northern Indiana Public Service Co., 5265 Hohman Avenue, Hammond, IN 46320.

93. J. Kulsetås, Division Manager/Research Director, Norwegian Electric Power Research Institute, Division of High Voltage Technology, N-7034 Trondheim, Norway.

94. E. Larsen, General Electric, ESDS Bldg. 2, Rm 642, One River Road, Schenectady, NY 12345.

95. Major Robert Launstein, Defense Nuclear Agency, DNA/RAEE, 6801 Telegraph Rd., Alexandria, VA 22310.

96. J. L. Layton, Systems Operation, Carroll Electric Membership Corp., 155 Temple Road, Carrollton, GA 30117.

97. G. R. Leidich, System Planning Engineering Dept., Centerior Energy, 6200 Oak Tree Boulevard, Independence, OH 44131.

98. R. C. Liebentritt, Omaha Public Power District, 444 South 16th Street Mall, Omaha, NE 68102-2247.

99. R. C. Liimatainen, Committee on Science, Space and Technology, 374 Rayburn House Office Bldg., Rm. B., Washington, DC 20515.

100. J. Lloyd, CEHND-ED-SY, U.S. Army, Engineering Division Huntsville, P.O. Box 1600, Huntsville, AL 35807.

101. C. L. Longmire, Mission Research Corporation, P.O. Drawer 719, Santa Barbara, CA 93102.

102. D. J. Lorden, New England Power Service, 25 Research Drive, Westborough, MA 01582.

103. A. P. Meliopoulos, Georgia Tech, School of Electrical Engineering, Atlanta, GA 30332.

104. S. R. Mendoza, Salt River Project, P.O. Box 52025, Phoenix, AZ 85072-2025.

105. N. V. Mesland, Tot Keuring Van Elektrotechnische, Materialen, 6800 ET Arnhem, P.O. Box 9035, The Netherlands.

106. D. E. Morrison, 333 Oxford Road, East Lansing, Michigan 48823.

107. Walter E. Myers, R&D Manager, Bonneville Power Administration, P. O. Box 3621, Portland, OR 97208.

108. D. L. Nickel, Manager, ABB Power Systems, Inc., 777 Penn Center Blvd., Pittsburgh, PA 15235-5927.

109. S. Nilsson, Program Manager, Electric Power Research Institute, Electrical Systems Division, 3412 Hillview Avenue, P.O. Box 10412, Palo Alto, CA 94303.

110. B. M. Pasternack, American Electric Power Service Corp., 1 Riverside Plaza, P.O. Box 16631, Columbus, OH 43216-6631.

111. J. Z. Ponder, PJM Interconnection, 955 Jefferson Ave., Norristown, PA 19426.

112. J. W. Porter, Electric Power Research Institute, Suite 100, 1019 Nineteenth St. N.W., Washington, DC 20036.

113. M. Rabinowitz, Electric Power Research Institute, 3412 Hillview Avenue, P.O. Box 10412, Palo Alto, CA 94303.

114. J. J. Ray, Division of Syst. Planning, BPA, P.O. Box 3621, Portland, OR 97208.

115. T. W. Reddock, Electrotek Concepts, Inc., 10305 Dutchtown Rd., Suite 103, Knoxville, TN 37932.

116. J. R. Rempel, Physicist, Defense Intelligence Agency, Washington, DC 20340-6761.

117. H. L. Robidoux, Metropolitan Edison Company, 2800 Pottsville Pike, P. O. Box 16001, Reading, PA 19640-0001.

118. F. Rosa, Division of System Intg., Nuclear Regulatory Commission, MS P1030, Washington, DC 20555.

119. V. G. Rose, Pacific Gas & Electric Co., 123 Mission Street, San Francisco, CA 94106.

120. C. H. Rush, Construction Department, Philadelphia Electric Co., 2301 Market St. (S25-1), Philadelphia, PA 19101.

121. J. E. Scalf, Florida Power & Light Company, P. O. Box 14000, 700 Universe Blvd., Juno Beach, FL 33408.

122. Virgil Schafer, Engineering Division Manager, Tri-State Generation and Trans. Assoc., 12076 Grant Street, Denver, CO 80233.

123. W. G. Schiffmacher, Long Island Lighting Company, Office of Engineering & Constr., 1660 Walt Whitman Road, Melville, NY 11747.

124. W. J. Scott, Hq DNA/RAEE, 6801 Telegraph Road, Alexandria, VA 22310-3398.

125. Joe Sefcik, Nuclear Design, Lawrence Livermore National Lab, P.O. Box 808, L-22, Livermore, CA 94550.

126. C. H. Shih, Manager, Electrical Research, American Electric Power Service Corp., 1 Riverside Plaza, Columbus, OH 43215.

127. M. L. Sloan, Austin Research Associate, 1101 Capital of Texas Highway S., Building B, Suite 210, Austin, TX 78746.

128. R. B. Spence, Bonneville Power Administration, P.O. Box #3621 - MOEA, Portland, OR 97208.

129. G. I. Stillman, Research & Development, New York Power Authority, 1633 Broadway, New York, NY 10019.

130. P. Sullivan, Philadelphia Electric Co., 2301 Market Street (S10-1), Philadelphia, PA 19101.

131. R. L. Taylor, Director - Power Supply, Florida Power & Light Co., 9250 W. Flagler, Miami, FL 33102.

132. L. L. Taylor, Northern States Power Company, 414 Nicollet Mall, Minneapolis, MN 55401.

133. E. R. Taylor, ABB Power Systems, Inc. , 777 Penn Center Blvd., Pittsburgh, PA 15235-5927.

134. A. N. Terreri, Electrical Operations, Green Mountain Power Corp., P. O. Box 850, South Burlington, VT 05402.

135. F. M. Tesche, Consulting Scientist, 6921 Spanky Branch Dr., Dallas, TX 75248.

136. M. V. Thaden, Potomac Electric Power Co., 1900 Pennsylvania Ave., NW, Rm. 311, Washington, DC 20068.

137. G. F. Thompson, Northeast Utilities Service Co., P. O. Box 270, Hartford, CT 06141-0270.

138. J. Towle, 3906 Bagley Ave. N., Suite 100, Seattle, WA 98103.

139. E. F. Vance, 6885 Rendon Bloodworth Road, Fort Worth, TX 76140.

140. D. R. Volzka, Senior Project Engineer, Wisconsin Electric Power Company, 333 West Everett Street, Milwaukee, WI 53201.

141. Jan Wagers, Power Systems Planning, City of Colorado Springs, Department of Utilities, 30 South Nevado, Colorado Springs, CO 80903.

142. R. Walling, General Electric Company, Building 2, Rm 507, One River Road, Schenectady, NY 12345.

143. R. C. Webb, Defense Nuclear Agency, RAEE, 6801 Telegraph Road, Alexandria, VA 22310.

144. L. B. Wideman, Houston Lighting & Power Co., P. O. Box 1700, Houston, TX 77001.

145. E. P. Wigner, Consultant, 8 Ober Road, Princeton, NJ 08540.

146. M. W. Wik, Forsvarets Materielverk, Stockholm, S-11588, Sweden.

147. M. Williams, Professor, Department of Economics, Northern Illinois University, DeKalb, Illinois 60115.

148. D. Woodford, Suite 400, 1619 Pembina Ave., Winnipeg, Manitoba, R-3T-2G5, Canada.

149. S. E. Wright, Electric Power Research Institute, 3412 Hillview Ave., P.O. Box 10412, Palo Alto, CA 94303.

150. F. S. Young, Director, Electrical Systems Division, Electric Power Research Institute, P.O. Box 10412, Palo Alto, CA 94303 .

151. R. M. Youngs, Seattle City Light, 1015 Third Avenue, Seattle, WA 98104.

152. R. W. Zwickl, Space Environment Laboratory, Mail Stop R/E/SE, Boulder, CO 80303.

153. J. A. Zychinski, Union Electric Company, P. O. Box 149, M/C 661, St. Louis, MO 63166.

154. Office of Assistant Manager for Energy, Research and Development, DOE-ORO, P.O. Box 2001.

155-164. OSTI, U.S. Department of Energy, P.O. Box 62, Oak Ridge, TN 37831.

END

DATE FILMED

3/26/92